Free-Field Ground Settlement and Static Instability of Liquefiable Soil

By

Franklin Ricardo Olaya Trinidad

A dissertation submitted in partial satisfaction of the

requirements for the degree of

Doctor of Philosophy

in

Engineering - Civil and Environmental Engineering

in the

Graduate Division

of the

University of California, Berkeley

Committee in charge:

Professor Jonathan D. Bray, Chair
Professor Adda Athanasopoulos-Zekkos
Professor Douglas S. Dreger

Spring 2023

Abstract

Free-Field Ground Settlement and Static Instability of Liquefiable Soil

by

Franklin Ricardo Olaya Trinidad

Doctor of Philosophy in Engineering – Civil and Environmental Engineering

University of California, Berkeley

Professor Jonathan D. Bray, Chair

The likely amount of free-field ground settlement following soil liquefaction can be used as an engineering demand parameter to assess the ground damage due to liquefaction. Its estimation can be improved using recently collected laboratory test results from cyclic tests performed on uniform clean sand, uniform nonplastic silty sands, and uniform nonplastic silts, and from new liquefaction-induced ground settlement field case histories developed from the reconnaissance efforts conducted in Christchurch and Wellington in New Zealand after the 2010-2011 Canterbury earthquake series and the 2013-2016 northern South Island earthquakes, respectively. This new information has been incorporated in the development of a probabilistic procedure for estimating liquefaction-induced free-field ground settlement.

The strain potential of liquefied soil is studied using a large database of cyclic laboratory test results on nonplastic uniform clean sands, silty sands, and silts. This database enabled exploring the cyclic maximum shear strain and the post-liquefaction volumetric strain responses using different measures of state (i.e., relative density, void ratio, and state parameter). In contrast to current state-of-practice approaches that are based on clean sand, this study developed a series of probabilistic models that capture the post-liquefaction volumetric response of a wide range of nonplastic uniform soil.

To complement the insights gained from the laboratory testing, a comprehensive database of 205 well documented case histories of liquefaction-induced free-field ground settlement was developed. Well-documented field case histories provide valuable information about the interacting effects of variable soil properties within sites with differing stratigraphic profiles, and multi-directional ground shaking of differing intensities and duration. This information is key for developing robust empirical models. A case history results from the combination of a site with laterally consistent stratigraphy with at least one cone penetration test, an earthquake event, and post-liquefaction ground settlement measurements. In this thesis, case histories are classified into hydraulic fills and natural soil deposits. Hydraulic fills are relatively uniform hydraulically deposited structures whereas natural soils are heterogeneous layered systems that result from complex geological processes.

The proposed probabilistic model for estimating liquefaction-induced free-field ground settlement is based on the laboratory-based relationships for post-liquefaction volumetric strain developed through this research. Comparison against high-quality case histories led to the inclusion of adjustment factors in the model to capture field observations. As a result, the model captures the influence on settlement of the ground motion intensity and duration and the site's compressibility. The amount of ground settlement largely depends on the subsurface soil state. Hence, as part of this study, correlations to estimate relative density and the state parameter are developed to enable use of the laboratory-based volumetric strain models for a wide range of different soil types.

In engineering practice, the estimation of liquefaction-induced ground settlement is separated from the ground motion intensity measure estimate. Hence, settlement is typically estimated based on a single ground motion intensity measure. A performance-based engineering procedure is employed so the full range of the ground motion intensity measure is considered when estimating annual rates of exceedance of liquefaction-induced ground settlement. The procedure convolves the hazard calculation for the ground motion intensity measure with the probabilistic model for liquefaction-induced free-field ground settlement to produce hazard curves for liquefaction-induced ground settlement. The uncertainty in the inputs to the seismic hazard component and in the inputs to the ground settlement estimation are explicitly incorporated in the procedure using a logic tree approach. The proposed procedure can be used in practice to perform a performance-based assessment of liquefaction-induced ground settlement and its resulting damage to infrastructure.

Lastly, a soil specimen subjected to the constant shear drained stress path can transition suddenly from a stable drained shear condition to an unstable undrained mode of shear. It is a dangerous triggering mechanism because instability is triggered without warning and at small deformation levels (typically < 1% in shear strain). The constant shear drained-to-undrained mode of shear is thought to be a primary mechanism of static liquefaction flow failures. For example, it is thought to be the triggering mechanism leading to the Aberfan coal tip failure in 1966 and the Fundao mine tailings failure in 2015. However, the data available from tests performed with this stress path are largely limited to clean sands. Few tests have been performed on fine sand and silt tailings. Due to the relevance of this stress path as a triggering mechanism leading to instability of mine tailings materials, a series of dense-of-critical and loose-of-critical state constant shear drained stress path triaxial tests have been performed on test specimens of a tailings silty sand. Supporting laboratory tests that provide a thorough mechanical characterization of the material are provided (e.g., isotropically consolidated drained and undrained triaxial tests, and one-dimensional compression tests). The formulation of a generalized critical state constitutive model (i.e., NorSand) is extended so it reproduces key responses observed during the laboratory tests performed in this study. The extended NorSand constitutive model can be used to examine the field response of this material and similar tailings materials.

Table of contents

List of figures

List of tables

Acknowledgments

The research presented in this dissertation was possible due to the support from many institutions including the U.S. National Science Foundation (NSF) through Grant CMMI-1956248 and the California Department of Transportation (Caltrans) through Agreement 65A0774 Amendment Number TO 005. The Jane Lewis Fellowship at UC Berkeley through the 2019 and 2021 Awards supported the development of Chapter 6 of this thesis. Additionally, the College of Engineering at the University of California, Berkeley (UCB) provided support through the Faculty Chair in Earthquake Engineering Excellence. The financial support from the NSF and Caltrans is gratefully acknowledged. All opinions, recommendations, and conclusions expressed in this dissertation do not necessarily reflect the views of the above institutions.

I would like to express my deepest gratitude to my advisor, Professor Jonathan Bray. During my time at Berkeley, he has given me the freedom to explore my intellectual interests and taught me how to use research to solve impactful engineering questions. Through his personality, intellectual creativity, and dedication he has inspired me in multiple ways. Thanks to him, I have become a better researcher, engineer, and individual. It has been an honor and privilege to have worked with and learned from him. Thank you, Professor Bray, for being an advisor much beyond research.

I am grateful to Professor Norman Abrahamson. Even though he is perhaps one of the busiest individuals I have ever met, he always found the time to meet and kindly share his knowledge, insights, and advice. I truly admire his dedication to another's learning and his ability to explain complex concepts in ways that people of different professions can understand. Chapter 5 of this thesis could not have been possible without the help of Professor Abrahamson.

Professor Michael Riemer was instrumental in the completion of the laboratory work component of my research. I cannot thank him enough for teaching and guiding me through each stage of a successful experiment. Interpreting a test result is a key component of experimental work and I greatly benefited from his teachings and knowledge. I enjoyed very much our conversations on soil properties and soil response. Chapter 6 of this thesis is the result of our collaboration.

I am grateful to my committee members: Professors Adda Athanasopoulos-Zekkos and Douglas Dreger for their review and insightful comments. I enjoyed Prof. Dreger's seismology classes. They provided me with the fundamentals on strong motion seismology that strengthened my understanding of earthquake engineering.

A big thanks to Zorana Mijic, Greg Lavrentiadis, Camilo Pinilla Ramos, Fernanda Corvillón, and Dayu Apoji. Your support and friendship made my time at Berkeley amazing. My colleagues at Davis Hall who made my Ph.D. journey an enjoyable learning experience: Daniel Hutabarat, Chris Bain, Tessa Williams, Xinyi Qian, Yuval Keissar, and

Hasitha Sithadara. My sincere thanks to the GeoSystems Engineering faculty at UC Berkeley: Professors Kenichi Soga, Robert Kayen, Dimitrios Zekkos, and Nicholas Sitar.

I also want to thank the professionals that mentored me early in my career, the late Dr. Ken Been for always making the time to answer my technical questions, and especially Mr. Michael Jefferies. Mike is one of the brightest engineers and researchers I have known, he always selflessly provided advice and shared his knowledge. Mike was pivotal in the development of Chapter 6 of this thesis.

Most of all, I want to acknowledge my dear family. I would not be the person I am today, and I would not have written this thesis if it weren't for the love and teachings of my parents Orlando and Rosa. Thanks to my older brother Orlando for his unconditional support. All these years Orlando has been an exceptional brother and friend. I dedicate this work to you three.

1 Introduction

1.1 Overview

Ground settlement caused by soil liquefaction at level sites can be detrimental to lifeline systems, buried structures, and shallow-founded buildings, particularly if differential. Likewise, static instabilities can trigger uncontrolled flow failures as has been observed in recent tailings dams failures. In this thesis, performance-based probabilistic procedures are developed to quantify the likely amount of liquefaction-induced ground settlement. In addition, results from a series of advanced laboratory tests and numerical modeling analyses on a tailings silty sand are presented to identify key instability patterns.

Several widely used field methods for estimating post-liquefaction ground deformation are based on the Ishihara and Yoshimine (1992) laboratory data from one series of cyclic simple shear tests performed on one uniform clean sand reconstituted to three relative densities. It is not clear if the trends of this one dataset are applicable to other clean sands, nonplastic silty sands, and nonplastic silts. In this thesis, a database of 579 test results on post-liquefaction volumetric strain, including 299 test results that relate maximum shear strain to the factor of safety against liquefaction triggering, is compiled and used to examine trends for these soils. The database includes post-cyclic test data on 10 clean sands, 2 gravels, 3 silty sands, 5 silts, and 3 clayey soils. The enlarged cyclic testing database is used to develop models that estimate post-liquefaction volumetric strain and maximum shear strain as a function of soil type, state, and seismic demand. The models are applicable to uniform nonplastic soil. The state parameter is used in addition to relative density and void ratio to characterize the state of the soil. Correlations between these parameters enable the full dataset to inform the models.

Robust procedures should be based on well documented case histories. Consequently, a comprehensive database of 205 ground settlement case histories is developed with the goal to support the development of improved liquefaction-induced ground settlement procedures. This study takes advantage of the numerous site investigations and ground motion recordings following the 2010-2011 Canterbury earthquake sequence and the 2013-2016 northern South Island, New Zealand earthquakes. The geotechnical characteristics of the sites are described, and the procedures used to process the CPT data and the models used to estimate ground motion intensity measures are summarized. The survey techniques employed to estimate liquefaction-induced ground settlement are discussed. The characteristics of a well-defined post-liquefaction ground settlement field case history is shared to illustrate the methodology employed in this study. The database is available as an electronic *flatfile*. Supporting information compiled in this study, such as electronic CPT data and detailed descriptions of the case histories, are shared.

A probabilistic CPT-based procedure for estimating post-liquefaction ground settlement is developed using laboratory and field case history databases, and laboratory-based volumetric strain models. Adjustment factors enable the procedure to capture field observations of post-liquefaction ground settlement. The proposed ground settlement procedure is combined with shear and ejecta-induced settlement procedures to estimate liquefaction-induced building settlement.

Current state-of-practice procedures for assessing liquefaction-induced free-field ground settlement separates the estimation of seismic demand from the ground settlement calculation. Typically, the design ground motion is obtained based on a required return period (or hazard level) and then settlement is computed using the chosen ground motion. In this kind of approach, it is assumed that the hazard level associated with the ground motion is consistent with that of the ground settlement. This assumption may be invalid as design ground motions are usually selected to be above the median motion (e.g., hazard level of 2% probability of exceedance in 50 years), whereas in the settlement calculation median estimates of the input parameters are used (e.g., median estimate of the factor of safety against liquefaction). Alternatively, the probabilistic model for estimating liquefaction-induced free-field ground settlement can be implemented in a performance-based approach that combines the seismic hazard evaluation with the probability of exceeding a given value of settlement to produce hazard curves of free-field ground settlement. The uncertainties in the ground motion hazard and in the settlement model can be included so the full range of settlement hazard curves are obtained. The advantage of the performance-based approach is that it relates hazard with ground settlement in a consistent manner.

Conventionally, soils approach failure with increasing ratio of deviatoric stress to mean effective stress. This situation represents active loading on a soil element (i.e., increment of deviator stress). However, recent failures of tailings dams (e.g., Fundao in 2015) indicate failure can be triggered by a reduction of the mean effective stress while the deviatoric stress is kept constant. This kind of mechanism leading to failure is known as the Constant Shear Drained (CSD) stress path. This unconventional failure mechanism is brittle and has been investigated mostly for clean sands. In this thesis the CSD stress path is investigated for a sample of a tailings silty sand using advanced laboratory testing and numerical modeling. The tailings are characterized by a series of element tests including index testing, one-dimensional compression tests, and isotropically consolidated drained and undrained triaxial tests. The testing enabled the calibration of the NorSand critical state constitutive model. NorSand was further modified to better capture the yielding mechanisms under unloading induced by the CSD stress path.

1.2 Organization

This thesis is organized in the following chapters:

- Chapter 2 presents the development of functional models for estimating the maximum shear strain during cyclic loading and post-liquefaction volumetric strain of soil. First, the development of a comprehensive database of laboratory test results is presented. 579 test results on post-liquefaction volumetric strain and 299 test results that relate maximum shear strain to the factor of safety against liquefaction triggering were collected. Then, relative density, void ratio, and the state parameter were used to classify the data and regression analyses. The proposed models are compared against the widely used curves of Ishihara and Yoshimine (1992). A new correlation to estimate the state parameter is also presented. Finally, the models are probabilistic and the uncertainty in the estimate is provided for each model.

- Chapter 3 describes the analysis and collection of CPT-based case histories of post-liquefaction free-field ground settlement. A definition of what constitutes a case history is first presented followed by detailed descriptions of the geotechnical characteristics of the case histories, available CPT data, and groundwater measurements. The correlations used to estimate the in-situ soil state and the liquefaction triggering procedures employed are described. As part of the case history development process a number of ground motion intensity measures and liquefaction severity indexes were also obtained for each case history. Finally, the sources and assessment of free-field ground settlement are discussed. The main product of this chapter are electronic files containing a flatfile with the case histories and supporting information.
- Chapter 4 presents the formulation of a probabilistic procedure for estimating liquefaction-induced free-field ground settlement. This procedure captures the influence of the ground motion characteristics (e.g., intensity and duration) at the site in the development of earthquake-induced cyclic shear strain and the resulting volumetric strain of soil largely due to its state. Calibration factors as a function of magnitude (MF) and soil compressibility (I_{c15}) are introduced and explained. Finally, a correction factor (C) that accounts for the system response in the field is also presented.
- Chapter 5 describes the implementation of the probabilistic model for estimating liquefaction-induced free-field ground settlement in the performance-based approach. State-of-the-practice approaches for assessing liquefaction-induced ground settlement are summarized. Then, the development of the performance-based procedure is presented based on the convolution of the ground motion seismic hazard with the probabilistic model for liquefaction-induced ground settlement. The main sources of aleatory and epistemic uncertainty are discussed and an example that illustrates their treatment is presented.
- Chapter 6 provides advanced laboratory tests including index testing, one-dimensional compression tests, and isotropically consolidated drained and undrained triaxial tests to mechanically characterize a sample of tailings silty sand. The results of the testing program are used to calibrate the critical state NorSand constitutive model. Then, attention is directed to the constant shear drained stress path. Results from a series of advanced CSD triaxial tests are presented and key behaviors are described. The NorSand constitutive model is extended so it captures correctly the responses observed in the laboratory. The key modifications to the constitutive model are highlighted and the obtained simulated responses described.

2 Strain Potential of Liquefied Soil

The contents of this chapter are primarily from a journal article published in the Journal of Geotechnical and Geoenvironmental Engineering from the American Society of Civil Engineers (ASCE) by Olaya, F.R. and Bray, J.D. entitled: "Strain Potential of Liquefied Soil."

2.1 Introduction

Saturated soil under cyclic loading accumulates shear strain that generates excess pore-water pressure that reduces effective stress. Depending on the intensity and duration of the cyclic loading, the generated excess pore-water pressure can trigger liquefaction. At a free-field, level ground site, liquefaction triggering and the dissipation of the subsequent excess pore-water pressure in the soil produce volumetric strain resulting from sedimentation and reconsolidation processes. The accumulation of volumetric strain in the soil deposit leads to ground settlement that can damage structures, especially if differential. For sites with sloping ground or a free-face slope nearby, the accumulation of shear strain can produce lateral spreads. Lateral spreading of the ground is typically non-uniform with great potential to damage infrastructure. The quantification of the likely amount of ground deformation resulting from these liquefaction effects is important. However, the processes involved in liquefaction-induced volumetric strain and shear strain accumulation in soil deposits are complex and often not captured by numerical simulations.

Empirical procedures are routinely used in engineering practice because they provide reliable estimates of the observed ground performance. Researchers have developed empirical procedures to estimate liquefaction-induced ground settlement and lateral movement using field case history data with models informed by the results of laboratory tests. To analyze trends in the data, the complex processes involved in liquefaction triggering and its consequences are captured using proxies that represent the state of the soil and the seismic demand. Widely used cone penetration test (CPT)-based empirical methods for estimating post-liquefaction ground settlement and lateral spread displacement, such as Zhang et al. (2002) and Idriss and Boulanger (2008), are based on the set of liquefaction test data and family of curves developed by Ishihara and Yoshimine (1992). As shown in Figure 2.1, the calculated factor of safety against liquefaction (FS_L) is used with an estimate of the initial relative density (D_r) of each layer of the liquefied soil to estimate the maximum shear strain (γ_{max}) potential, which is then used with D_r again to estimate the post-liquefaction volumetric strain (ε_v) of each soil layer.

Lee and Albaisa (1974) and Nagase and Ishihara (1988) showed that ε_v increased systematically with increasing values of excess pore-water pressure ratio (r_u) up to a r_u of about 0.9. Once r_u reaches 1.0, volumetric strain is not correlated to r_u as ε_v continues to increase significantly once $r_u = 1.0$. Silver and Seed (1971), Youd (1972), and Tokimatsu and Seed (1987) satisfactorily used cyclic shear strain to estimate seismic-induced sand compression. Other researchers (e.g., Tatsuoka et al. 1984, Ishihara and Yoshimine 1992, and Wu 2002) also found that γ_{max} correlates well with ε_v. Although other parameters have been proposed for estimating ε_v (e.g., the cumulative shear strain; Sento et al. 2004, Kazama 2011) it is challenging to estimate reliably in a straightforward manner the shear strain-

time history in forward analyses. Conversely, γ_{max} can be correlated to FS_L, which is routinely obtained in a liquefaction triggering assessment. Consequently, γ_{max} has been used widely in engineering practice to estimate ε_v. Therefore, test data are characterized in terms of ε_v and γ_{max} in this study.

The often-used Ishihara and Yoshimine (1992) data and relationships provide key insights. They have formed a sound basis for the development of procedures to estimate liquefaction-induced shear strain and post-liquefaction volumetric strain in clean sand deposits that respond like Fuji River sand. However, the Ishihara and Yoshimine (1992) data interpretation and family of curves are derived from one series of cyclic simple shear (CSS) tests performed on just one uniform clean sand reconstituted to three different relative densities (i.e., 47%, 73%, and 93%) and tested at one vertical effective confining stress (i.e., 196 kPa). It is not known if the relationships developed from test data on one uniform clean sand can be applied to other clean sands with other gradations, nonplastic silty sands, or nonplastic silts (e.g., Bray et al. 2017). Recognizing this issue, the examination of more experimental data is warranted. This is the primary motivation of this study.

A comprehensive laboratory database of maximum shear strain and post-liquefaction volumetric strain from 10 clean sands, 2 gravels, 3 silty sands, 5 silts, and 3 clayey soils was compiled and interpreted. A subset of this enlarged database contained enough information to also interpret the relation of the factor of safety against liquefaction and maximum shear strain. The larger database enables the evaluation of trends of the variation of γ_{max}, ε_v, and FS_L with other parameters, including three soil state indexes (the state parameter (ψ_o), relative density, and void ratio (e_o)) for a wider range of soils than examined previously. The findings from this examination supports the development of new models relating γ_{max}, ε_v, and FS_L as a function of ψ_o, D_r, and e_o. A relationship to estimate ψ_o based on D_r is developed when it is not available. The models of cyclic-induced maximum shear strain and post-liquefaction volumetric strain can be used to develop new liquefaction ground deformation procedures.

2.2 Strain Potential Laboratory Database

The laboratory data included in the expanded strain potential database contain information of grain size distribution, initial void ratio or relative density, test type and conditions, and shear strain and volumetric strain measurements. Studies including cyclic resistance ratio (*CRR*) vs. number of load cycles (N_c) for different shear strain levels were used to generate additional information on γ_{max} vs. FS_L. The test results compiled for this study involve post-liquefaction reconsolidation under either K_o or isotropic conditions. Once the cyclic shear stage was completed, the specimens were brought to a zero-lateral-strain equilibrium position to minimize residual strains within the specimen to capture free-field conditions and then drainage valves were opened to allow reconsolidation. Table 2.1 summarizes relevant index properties, such as particle gradation, fines content (*FC*), and plasticity index (*PI*), and test conditions, such as test type, D_r, and vertical effective confinement pressure (σ'_{vc}). Specimen preparation and the applied cyclic stress ratio (*CSR*) were also recorded in the database, in addition to the measured γ_{max} and $\varepsilon_{v.}$ for each series of tests. Additional details of the compiled database are provided in Table A1 of Appendix A. Figure 2.2 displays the range of grain size distributions of the soils in the database.

The laboratory cyclic test database contains 579 γ_{max} - ε_v data points and 299 γ_{max} - FS_L data points. Initially, the datasets on γ_{max} - ε_v for clean sand and gravel materials are examined. Then nonplastic silty sand test data is evaluated, followed by nonplastic silt and low-plasticity silt. Lastly, the volumetric strain response of some clayey soils in cyclic testing is examined because laboratory tests on these materials indicate it is not zero. Like Ishihara and Yoshimine (1992) and several other researchers examining uniform sand data, D_r is employed to bin the data. Bolton (1986) showed that the shear response of different clean sands can be grouped and characterized using D_r provided these sands are of similar uniform gradations. Duncan et al. (2014) also showed D_r is an efficient parameter for characterizing the strength of granular materials of similar gradations represented by their coefficient of uniformity (C_u). Likewise, Whang (2001) analyzed seismically induced compression of different sands using D_r. Later, Duku et al. (2008) combined 16 different sands using D_r to develop a seismic recompression model of a broad range of uniform sands. Engineers often use D_r to characterize the state of a sand, and it is a primary parameter for several constitutive models for sand (e.g., Boulanger and Ziotopoulou 2015). Most of the test data in this study are of uniform clean sands (C_u < 4.5), with only some data on well graded materials which were used only to examine the effects of well graded sands compared to uniform sands. Model development was restricted to uniform soils. In addition to D_r, e_o is employed, which is necessary for plastic soils. Lastly, there is merit to moving from using D_r to using ψ_o as it captures the interacting effects of soil density and confining stress. Thus, the data in which ψ_o can be estimated are interpreted in terms of the state parameter.

2.3 Volumetric Strain Potential in Terms of Relative Density

2.3.1 Volumetric Strain Response of Clean Sand

To evaluate whether all clean uniform sands should necessarily exhibit the same volumetric response to cyclic loading as Fuji River sand, D_r is used initially to characterize the state of the sand. As mentioned previously, D_r has often been used to characterize the state of uniform sand (e.g., Bolton 1986, Whang 2001, Duncan et al. 2014). Data from an additional nine clean uniform sands from different origins, formation processes, and gradations were collected and processed to produce 177 additional data points. The new data cover a wider range of D_r values ranging from 24% to 92%. The enlarged database provides a more robust basis for developing a generalized γ_{max} - ε_v model for clean uniform sand.

The data were subdivided into 10% bins of D_r to explore the influence of the sand's initial state on its post-liquefaction response and to estimate mean (μ) values of ε_v and the uncertainty of this estimate for each bin. Hence, D_r is treated as an independent variable in this part of the assessment. Eight D_r bins were generated, i.e., from 20% - 30% to 90% - 100%, with representative results shown in Figure 2.3 where uniform sand γ_{max} - ε_v data are shown along with the Ishihara and Yoshimine (1992) data points in lighter color for comparison.

Examination of the test data provides useful insights (see Figure A1 in Appendix A for more data than those shown in Figure 2.3): (1) ε_v measurements have significant scatter for each bin of D_r; (2) σ'_{vc} does not have a significant effect on ε_v over the range of σ'_{vc} = 40 –

400 kPa; (3) isotropic reconsolidation (triaxial conditions) and K_o reconsolidation (one-dimensional conditions) produce similar amounts of ε_v; (4) ε_v depends primarily on the induced γ_{max} and not the type of loading; (5) a direct relationship between ε_v and γ_{max} exists, (6) an inverse relationship between ε_v and D_r exists; (7) ε_v increases rapidly as the soil approaches initial liquefaction; and (8) ε_v increases linearly with increasing γ_{max} up to a limiting shear stain of about γ_{max} = 7% to 9% after which ε_v remains relatively constant (within the limits of its inherent variability) at larger shear strain.

The dispersion of the ε_v measurements can be initially characterized by means of a simple linear regression performed over each D_r bin with the standard error of the estimate (standard error) used as the metric for comparison. If an individual uniform clean sand dataset is analyzed (e.g., Ishihara and Yoshimine 1992), the standard error of the ε_v data with respect to the linear fit is usually less than 0.4%. When the results from tests on several uniform clean sands are combined, the standard error for each D_r bin of test data generally increases (e.g., 0.7% to 0.8%) showing that the variability in ε_v for a general clean uniform sand could easily be larger than what is implied in the original Ishihara and Yoshimine (1992) dataset. Hence, the inclusion of several clean sand datasets enables more robust estimates of the general response of a generic uniform clean sand over a wider range of conditions (e.g., larger range of D_r values) with a comprehensive characterization of the overall variability. Importantly, the additional sand data also enable the identification of trends that emerge through combining the individual datasets. Despite the increased variability, the data of several uniform clean sands across the different D_r bins support a linear relationship between γ_{max} - ε_v up to $\gamma_{max} \approx$ 7% to 9%, and past $\gamma_{max} \approx$ 9%, a ε_v plateau is observed. In addition, the larger dataset indicates the Ishihara and Yoshimine (1992) relationship slightly underestimates ε_v for high D_r (≥70%) values (e.g., Figure 2.3b). Conversely, the Ishihara and Yoshimine (1992) relationship tends to overestimate ε_v for low D_r values (≤ 50%). Hence, the development of an updated relationship that accounts for the observed variability is warranted.

2.3.2 Volumetric Strain Response of Nonplastic Silty Sand

Cubrinovski and Ishihara (2000) and Jefferies and Been (2016) showed, with all other conditions maintained, nonplastic fines increase the sand's compressibility, which reduces its penetration and cyclic resistance. Empirical liquefaction triggering methods deal with this difference in penetration resistance in more compressible nonplastic silty sand through an equivalent-clean-sand penetration resistance with the use of a fines content correction (e.g., Idriss and Boulanger 2008). This correction maps the penetration resistance of a silty sand to that of an equivalent-clean-sand so that the liquefaction evaluation can be performed in the clean sand domain where most of the adjustment factors to the cyclic resistance (e.g., magnitude scaling factor) have been developed. However, researchers have questioned whether this corrected equivalent-clean-sand penetration resistance should be used directly with empirically based clean sand γ_{max} - ε_v models (e.g., Zhang et al. 2002, Bray et al. 2017). This issue warrants an examination of silty soil test data to better understand the post-liquefaction response of silty soil.

Cubrinovski (2019) used D_r to examine field-based methods of liquefaction triggering of sands with different amounts of nonplastic fines. He found D_r of a high *FC* soil can be

used to assess the liquefaction potential of sand with fines, and it can be linked directly to that of clean sand to aid in the interpretation of laboratory studies. Use of D_r enables one to explore if clean sands and nonplastic silty sands prepared at the same D_r under the same effective confining stress and sheared to the same γ_{max} develop similar ε_v. The maximum and minimum void ratio tests required to define D_r are typically reserved for soil with less than 5-15% fines. However, Cubrinovski and Ishihara (2002) found that the Japanese Standard method, yielded consistent e_{min} and e_{max} values for sands with nonplastic fines contents of up to 35%. Recently, Mijic et al. (2021a) obtained reasonable e_{min} and e_{max} values for nonplastic silty sand and nonplastic sandy silt with *FC* up to 70%. Moreover, their e_{min} and e_{max} values were not unreasonable for nonplastic silt up to 100% fines. Based on the findings of these studies, D_r is used to enable sand, nonplastic silty sand, and nonplastic silt data of uniform gradations to be compared and interpreted. As noted in previous studies (e.g., Cubrinovski and Ishihara 2002, Thevanayagam et al. 2002), the maximum void ratio decreases with increasing *FC* from 0% to about 30%, and then increases at a higher rate with increasing *FC* beyond about 30%. A *FC* of about 30% marks the transition from a sand-dominated particle structure to a fines-dominated particle structure for nonplastic soil. If composed of similarly shaped particles of the same mineralogy with similar C_u values (i.e., similar compressibility), one might assume for practical purposes a uniform, fine clean sand (SP) responds similarly to a uniform, nonplastic silty sand (SM) and to a uniform, coarse nonplastic silt (ML) if at the same D_r and confining stress. Significant changes in soil response are not expected for soils composed of uniform distributions of similarly shaped quartz particles that cross the #200 sieve at different points (Mijic et al. 2021b). Although the state parameter would be a better unifying index of the state of these soils, most datasets do not provide the steady state line (SSL). Hence, D_r is also used until more ψ_o data are available.

Figure 2.4 shows data from Markham (2015) (*FC* = 6% to 12%) and Beyzaei (2017) (*FC* = 9% to 10%) corresponding to D_r = 70% - 80%. The uniform silty sand (C_u < 4.2) test results are plotted in solid black whereas uniform clean sand (C_u = 1.5 - 3.2) data are plotted in lighter colors for comparison. These test results show that uniform nonplastic silty sand and clean sand produced similar values of ε_v = 1.4% to 2.3% at γ_{max} = 5% to 9%. Conversely, the Toriihara et al. (2000) well graded silty sand data (C_u =18) differ significantly. The ε_v values in this test series are systematically higher than the other silty sand data and clean sand data. This is consistent with the extreme void ratios of this silty sand of e_{min} = 0.94 and e_{max} = 1.53, which are typical of compressible fine-grained soil. Additionally, Tsukamoto et al. (2004) reported this sand could achieve D_r as high as 112% which suggests grain crushing. Hence, it is likely that the unusually high ε_v values of the Toriihara et al. (2000) dataset are due to the high compressibility of the fine matrix and some particle breakage upon shearing. The results of the Markham (2015) and Beyzaei (2017) uniform SM test data are consistent with the SP results discussed previously. The dispersion of the SM test data in each D_r bin is illustrated with the standard error of the linear model estimate, which varies from 0.35% to 0.75%. Data also shows that the standard error increases significantly when the data are combined because there is little overlap in the smaller SM dataset. Additional test results on silty sands are provided in Appendix A (Figure A2).

2.3.3 Volumetric Strain Response of Silt

Cubrinovski and Ishihara (2002) and Thevanayagam et al. (2002) found that the finer fraction controls particle fabric and response of soils with *FC* greater than about 30% indicating that sands with a *FC* greater than about 30% respond more like a silt than a clean sand. Herein, nonplastic silty sand with *FC* greater than about 30% are combined with the data on nonplastic silts classified using the Unified Soil Classification System (USCS) to examine the volumetric response of nonplastic silt. Bray and Sancio (2006), Beyzaei et al. (2018b), Markham et al. (2018), and other researchers have shown that nonplastic silts liquefy in a manner similar to medium-dense angular clean sands in what is termed cyclic mobility. As discussed previously, D_r can be used to characterize the state of nonplastic silt data of uniform gradations (e.g., Mijic et al. 2021a, b).

Beyzaei (2017) reports a series of cyclic triaxial tests with post-liquefaction reconsolidation measurements on Christchurch nonplastic silts with D_r ranging from 47% to 90%. A total of eleven γ_{max} - ε_v data points were collected from her study and plotted to compare with the larger clean sand data (See Figure A3). The standard error of the linear model estimate of the limited Beyzaei (2017) ML test data is 0.20% to 0.60%. A subset of Beyzaei (2017) data is presented in Figure 2.5 with the clean sand data discussed previously shown in lighter colors for D_r = 60% - 70%. The results indicate the uniform nonplastic silt reconsolidates similar amounts as the uniform clean sand across a wide range of densities. These uniformly graded nonplastic silt test data provide no basis for arguing these silts respond differently than uniform clean sand in its post-liquefaction volumetric strain potential. Nonplastic silts with D_r = 61% to 67% in Figure 2.5 reconsolidate similar amounts compared to Kizilirmak River sand with D_r = 62% to 69% and Toyoura sand with D_r = 60%. The nonplastic silt results presented in Figure 2.5 combined with those shown in Figure 2.4 (as well as those shown in Appendix A, Figures A1-A3) indicate uniformly graded nonplastic silty sand and uniformly graded nonplastic silt reconsolidate similar amounts as uniform clean sand if at similar relative densities under similar demands. Due to the limited amount of reconsolidation testing of silty soil relative to that of clean sand, additional testing of nonplastic silty soils is warranted.

2.4 Volumetric Strain Potential in Terms of Relative Density

Initial void ratio (e_o) can be measured accurately in laboratory test specimens of nonplastic soils and soils with plasticity. As opposed to D_r, it can be used reliably to describe the state of soils with plastic fines. Given the intrinsic relation between e_o and D_r for soils of similar gradation, void ratio can track with relative density for clean sand so its use as a unifying state index merits consideration (Figure A4 in Appendix A). In addition, void ratio is a fundamental state index related directly to soil compressibility and strength (Roscoe et al. 1958). Therefore, void ratio is evaluated for its potential to estimate the post-liquefaction volumetric strain of soil.

2.4.1 Volumetric Strain Response of Clean Sand

The γ_{max} - ε_v data from 10 different uniform clean sands analyzed previously in terms

of D_r is re-interpreted using e_o. A linear variation of e_o from 0.53 to 0.81 is observed as D_r reduces from about 90% to 30% for these sands, with e_o varying within a narrower range than D_r. A bin size of 0.05 for e_o is used to interpret the data better than when using a larger bin size which masks details and trends in the data. The standard error of the linear model estimate of ε_v as a function of e_o for an individual uniform clean sand ranges from 0.17% to 0.52%. Combining datasets increases standard error from 0.25% to 0.87%.

The γ_{max} - ε_v data for a representative void ratio bin e_o = 0.65 – 0.70 are shown in Figure 2.6a with a proposed bilinear model that will be described later. Additional insights are gained when examining the data in terms of e_o. For example, the results of the Wu (2002) data of Monterey sand prepared to D_r = 50% to 55% do not belong with the Ishihara and Yoshimine (1992) data of Fuji River sand prepared to D_r = 47% (Figure 2.3a). However, when those two same datasets are evaluated in terms of e_o (Figure 2.6a), the Wu (2002) data has e_o ranging from 0.65 to 0.68 and the Ishihara and Yoshimine (1992) data has e_o = 0.67, so the datasets are now in the same bin. This classification by e_o shows agreement between these two datasets with clear trends in the ε_v -γ_{max} relationships. Similar trends are observed in Figure A5 of Appendix A for other e_o bins.

2.4.2 Volumetric Strain Response of Silty Sand

The nonplastic silty sand data discussed in terms of D_r is also re-interpreted using their e_o. Test results on nonplastic silty sand cover e_o values from 0.70 to 0.87, with representative data shown in e_o = 0.75 – 0.80 bin as shown in Figures 2.6b. ε_v varies from 1.5% to 1.9% for γ_{max} = 5.0% to 6.6% (except for one outlier at γ_{max} = 10.6%). Overall, the silty sand data agree with the linear trend observed in the clean sand data shown in lighter color. Hence, data in Figure 2.6b and the additional data in Figure A5 indicate that the silty sand data and the clean sand data can be grouped and used together for the development of γ_{max} - ε_v models based on e_o.

All these data correspond to $\gamma_{max} \leq$ 8%, where no plateau is reached yet. Similar to what was observed in clean sands, e_o classifies silty sand slightly differently than D_r, i.e., data grouped together in a given D_r bin (Figure 2.4), belongs to different e_o bins (Figures 2.6b). However, regardless of how the data is classified, both D_r and e_o indicate that uniform nonplastic silty sand and uniform clean sand respond similarly. Moreover, the data in Figure 2.6b vary within a narrow range of ε_v and γ_{max} that provides a measure of the dispersion of the silty sand data classified in terms of e_o. This dispersion is consistent with that observed in the larger clean sand datasets in Figure 2.6a. Despite the limited number of test results on nonplastic silty sands, these data show that higher e_o values are related to higher ε_v, and that bilinear models for γ_{max} - ε_v can fit both soils.

2.4.3 Volumetric Strain Response of Silt

The post-liquefaction volumetric strain potential of nonplastic silt and low-plasticity silt can be examined in terms of e_o. As observed for the clean sand data, linear relationships between e_o and D_r are observed for silty soil where e_o varies from 0.60 to 1.26 for a change of D_r from 99% to 20%. Inspection of this trend confirm that silt can exist naturally at

higher void ratios than sand and that silty soil deposits with relatively high void ratios (i.e., $e_o > 0.80$) are likely to reconsolidate more than sand deposits subjected to similar levels of earthquake-induced γ_{max}.

The uniform nonplastic silt data of Beyzaei (2017) is re-evaluated using e_o. Most of the silt data in this study are in the e_o range from 0.70 to 0.90. Figure 2.7a presents representative data in the $e_o = 0.70 – 0.75$ bin where ε_v increases linearly from 1.3% to 1.7% as γ_{max} increases from 4.8% to 6.7%. This trend is consistent with that observed in the uniform clean sand data. Figures 2.5 and 2.7a show that e_o classifies the nonplastic silt data differently than D_r. For example, the Wu (2002) data with $e_o = 0.70 – 0.74$ correspond to D_r = 40%-50% and 60%-70%, whereas the Beyzaei (2017) silt data with $e_o = 0.73 – 0.74$ correspond to D_r = 80%-90%. Similar to nonplastic silty sands, the nonplastic silt in this study's database were sheared to $\gamma_{max} \leq 8\%$ where no plateau developed yet. It is assumed the plateau of constant ε_v develops at $\gamma_{max} \geq 8\%$ as it was observed in the clean sands.

Some reconsolidation testing is also available on low-plasticity clayey silt with $0 < PI \leq 12$. Although low plasticity clayey silty soil can undergo cyclic mobility (e.g., Bray and Sancio 2006), the addition of clay minerals can modify the cyclic response of a silt by limiting excess pore water pressure generation and dissipating relatively more energy in each load cycle (Idriss and Boulanger 2008). As part of this study, reconsolidation of two low-plasticity silty soils from Adapazari and Christchurch (Sancio 2003 and Beyzaei 2017, respectively) was analyzed using e_o as the independent variable. Low-plasticity silt post-liquefaction volumetric strain data with e_o as the independent variable are presented in Figure 2.7b. The low-plasticity silts γ_{max} - ε_v data along with the same e_o-dependent bilinear model formulation employed for clean sand, nonplastic silty sand, and nonplastic silt show that a linear trend between ε_v and γ_{max} exists for $PI \leq 12$ silts up to $\gamma_{max} = 8\%$ after which a ε_v plateau is apparent. Though there are differences in grain size and plasticity, the e_o-based classification of ε_v vs. γ_{max} data captures the overall volumetric strain response of nonplastic soils and low-plasticity silts of uniform gradation with a single bi-linear model formulation that will be described later. Additional data on silts are shared in Appendix A, Figure A6.

The empirical data on uniform clean sand, uniform silty sand, uniform nonplastic silt, and low-plasticity silt presented in this study indicate that e_o may be used to characterize the post-liquefaction strain potential of these soils. e_o is advantageous relative to D_r for soils with high contents of fines because e_o is more widely and better known than D_r for silts. However, it should be noted that the data analyzed herein come from laboratory tests performed under known initial state and controlled boundary conditions. These two conditions are not typically met in the field where the in-situ e_o is difficult to estimate.

2.4.4 Volumetric Strain Response of Clayey Soil

Test data on plastic silts ($PI > 12$) and clays (as per USCS) indicate the excess pore-water pressure generated by cyclic loading can be as high as $r_u = 0.7$ or 0.8 (Donahue 2007). Reconsolidation of the test specimens produce significant volumetric strains even though liquefaction is not triggered. Of the 52 clayey soil test results are available for this study, 30 of the tests by Bilge (2010) were sheared to $\gamma_{max} \leq 2\%$, which does not fully inform ε_v relationships in terms of γ_{max}. The clayey soil tested to $\gamma_{max} > 2\%$ have $e_o = 0.84$ to 1.7 and $13 \leq PI \leq 53$. As shown in Figure 2.8, no appreciable differences in ε_v are observed as a

function of e_o and *PI*. It is possible to capture the response of all clayey soils in this study with a single bi-linear model. Doing so is consistent with observations made from laboratory-based liquefaction tests studies where fine-grained clayey soils with *PI* > 12 develop similar stress-strain loops and similar pore-water pressure time histories. Data suggests that ε_v increases from 0 to about 3.3% in a linear manner with increasing γ_{max} from 0 to 8.0%, after which a plateau at $\varepsilon_v \approx 3.3\%$ is apparent. Additional post-liquefaction reconsolidation testing of clayey soils is warranted to examine these trends further before developing findings for clayey soils.

2.5 Volumetric Strain Potential in Terms of the State Parameter

The steady state line (SSL) parameters of two clean sands (Toyoura and Ottawa), six sands with 5% < *FC* ≤ 12% (Christchurch SP-ML), one silty sand (Christchurch SM), and three silts (Christchurch ML) are available in the compiled database. Testing of these nonplastic soils produced 118 data points that were processed further to obtain their initial state parameter (ψ_o) as defined by Been and Jefferies (1985) as

$$\psi_o = (e_o - e_c)|_{p_o'} \tag{2.1}$$

where e_o is the current (in-situ) void ratio at current mean effective stress, p'_o, and e_c is the void ratio at the critical state at the same p'_o. Hence, ψ_o characterizes the state of the soil by capturing simultaneously the influence of density and confining stress, as well as other factors such as grain size and shape and soil compressibility, using the SSL as a reference state. Jefferies and Been (2016) demonstrated that ψ_o provides a sound basis for describing and modeling soil response across a wide range of stress levels and loading conditions. Thus, from a mechanics perspective it is desirable to develop models for γ_{max} - ε_v based on ψ_o.

Shuttle and Cunning (2007, 2008) showed that the limit between contractive and dilative response of cohesionless soils correspond to $\psi_o \approx$ -0.05. Jefferies and Been (2016) suggested that the contractive/dilative response threshold of ψ_o = -0.05 is representative of simple shear conditions, whereas ψ_o = -0.08 is more representative of shear under triaxial conditions. Robertson (2016) and Mayne and Styler (2018) adopted ψ_o = -0.05 as the limit between contractive and dilative response when the CPT is used to estimate ψ_o in the field. The sandy and silty soils in this database also indicated soils with ψ_o < -0.05 generated ε_v corresponding to dilative responses, which is consistent with these studies. The standard error of the linear estimate of ε_v as a function of ψ_o for an individual uniform clean sand is usually less than 0.53%. The standard error increases if datasets are combined, i.e., 0.36% to 0.98%.

Presentation of the volumetric strain vs. maximum shear strain test data in terms of ψ_o for two representative bins of data are shown in Figure 2.9. The relative density corresponding to each data point in the state parameter plots is also provided. In the ψ_o = -0.05 to 0.0 data range shown in Figure 2.9a, sands with D_r ranging from 24% to 64% and silts with D_r about 80% have similar ψ_o values of -0.024 to -0.009 (i.e., $\Delta\psi_o$ = 0.015). As illustrated in Figure 2.9b, test data on soils with D_r = 66%, 75%, and 90% (a difference of 24%) are represented by ψ_o = -0.162 to -0.170 ($\Delta\psi_o$ = 0.008), indicating that some soils

with different D_r values are at similar initial states in terms of ψ_o. Test specimens with similar ψ_o exhibit similar ε_v when they are subjected to the same level of γ_{max}. Similar observations in terms of stress-strain response curves and liquefaction susceptibility were reported by Been and Jefferies (1985). Although the state parameter is an informative index of the state of soil, its use in developing models is limited by the relatively few studies that provide the SSL (i.e., only about one-fifth of the studies in this database had SSL data). Thus, models using D_r and e_o are also developed because they have more data.

2.6 Laboratory-Based Models of Volumetric Strain Response of Soil

2.6.1 Regression Analysis of the γ_{max} - ε_v Database

Ishihara and Yoshimine (1992) developed their widely used chart containing FS_L - ε_v contours dependent on a clean sand's D_r to develop a procedure to estimate the post-liquefaction settlement of natural sand deposits. Zhang et al. (2002) and Idriss and Boulanger (2008) developed relationships that approximated the Ishihara and Yoshimine (1992) curves to incorporate into their CPT-based procedures. However, these procedures do not clearly state the coupling among FS_L, γ_{max}, and ε_v, and they do not measure the uncertainty of the post-liquefaction ground settlement. Moreover, all procedures based on the Ishihara and Yoshimine (1992) curves are based on laboratory testing of just one clean sand. Cetin et al. (2009b) developed a probabilistic SPT-based post-liquefaction ground settlement procedure using results of a series of laboratory testing on clean sands, including Wu (2002); however, a probabilistic CPT-based procedure is also required in support of performance-based earthquake engineering. In this study, models relating ε_v, γ_{max}, and FS_L are developed for a range of soil types using D_r, e_o, and ψ_o as independent variables and with quantification of the uncertainty of the estimate of volumetric strain.

The assembled database on uniform clean sand, uniform nonplastic silty sand, uniform nonplastic silt and low-plasticity silt indicates ε_v increases linearly with increasing γ_{max} up to a γ_{max} threshold value ($\bar{\gamma}$) of about 7% to 9% for a given soil state, after which ε_v remains relatively constant with increasing shear strain. Accordingly, a bi-linear model for ε_v vs. γ_{max} was adopted with its break point at $\gamma_{max} = \bar{\gamma}$ as

$$\varepsilon_v = \theta \cdot \min(\gamma_{max}, \bar{\gamma}) \cdot e^{\varepsilon} \tag{2.2}$$

where θ represents the model parameters and ε is the error in the estimate. The function defined by Eq. 2.3 is minimized to determine the model parameters.

$$f(\boldsymbol{\theta}, \boldsymbol{\varepsilon_v}, \boldsymbol{\gamma_{max}}, \boldsymbol{\omega}) = \sum_i \left[\omega_i \cdot \left(Ln\,(\varepsilon_{v_i}) - Ln(\theta_i \cdot \min(\gamma_{max\,i}, \bar{\gamma})) \right)^2 \mid \theta \right] \tag{2.3}$$

The term $f\,(\boldsymbol{\theta}, \boldsymbol{\varepsilon_v}, \boldsymbol{\gamma_{max}}, \boldsymbol{\omega})$ is a vector-valued function where vector $\boldsymbol{\omega}$ contains a series of weights ϵ [0, 1] used in the nonlinear regression. The weights were assigned based on the quality, completeness, and extent of the test information. The primary test information are index properties, test type, liquefaction triggering criterion, CRR curves, γ_{max}, and ε_v. Four classes of data were used in this database to represent the quality, completeness, and extent

of the test information as summarized in Table 2.1 in a relative sense according to: "A" with weight = 1; "B" with weight = 0.5; "C" with weight = 0.25; and "D" with weight = 0. Cyclic triaxial testing, with its relatively larger test specimens and hence better resolution in volumetric strain measurements, was generally ranked higher than cyclic simple shear data; however, other variables were considered. The widely regarded dataset from Ishihara and Yoshimine (1992), which was developed using simple shear tests with irregular loading, was assigned as Class A. Class B and Class C datasets had some non-critical characteristics about soil grain size or test conditions not reported. Additionally, Class C datasets had obvious outliers as defined below. The data class criteria are summarized as follow:

- A: Cyclic triaxial test or irregularly loaded cyclic simple shear test. Soil grain size characteristics, and test conditions are sufficiently described; information is available in tables or plots.
- B: Cyclic triaxial or cyclic simple shear test. Some non-critical characteristics about soil grain size characteristics or test conditions were not reported; information is available in tables or plots.
- C: Cyclic triaxial or cyclic simple shear test. Some non-critical information about materials and test conditions were not reported; obvious outliers exist (i.e., an outlier is a data point in a dataset that has more than a 2% volumetric strain deviation from its mean value).
- D: Not satisfying the criteria for classes A, B, or C.

In examining the data there is not a clear value of γ_{max} at which the ε_v plateau starts; rather it ranges from 7% to 9%. Two break points (i.e., $\bar{\gamma}$ = 8% or 9%) in the bi-linear regression models were evaluated to explore this issue. Using $\bar{\gamma}$ = 8% rendered slightly higher coefficient of determination (R^2) and slightly smaller standard deviations across the three state indexes discussed in this Chapter, and therefore, the proposed models in this study use $\bar{\gamma}$ = 8%. Linear, quadratic, and exponential forms for θ were evaluated considering not only how well the data are fit but also considering that θ should allow the model to reproduce mechanistically sound responses over a wide range of densities. For example, data from Ishihara and Yoshimine (1992), Wu (2002), and Cetin et al. (2009a) show that ε_v increases at a higher rate as D_r decreases towards low D_r values. This trend in soil response needs to be captured by the chosen form of θ.

2.6.2 γ_{max} - ε_v Model for Relative Density

It has been shown that uniform clean sand, gravel, nonplastic silty sand**,** and nonplastic silt can be categorized using D_r. After examining separately and observing similar responses, all these data were used in the regression analyses to develop a ε_v - γ_{max} model by setting the model parameter θ in Eq. 2.2 to be a function of D_r. Following the minimization defined by Eq. 2.3, a series of nonlinear regression analyses of the uniform nonplastic soil data were performed using different mathematical forms for θ, first over the entire dataset and then over each individual D_r bin for each trial of θ until an efficient form was found. The resulting model to estimate ε_v (in %) as function of γ_{max} (in %) for a specified value of D_r (in decimal) is:

$$\varepsilon_v = 1.14 \cdot \exp(-2.0 \cdot D_r) \cdot \min(\gamma_{max}, 8\%) \cdot e^{\varepsilon} \quad (2.4)$$

where ε represents the model residual. The form of this model is like that proposed by Yoshimine et al. (2006). The quantile-quantile distribution of residuals obtained from the proposed model was evaluated to select the appropriate scale for the standard deviation (σ). The proposed ε_v - γ_{max} model residuals are normally distributed and unbiased with zero mean and σ = 0.62 in natural log units.

The proposed bi-linear model and the ±1σ range for D_r = 70% - 80% are illustrated in Figure 2.10a where the observed data trends are captured well. The proposed model contours for D_r values from 30% to 90% are shown in Figure 2.10b along with the Ishihara and Yoshimine (1992) clean sand curves for comparison. The results of the regression analyses using the enlarged database indicate ε_v should vary within a slightly narrower range than envisioned previously. For example, the proposed model estimates a maximum $\varepsilon_v \approx 4.1\%$ at large shear strain for D_r = 40%, which is lower than the Ishihara and Yoshimine (1992) estimate of 4.5%. At a high D_r = 90%, the proposed model calculates a maximum $\varepsilon_v \approx 1.5\%$, which is slightly higher than the Ishihara and Yoshimine (1992) estimate of 1.3%. At γ_{max} smaller than 8%, there are also differences in the slope of the linear part of the model, particularly at low densities ($D_r \leq 40\%$) and high densities ($D_r \geq 70\%$). These observed changes are important for CPT applications where the soil profile is subdivided in several layers with different D_r.

The relative performance of the strain potential models is presented in terms of the coefficient of determination, R^2, as it is a measure of how well a model explains the data in each D_r bin and enables comparison with the Yoshimine et al. (2006) model. Ishihara and Yoshimine (1992) did not provide a functional form to their curves so the R^2 of this study's model is compared with that of the Yoshimine et al. (2006) approximation of their curves. Table 2.2 summarizes the R^2 values for each D_r bin. The R^2 values of the proposed model are slightly better than those of the Yoshimine et al. (2006) model. The higher R^2 values achieved with the new model indicate that it is better constrained by new test data at low and high relative densities. Eq. 2.4 is proposed for uniform nonplastic soils, i.e., gravel, clean sand, nonplastic silty sand**,** and nonplastic silt. There is not a significant difference in estimating ε_v due to soil type if D_r is used to characterize the state of these uniformly graded soils using the Japanese e_{max} and e_{min} standards (JIS A 1224:2000).

2.6.3 γ_{max} - ε_v Model for Void Ratio

Similar to the D_r-based model, linear, quadratic, and exponential forms of the model were evaluated to develop a γ_{max} - ε_v model in terms of void ratio. The resulting model to estimate ε_v (in %) as function of γ_{max} (in %) for a specified value of e_o (in decimal) is:

$$\varepsilon_v = 0.07 \cdot \exp(1.98 \cdot e_o) \cdot \min(\gamma_{max}, 8\%) \cdot e^{\varepsilon} \quad (2.5)$$

The model residuals are zero mean normally distributed with σ = 0.58 in natural log units.

Figure 2.11a shows the proposed model for e_o = 0.65 to 0.70 where mostly sand data are included. The proposed model is also compared with silty sand data in the e_o = 0.75 –

0.80 range in Figure 2.6b and with nonplastic silt and low-plasticity silt data in the e_o = 0.70 – 0.75 and e_o = 0.85 – 0.90 bins, respectively in Figure 2.7. The proposed e_o-based model captures reasonably well the ε_v - γ_{max} data over a range of materials and states. The ε_v - γ_{max} contours for e_o values between 0.5 to 1.1 are shown in Figure 2.11b, where ε_v varies from around 1.5% to a 5% over this range of e_o. Table 2.2 presents the R^2 values of the proposed model for each e_o bin. Overall, the e_o-based model performs satisfactorily; however, it may sometimes not capture well clean sand response, specially at high e_o and large γ_{max} (see Figure A9 in Appendix A). Therefore, it should only be used when ψ_o or D_r are not known reliably. Eq. 2.5 is proposed to be used primarily with uniform nonplastic fine soils and uniform low-plasticity soils.

2.6.4 γ_{max} - ε_v Model for the State Parameter

Test data presented in Figure 2.9 showed the state parameter has potential for categorizing the volumetric strain of uniform clean sand, silty sand, and nonplastic silt in a unified manner. Although the state parameter shows promise, there are fewer data available because the SSL was not determined in most of the testing programs. Thus, the γ_{max} - ε_v model for ψ_o developed in this study is considered preliminary. Additionally, there is greater uncertainty in estimating ψ_o in-situ relative to D_r and e_o. The model developed to estimate ε_v (in %) as function of γ_{max} (in %) for a specified value of ψ_o (in decimal) is:

$$\varepsilon_v = 0.50 \cdot \exp(4.0 \cdot \psi_o) \cdot \min(\gamma_{max}, 8\%) \cdot e^{\varepsilon} \qquad (2.6)$$

The model residuals are zero mean normally distributed with σ = 0.56 in natural log units. Initially, the dilative/contractive threshold of ψ_o = *-0.05* was included in the regression analysis because the response of soil changes significantly across this threshold. The results from various regression analyses were compared first over the entire database, next using the database divided in two groups one with ψ_o < *-0.05* and a second one with $\psi_o \geq$ *-0.05*, and finally over each individual ψ_o bin. However, the trends in the data and the scatter were not explained better by including the threshold ψ_o = *-0.05* in the regression. Hence, the model was simplified to the version presented in Eq. 2.6.

The proposed bi-linear model and the ±1σ range for ψ_o = -0.15 to -0.10 are illustrated in Figures 2.12a where the observed data trends are captured well. The proposed model contours for ψ_o values from -0.25 to 0.05 are shown in Figure 2.12b. Like the D_r-based and e_o-based models, ε_{v_max} varies within a range of about 1.5% to about 5% for the range of test data available. Table 2.2 lists the R^2 values of the proposed model for each ψ_o bin. Overall, the ψ_o-based model performs reasonably well considering the limitations of the data. Importantly, the R^2 values are highest for ψ_o between -0.20 and -0.10, which corresponds to the range of ψ_o encountered in many natural soil deposits. Eq. 2.6 may be used with uniform nonplastic soils, although caution is warranted as the database used to develop this model is limited.

Normalizing ψ_o by the slope of the steady-state line λ_{10} provides a measure of potential stress loss as ψ_o/λ_{10} represents the ratio of the current mean effective stress (p_o') to the mean effective stress at the critical state at the same void ratio (p'_c) and $p_o'/p'_c = exp(-\psi_o/\lambda_{10})$. The normalized state parameter ψ_o/λ_{10} captures an undrained load path appropriate for

liquefaction, so there is merit in developing an alternative γ_{max} - ε_v model based on ψ_o/λ_{10}. In the database, λ_{10} ranges from 0.025 to 0.129 (typical of clean sand to silty sand) with much of the volumetric strain data in the ψ_o/λ_{10} range of -6.0 to 2.0. Different bin widths were investigated, and a bin width of 1.25 grouped the data evenly with ψ_o/λ_{10} = -1.25 and 0.0 corresponding approximately to ψ_o = -0.05 and 0.0, respectively. The proposed bi-linear model defined in Eq. 2.7 and shown in Figure 2.13 has zero mean natural log residuals with σ = 0.46 in natural log units.

$$\varepsilon_v = 0.48 \cdot \exp\left(0.21 \cdot (\psi_o/\lambda_{10})\right) \cdot \min(\gamma_{max}, 8\%) \cdot e^{\varepsilon} \quad (2.7)$$

2.7 Maximum Shear Strain Potential of Liquefied Soil

Nagase and Ishihara (1988) assessed the results of many consistently prepared cyclic simple shear tests subjected to irregular and sinusoidal cyclic loads to identify that initial liquefaction (FS_L = 1.0) occurred at a single-amplitude shear strain ($\gamma_{cyc,SA}$) between 3% to 3.5%. Later, Ishihara and Yoshimine (1992) recognized that 3.5% $\gamma_{cyc,\,SA}$ is a convenient threshold because it is consistent with the 5% double-amplitude axial strain ($\gamma_{cyc,DA}$) criterion used in cyclic triaxial tests. Moreover, they identified an inverse relationship between FS_L and γ_{max}. Although other researchers have suggested slightly different strain criteria for defining the onset of liquefaction (e.g., Wu et al. 2004 adopted 3% $\gamma_{cyc,SA}$ based on their cyclic simple shear tests), $\gamma_{cyc,SA}$ = 3.5% is adopted in this study to be consistent with the Ishihara and Yoshimine (1992) database. In cyclic simple shear tests, the CSR corresponding to $\gamma_{cyc,SA} \approx$ 3.5% is termed the cyclic resistance ratio (CRR). The locus of several CRR points corresponding to different equivalent load cycle values (N_c) is called the CRR curve, and N_c = 15 represents the equivalent number of load cycles of a reference earthquake moment magnitude of 7.5 (Seed et al. 1975; Seed 1979). Different cyclic resistance curves would be obtained if different $\gamma_{cyc,SA}$ values were selected. For N_c = 15, the CRR at $\gamma_{cyc,\,SA}$ = 3.5% ($CRR_{3.5\%}$) is linked to FS_L = 1.0 while the CSR at other levels of shear strain will correspond to $FS_L = CRR_{3.5\%}/CSR$. Therefore, CSRs generated at different γ_{max} (e.g., 1%, 3.5%, 7%) can be used to generate different pairs of FS_L and γ_{max}.

From the Fuji River clean sand dataset prepared at D_r = 47%, 73% and 93%, 164 FS_L - γ_{max} data points were available. Wu (2002), Sancio (2003), Markham (2015), and Beyzaei (2017) performed liquefaction resistance tests from which information about CRR vs N_c for $\gamma_{cyc,SA}$ = 3.5% and CSR for $\gamma_{cyc,SA}$ levels other than 3.5% could be retrieved. This information was re-interpreted following the Ishihara and Yoshimine (1992) procedure described previously to generate 62 additional FS_L - γ_{max} data points corresponding to uniform clean sands, uniform nonplastic silty sands, and uniform nonplastic silts for D_r from 45% to 92%. Additionally, test results from Tsukamoto et al. (2004) were re-evaluated and filtered to produce 62 FS_L - γ_{max} data points corresponding to Toyoura sand and Kobe gravel prepared at D_r = 60% to 90%. Lastly, 11 FS_L - γ_{max} data points corresponding to Kobe silty sands prepared at D_r = 72% and 84% from Toriihara et al. (2000) were obtained. Thus, 299 FS_L - γ_{max} data points covering a wide range of relative densities and nonplastic uniform soil types were available for this study as noted in Table 2.1. The new FS_L - γ_{max} dataset is larger than that developed by Ishihara and Yoshimine (1992), and it includes a wide range of soil types as opposed to one clean sand.

The proposed models for γ_{max} as function of FS_L are developed primarily to capture the trends observed in the enlarged database and the data class defined previously. However, the models are not only driven by test data. Two physical constraints are introduced so physically meaningful estimates of γ_{max} are obtained. First, the model must be consistent with the strain level corresponding to FS_L = 1.0 used during the laboratory data reduction; thus, the model is forced to pass though the point (γ_{max}, FS_L) = (3.5%, 1.0) regardless of the soil's state. Second, the model assumes γ_{max} = 0 if $FS_L \geq 2.0$ based on the findings of Dobry and Ladd (1980) who showed clean sand sheared to $\gamma_{max} \leq 0.01\%$ (volumetric threshold strain) developed negligible excess pore-water pressure ($r_u \approx 0$). This is also supported by Marcuson et al. (1990) who showed r_u is on average less than 0.1 if $FS_L \geq 2.0$, and by Nagase and Ishihara (1988) who showed negligible ε_v are generated (which implies negligible γ_{max}), if $r_u < 0.3$. The test results in this database also indicate γ_{max} approaches zero as FS_L approaches 2.0.

2.7.1 FS_L - γ_{max} Model for Relative Density

Examination of the enlarged database indicates that it is appropriate to adjust the trends presented by Ishihara and Yoshimine (1992) to fit the larger dataset better. Initial regressions indicated that a hyperbolic relationship captures the FS_L - γ_{max} data trends well. Thus, hyperbolic forms with different degrees of freedom, including the two constraints discussed previously, were investigated. To avoid having curves at different D_r values cross when relating FS_L and strain potential as will be discussed later, the model required a slightly different curvature once FS_L = 1.0 is crossed; this is particularly important at high D_r. The nonlinear weighted regression resulted in a hyperbolic model that depends on one parameter (A) that is a function of D_r (in decimal) as

$$\gamma_{max} = 3.5 \cdot \left[\frac{2^A - {FS_L}^A}{2^A - 1}\right] \cdot e^{\varepsilon} \qquad (2.8)$$

$$\gamma_{max} = 0\,; \quad \text{for } FS_L \geq 2.0$$

where

$$A = \begin{cases} -2.8 \cdot {D_r}^2 + 10.2 \cdot D_r - 9.8\,; & FS_L \geq 1.0 \\ -275 \cdot exp(-6.6 \cdot D_r)\,; & FS_L < 1.0 \end{cases}$$

The model residuals (ε) are zero mean normally distributed with σ = 0.88 in natural log units. The residuals of the model were analyzed using the same approach as the residuals of the ε_v - γ_{max} models. The quantile-quantile evaluation of residuals supports using natural log residuals. The obtained R^2 values of the proposed model for each D_r bin are listed in Table 2.2.

The proposed model with FS_L - γ_{max} data plotted for two D_r bins are presented in Figure 2.14 with the Yoshimine et al. (2006) model for comparison (additional D_r bins are shown in Figure A11 of Appendix A). Significant scatter exists in the data, especially among data from different sources. For sand at looser states (Figure 2.14a), the additional test data and the Ishihara and Yoshimine (1992) data show similar scatter with the proposed model deviating slightly from the Yoshimine et al. (2006) model. Conversely, the Tsukamoto et al. (2004) data and the additional data from this study for denser soils shown in Figure

2.14b indicate γ_{max} reduces more than what is implied by Ishihara and Yoshimine (1992) data when FS_L exceeds 1.0. The proposed model exhibits stronger curvature than the existing relationship for dense soil. For D_r = 80% - 90%, the proposed model estimates larger γ_{max} than Yoshimine et al. (2006) at low FS_L (e.g., the proposed model estimates γ_{max} ≈ 8.2% for FS_L = 0.6; whereas the other model estimates γ_{max} ≈ 7%). Conversely, at $FS_L \geq$ 1.0 the proposed model estimates smaller γ_{max} than the Yoshimine et al. (2006) model. The proposed model provides improved estimates of γ_{max} at high D_r and high FS_L. The proposed model's fit for other D_r bins can be examined in Appendix A. Eq. 2.8 can be used in conjunction with Eq. 2.4 to estimate γ_{max} and ε_v for uniform nonplastic soil.

2.7.2 FS_L - γ_{max} Model for Void Ratio

The $FS_L - \gamma_{max}$ data can also be evaluated in terms of e_o, with e_o = 0.54 to 0.99. A representative e_o bin is shown in Figure 2.15 along with the proposed model of Eq. 2.9 (additional e_o bins are shown in Figure A12). Similar to the observations from the D_r categorization, significant scatter is observed. Aside from some minor differences, the trends observed using D_r are maintained in the e_o model. For instance, γ_{max} increases rapidly once FS_L < 1.0 at high void ratios (i.e., e_o > 0.70) in Figure 2.15. Following the approach discussed previously, the $FS_L - \gamma_{max}$ data were regressed using a hyperbolic model with two constraints with a change in curvature at FS_L = 1.0. The model parameter (B) is set to be a function of e_o (in decimal) as presented in Eq. 2.9.

$$\gamma_{max} = 3.5 \cdot \left[\frac{2^B - {FS_L}^B}{2^B - 1}\right] \cdot e^{\varepsilon} \qquad (2.9)$$

$$\gamma_{max} = 0\,; \quad \text{for } F_L \geq 2.0$$

where

$$B = \begin{cases} -5.33 \cdot e_o^2 + 2.67 \cdot e_o - 2.4\,;\ FS_L \geq 1.0 \\ -9 \cdot 10^{-3} \cdot exp(8.1 \cdot e_o);\ FS_L < 1.0 \end{cases}$$

The model residuals (ε) follow a zero mean normal distribution with σ = 0.89 in natural log units. The proposed model's fit for other e_o bins can be found in Appendix A. The obtained R^2 values of the proposed model for each e_o bin are listed in Table 2.2. Similar to the observation made during the development of the ε_v - γ_{max} model in terms of e_o, sand data at high e_o are not as well captured by e_o. Eq. 2.9 can be used in conjunction with Eq. 2.5 to estimate γ_{max} and ε_v for uniform nonplastic soil.

2.7.3 Relation Between Relative Density and the State Parameter

Currently, there is not enough FS_L - γ_{max} data available to develop a model using ψ_o. Instead, the current database allows the development and calibration of a relationship between D_r and ψ_o that delivers consistent estimates of ψ_o based on D_r. The calculation of ψ_o requires knowledge of the soil's SSL, and developing the SSL requires a series of specifically designed laboratory tests, which are not typically performed for most projects. However, the Bolton (1986) normalized dilatancy index equation can be used for a zero-dilation condition for sand to develop an estimate of relative density at the critical state

($D_{r_{cs}}$) (Mitchell and Soga 2005) as

$$1 = D_{r_{cs}} \cdot Ln(\sigma'_{cr}/\sigma'_{c}) \tag{2.10}$$

where σ'_{cr} is soil's crushing stress and σ'_{c} the effective normal/confining stress. This equation can be expanded to focus on e_{cs} as

$$e_{max} - e_{cs} = (e_{max} - e_{min})/Ln(\sigma'_{cr}/\sigma'_{c}) \tag{2.11}$$

Using the definition of D_r in conjunction with Eq. 2.10, ψ_o can be obtained as

$$\psi_o = e_o - e_{cs} = \xi \cdot (e_{max} - e_{min}) \left[1/Ln(\sigma'_{cr}/\sigma'_{c}) - D_{r_o}\right] \tag{2.12}$$

where D_{ro} is the in-situ D_r and the coefficient ξ is introduced as an adjustment factor that accounts for the aspects not captured by Eq. 2.12 and the variability of the individual relationships used to develop Eq. 2.12**.** For example, there is significant variability in estimation of ($e_{max} - e_{min}$), and Eq. 2.10 may not have the appropriate form for all soils. The ξ factor was determined through a calibration process using the collected testing database to account for the sources of error in the approximation of Eq. 2.12.

Examination of Eq. 2.12 using the test database showed the estimated ψ_o is not too sensitive to σ'_{cr}, so typical values estimated from Mitchell and Soga (2005) were used (i.e., 8000 kPa for silt; 10000 kPa for silty sand; and 20000 kPa for clean sand). The average of the soil-dependent correlation of Cubrinovski and Ishihara (2002) was used to estimate ($e_{max} - e_{min}$). Figure 2.16 displays the relationship of ξ with *FC* for about 60 test results, which is provided as

$$\xi = 0.724 \cdot \exp(-0.031 \cdot FC) \tag{2.13}$$

where *FC* is expressed in percent as an integer and ξ has an average value of about 0.75 for uniform clean sand, 0.5 for uniform silty sand, and 0.1 for uniform silt. The small ξ for sandy silt and silt are due to ξ correcting for the factors described previously in addition to accounting for the application of the Bolton SSL equation to soils with high *FC*. The R^2 of Eq. 2.13 for ξ is 0.77. Site-specific measurements should be used to improve the reliability of Eq. 2.13 when possible as its current form is recommended for preliminary estimates.

2.8 Relating FS_L and Strain Potential

Ishihara and Yoshimine (1992) developed a widely used figure to estimate ε_v or γ_{max} vs. FS_L as a function of a sand's D_r to estimate liquefaction-induced ground settlement or lateral spreading. Yoshimine et al. (2006) developed equations to capture the individual $FS_L - \gamma_{max}$ and ε_v - γ_{max} relationships presented in Ishihara and Yoshimine (1992). However, the D_r contours drawn by Ishihara and Yoshimine (1992) in their ε_v vs. FS_L figure cannot be obtained by combining the $FS_L - \gamma_{max}$ and ε_v - γ_{max} equations presented in Yoshimine et al. (2006). For example, the Yoshimine et al. (2006) contours in their ε_v vs. FS_L figure cross each other for $D_r \leq 60\%$ when $FS_L \geq 1.0$; whereas the D_r contours drawn by Ishihara and

Yoshimine (1992) do not cross. The shape of their D_r-dependent $FS_L - \gamma_{max}$ relationships when $FS_L \geq 1.0$, especially for high D_r values, is the primary cause of the inconsistency that results when combining the Yoshimine et al. (2006) equations. Using a model with slightly different curvatures once $FS_L = 1.0$ is crossed avoids this issue.

The models presented in this Chapter provide alternative estimates of ε_v and γ_{max} using three measures of the soil's state and the FS_L as a proxy for the seismic demand. These models can be combined to estimate post-liquefaction volumetric-induced free-field ground settlement in a consistent manner. The proposed models presented in Eqs. 8 and 9 avoid the issue described previously by using different curvatures when $FS_L \geq 1.0$ and $FS_L < 1.0$. The relationship between ε_v and FS_L as a function of D_r obtained from combining the $FS_L - \gamma_{max}$ and ε_v - γ_{max} models in this study (i.e., Eqs. 4 and 8) is shown in Figure 2.17 as an example. The proposed equations provide D_r curves that do not cross.

2.9 Conclusion

The primary basis of several of the empirical methods used in engineering practice to estimate post-liquefaction ground deformation is the laboratory data from one series of cyclic simple shear tests performed on one uniform clean sand reconstituted to three relative densities. An enlarged database containing 579 ε_v and 299 γ_{max} data points from cyclic tests on 10 uniform clean sands, 2 gravels, 3 silty sands, and 5 silts was developed to investigate if the trends of this one uniform sand dataset are applicable to other uniform clean sands, uniform nonplastic silty sands, and uniform nonplastic silts. The enlarged database provides a basis to evaluate the effects of parameters such as particle size, PI, D_r, e_o, ψ_o, and FS_L, and to develop models to estimate liquefaction-induced maximum shear strain and post-liquefaction volumetric strain. The proposed models include the uncertainty in the estimate.

The volumetric response of clean sand, nonplastic silty sand, and nonplastic silt in cyclic tests can be interpreted in a unified manner using the state parameter. However, the ψ_o-based model developed in this study is considered preliminary due to the relative sparseness of the data available. It is hoped the ψ_o-based model will be refined as more steady state test data become available. As an alternative to the state parameter, relative density can continue to be used to capture the volumetric response of uniform clean sand. Moreover, a D_r-based model can provide insights on the volumetric response of uniform nonplastic silty sand and uniform nonplastic silt. Whereas the D_r-based model of Ishihara and Yoshimine (1992) is based on the results of just one sand, the proposed D_r-based model is based on a larger database of uniform nonplastic soils. For soils where D_r can be obtained reliably, D_r provides a practical means for categorizing post-liquefaction reconsolidation data. In cases when neither ψ_o or D_r are available, void ratio can be used as the independent variable to characterize the liquefaction strain potential of nonplastic and low-plasticity silts. The database supports the use of bi-linear models to capture the ε_v - γ_{max} relationship for uniform nonplastic soils using ψ_o, D_r, and e_o. The maximum volumetric strain is reached at a maximum shear strain of 8%. The results of the regression analyses using the enlarged database on nonplastic soil indicate ε_v should vary within a narrower range than estimated using the Ishihara and Yoshimine (1992) model.

The compiled database in conjunction with the concept of the volumetric threshold

strain were used to propose new hyperbolic relationships for FS_L vs. γ_{max} with D_r as the primary independent variable for uniform nonplastic soils. A FS_L - γ_{max} proposed model is also presented in terms of e_o. These new models implement equations that produce different curvature above and below FS_L = 1.0 so consistent strain measures are obtained for different values of D_r and e_o. The current database does not contain enough data to develop a reliable FS_L - γ_{max} model in terms of ψ_o. Instead, the available data were used to estimate ψ_o based on the soil's D_r. When combined, the proposed $FS_L - \gamma_{max}$ and ε_v - γ_{max} models developed in this study produce consistent D_r-dependent ε_v vs. FS_L contours.

Additional cyclic testing, especially of well graded clean sand, nonplastic silty sand, nonplastic silt, and low-plasticity silt, considering different states and confining stress are warranted to enhance the current database. Steady state testing should be performed so the ψ_o-based model can be refined. Some of the testing should be performed before liquefaction is triggered and other testing continued well after liquefaction is triggered to strengthen the FS_L - γ_{max} models. Lastly, the proposed models can be used as the basis for developing field-based probabilistic liquefaction-induced volumetric strain and shear strain procedures for a wide range of soils. Limitations of the laboratory-based models (e.g., lack of SSL data) and differences of laboratory testing and field responses of soil (e.g., time under confinement effects for soil that does not liquefy) should be considered when applying the proposed laboratory models to field applications.

Table 2.1. Liquefied soil strain potential laboratory test data

ID	Study	Test Type[4]	Index Properties				Test Conditions		Number of Tests		Data Class
			PI[5]	C_u	FC (%)	USCS	Initial D_r (%)	Confinement (kPa)	ε_v- γ_{max}	γ_{max}-FS_L	
1	Tatsuoka et al. 1984	CTS	NP	2.4	~1	SP	55-86	196	12	-	A
2	Chin 1987	CTX	NP	2.65	0	SP	60	74	16	-	B
3	Ishihara & Yoshimine 1992[1]	CSS	NP	3.2	0	SP	47, 73, 93	196	200	164	A
4	Shamoto et al. 1996	CTX	NP	1.55	0.1	SP	50	100	12	-	A
5	Wu 2002	CSS	NP	1.3	0	SP	38-87	34-182	35	12	B
6	Sancio 2003[2]	CTX	2-25	1.6-2.8	68-100	CL, ML, MH	NA	25-300	32	14	A
7	Tsukamoto et al. 2004	Large CTX	NP	1.55	0	SP	60-80	98	43	38	A
8	Porcino and Caridi 2007	CSS	NP	1.5	0	SP	40-75	100	2	-	B
9	Cetin et al. 2009a	CTX	NP	2.4	0	SP	35-85	100	35	-	B
10	Thevanayagam & Shenthan 2010	CTX	NP	1.7	0	SP	32-81	100	6	-	A
11	Markham 2015	CTX	2-5	1.9-4.2	2.6-95	SP-SM / ML	58-86	37-210	21	4	A
12	Parra 2016	CSS	NP	1.6	< 1	SP	24-85	50-404	14	-	B
13	Beyzaei 2017	CTX	0-15	1.3-2.8	1-100	ML, CL, SP-SM	47-90	35-113	38	32	A
14	Hubler 2017	Large CSS	NP	1.6	0	SP	50, 90	100	2	-	B
15	Toriihara et al. 2000	CTX	NP	18	20	SM	72-112	NA	25	11	D
16	Donahue 2007[3]	CTX	10	>30	77	CL	NA	50	2	-	A
17	Wang & Luna 2014	CTX	6	30	80	ML	NA	90	12	-	C
18	Bilge 2010	CTX	5-59	~ 60	39-97	ML - CH	NA	NA	41	-	B
19	Tsukamoto et al. 2004	Large CTX	NP	35	8	GW-GM	65-90	98	29	24	A
20	Hubler 2017	Large CSS	NP	1.6	0	GP	44, 81	100	2	-	B

Notes: 1. Ishihara and Yoshimine (1992) reinterpreted the test results first published by Nagase and Ishihara (1988); 2. Range of e_{min} and e_{max} estimated from Soils A and G as reported by Donahue (2007); 3. Donahue (2007) reports volumetric reconsolidation results for Soil "G" only; 4. CTS: Cyclic torsional shear; CSS: Cyclic simple shear test; CTX: Cyclic triaxial test; 5. NP: Nonplastic, NA: Not available; 6. Ishihara and Yoshimine (1992) and Tsukamoto et al. (2004) used irregular shear stress time-histories; and 7. Undrained CTX: $\gamma_{max} = 1.5\ \varepsilon_{max}$

Table 2.2. Coefficient of determination (R^2) of the proposed models

γ_{max} - ε_v model							FS_L - γ_{max} model				
Relative density, D_r			Void ratio, e_o		State parameter, ψ_o		Relative density, D_r			Void ratio, e_o	
D_r	Proposed model R^2	Y06 model[1] R^2	e_o	Proposed model R^2	ψ_o	Proposed model R^2	D_r	Proposed model R^2	Y06 model[1] R^2	e_o	Proposed model R^2
40 - 50	0.63	0.56	0.85 – 0.90	0.67	0.05 to 0.05	0.27	40 - 50	0.47	0.41	0.80 – 0.85	0.27
50 – 60	0.54	0.54	0.80 – 0.85	0.79	-0.05 to 0.0	0.46	50 – 60	-	-	0.75 – 0.80	0.79
60 – 70	0.58	0.57	0.75 - 0.80	0.57	-0.10 to -0.05	0.37	60 – 70	0.79	0.71	0.70 – 0.75	0.22
70 – 80	0.55	0.49	0.70 - 0.75	0.54	-0.15 to -0.10	0.76	70 – 80	0.63	0.4	0.65 – 0.70	0.69
80 – 90	0.34	0.22	0.65 - 0.70	0.59	-0.20 to -0.15	0.74	80 – 90	0.44	0.62	0.60 – 0.65	0.14
90 - 100	0.53	0.43	0.60 - 0.65	0.43	-0.25 to -0.20	0.48	90 - 100	0.58	0.62	0.55 – 0.60	0.49

Note 1. The Yoshimine et al. 2006 (Y06) bi-linear model is a parametrization of the Ishihara and Yoshimine 1992 curves.

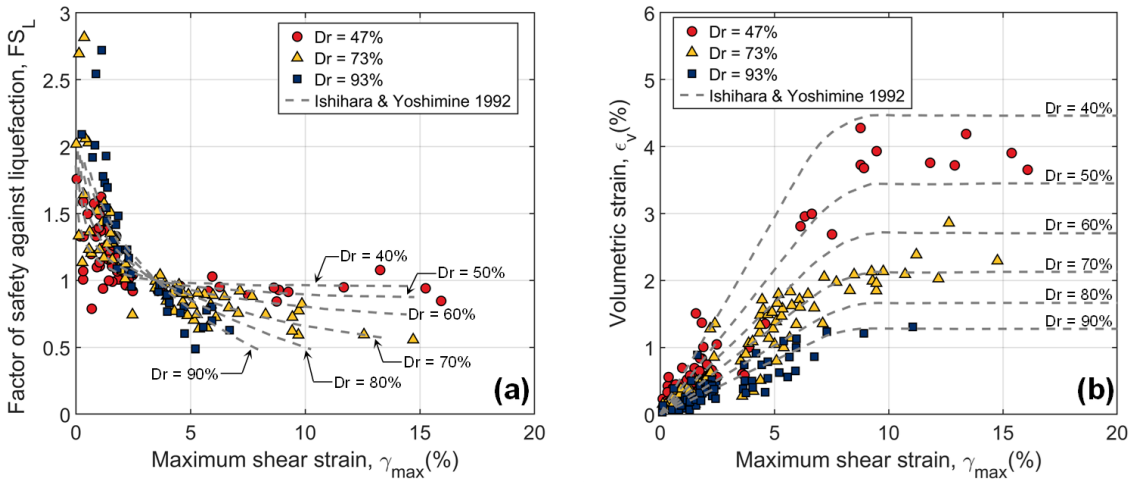

Figure 2.1. Uniform clean sand data from Ishihara and Yoshimine 1992.

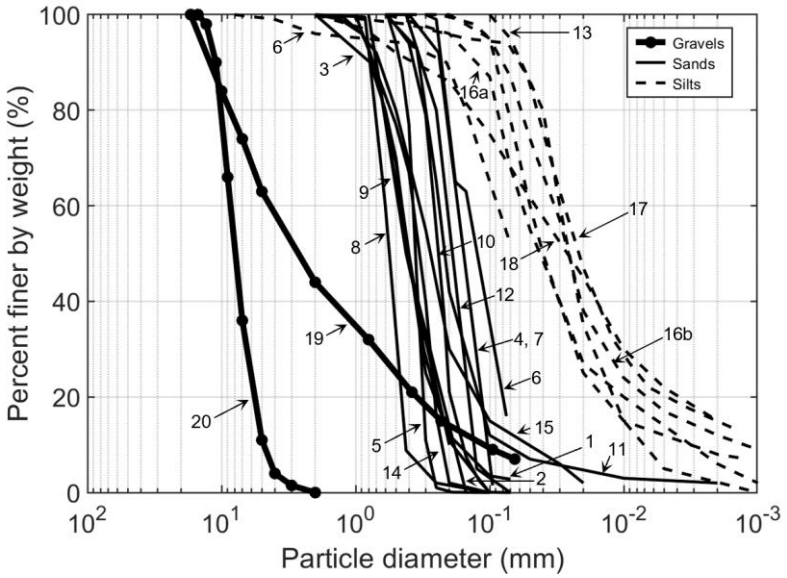

Figure 2.2. Available grain size distribution of soils in the database. Numbers indicate soil's ID in Table 2.1.

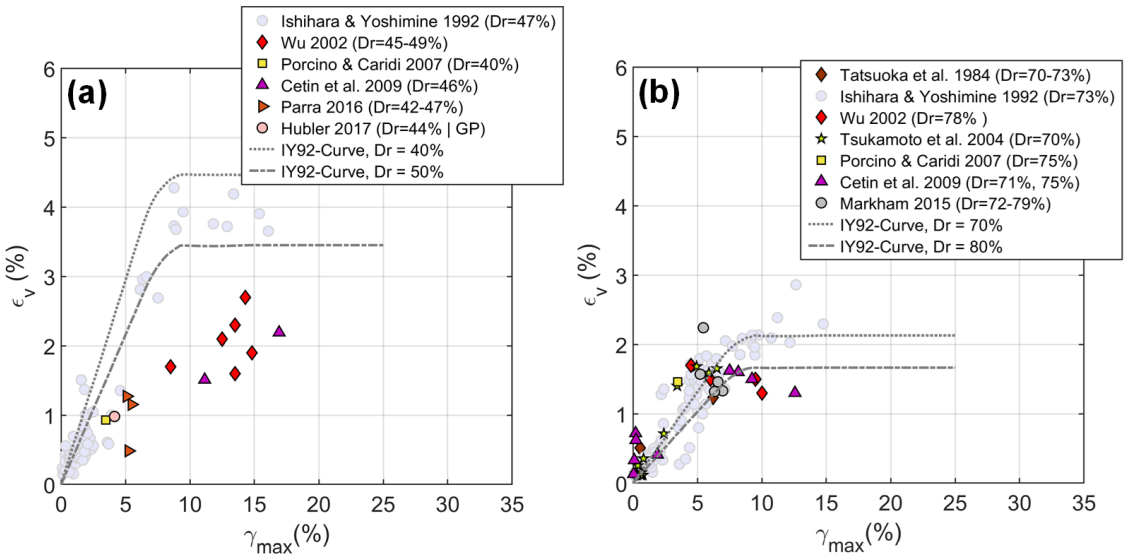

Figure 2.3. Clean uniform sand $\varepsilon_v - \gamma_{max}$ data for (a) D_r = 50% - 60%, (b) D_r = 70% - 80. Ishihara and Yoshimine 1992 data are shown in light blue for reference.

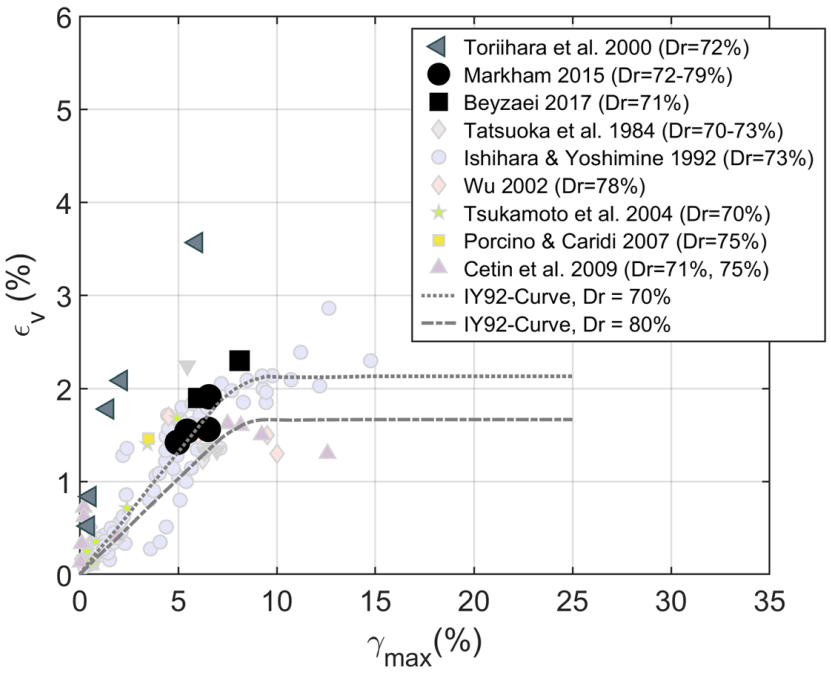

Figure 2.4. Nonplastic to low-plasticity silty sand $\varepsilon_v - \gamma_{max}$ data for D_r = 70% - 80%. Clean uniform sand data shown in light colors.

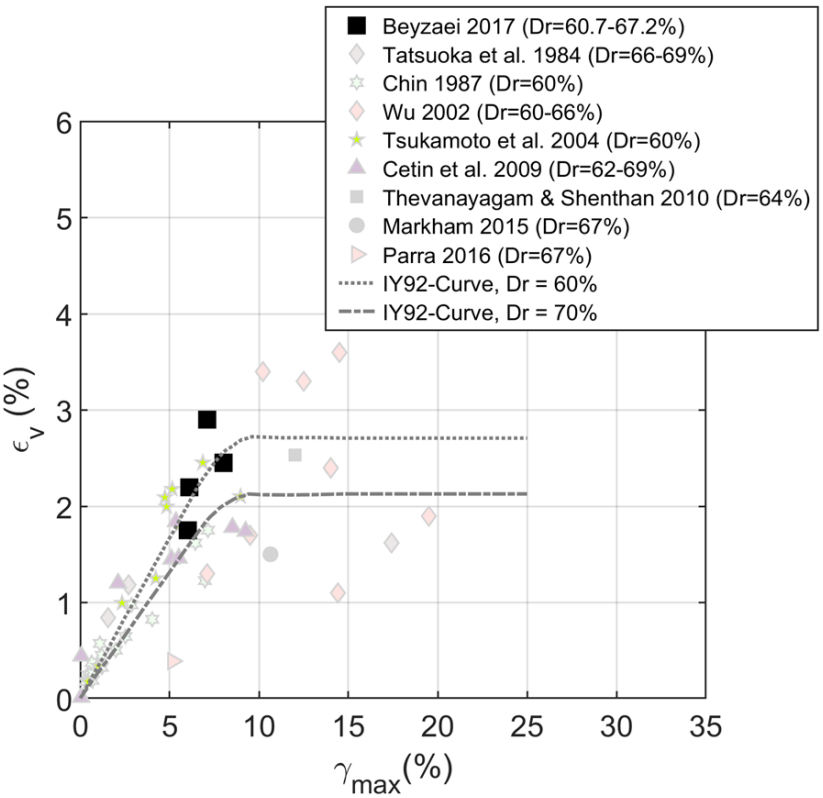

Figure 2.5. Nonplastic uniform silt $\varepsilon_v - \gamma_{max}$ data for D_r = 60% - 70%. Clean uniform sand data shown in light colors.

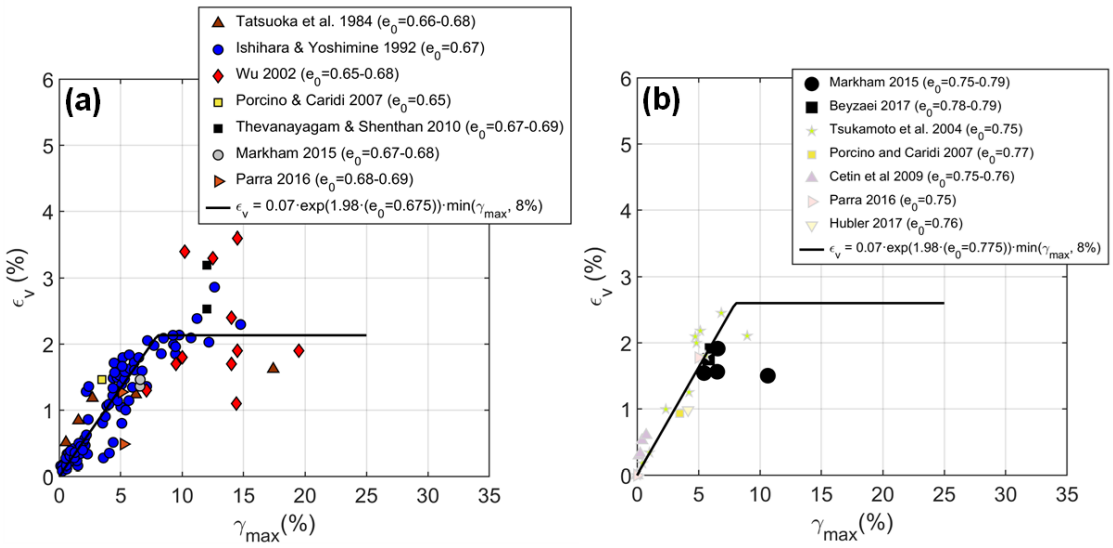

Figure 2.6. $\varepsilon_v - \gamma_{max}$ data in terms of void ratio for clean uniform sand: (a) e_o = 0.65 – 0.70, and for silty sand: (b) e_o = 0.75 – 0.80.

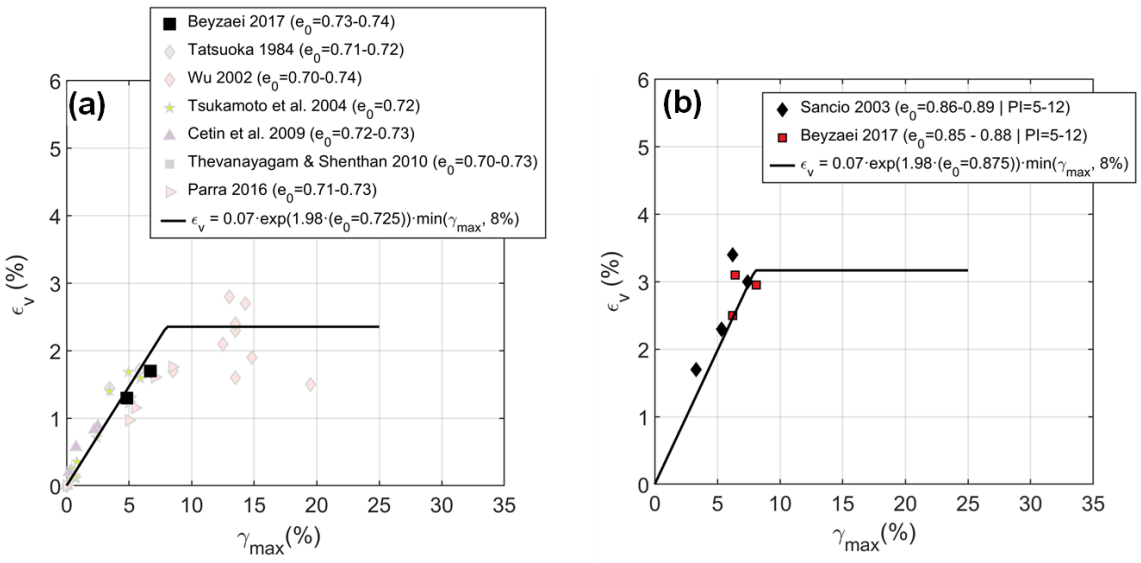

Figure 2.7. $\varepsilon_v - \gamma_{max}$ data in terms of void ratio for nonplastic uniform silt: (a) e_o = 0.70 – 0.75, and for low-plasticity uniform silt: (b) e_o = 0.85 – 0.90.

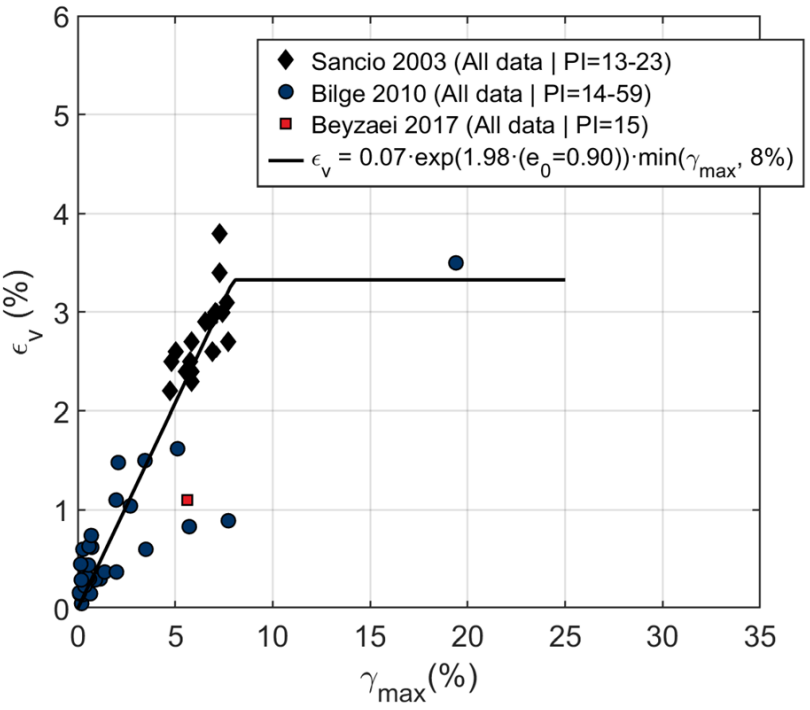

Figure 2.8.. Clayey soil $\varepsilon_v - \gamma_{max}$ data in terms of void ratio.

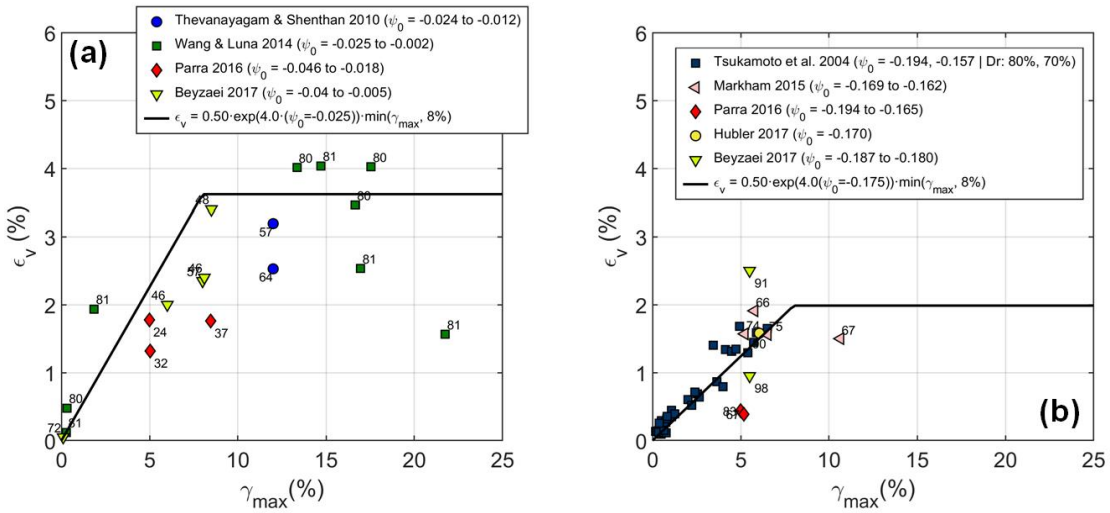

Figure 2.9. $\varepsilon_v - \gamma_{max}$ data in terms of state parameter: (a) ψ_0 = -0.05 to 0.0, and (b) ψ_0 = -0.20 to -0.15. Relative density (in %) provided next to data point.

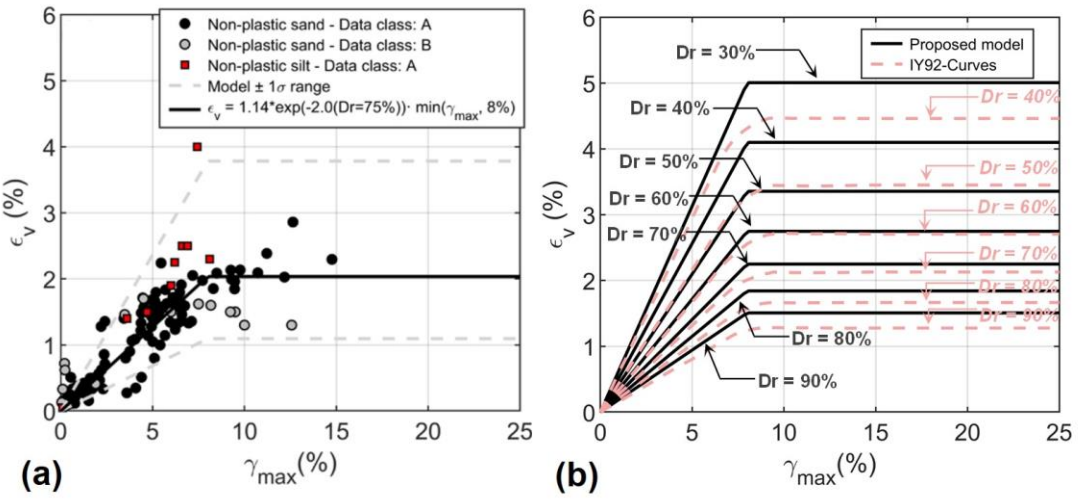

Figure 2.10. Nonplastic uniform soil $\varepsilon_v - \gamma_{max}$ proposed model in terms relative density: (a) D_r = 70% - 80%, and (b) model contours.

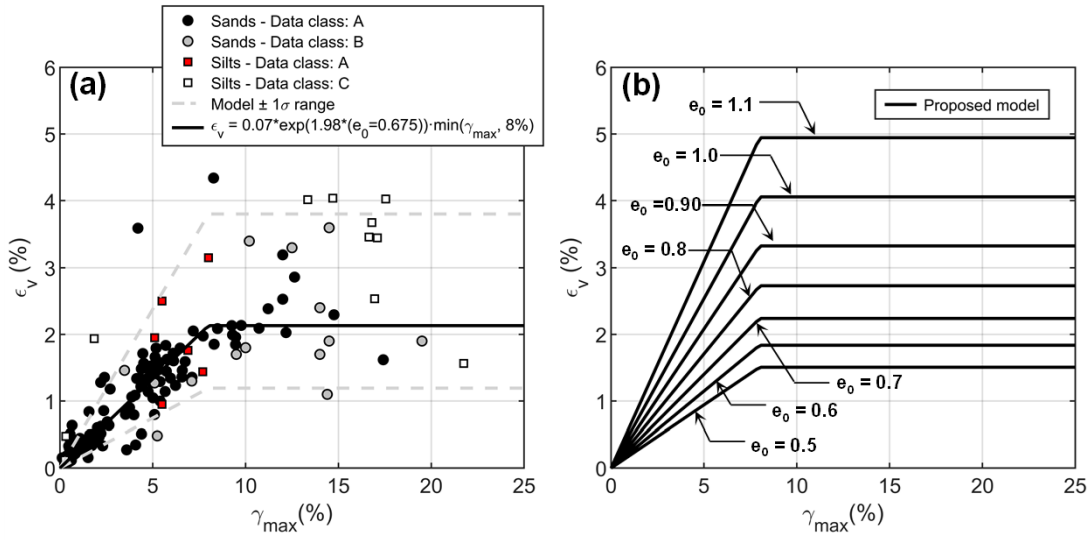

Figure 2.11. Nonplastic uniform and low-plasticity uniform soil $\varepsilon_v - \gamma_{max}$ proposed model in terms of void ratio: (a) e_o = 0.65 – 0.70, and (b) model contours.

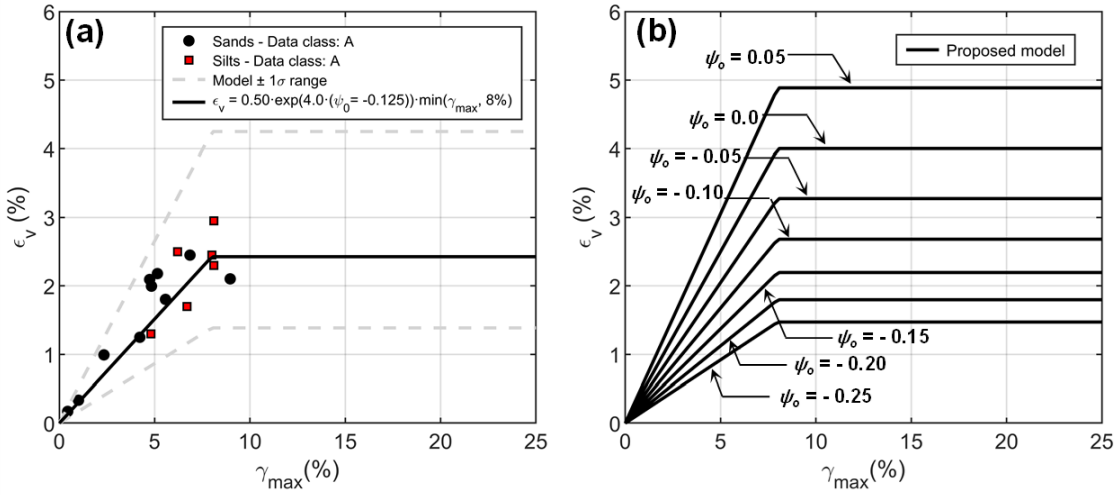

Figure 2.12. Nonplastic uniform soil $\varepsilon_v - \gamma_{max}$ proposed model in terms of state parameter: (a) ψ_0 = -0.15 to -0.10, and (b) model contours.

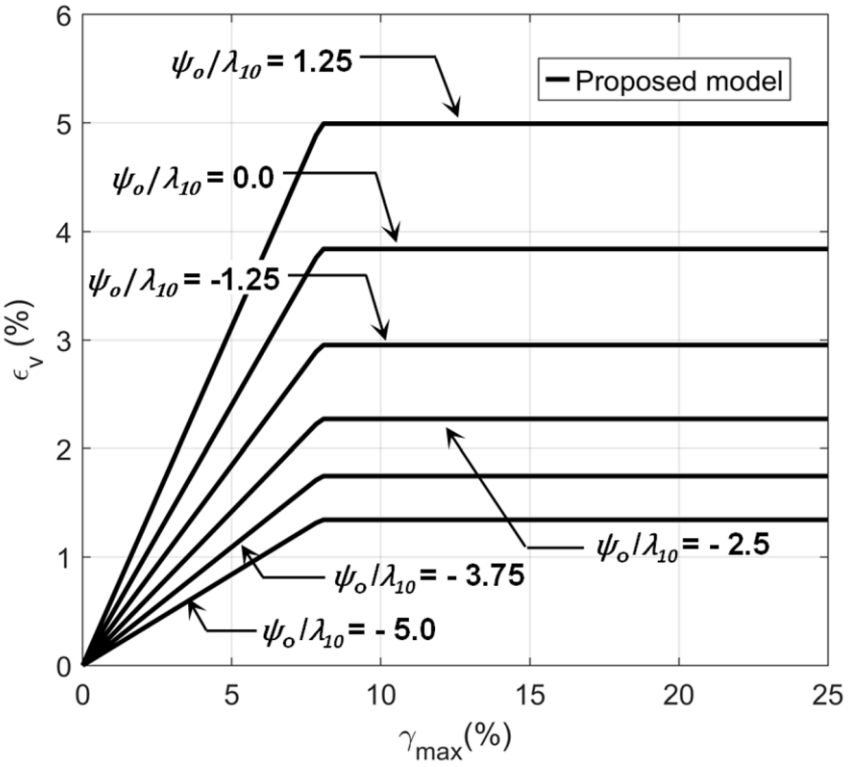

Figure 2.13. Nonplastic uniform soil $\varepsilon_v - \gamma_{max}$ proposed model in terms of the normalized state parameter (ψ_o/λ_{10}).

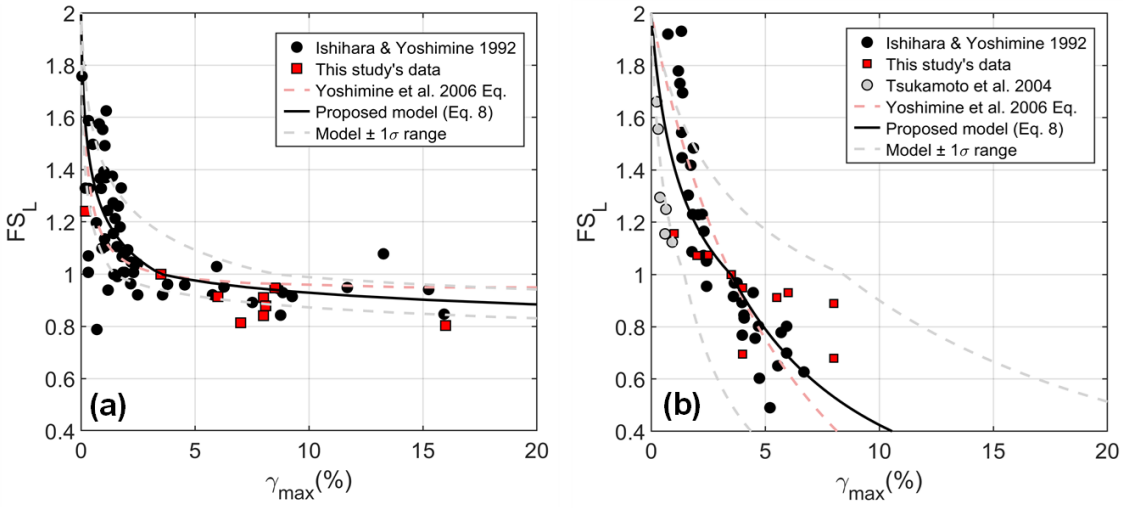

Figure 2.14. γ_{max} – FS_L data and proposed model in terms relative density: (a) D_r = 40% - 50% and (b) D_r = 90% - 100%.

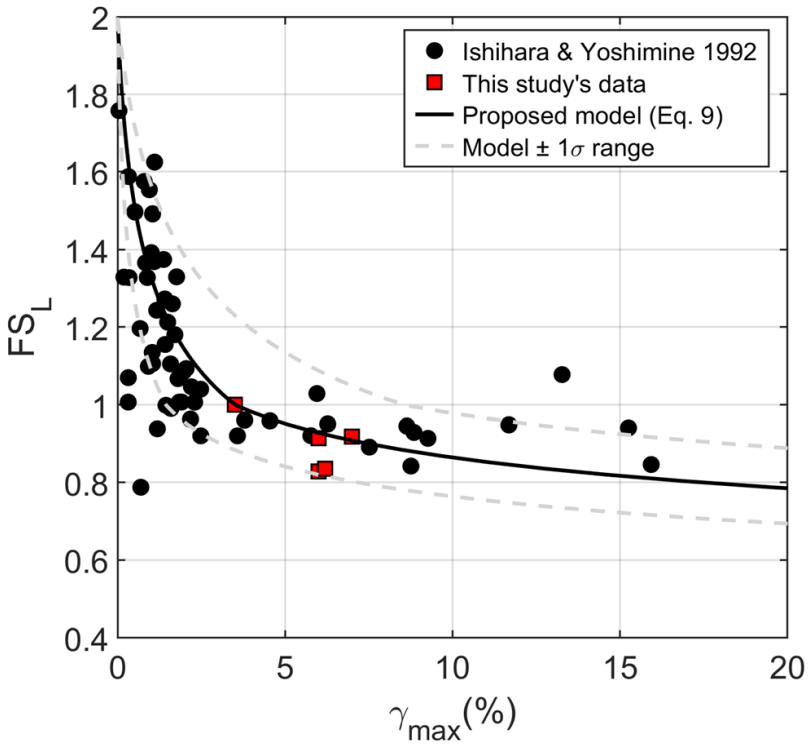

Figure 2.15. γ_{max} – FS_L data and proposed model in terms of void ratio: e_o = 0.80 – 0.85.

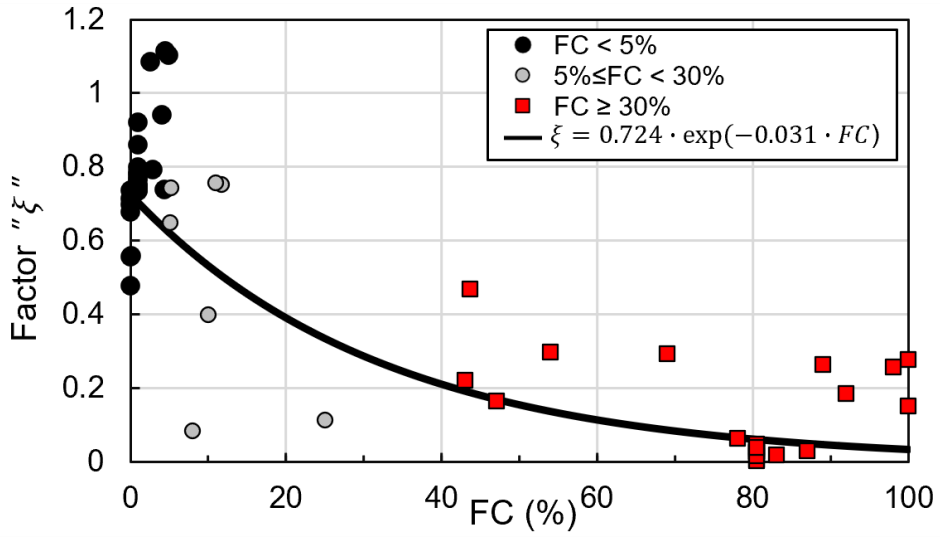

Figure 2.16. Factor ξ in the state parameter relationship.

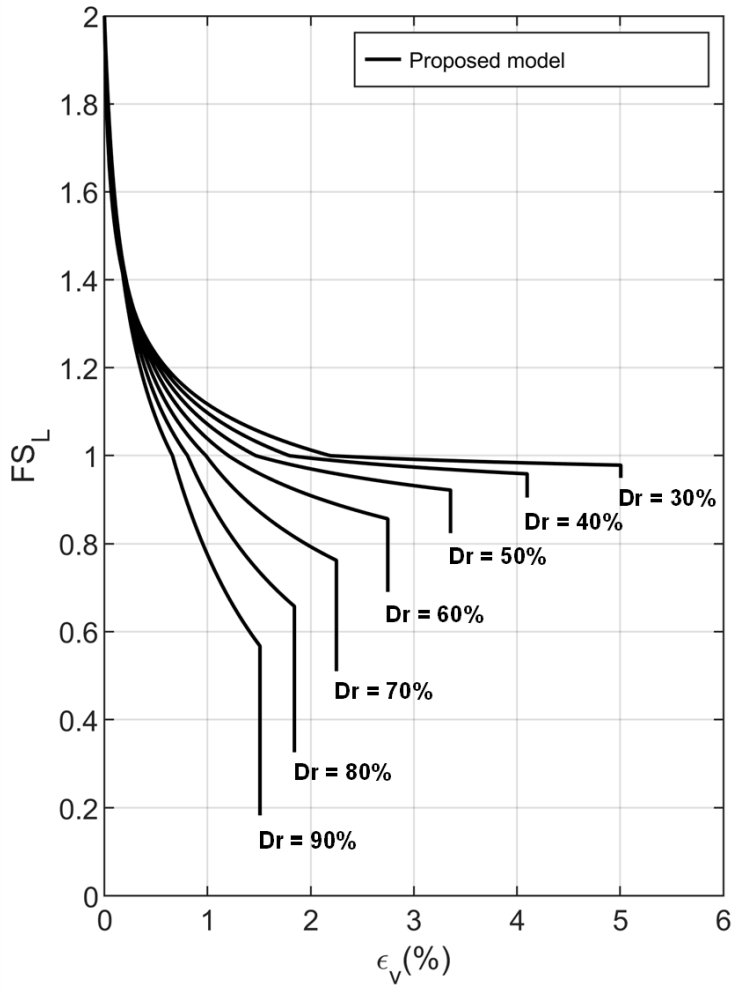

Figure 2.17. Relationship between ε_v and FS_L in terms of D_r

3 Post-Liquefaction Free-field Ground Settlement Case Histories

The contents of this chapter are primarily from a journal article published in the ISSMGE International Journal of Geoengineering Case Histories by Olaya, F.R. and Bray, J.D. entitled: "Post-Liquefaction Free-Field Ground Settlement Case Histories."

3.1 Introduction

Free-field, level ground, liquefaction-induced settlement is a key mechanism of ground failure (e.g., Lee and Albaisa 1974, Ishihara and Yoshimine 1992, and Bray and Macedo 2017). It can be treated as an index of ground damage due to liquefaction in the Pacific Earthquake Engineering Research (PEER) Center performance-based earthquake engineering framework (Deierlein et al. 2003). Liquefaction-induced ground settlement can damage infrastructure, such as buried utilities or light-weight structures with shallow foundations, as reported in the Marina District after the 1989 Loma Prieta earthquake (O'Rourke and Roth 1990). The amount of ground settlement and the time it takes for the settlement to occur depend primarily on the subsurface soil conditions and the earthquake ground shaking.

The mechanisms of liquefaction-induced ground settlement are related to complex particle sedimentation and soil reconsolidation processes that occur during and after earthquake shaking. Sedimentation and reconsolidation occurring within a soil unit are difficult to be captured by continuum-based numerical simulations. Hence, current engineering practice relies on semiempirical models that are based on and validated against field case histories. Early models (e.g., Tokimatsu and Seed 1987, and Ishihara and Yoshimine 1992) were developed considering a relatively small number of case histories, usually characterized with the standard penetration test (SPT). More recent models based on the cone penetration test (CPT) have been widely adopted because of the CPT's superior repeatability and nearly continuous profiling relative to the SPT. However, these methods (e.g., Zhang et al. 2002, Yoshimine et al. 2006, and Idriss and Boulanger 2008) still suffer from being validated against a limited number of field case histories. Consequently, these procedures were developed deterministically with no quantification of the uncertainty of the liquefaction-induced ground settlement estimate.

Assessment of liquefaction-induced ground damage under performance-based frameworks provides valuable information for seismic design. In geotechnical engineering, robust probabilistic procedures for estimating post-liquefaction free-field settlements are required. The initial step in the development of these procedures is a comprehensive database of field case histories that represents sites of different formation processes, with uniform or interlayered stratigraphy, which were subjected to ground motions of different intensities and durations.

Obtaining field case histories with reliable pre- and post-earthquake ground elevation measurements is one of the primary limitations in the development of predictive models of liquefaction-induced settlement. CPT-based investigations and topographic surveys

conducted by the United States Geological Survey (USGS) following the 1989 Loma Prieta earthquake produced some of the first CPT-based well-documented case histories of post-liquefaction settlement in the United States (US). Additional case histories have been gradually becoming available as records of land damage were made available after major earthquakes (e.g., 1999 Chi-Chi, Taiwan and 2011 Tohoku, Japan). Reconnaissance efforts conducted in Christchurch, New Zealand (NZ) after the 2010-2011 Canterbury earthquake sequence have contributed much data related to ground motion recordings, patterns of seismic ground performance, and ground characterization, largely through CPTs, areal imagery, LiDAR measurements, and extensive subsurface characterization campaigns. The combination of this information provides a great opportunity to advance current empirical models. Research by the University of Canterbury, University of California - Berkeley, University of Texas at Austin, and Tonkin + Taylor produced an initial set of 55 well documented sites with predominantly low levels of land damage (Russell and van Ballegoy 2015, and Cubrinovski et al. 2019). Most of these sites correspond to locations where none-to-minor land damage was observed even though simplified liquefaction methods anticipated severe surface manifestations. An additional 34 sites were developed by Mijic et al. (2021c) with the objective to include sites with and without liquefaction manifestations that show no major discrepancies between the estimates from simplified liquefaction methods and the actual field observations. Of these two sets of sites in Christchurch, those with free-field, level ground conditions were investigated further as part of this study. Field case histories in Wellington, NZ from other recent earthquakes were also added.

The primary objective of this Chapter is to document field case histories of post-liquefaction free-field, level ground settlement. Because the CPT has become the preferred in-situ test in research and practice due to its higher reliability compared to the SPT (NRC 2016), only case histories with CPT data available were collected. In addition to ground settlement data and soil profile information, CPT-derived parameters such as the soil behavior type index (I_c, Robertson 2009a) are also documented. The characteristics of the ground motions associated with the case histories are documented through intensity measures (*IMs*) like the ground surface peak ground acceleration (*PGA*), 5%-damped spectral acceleration (S_a), cumulative absolute velocity (*CAV*), and Arias intensity (I_A). A flatfile containing the synthesis of parameters for each case history is provided as an electronic file in addition to the raw electronic CPT soundings (when publicly available) and appendices detailing each case history. These field case histories can be used subsequently in the development of new empirically based probabilistic methods that account for the uncertainty in the settlement estimates to support performance-based earthquake engineering approaches.

3.2 Previous Studies

3.2.1 SPT-Based Case Histories

The landmark works of Tokimatsu and Seed (1987) and Ishihara and Yoshimine (1992) provided useful engineering procedures to estimate free-field post-liquefaction ground settlement based on SPT data. Their procedures are rooted in laboratory-based relationships between the relative density (D_r), the factor of safety against liquefaction

triggering (FSL), and reconsolidation volumetric strains (ε_v). Ishihara and Yoshimine (1992) used 6 SPT case histories from the 1964 Niigata, Japan moment magnitude (M_w) 7.5 earthquake to evaluate the reliability of their procedure. The Niigata sites are predominantly sand deposits with a few localized thin silt lenses. A *PGA* of 0.16 g recorded at a nearby strong motion station was assumed to be representative of the seismic demand at the sites (Ishihara and Yoshimine, 1992).

Wu and Seed (2004) developed a ground settlement procedure based on cyclic tests performed on Monterey 0/30 sand. In contrast to Ishihara and Yoshimine (1992), their model uses a M_w = 7.5 cyclic stress ratio ($CSR_{7.5}$) as a demand term and the overburden-corrected, energy-corrected, clean sand equivalent blow count, $(N_1)_{60,cs}$, as the resistance term. A total of 14 SPT case histories from 7 earthquakes were collected to validate their model. However, in their database they included the Moss Landing site that experienced lateral spreading in the 1989 Loma Prieta earthquake (Kayen and Mitchell, 1997). Thus, this case history was affected by lateral deformation in addition to free-field reconsolidation settlement.

Cetin et al. (2009b) expanded the Wu and Seed (2004) laboratory clean sand data to develop a probabilistic post-liquefaction ground settlement model. In this model, the demand term is defined as CSR_{field} which is the *CSR* corrected for magnitude, unidirectionality of shaking and atmospheric pressure while $(N_1)_{60,cs}$ is kept as the resistance term. For model validation and additional regression analyses, 49 well-documented SPT case histories were collected. They also used these case histories to quantify the variability in the settlement estimate. Some of the case histories in Cetin et al. (2009b) are reported to have been also affected by lateral displacements in the range of 200 mm to 600 mm.

Recently, Mesri et al. (2018) developed a predictive model that depends on the coefficient of vertical compression (m_{vs}) and the excess pore-water pressure generated by the earthquake (u_g). These parameters are formulated as a function of the energy-corrected SPT blow count N60 and FSL. For validation, they used ground settlement observations from 78 case histories from earthquakes with M_w between 7.1 and 8.0, and *PGA* ranging from 0.16 *g* to 0.35 *g*.

The number of SPT case histories of post-liquefaction free-field ground settlement have grown from less than 10 to almost 80 over the last three decades as a result of different research efforts following important earthquake events. Despite these advancements, borehole logs with well documented, reliable SPT data are not readily available and differences between the interpretation of the case histories among the different studies exist. Also, the SPT case histories discussed previously are largely influenced by data from the 1989 Loma Prieta and 1995 Hyogoken Nambu earthquakes. These two events contribute with 80% and 70% of the total number of case histories in the Cetin et al. (2009b) and Mesri et al. (2018) databases, respectively.

3.2.2 CPT-Based Case Histories

Zhang et al. (2002) adapted the Ishihara and Yoshimine (1992) relationship between the factor of safety against liquefaction and reconsolidation volumetric strains to develop a widely used CPT method for estimating liquefaction-induced ground settlement. As part of the study, they developed case histories in the Marina District and Treasure Island after

the M_w 6.9 1989 Loma Prieta earthquake to validate their method. A total of 11 sites were documented and interpreted. These sites generally consist of hydraulic sandy fill on top of natural sand deposits that overly clay deposits and experienced *PGAs* between 0.12 *g* to 0.24 *g*.

Juang et al. (2013) expanded the work of Zhang et al. (2002) by including the probability of liquefaction into the model formulation and by extending the number of free-field settlement case histories to 32. Many sites investigated following the 1999 Chi-Chi earthquake were added to the cases previously reported by Zhang et al. (2002). The Chi-Chi case histories supplies data with recorded *PGAs* up to 0.79 *g*, which adds valuable information to the range of *PGAs* covered by previous case histories. Juang et al. (2013) also reported 32 additional "building case histories" (i.e., cases where the settlement is influenced by building movement).

Sadeghi et al. (2021) performed a series of numerical analyses assuming different soil conditions and ground motion parameters to develop a synthetic dataset of post-shaking settlement. This synthetic dataset was then used as the basis for a functional predictive model. Their model was subsequently compared with 32 free-field ground settlement case histories. Similar to the SPT case histories discussed previously, the CPT case histories presented by Sadeghi et al. (2021) show an important overlap with previous studies (e.g., Juang et al. 2013) with the main addition by Sadeghi et al. (2021) being the inclusion of 6 case histories from the 2010-2011 Canterbury earthquake sequence in Christchurch.

Figure 3.1 shows the growth of the number of SPT and CPT case histories over the last three decades (including the number of case histories added in this study). Before this study, the number of CPT case histories of post-liquefaction free-field ground settlement was less than half of the number of the SPT cases, despite the superiority of the CPT in characterizing the ground relative to the SPT. Additionally, previous liquefaction-induced ground settlement databases do not provide a clear definition of what constitutes a field case history. From the cases discussed previously, it appears that many of the case histories have been defined using a single CPT. This is potentially problematic because closely spaced CPTs are correlated and should not be treated as independent case histories. Moreover, the spatial variability of a site cannot be evaluated if there is only one CPT defining the ground conditions at a site.

3.3 Case Histories and Data Documentation

3.3.1 Post-liquefaction Ground Settlement Case History Definition

The field case histories developed for this study are a collection of subsurface geotechnical data derived mainly from surficial geological information and CPT penetration data; groundwater depth; observations of field performance in the form of pre- and post-event topographic surveys, LiDAR data, or satellite imagery; and characterization of the ground motion associated to the occurrence of liquefaction at the site. In addition to Mw, earthquake ground shaking in liquefaction evaluations is commonly represented by intensity measures (*IMs*) such as *PGA*, S_a, *CAV*, or I_A. Obtaining field case histories with reliable pre- and post-earthquake ground surface elevation measurements is the primary limitation in the development of post-liquefaction ground settlement case histories.

In this study, a case history is defined as the combination of: (1) a site with laterally

consistent soil stratigraphy with at least one CPT, (2) an earthquake event represented by its M_w, ground surface *PGA*, or other intensity measures, and (3) consistent post-liquefaction volumetric-induced free-field, level ground settlement measurements. A site is not defined by a CPT. Instead, a site is defined by its consistent geology and seismic performance. Thus, each case history is a site characterized by a geometric mean set of CPT-derived parameters, which undergoes an estimated level of earthquake shaking, wherein the liquefaction-induced ground settlement was measured. Sites characterized by several CPTs are valuable as they capture the average subsurface conditions and the variability of the CPT parameters across a site. For sites with multiple CPT soundings or multiple point settlement measurements, geometric means of these values are used to represent central values in the case history.

3.3.2 Case History Descriptions

Well-documented field case histories provide valuable information about the interaction effects of variable soil properties, stratigraphy, and multi-directional shaking. This information is key for developing robust empirical models (e.g., Bray et al. 2017). In the context of developing an empirical model, ground motion *IMs* have been used successfully (e.g., Bray and Macedo 2017, Bullock et al. 2019) with representative soil parameters and site conditions presented in the form of soil types captured by indices such as the soil behavior type index (I_c, Robertson 2009a), relative density (D_r) or the state parameter (ψ_o, Been and Jefferies 1985). Before presenting the methodology used to generate the selected *IMs* and soil parameters, a brief description of the site characteristics of the case histories is presented as it provides the necessary background for interpretation of these case histories. In addition, sources of CPT and other field data are given.

Post-earthquake reconnaissance efforts by Bennett (1990), Power et al. (1998), and Hryciw (1991) are the source of the subsurface geotechnical characteristics and post-liquefaction settlement data for the Marina District and Treasure Island sites following the 1989 Loma Prieta earthquake. The Marina District is an 8 m to 10 m thick hydraulic fill site composed of clean to silty sands (SP, SP-SM) with fines content (*FC*) up to 21%. Underlaying the sandy fill is the San Francisco Young Bay Mud clay deposit. Treasure Island is a hydraulic fill located 6.5 km from Marina District. It consists of an 8 m thick, clean to silty sand fill followed by a shoal sand unit of similar thickness overlying the San Francisco Young Bay Mud deposit. The fill and shoal are of similar gradation (*FC* up to 40%) but the shoal deposit shows some clay bridging of particles, particle interlocking, and other fabric effects.

CPT raw data were obtained from the USGS (2021a)/Holzer et al. (2010), the Next Generation Liquefaction Project (NGL, Zimmaro et al. 2019, accessed 2021), and from ENGEO (2015, 2019a, 2019b and 2019c). With the geotechnical and topographic data and the available CPTs, 4 and 5 case histories were defined in the Marina District and Treasure Island, respectively, for the 1989 Loma Prieta earthquake.

Juang et al. (2002) summarize findings from the reconnaissance mission of the Taiwanese National Center for Research in Earthquake Engineering (NCREE) in the cities of Yuanlin and Wufeng. Lee et al. (2011) and Chu et al. (2003) performed additional ground investigations and topographic surveys. Their results provide information about the geotechnical characteristics and post-liquefaction settlement for the Yuanlin and Wufeng

sites after the 1999 Chi-Chi, Taiwan earthquake. The Yuanlin site is composed of a series of fine silty sand layers of variable FC and silt layers with occasional clay lenses. The soil in Wufeng is composed of layers of silty sand, sandy silt, and silty clay up to a depth of about 20 m . The fine fraction of the soils at the Wufeng sites have a plasticity index (*PI*) typically less than 7 (Lee et al. 2011). CPT data were obtained from the investigation campaigns documented by Chu et al. (2004) and Juang (2002). Based on this information, 3 case histories were defined in Yuanlin and 3 other cases in Wufeng for the 1999 Chi-Chi earthquake.

The stratigraphy, soil types, and the effects of liquefaction experienced at CentrePort in Wellington after the 2013 Cook Strait, 2013 Lake Grassmere, and 2016 Kaikoura earthquakes have been documented extensively in the studies by Cubrinovski et al. (2018), Bray et al. (2019), Dhakal et al. (2020), and Dhakal et al. (2022). CentrePort is a 10 m to 20 m thick hydraulic fill where first 2 m to 3 m correspond to a compacted layer (crust) generally above the groundwater level. An older reclamation constructed in 1910s was constructed by placing a 1 m to 7 m thick layer of a gravel-sand-silt mixture which overlies a 1 m to 6 m of gravelly sand. The most recent reclamation (i.e., the Thorndon reclamation) consists of a 10 m of sandy gravel fill below the crust. For both types of fills, the sandy gravel and gravel-sand-silt mixtures, the sand and silt fractions make up between 20% and 50% of the fill. Following the fill materials, uncompacted marine sediments of 1 m to 4 m of thickness and composed of clays, silty clays and sands are found. CPT data have been shared through a research effort led by the Univ. of Canterbury in collaboration with the Univ. of California – Berkeley, Tonkin + Taylor, Ltd., and CentrePort. At the time of this study, the electronic data, which was available for this study, are not approved by CentrePort to be released publicly. However, much of the information is available to the public through the publications mentioned previously. A total of 27 case histories have been developed for CentrePort for primarily the 2016 Kaikoura and 2013 Lake Grassmere earthquakes with one case for the 2013 Cook Strait earthquake.

The Christchurch liquefaction vulnerability study by Tonkin + Taylor (Russell and van Ballegoy, 2015) documented and investigated land damage throughout Christchurch after the 2010-2011 Canterbury earthquake sequence. As a result, a set of well-documented 55 sites with varying levels of ground damage was defined and used to study liquefaction triggering and its effects (Cubrinovski et al. 2019). Mijic et al. (2021c) complemented the existing 55 sites with 34 additional sites to arrive at an unbiased set of sites with levels of liquefaction manifestations from none-to-severe. The set of 89 sites in Christchurch can be broadly classified into sites of relatively continuous (thick) sandy materials and sites with different degrees of stratification with presence of interbedded sandy, silty, and clayey materials (Beyzaei et al. 2018a). These surficial sand, silt, and gravel deposits vary in thickness from less than 10 m to over 40 m in the northern and eastern part of Christchurch whereas swamp deposits of the same thickness and composed of sand, silt, clay, and peat are in the southwestern part of the city. Underlying these soils, a sequence of thick layers of gravels and sands with silts are found (Markham et al. 2016). High-quality pre- and post-earthquake LiDAR surveys data, CPT recordings and soil boring logs were obtained from the New Zealand Geotechnical Database (2021). Information for the 2010 Darfield, 2011 Christchurch, and June 2011 earthquakes were processed to develop a total of 157 case histories in Christchurch.

Tokimatsu et al. (2012) and Kokusho et al. (2014) document field data of the hydraulic

fills in Urayasu, Japan. The reclaimed land of Urayasu is an 8 m thick hydraulic fill composed of loose silty sands and sandy silts that sit atop a soft to firm clay stratum about 10 to 40 m thick. Information regarding the overall seismic performance and the range of observed settlements in Urayasu are provided in Katsumata and Tokimatsu (2012) and Cox et al. (2013). In addition to providing ranges of free-field ground settlement, Cox et al. (2013) shows CPT data at 6 different locations in Urayasu. With this information, 6 case histories are developed for the Urayasu sites shaken by the 2011 Tohoko earthquake.

Initially 213 case histories were collected, processed, and examined. Through closer examination, 6 cases were removed from the database because they were potentially affected by liquefaction-induced lateral ground movements due to buried stream channels or buried structures such as pools. Preliminary regression analysis of the settlement data of the remaining cases identified 2 outliers that were more than 3 standard deviations from the median of the regression of the data. Simplified liquefaction triggering procedures indicated these 2 cases were marginal liquefaction cases, so they were removed.

The final database contains 205 case histories with 967 CPTs. Table 3.1 summarizes the characteristics of the assembled 205 CPT case histories of post-liquefaction free-field, level ground settlement. Each case history is described in detail in a flatfile shared in Appendix B, which includes the latitude and longitude of each site. The publicly available electronic CPT data and the details of each field case history are also available in Appendix B.

Reclaimed land is typically the product of sequential hydraulic filling of borrowed granular material. This construction method results in relatively uniform and loose fills typically overlying marine sediments. The hydraulic fills in the database are usually less than 10 m thick and are typically comprised of silty sands to sandy silts (with exception of CentrePort which has a significant fraction of gravel). Case histories of the performance of hydraulic fills, such as those during the 1995 Kobe earthquake (e.g., Yasuda et al. 1996), indicate that uniformly constructed hydraulic fills tend to exhibit relatively uniform settlement. Conversely, natural soil deposits are inherently heterogenous as a consequence of complex depositional processes that can show significant spatial variability in addition to other age-related effects. The assessment of liquefaction performance in the Christchurch (Beyzaei et al. 2018a) illustrates the effects of depositional processes on ground performance. Due to the differing formation processes and their seismic response, the case histories are classified into the two primary categories of natural soil deposits and hydraulic fills. Of the 205 case histories, 163 cases are classified as natural soil deposits and 42 cases are classified as hydraulic fills.

3.3.3 CPT Data

The raw electronic CPT profiles were evaluated before being processed. CPTs with the following characteristics were not used in this study:

a) CPTs with incomplete data (e.g., missing data in the upper 10 m of the profile below the groundwater level),
b) Very short CPT profiles (i.e., $\leq$ 5 m depth of penetration), and
c) Trace of a CPT differed markedly from the traces of the other CPTs at the site.

Figure 3.2 shows an example of an excluded CPT (i.e., CPT 56472 shown in red) with normalized tip resistance (q_{c1N}) and I_c profiles markedly different from the q_{c1N} and I_c profiles of the other CPTs defining the Shirley Intermediate School site. CPT 56472 defines the northern edge of the Shirley Intermediate School site, as it contains noticeably more gravel and is significantly denser than the soil profiles described by the other CPTs located closer to the center of the site.

3.3.4 Groundwater Depth

Groundwater table (GWT) depths at CPT locations in the Marina District were estimated by Bennett (1990) from boring logs. A mean GWT depth of 2.90 m is representative of the site with exception of the southeast area where a GWT depth of 5.40 m is more representative. The GWT in Treasure Island is related to the sea mean lower low water (MLLW). At the time of the 1989 Loma Prieta earthquake, the GWT depth was estimated between 0.90 m and 2.0 m. Juang et al. (2002) reports GWT depth estimated by the NCREE reconnaissance effort. Depths of 0.5 m to 4.0 m and 0.5 m to 5.0 m are estimated in Yuanlin and Wufeng, respectively, at the time of the 1999 Chi-Chi earthquake. An analysis of piezometer data in CentrePort by Dhakal et al. (2020) indicates that the GWT depth varied between 2.0 m and 4.0 m during the 2013-2016 earthquake sequence. In Christchurch, event-specific GWT depths have been obtained from wells installed prior to and after the Darfield 2010 earthquake combined with LiDAR data. The GWT levels in the wells measured prior to the Christchurch 2011 and June 2011 events were used to generate surfaces of GWT depth for these earthquakes. Lastly, similar to other hydraulic fills, the GWT depth in the Urayasu site is relatively uniform and varies within 0.5 m to 3.0 m (Tokimatsu et al. 2012).

3.3.5 Derivation of CPT-Based Parameters

Each CPT sounding provides corrected cone resistance (q_t, often also referred to as q_c in the literature), sleeve friction (f_s), and dynamic pore pressure (u_2) measurements. The combination of these measurements permits the interpretation of the stratigraphy and characterization of soil behavior type index with depth. In addition, there exist several mechanistically based correlations that relate cone measurements to different soil properties and parameters (e.g., relative density and peak effective friction angle). The ability to obtain reliable estimates of engineering soil properties is one of the major advantages of the CPT in engineering practice.

The soil behavior type index is a useful CPT-derived parameter. It classifies the soil based on the in-situ type of response during shearing (e.g., sand-like or clay-like, and loose or dense). In addition, an $I_c = 2.6$ threshold is typically adopted in simplified liquefaction triggering methods to identify soils with $I_c \geq 2.6$ as non-liquefiable. The I_c relationship proposed by Robertson (2009a) as shown in Eq. 3.1 is used in this study.

$$I_c = [(3.47 - \log Q_t)^2 + (\log F_r + 1.22)^2]^{0.5} \quad (3.1)$$

where the normalized tip resistance, $Q_t = (q_t - \sigma_v)/\sigma'_v$; the normalize friction ration, $F_r = f_s/(q_t - \sigma_v)$; and σ_v and σ'_v are the total and effective vertical stresses, respectively.

An estimate of *FC* is also required in routine triggering methods as well as in other informative correlations. Idriss and Boulanger (2008) recommend measuring the *FC* directly from representative samples; however, this may not be practical in many engineering applications. Even though discrepancies between I_c and *FC* classifications are expected (e.g., Robertson 2009a and Beyzaei et al. 2018b), correlations between I_c and *FC* have been proposed and implemented in practice and research. The *FC* (in %) relationship of Boulanger and Idriss (2016) as shown in Eq. 3.2 is used in this study.

$$FC = 80(I_c + C_{FC}) - 137 \tag{3.2}$$

where C_{FC} is a calibration parameter that is set to zero to obtain a global average relationship. If site-specific data are available, a material-specific calibrated C_{FC} can be used. For example, Maurer et al. (2019a) evaluated many field samples and CPT data and suggested using C_{FC} = 0.13 for the soil deposits in Christchurch.

The CPT data can also be used to obtain estimates of soil state. Relative density (D_r) and the state parameter (ψ_o) are used in this study. D_r (in %) is estimated using the correlation developed by Bray and Olaya (2023) defined in Eq. 3.3, which is based on data at natural silty sand deposits in Christchurch in which high-quality samples were retrieved only 1 m to 2 m from a CPT that defined the normalized cone resistance (qc1n as defined by Boulanger and Idriss 2016) and I_c over well-defined soil layers. As an alternative to this new correlation, the Robertson and Cabal (2015) CPT-based D_r (in %) correlation for clean sand defined in Eq. 3.4 is used by extending it to capture silty soil with I_c > 1.64 through application of the clean sand correction factor (K_c) of Robertson and Wride (1998).

$$D_r = \begin{cases} \sqrt{\dfrac{q_{c1n}}{290}} \cdot 100 & \text{for } I_c < 1.6 \\ \sqrt{\dfrac{q_{c1n} \cdot I_c^{3.5}}{1500}} \cdot 100 & \text{for } 1.6 \le I_c \le 2.6 \end{cases} \tag{3.3}$$

$$D_r = \sqrt{\frac{Q_{tn,cs}}{350}} \cdot 100 \tag{3.4}$$

where the normalized clean-sand-equivalent cone resistance, $Q_{tn,cs} = K_c \cdot Q_{tn}$, $K_c = 5.581 I_c^3 - 0.403 I_c^4 - 21.63 I_c^2 + 33.75 I_c - 17.88$ if I_c > 1.64, and Q_{tn} is the normalized CPT penetration resistance as defined by Robertson and Cabal (2015).

The Robertson and Cabal (2015) correlation was developed based on clean sand data from calibration chamber tests. The $Q_{tn,cs}$ term permits extending the application of the correlation to silty sands by means of the clean-sand-equivalent resistance correction. In contrast, the Bray and Olaya (2023) correlation was developed directly using closely spaced high-quality CPT and laboratory test data on clean and silty sands in Christchurch (i.e., Markham 2015 and Beyzaei 2017); hence, a clean-sand-equivalent correction is not needed. However, both correlations use normalized cone resistance and soil behavior type index values to estimate relative density. The average of both relationships is used in this study to use an unbiased mean-centered estimation of D_r. Figure 3.3 shows the *FC* and D_r

correlations employed in this study.

The state parameter (ψ_o in decimal) is estimated using the correlations of Robertson (2010), which is provided in Eq. 3.5, and of Olaya and Bray (2022b), which is provided in Eqs. 3.6 and 3.7.

$$\psi_o = 0.485 - 0.314 \cdot \log Q_{tn,cs} \tag{3.5}$$

$$\psi_o = \xi \cdot (e_{max} - e_{min}) \left[1/\mathrm{Ln}(\sigma'_{cr}/\sigma'_v) - D_{r_o}\right] \tag{3.6}$$

$$\xi = 0.724 \cdot \exp(-0.031 \cdot FC) \tag{3.7}$$

where ξ is a calibration parameter, (e_{max} - e_{min}) is the void ratio range of the soil, σ'_{cr} is the crushing pressure, σ'_v is the vertical effective stress, and D_{r_o} is an estimate of the initial D_r expressed in decimal. Examination of Eq. 3.6 showed the estimate of ψ_o is not too sensitive to σ'_{cr}, so typical values provided by Mitchell and Soga (2005) may be used (i.e., 8000 kPa for silt; 10000 kPa for silty sand; and 20000 kPa for clean sand). The average of the soil-dependent correlation of Cubrinovski and Ishihara (2002) is used to estimate $e_{max} - e_{min}$ as

$$e_{max} - e_{min} = \begin{cases} 0.43 + 0.00867 \cdot FC, & FC < 30 \\ 0.57 + 0.004 \cdot FC, & FC \geq 30 \end{cases} \tag{8}$$

where FC is expressed in percent as an integer. Typical values of $e_{max} - e_{min}$ are 0.45 for clean sand, 0.65 for silty sand, and 0.80 for silt.

The Robertson (2010) correlation for ψ_o has been derived based on clean sand data and it is extended to silty sands through the use of $Q_{tn,cs}$. The Olaya and Bray (2022b) relationship is based on critical state theory concepts and was calibrated using laboratory test data on clean and silty sands. The average of both correlations is used as a representative mean estimate in this study.

3.3.6 Liquefaction Triggering Evaluation

Two simplified liquefaction triggering methods were used to compute the factor of safety against liquefaction (FS_L). Within each triggering method, a probability of liquefaction, P_L = 50% was used so that median estimates of FS_L are obtained. The methods of Boulanger and Idriss (2016) and Robertson and Wride (1998) with the modifications in Robertson (2009b) were used. While the Boulanger and Idriss (2016) method is also provided in a probabilistic framework, the Robertson and Wride (1998) is not. The work of Ku et al. (2012) was used to adjust the Robertson and Wride (1998) method to achieve P_L = 50%. The average of the median (P_L = 50%) FS_L estimates of Boulanger and Idriss (2016) and of Robertson and Wride (1998)/Robertson (2009b)/Ku et al. (2012) is used in the database.

3.3.7 Ground Motion Intensity Measures and Liquefaction Severity Indexes

The seismic demand at case histories sites is represented with surface ground motion intensity measures (e.g., PGA, and S_{a1} = Sa at a period of T = 1 s). At sites with ground

motion recordings available from nearby stations (e.g., CentrePort), *IMs* derived from the recordings are used. When no ground motion recordings were available in the vicinity of the site, average median estimates obtained from ground motion models (GMMs) for S_a are used. For the Christchurch sites, the Bradley (2014) procedure was used to estimate values of *PGA* and S_{a1} conditioned on observed spectral accelerations at strong motion stations throughout Christchurch. For sites without an event-specific GMM, the NGA-West2 set of models (Gregor et al. 2014) were used.

The time-averaged 30 m soil shear wave velocity (V_{S30}) is commonly used as a site parameter describing the near-surface soil conditions in GMMs, so V_{S30} values are provided for all case histories. Direct measurements of V_s at the sites are limited. McGann et al. (2017) used V_s and CPT measurements throughout Christchurch to develop a Christchurch-specific empirical model for V_{S30}. Vantassel et al. (2018) used the multichannel analysis of surface wave (MASW) and microtremor array measurements (MAM) to develop V_s profiles in CentrePort. Cox et al. (2013) provide V_s measurements at the 6 different locations where they advanced the CPTs in Urayasu. Liu et al. (2015) used the measured V_{S30} from the dense Taiwanese strong motion station array to estimate V_{S30} at locations in Taiwan. Similarly, USGS (2021b), and the California Department of Conservation (2021) developed estimates of V_{S30} using Vs measurements for the Marina District and Treasure Island sites. Site-specific V_s and V_{S30} data were used when available instead of generic CPT correlations for V_s.

In simplified liquefaction triggering assessments, M_w is used as a proxy for shaking duration effects while horizontal ground surface *PGA* defines the ground motion intensity at the site. Research on the effects of liquefaction (e.g., Bray and Macedo 2017 and Bullock et al. 2019) have shown that the spectral acceleration at a degraded period of the site, *T'* (*SaT'*), *CAV*, and I_A have good potential as ground displacement predictor variables, hence they are also included. To estimate *CAV* and I_A, this study employs the GMMs of Campbell and Bozorgnia (2012), Abrahamson et al. (2016), and Macedo et al. (2021) for shallow crustal regions and the GMMs of Foulser-Piggott and Goda (2015) and Macedo et al. (2019) for subduction zone earthquakes. Figure 3.4 presents the distribution of V_{S30} and the ground motion IMs developed for the database of this study.

Liquefaction-induced ground damage severity indexes have been developed to relate the FS_L to the degree of observed ground damage. Previous research (e.g., Maurer et al. 2014, and Hutabarat and Bray 2021) have shown that the accuracy of different liquefaction indices depends greatly on the site's stratigraphy and the site's system response to earthquake shaking. Therefore, it is informative to include relevant liquefaction indices as part of the case histories development so that the correspondence between liquefaction-induced ground settlement and different liquefaction indices can be explored. The Liquefaction Index Potential (*LPI*), the Ishihara-inspired LPI (LPI_{ish}), and the Liquefaction Severity Number (*LSN*) were computed in this study (each index is defined in Maurer et al. 2019b). In addition, the Liquefaction Demand parameter (L_D) and the Crust Resistance parameter (C_R) as defined by Hutabarat and Bray (2022) are also provided for each site.

3.3.8 Free-Field Ground Settlement Measurement

Vertical ground settlement in the Marina District after the 1989 Loma Prieta earthquake was estimated by Bennett (1990) as the difference in elevation from surveys conducted in

1961, 1974, and 1989 (post-earthquake). The settlement component due to compression of the bay mud and consolidation of the fill was assessed using the difference between the 1961 and 1974 surveys. At first, the 1974 – 1961 settlement was planned to be subtracted from the 1974 – 1989 settlement to isolate the earthquake induced settlement. However, Bennett (1990) pointed out that many uncertainties were not captured by the topographic surveys; hence, it was recommended to use the settlement between 1974 and 1989 as the post-earthquake settlement because it may provide an estimate that accounts for these uncertainties. For Treasure Island, the settlement after the 1989 Loma Prieta earthquake was estimated by Bennett (1998) using topographic survey data at a few free-field locations that were next to pile supported buildings assumed not to have settled due to the earthquake.

For the Yuanlin and Wufeng sites, land subsidence measurements after the 1999 Chi-Chi earthquake were conducted by the Taiwanese National Center for Research in Earthquake Engineering (NCREE) and are documented in Juang (2002) and Juang et al. (2013). Lee et al. (2011) discusses additional ground settlement measurements that were carried out in 2005 employing GPS surveys, reconnaissance reports, and site photographs for the Wufeng area. These two survey campaigns were used to estimate the post-liquefaction ground settlement at sites in Yuanlin and Wufeng.

Ground settlement at CentrePort following the 2013 Cook Strait and 2013 Lake Grassmere earthquakes was estimated primarily by manual field surveys as part of damage inspection campaigns. Settlement measurements are limited for the 2013 Cook Strait event while for the 2013 Lake Grassmere settlement estimates are available for several locations. Shortly after the 2016 Kaikoura earthquake, ground settlements were documented from manual surveys. Later, terrestrial and areal LiDAR surveys were conducted in CentrePort and subsequent point estimates of settlement were calculated (Cubrinovski et al. 2018). Using these point measurements, settlement contours covering the CentrePort area were developed and shared in Dhakal et al. (2022). The latter, more precise settlement data were used in this study.

In Christchurch, LiDAR point cloud data were processed with Global Mapper to generate elevation models for total settlement, tectonic movement, and net ground subsidence (Mijic et al. 2021c). These elevation models were further complemented with flight error estimates and localized ejecta-induced settlements. These LiDAR-based elevation models form the basis of the post-liquefaction ground settlement estimates after the 2010 Darfield, 2011 Christchurch, and June 2011 earthquakes.

Katsumata and Tokimatsu (2012) report the amount of ground settlement following the 2011 Tohoku earthquake. For these case histories, ground settlement was carefully measured at multiple locations using pile-supported structures that showed no evidence of displacement as a reference. These point-based measurements were later used to develop a map of post-liquefaction ground settlement.

The more densely surveyed areas, such as Marina District and Christchurch, provide insights into the range in which the ground settlement varies. Accordingly, a mean value and range of settlement were estimated based on field measurements, soil characteristics, and the degree of liquefaction observed at the site.

3.4 Example of the Definition of a Case History

Figure 3.5 illustrates the definition of a case history in CentrePort, Wellington. This

case history corresponds to the performance at Site 4 after the 2016 Kaikoura M_w 7.8 earthquake. Site 4 is within a part of CentrePort built with dumped sandy gravel fill of thickness from 10 m to 15 m which overlies marine sediments and the Wellington alluvium. The sand-silt fractions of the gravelly fill range between 30% and 70%. Additional information on the stratigraphy, soil types, and the effects of liquefaction after the 2016 Kaikoura earthquake are available in Cubrinovski et al. (2018), Dhakal et al. (2020), and Dhakal et al. (2022). Site 4 is characterized by the 6 CPTs shown in Figure 3.5 with the groundwater table located between 3.0 m to 3.5 m below the ground surface. The CPT data (e.g., q_{c1n} and I_c) and liquefaction parameters (e.g., FS_L and LSN) were used to define the extent of a site. They are relatively consistent for the 6 CPTs advanced at Site 4. The average of the D_r estimated using Eq. 3.3 and Eq. 3.4 varies between 30% and 95% for this site and the average of the P_L = 50% FS_L estimated using the Boulanger and Idriss (2016) and Robertson and Wride (1998)/Robertson (2009b)/Ku et al. (2012) procedures vary between 0.30 and 2.0. The surveyed mean ground settlement varies within the range of 200 mm to 350 mm across most of the site. Lastly, the *PGA* at nonliquefied ground surface conditions was estimated to be 0.25 g with nearby strong motion stations that are not affected by liquefaction.

3.5 Conclusion

A comprehensive database of 205 CPT field case histories of post-liquefaction free-field ground settlement is developed. The case histories are classified into 163 natural soil deposit sites and 42 hydraulic fill sites, because these sites differ in their formation processes and spatial variability.

As part of the case histories characterization, a total of 966 CPTs were processed using several state-of-the-practice correlations and liquefaction triggering procedures. The in-situ state of the soil was characterized using the correlations of Robertson and Cabal (2015) and Bray and Olaya (2023) for the relative density and Robertson (2010) and Olaya and Bray (2022b) for the state parameter. The simplified liquefaction triggering methods of Boulanger and Idriss (2016) and Robertson and Wride (1998)/Robertson (2009b)/Ku et al. (2012) were employed. The use of at least two relationships for these key parameters provides mean-centered estimates of soil properties and liquefaction triggering.

The seismic demand associated with each case history is reported by means of the earthquake moment magnitude and a series of intensity measures that have been shown to correlate well with earthquake-induced ground and building displacements. Ground motion recordings were used directly to derive intensity measures at sites with nearby recordings available whereas for sites with no ground motion recordings, mean estimates from ground motion models were used. V_{s30} values are also provided for each case history because it provides an index for site response amplification and is used in modern ground motion models.

Best estimates of liquefaction-induced free-field settlement measurements are provided for each case history. The estimation of post-liquefaction settlement is difficult because in addition to the site's intrinsic spatial variability, there always exists uncertainty in the pre- and post-earthquake ground elevation surveys. Hence, for each site, a mean of settlement was estimated based on the topographic measurements, soil characteristics, and the degree of liquefaction observed at the site. To complement the mean settlement estimate, a range

of the ground settlement is also provided.

A *flatfile* summarizing the characteristics of the 205 case histories is the primary product of this chapter. It is shared as an electronic *Excel* file named *App_B_Free-field_Settl_case_histories_Flatfile_5SEP2022.xlsx* available in Appendix B. In addition, the publicly available CPT data that support the case histories development and the details of each field case history are also provided in Appendix B.

Table 3.1. Summary of Free-field Settlement Case Histories (See Appendix B for additional information)

Location	Earthquake	Case histories	CPTs	Type of deposit
Marina District, California	1989 Loma Prieta	4	8	Hydraulic fill
Treasure Island, California		5	84	
Wufeng, Taiwan	1999 Chi-Chi	3	3	Natural soil
Yuanlin, Taiwan		3	4	
CentrePort, Wellington	2013 Cook Strait	1	8	Hydraulic fill
	2013 Lake Grassmere	13	69	
	2016 Kaikoura	13	69	
Christchurch, New Zealand	2010 Darfield	45	210	Natural soil
	2011 Christchurch	47	220	
	2011 June	65	285	
Urayasu, Japan	2011 Tohoku	6	6	Hydraulic fill

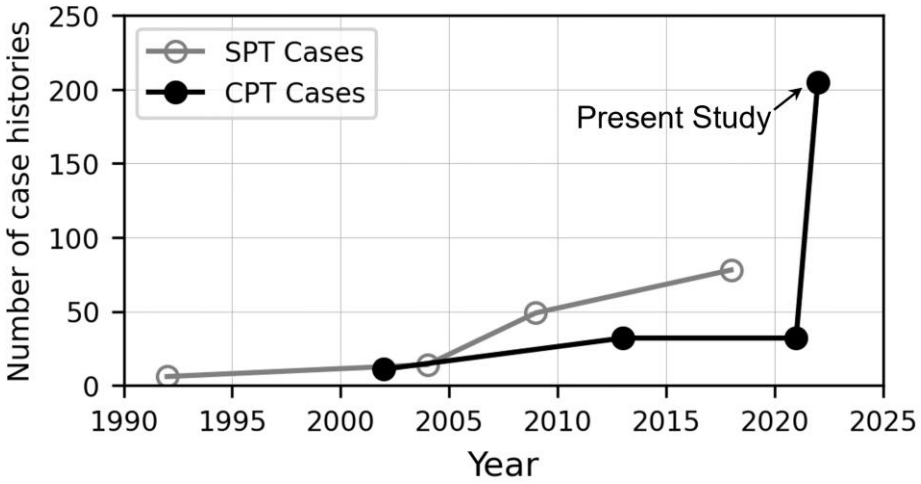

Figure 3.1. Growth of number of liquefaction-induced ground settlement field case histories

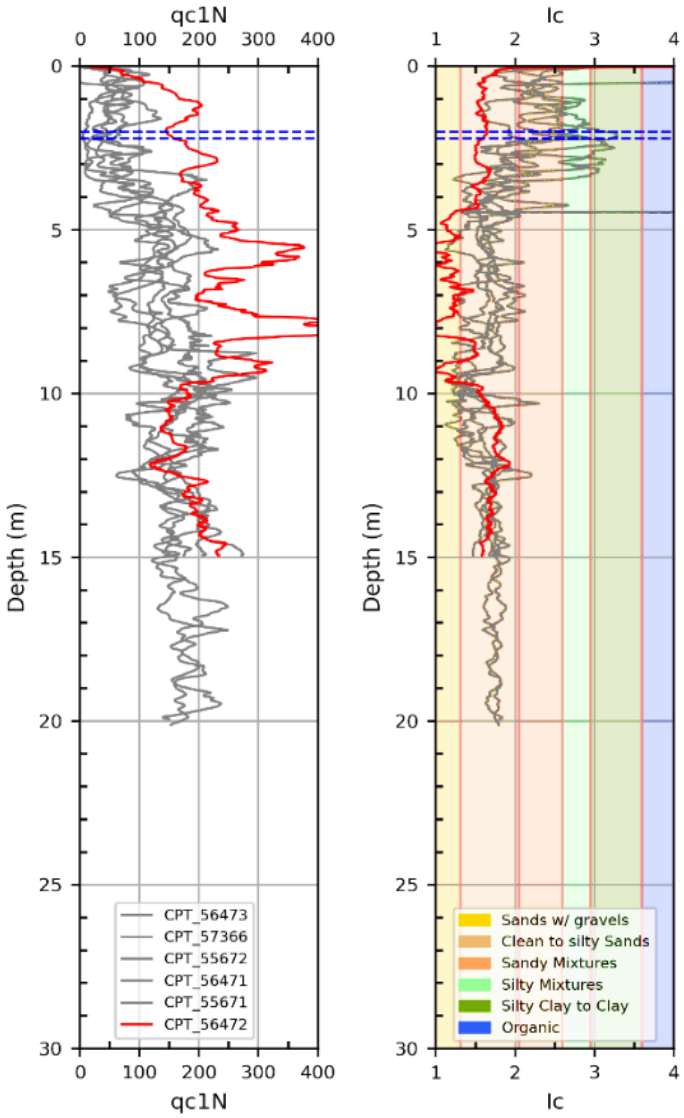

Figure 3.2. Example of an excluded CPT at a site (CPT 56472 in red at the Shirley Intermediate School site)

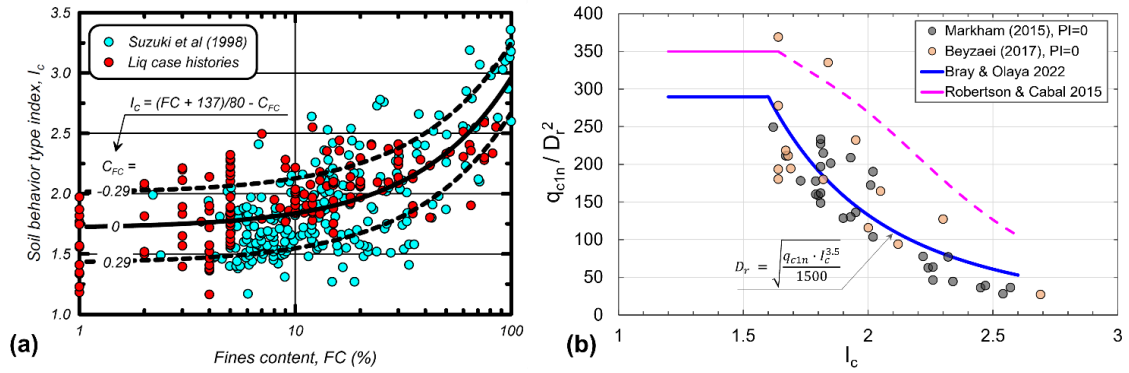

Figure 3.3. CPT-based (a) Fines content correlation of Boulanger and Idriss (2016) and (b) Relative density correlations of Bray and Olaya (2023) for natural soil deposits and inferred from Robertson and Cabal (2015)

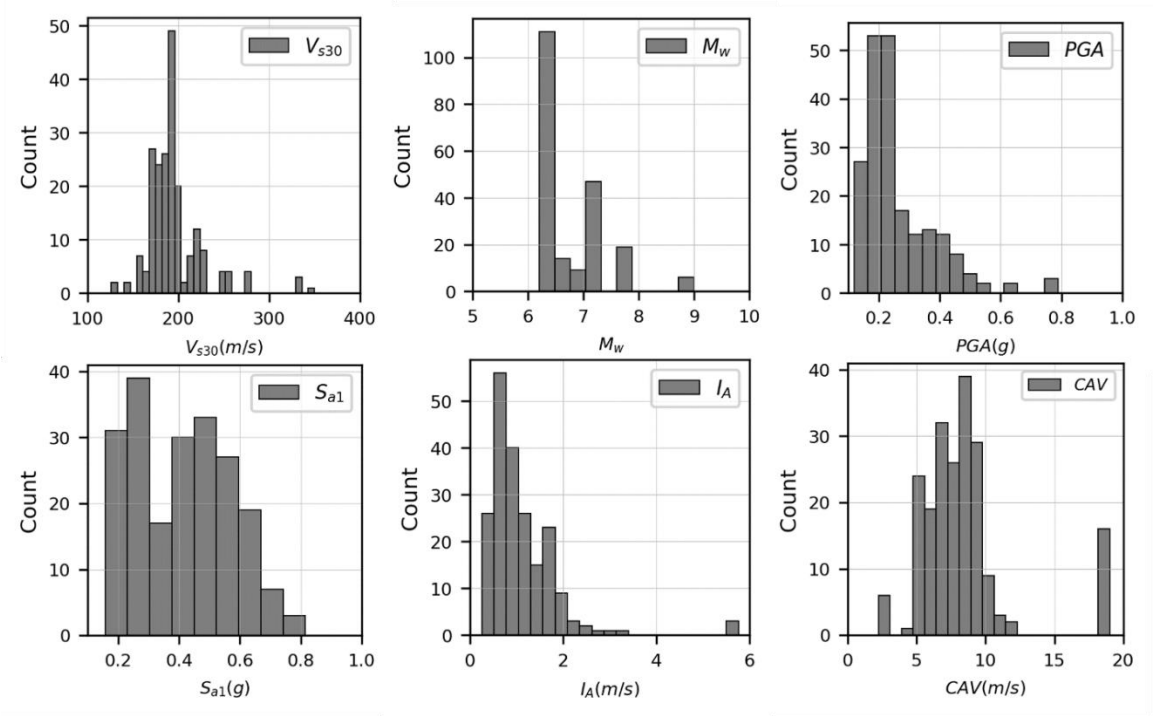

Figure 3.4. Distribution of V_{s30} and key Intensity Measures in the database

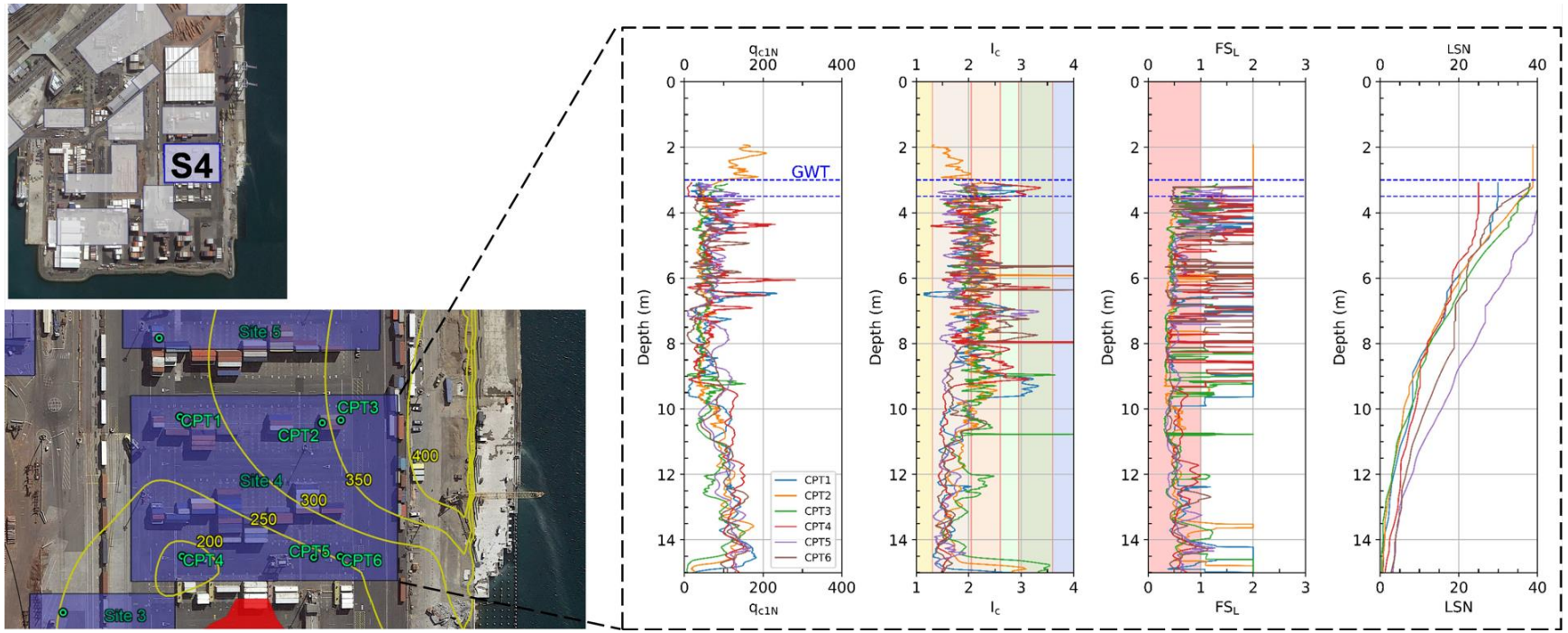

Figure 3.5. CentrePort with enlarged image of Site 4 showing CPT locations and mean ground settlement (mm) contours with q_{c1n}, I_c, FS_L, and *LSN* profiles. Images from Google Earth®

4 Probabilistic Model for Estimating Post-Liquefaction Free-Field Ground Settlement

The contents of this chapter are primarily from a journal article published in the Journal of Geotechnical and Geoenvironmental Engineering from the American Society of Civil Engineers (ASCE) by Bray, J.D. and Olaya, F.R. entitled: "Evaluating Liquefaction Effects."

4.1 Introduction

4.1.1 Background

The consequences of triggering soil liquefaction in a soil deposit can be negligible to severe. At the element level, the accumulation of shear strain beyond the volumetric threshold shear strain in a soil layer generates excess pore-water pressure that reduces effective stress (Dobry and Ladd 1980). The stiffness and strength of a soil element can degrade rapidly as its effective stress reduces to a low value. Understanding, characterizing, and modeling the cyclic response of a soil unit that is susceptible to liquefaction is crucial to evaluating the effects of liquefaction at a site. However, the system response of the entire soil deposit should also be evaluated to assess the effects of soil liquefaction at the site. For example, a site with a nearby free-face slope that imposes a significant static driving stress can undergo a damaging lateral spread if a continuous soil layer liquefies. Conversely, gently sloping ground with isolated soil units that liquefy may not displace because the liquefied soil units are not laterally continuous. At some level ground sites, the formation of sediment ejecta produces extensive ground cracking and the loss of foundation support, which damages infrastructure. At other level ground sites, earthquake shaking triggers soil liquefaction in a deep soil layer that is well below building foundations so that damaging shear-induced displacement does not develop. In these cases, the dissipation of the excess pore-water pressure in the soil can still produce ground settlement due to sedimentation and reconsolidation volumetric strain processes; however, the ground settlement may be uniform and moderate, so it causes no infrastructure damage.

Performance-based engineering requires robust methods to evaluate liquefaction effects. Nonlinear dynamic soil structure interaction (SSI) effective stress analyses can provide key insights as well as reasonable estimates of liquefaction-induced ground and building movements. Nonlinear effective stress analysis can capture the element response of soil and the system response of the soil deposit, if performed with sound soil constitutive models that are calibrated and validated to capture the element response of soil and employed in numerical models that capture system response features (e.g., seismic site response, soil layering, and water flow). Alternatively, empirical procedures may be used in engineering practice because they can be calibrated to estimate reliably the observed ground and building performance. Researchers have developed empirical procedures to estimate liquefaction-induced ground settlement and lateral movement using field case history data with models informed by laboratory test results and mechanics. In these methods, the complex processes involved in liquefaction triggering and its consequences

are captured using proxies that represent the state of the soil and the seismic demand. For example, cone penetration test (CPT)-based empirical methods for estimating liquefaction-induced level ground settlement and sloping ground lateral spread displacement methods are widely used in engineering practice (e.g., Zhang et al. 2002, 2004). There is merit to developing alternative methods, especially if the empirical methods are informed by new field case histories that explore the response of a wider range of soil types and seismic demands.

In this Chapter, soil liquefaction effects of level ground sites composed of sand, sandy gravel, silty sand, nonplastic silt, and slightly plastic clayey silt with and without structures are explored. The element and system responses of the individual soil layers and the soil deposits they form are examined. Soil system responses are investigated to characterize the severity of soil ejecta so its effects on infrastructure can be assessed. A probabilistic CPT-based procedure for estimating post-liquefaction ground settlement is presented. Recommendations for its use in engineering practice are shared.

4.1.2 Liquefaction-Induced Building Movements

Liquefaction has the potential to damage buildings. The bearing capacity failure of buildings, such as the 5-story building in Adapazai, Turkey shown in Figure 4.1a, the settlement and lateral displacement of another building in Adapazari shown in Figure 4.1b, and the ejecta-induced settlement of a 2-story building in Christchurch, New Zealand shown in Figure 4.1c illustrate some of the direct consequences of liquefaction on buildings with shallow foundations (Bray and Stewart 2002, Bray et al. 2004, 2014). The fire shown in Figure 4.1d that consumed part of Kobe, Japan reminds engineers of indirect consequences of liquefaction that can devastate a city (Akai et al. 1995). In numerous other post-earthquake photographs (not shown), there is no discernable damage to buildings even though current procedures indicate the factor of safety against liquefaction triggering (FS_L) is well less than one (e.g., Beyzaei et al. 2018b). Thus, the effects of liquefaction on buildings can be negligible to severe.

Several of the key mechanisms of liquefaction-induced building settlement are illustrated in Figure 4.2. They can be categorized as shear-induced, volumetric-induced, or ejecta-induced deformation and estimated separately as recommended by Bray and Macedo (2017). Alternatively, the mechanisms can be combined in estimating liquefaction-induced building settlement as recommended by Bullock et al. (2019). The former approach is employed in this study to examine the contribution of each component of settlement. Ejecta are not produced in some cases (i.e., thick nonliquefiable crust overlying a thin liquefied soil layer) and it is severe in other cases, so there is merit to separating it from the other two mechanisms. Moreover, the shear-induced component of settlement governs in some cases, and in other cases when the liquefiable layer is deep, it is negligible. Lastly, uniform volumetric-induced ground settlement contributes to total building settlement without tilt, whereas differential volumetric-induced ground settlement contributes to differential building settlement and tilt. Bray and Macedo (2017) proposed a CPT-based probabilistic method to estimate shear-induced liquefaction building settlement. Hutabarat and Bray (2022) proposed a CPT-based method to categorize liquefaction ejecta severity which is used in this Chapter to develop an estimate of this component of settlement. A probabilistic CPT-based method to estimate volumetric-

induced ground settlement is proposed in this Chapter. Before discussing these topics, it is useful to summarize some of the key aspects of soil liquefaction at the element and system response levels.

4.2 Post-Liquefaction Volumetric-Induced Ground Settlement

4.2.1 Motivation

Deterministic CPT-based post-liquefaction ground settlement procedures are widely used in practice (e.g., Zhang et al. 2002, and Idriss and Boulanger 2008). A probabilistic CPT-based post-liquefaction ground settlement procedure is required in support of performance-based earthquake engineering. Cetin et al. (2009b) developed a probabilistic SPT-based post-liquefaction ground settlement procedure, but the CPT is superior to the SPT as discussed previously. Therefore, a probabilistic CPT-based post-liquefaction ground settlement procedure for free-field, level ground conditions is developed. It takes advantage of the results of a comprehensive database of laboratory tests with post-cyclic volumetric reconsolidation (Olaya and Bray 2022b) and a comprehensive database of field case histories of sites undergoing post-liquefaction volumetric-induced ground settlement (Olaya and Bray 2022a). In contrast, several of the current CPT-based post-liquefaction ground settlement procedures have comparisons against a limited number of case histories, and they are based solely on the Ishihara and Yoshimine (1992) family of curves derived from CSS tests performed on one uniform clean sand (i.e., Fuji River Sand with FC = 0%, e_{max} = 1.064, e_{min} = 0.529, coefficient of uniformity, C_u = 3.2, and median grain size, D_{50} = 0.4 mm) reconstituted to three different relative densities (i.e., 47%, 73%, and 93%) and tested at one vertical effective confining stress (i.e., 196 kPa). Although these methods have been shown to produce reasonable results, it has not been determined if the relationships developed from test data on just one uniform clean sand can be applied to other clean sands with other particle shapes and gradations, nonplastic silty sands, and nonplastic silts (Bray et al. 2017).

4.2.2 Post-Liquefaction Laboratory Tests

Olaya and Bray (2022b) developed a database of 579 test results on post-liquefaction volumetric strain (ε_v), including 299 test results that relate maximum shear strain (γ_{max}) to the factor of safety against liquefaction triggering (FS_L). The database includes post-cyclic test data on 10 clean sands, 2 gravels, 3 silty sands, 5 silts, and 3 clayey soils. The results of the numerous cyclic tests on a wide range of soil types enabled key trends of the effects of state, stress, soil type, gradation, etc. on the development of post-liquefaction volumetric strain to be identified. Their study found that uniform clean sand, gravel, nonplastic silty sand**,** and nonplastic silt test resu lts could be captured in a unified manner using either D_r, ψ_o, or e_o to characterize the state of the soil. Post-liquefaction volumetric strain depended primarily on the state of the soil and the induced γ_{max}. The type of loading or effective confining stress (within the range of 40-400 kPa) were less important. Olaya and Bray (2022b) developed models using either D_r, ψ_o, or e_o as the independent variable to estimate

ε_v for uniform clean sand, nonplastic silty sand, and nonplastic silt with quantification of the uncertainty of the estimate of volumetric strain. They also developed new models that estimate γ_{max} as a function of FS_L for uniform clean sand, nonplastic silty sand, and nonplastic silt with quantification of the uncertainty of the estimate. These experimentally based models can be used to inform the characteristics of an empirical CPT-based post-liquefaction model used to fit the case history data.

Like Ishihara and Yoshimine (1992) and several other researchers examining uniform sand data, D_r was examined first as the independent variable to characterize the state of the uniform nonplastic soil. Only nonplastic soils with $C_u < 4.5$ were considered because D_r has been shown to be a reasonable parameter for comparing the state of different nonplastic soils if they are of uniform gradation. For instance, Bolton (1986) showed that the shear response of different clean sands can be grouped and characterized using D_r provided these sands are of similar uniform gradations. Duncan et al. (2014) also showed D_r is an efficient parameter for characterizing the strength of granular materials of sands with similar C_u values. Whang (2001) analyzed seismically induced compression of different sands using D_r, and Duku et al. (2008) combined 16 different sands using D_r to develop a seismic compression model appliable to a broad range of uniform sands. As discussed previously, Cubrinovski (2019) found D_r could be used to assess the liquefaction potential of nonplastic silty sand and tied directly to the D_r of uniform clean sand to compare responses of different soil types. Mijic et al. (2021a) also found comparable soil responses for uniform clean sand, uniform nonplastic silty sand, and uniform nonplastic silt with *FC* up to 70%.

4.2.3 Post-Liquefaction Volumetric Strain Models

Use of D_r enabled confirmation that uniform clean sands and uniform nonplastic silty sands at the same D_r under the same effective confining stress and sheared to the same γ_{max} develop similar ε_v as shown in Figure 4.3 (Olaya and Bray 2022b). All clean sand data shown in Figure 4.3a and silty sand data shown in Figure 4.3b with $C_u < 4$ exhibit consistent responses. The only data that are inconsistent with the overall trends are tests by Toriihara et al. (2000) of sand with compressible/crushable fine soil matrix with $C_u = 18$ (shown in Figure 4.3b). Similarly, uniform sand, uniform nonplastic silty sand, and uniform nonplastic silt test specimens at the same ψ_o develop similar ε_v when sheared to the same γ_{max} (Olaya and Bray 2022b).

Olaya and Bray (2022b) performed a series of nonlinear regression analyses of the uniform nonplastic soil data using different functional forms, first over the entire dataset and then over individual 10% bins of D_r (e.g., 50% to 60%) to find an efficient and sufficient model. For a specific D_r bin of test results, ε_v increases directly proportional to γ_{max} until it becomes constant at $\gamma_{max} > 8\%$. The resulting model to estimate ε_v (in %) as function of γ_{max} (in %) for a specified value of D_r (in decimal) is:

$$\varepsilon_v = 1.14 \cdot \exp\left(-2.0 \cdot D_r\right) \cdot \min(\gamma_{max}, 8\%) \cdot e^{\varepsilon} \tag{4.1}$$

where ε represents the model residuals which are normally distributed and unbiased with zero mean with $\sigma = 0.62$ in natural log units. The variability in estimating ε_v includes

within-material testing variability and between-material variability. High-quality, extensive testing of just one material had lower variability (e.g., $\sigma = 0.36$ and 0.41 for the Ishihara and Yoshimine 1992 and Shamoto et al. 1996 datasets, respectively). Thus, the σ in Eq. 4.1 could be reduced if sufficient ε_v data on a specific soil was available, however, its bias from the median estimate for that material would need to be considered. The Olaya and Bray (2022b) bi-linear model and the $\pm 1\sigma$ range for D_r = 70% - 80% are illustrated in Figure 4.4a where the observed data trends are captured well. The proposed model contours for D_r values from 30% to 90% are shown in Figure 4.4b along with the Ishihara and Yoshimine (1992) clean sand curves for comparison. The results of the regression analyses using the enlarged database indicate ε_v varies within a slightly narrower range than envisioned previously. It is important to capture these variations in ε_v in CPT procedures that track changes of D_r in a soil deposit.

Although the initial state parameter captures the volumetric strain potential of uniform clean sand, silty sand, and nonplastic silt in a unified manner, the ψ_o data are only one-fifth of the D_r data because the SSL is not determined in most testing programs (Olaya and Bray 2022b). Accordingly, the ψ_o model is preliminary. Additionally, there is greater uncertainty in estimating ψ_o in situ relative to estimating D_r. The model developed to estimate ε_v (in %) as function of γ_{max} (in %) for a specified value of ψ_o (in decimal) is:

$$\varepsilon_v = 0.50 \cdot \exp\left(4.0 \cdot \psi_o\right) \cdot \min(\gamma_{max}, 8\%) \cdot e^{\varepsilon} \tag{4.2}$$

The model residuals are zero mean normally distributed with $\sigma = 0.56$ in natural log units. The proposed bi-linear model and the $\pm 1\sigma$ range for ψ_o = -0.15 to -0.10 are illustrated in Figure 4.5a where the observed data trends are captured well. The proposed model contours for ψ_o values from -0.25 to 0.05 are shown in Figure 4.5b. Like the D_r-based models, the maximum ε_v varies within a range of about 1.5% to about 5% for the range of test data available. Overall, the ψ_o-based model performs reasonably well considering the limitations of the data (Olaya and Bray 2022b). Experimental programs should establish the SSL of the tested soil so ψ_o-based models can be refined.

4.2.4 Maximum Shear Strain Potential Model

Ishihara and Yoshimine (1992) recognized that initial liquefaction was triggered (FS_L = 1.0) in numerous CSS tests at a single-amplitude shear strain ($\gamma_{cyc,SA}$) of about 3.5%, which is consistent with the 5% double-amplitude axial strain ($\gamma_{cyc,DA}$) criterion often used with CTX tests. They also noted an inverse relationship between FS_L and γ_{max}. Initial regressions of the enlarged Olaya and Bray (2022b) database indicated that a hyperbolic relationship captures the FS_L - γ_{max} data trends well. To avoid having FS_L - ε_v curves at different D_r values cross when relating FS_L and strain potential, the model requires slightly different curvature once FS_L = 1.0 is crossed. Their hyperbolic model depends on one parameter (A) that is a function of D_r (in decimal) as

$$\gamma_{max} = 3.5 \cdot \left[\frac{2^A - {FS_L}^A}{2^A - 1}\right] \cdot e^{\varepsilon} \tag{4.3}$$

$$\gamma_{max} = 0\,; \quad \text{for } FS_L \geq 2.0$$

where

$$A = \begin{cases} -2.8 \cdot {D_r}^2 + 10.2 \cdot D_r - 9.8\,; & FS_L \geq 1.0 \\ -275 \cdot exp(-6.6 \cdot D_r); & FS_L < 1.0 \end{cases}$$

The model residuals (ε) are zero mean normally distributed with $\sigma = 0.88$ in natural log units. The proposed FS_L - γ_{max} model for the D_r = 40-50% bin is shown in Figure 4.6 with the Yoshimine et al. (2006) model for comparison. The additional test data and the Ishihara and Yoshimine (1992) data show similar scatter with the Olaya and Bray (2022b) model deviating slightly from the Yoshimine et al. (2006) model. Differences in the models are larger for denser soils. There is not enough ψ_o data available to develop a robust FS_L - γ_{max} model for ψ_o. Olaya and Bray (2022b) developed a relationship to link ψ_o to D_r, so the D_r-based FS_L - γ_{max} is used with the ψ_o-based γ_{max} - ε_v model to estimate post-liquefaction volumetric strain, which requires γ_{max} as an input.

4.2.5 Relating FS_L and Volumetric Strain Potential

Ishihara and Yoshimine (1992) developed a widely used figure to estimate ε_v or γ_{max} vs. FS_L as a function of a sand's D_r to estimate liquefaction-induced ground settlement or lateral spreading. The Olaya and Bray (2022b) models discussed previously provide alternative estimates of ε_v and γ_{max} using either D_r or ψ_o as a measure of the soil's state and FS_L as a proxy for the seismic demand. These models can be combined to estimate post-liquefaction volumetric-induced free-field ground settlement in a consistent manner. The models defined by Eqs. 4.1 and 4.3 describe the relationship between ε_v and FS_L as a function of D_r as shown in Figure 4.7. Importantly, the combined equations provide D_r curves that do not cross, unlike other models.

4.2.6 Post-Liquefaction Ground Settlement Field Case Histories

Post-liquefaction-induced ground settlement is a complex process resulting from the combined effects of particle sedimentation and soil reconsolidation due to post-shaking dissipation of excess pore-water pressure. Available CPT-based empirical models to estimate liquefaction-induced settlement for free-field level ground conditions are based on a limited number of field case histories. Consequently, it is difficult to quantify uncertainty in the estimate of post-liquefaction settlement with the limited number of field case histories available. To remedy this deficiency, Olaya and Bray (2022a) developed a database of 205 well documented ground settlement case histories to support the development of an improved probabilistic CPT-based liquefaction-induced ground settlement procedure. Their study takes advantage of the numerous site investigations, ground motion recordings, and LiDAR surveys performed following the 2010-2011 Canterbury earthquake sequence and the 2013-2016 northern South Island, New Zealand earthquakes.

Obtaining field case histories with reliable pre- and post-earthquake ground surface elevation measurements is the primary limitation in the development of post-liquefaction ground settlement case histories. CPT-based investigations and topographic surveys conducted by the US Geological Survey (USGS) following the 1989 Loma Prieta

earthquake produced some of the first CPT-based well-documented case histories of post-liquefaction settlement. Additional case histories have gradually become available. However, the reconnaissance efforts conducted in Christchurch after the 2010-2011 Canterbury earthquakes produced an unparalleled amount of diverse and high-quality data with ground motion recordings, ground performance observations for four major earthquakes, aerial imagery, LiDAR measurements, and subsurface characterization, largely through CPTs. Research teams developed an initial set of 55 well documented sites to investigate cases where none-to-minor land damage was observed even though simplified liquefaction methods estimated severe surface manifestations (e.g., Russell and van Ballegoy 2015, and Cubrinovski et al. 2019). Mijic et al. (2022) developed 34 additional sites with the objective to include sites with and without liquefaction manifestations that show no major discrepancies between the estimates from simplified liquefaction methods and the actual field observations. Free-field, level ground sites in these two datasets were examined to enlarge the post-liquefaction ground settlement database. Additionally, well documented sites in Wellington, New Zealand that experienced three major earthquakes, including the 2016 Kaikoura earthquake, were added to the Olaya and Bray (2022a) database. The final compilation of free-field level ground post-liquefaction settlement case histories by Olaya and Bray (2022a) is summarized in Table 3.1. There are 205 case histories at sites described by 967 CPTs with reliable ground settlement measurements.

Olaya and Bray (2022a) defined a case history as the combination of: (1) a site with laterally uniform soil stratigraphy with at least one CPT, (2) an earthquake event represented by its M_w, ground surface PGA or other intensity measures, and (3) consistent post-liquefaction volumetric-induced free-field, level ground settlement measurements. A site is not defined by a CPT. Instead, a site is defined by its consistent geology and seismic performance. Thus, each case history is a site characterized by a geometric mean set of CPT-derived parameters, which undergoes an estimated level of earthquake shaking, wherein the liquefaction-induced ground settlement was measured. Sites characterized with several CPTs are valuable as they capture the average subsurface conditions and the variability of the CPT parameters across a site. For sites with multiple CPT soundings or multiple point settlement measurements, geometric means of these values are used to represent central values in the case history.

An illustrative definition of a case history is depicted in Figure 4.8. The stratigraphy, soil types, and the effects of liquefaction experienced at CentrePort in Wellington after the 2013 Cook Strait, 2013 Lake Grassmere, and 2016 Kaikoura earthquakes have been documented extensively (e.g., Cubrinovski et al. 2018, Dhakal et al. 2020, and Dhakal et al. 2022). CPT data were collected through a collaborative research effort led by the Univ. of Canterbury with the Univ. of California, Berkeley, Tonkin + Taylor, Ltd., and CentrePort. Site 4 is within a part of CentrePort built with dumped sandy gravel fill. The sand-silt fractions of the gravelly fill are between 30% and 70%. The CPT data (e.g., q_{c1n}, I_c,) and liquefaction parameters (e.g., FS_L, and LSN) were used to define the extent of a site. They are relatively consistent for the 6 CPTs advanced in Site 4. Additionally, the surveyed ground settlement varies within 200 mm to 350 mm across most of the site. Lastly, the M_w of the earthquake events are known, and PGA can be estimated with confidence with nearby strong motion stations that are not affected by liquefaction.

Reclaimed land is typically the product of sequential hydraulic filling of borrowed granular material. This construction method results in relatively uniform and loose fills typically overlying marine sediments. The hydraulic fills in the database are usually less than 10 m thick and are typically comprised of silty sands to sandy silts (with exception of CentrePort which has a significant fraction of gravel). Case histories of the performance of hydraulic fills, such as those during the 1995 Kobe earthquake (e.g., Yasuda et al. 1996), indicate that uniformly constructed hydraulic fills tend to exhibit relatively uniform settlement. Conversely, natural soil deposits are inherently heterogenous because of complex depositional processes that can show significant spatial variability in addition to other age-related effects. The assessment of liquefaction performance in Christchurch illustrates the effects of depositional processes on ground performance (Beyzaei et al. 2018a). Due to their differing formation processes and seismic performance, the case histories are classified into the two primary categories of natural soil deposits and hydraulic fills. Of the 205 case histories, 163 cases are natural soil deposits, and 42 cases are hydraulic fills.

4.3 Framework of the Procedure

The proposed probabilistic CPT-based liquefaction ground settlement procedure employs the framework of Ishihara and Yoshimine (1992), which is the framework used in several existing procedures (e.g., Zhang et al. 2002, and Idriss and Boulanger 2008). The post-liquefaction volumetric ground settlement (S_v) is calculated initially as

$$S_v = \sum_i \varepsilon_{v_i} \cdot \Delta Z_i \tag{4.4}$$

where ε_{v_i} is the median post-liquefaction volumetric strain calculated using the Olaya and Bray (2022b) model for all nonplastic soils, which is calculated using either its D_r-based or ψ_o-based FS_L-γ_{max} and γ_{max} - ε_v relationships in which FS_L and D_r or ψ_o are estimated using CPT data at each depth i, and ΔZ_i is the thickness of the unit at depth i. The procedure was developed using the mean FS_L at a probability of liquefaction triggering (P_L) of 50% calculated using two simplified liquefaction triggering procedures: (1) the Robertson and Wride (1998) procedure as updated by Robertson (2009b) and converted to a probabilistic method by Ku et al. (2012), and (2) the Boulanger and Idriss (2016) procedure. The intent is to use an unbiased mean-centered estimate of FS_L. Using P_L = 15% instead of P_L = 50% produces a conservative estimate of S_v. Use of one simplified liquefaction procedure or alternative procedures changes the estimate of FS_L in a manner dependent on the procedure(s) employed.

The proposed post-liquefaction ground settlement procedure also requires a CPT-based estimate of D_r or ψ_o. CPT-based correlations to estimate D_r are based on clean sand data (e.g., Tatsuoka et al. 1990). Correlations to estimate D_r as a function of CPT data in silty soil do not exist. To address this shortcoming, D_r data of high-quality DM nonplastic soil samples retrieved by Markham (2015) and Beyzaei (2017) within 2 m of CPTs in Christchurch were compiled and examined. These data are shown in Figure 4.9 in terms of q_{c1n}/D_r^2 vs. I_c. The q_{c1n}/D_r^2 relationship is widely used for clean sand (Robertson and Cabal 2015). The data in Figure 4.9 enables it to be used for silty soils as a function of soil

compressibility represented by I_c. The ratio q_{c1n}/D_r^2 decreases as soil compressibility increases (i.e., as I_c increases), because the CPT tip resistance decreases in more compressible soils if the soils have the same D_r. The proposed relationship was extended to capture sand with $I_c < 1.6$ using an average of the existing CPT-based D_r correlations for clean sand with $q_{c1n}/D_r^2 = 290$ as shown in Eq. 4.5 where D_r is expressed in decimal. The model residuals (ε) are zero mean normally distributed with $\sigma = 0.31$ in natural log units.

$$D_r = \begin{cases} \sqrt{\dfrac{q_{c1n}}{290}} \text{ for } I_c < 1.6 \\ \sqrt{\dfrac{q_{c1n} \cdot I_c^{3.5}}{1500}} \text{ for } 1.6 \le I_c \le 2.6 \end{cases} \quad (4.5)$$

As an alternative to the proposed model, the Robertson and Cabal (2015) CPT-based D_r correlation for clean sand is used. It is extended to capture silty soils with $I_c > 1.64$ using the clean sand correction factor (K_c) of Robertson and Wride (1998) with a compressibility factor of 350. The resulting relationship is also shown in Figure 4.9. Similar to what was done for FS_L, the average of the two D_r values estimated by these CPT correlations is used in the development of the post-liquefaction ground settlement procedure to develop a mean-centered estimate of D_r.

The average of two CPT-based correlations to estimate ψ_o is also used for the ψ_o-based volumetric strain model. Robertson (2010) developed a correlation to estimate ψ_o based on clean sand equivalent resistance ($Q_{tn,cs}$). As an alternative to this correlation, Olaya and Bray (2022b) developed a CPT correlation to estimate ψ_o based on clean sand and nonplastic silty sand and silt laboratory data with a generic SSL equation based on Bolton (1986) dilatancy index resulting in estimating ψ_o as

$$\psi_o = e_o - e_{cs} = \xi \cdot (e_{max} - e_{min}) \, [1 / ln(\sigma'_{cr}/\sigma'_c) - D_r] \quad (4.6)$$

where D_r is in decimal, σ'_{cr} is soil's crushing stress, σ'_c the effective normal/confining stress, and ξ is introduced as an adjustment factor that accounts for the assumptions required to convert the Bolton (1986) equation into Eq. 4.6 and the variability of the individual relationships used to develop Eq. 4.6 (e.g., variability in estimation of $e_{max} - e_{min}$). The ξ factor was developed through a calibration process using data from 60 laboratory tests to account for the sources of error in the approximation of Eq. 4.6 as

$$\xi = 0.724 \cdot \exp(-0.031 \cdot FC) \quad (4.7)$$

where FC is expressed in percent as an integer. Examination of Eq. 4.6 showed the estimate of ψ_o is not too sensitive to σ'_{cr}, so typical values provided by Mitchell and Soga (2005) are used (i.e., 8000 kPa for silt; 10000 kPa for silty sand; and 20000 kPa for clean sand). The average of the soil-dependent correlation of Cubrinovski and Ishihara (2002) is used to estimate $e_{max} - e_{min}$ as

$$e_{\max} - e_{\min} = \begin{cases} 0.43 + 0.00867 \cdot FC, & FC < 30 \\ 0.57 + 0.004 \cdot FC, & FC \geq 30 \end{cases} \quad (4.8)$$

where *FC* is expressed in percent as an integer. Typical values of $e_{max} - e_{min}$ are 0.45 for clean sand, 0.65 for silty sand, and 0.80 for silt.

4.4 Adjustments and Calibration of the Model

Residuals are calculated as $\ln(S_{v\_meas}) - \ln(S_{v\_est})$, where S_{v_meas} is the mean measured settlement and S_{v_est} is estimated from Eq. 4.4 using the median estimate of the Olaya and Bray (2022b) post-liquefaction volumetric strain model presented previously. The residuals obtained using Eq. 4.4 without adjustments are shown in Figure 4.10. These residuals show differences between estimates for natural soil deposits and hydraulic fills as expected due to their different depositional processes. It is apparent the laboratory-based model has different biases in its estimates of the settlement measured at natural soil deposit and hydraulic fill sites. In addition, evaluation of the distributions of the residuals shows bias as a function of a site's average I_c and bias as a function of the earthquake's M_w. Based on these observations, a calibration factor (*C*), a soil behavior factor (*SB*), and a magnitude factor (*MF*) are incorporated in the final model. The final regressions analyses were performed considering the effects of *C*, *SB*, and *MF* simultaneously. However, the results of the initial data analyses that led to the development of these factors are informative and discussed further in this section of this chapter. The calibration and correction factors are developed using the D_r -based strain potential models (Eqs. 4.1 and 4.3), and these factors are then applied to the ψ_o -based model because there is greater confidence at this time in the D_r -based model because it has more data and more established correlations to estimate D_r. Lastly, several depth-weighting factors (e.g., Cetin et al. 2009b, van Ballegoy et al. 2014) were investigated but a depth-weighting factor was not incorporated in the model because it did not reduce the standard deviation or the bias in the model. Moreover, sensitivity studies found the use of a depth-weighting factor made mechanistically incorrect adjustments to the post-liquefaction ground settlement estimate as a liquefiable layer of variable thickness was moved up and down in simplified soil profiles.

The calibration factor *C* is the result of the constant overall offset observed in the residuals of clean sand natural soil sites represented by an average I_c value in the upper 15 m of the profile (I_{c15}) < 1.8. This factor is due to inherent differences between the characteristics of natural soil deposits and the largely reconstituted or slightly disturbed soils used in the laboratory tests that form the basis of the Olaya and Bray (2022b) post-liquefaction volumetric strain model (e.g., soil fabric, time under sustained loading, *OCR*). Initially, the calibration factor was largely controlled by the Christchurch case histories because most of the natural soil deposit data are from Christchurch. To examine potential biases from the large set of Christchurch data, the residuals from a subset of non-Christchurch case histories, which lead to $C = 1.36$, were compared to the calibration factor of 1.71 obtained from the Christchurch case histories. The calibration factor was set to $C = 1.50$ to represent the conditions of a generic site. It is possible the Christchurch case histories with its robust LiDAR surveys captured more ground settlement resulting from liquefaction than older case histories or included ejecta-induced settlement not included in the older studies. The calibration factor is nearly one for hydraulic fills because the

characteristics of hydraulic fills (i.e., relatively young, constructed soils with fabric similar that in the laboratory test programs) are better captured by the soils tested in the laboratory (i.e., C =1.05 for hydraulic fill). The reason natural soils have C = 1.50 is not fully understood. It could be due in part to the systematically larger ground settlements measured in Christchurch through the LiDAR surveys or it could be that the CPT liquefaction triggering and relative density correlations for natural soils are offset from those developed for constructed soil in the field and laboratory.

After C is applied to the results, residuals are plotted against I_{c15} and the trends shown in Figures 4.11a and 4.11b for hydraulic fills and natural soil deposits, respectively, can be eliminated by applying a soil behavior factor (SB) shown in Figure 4.11c and calculated as

$$SB = \exp\left(-0.675 \cdot \max\left(I_{c_{15}}, 1.8\right) + 1.215\right) \tag{4.9}$$

where I_{c15} is the average I_c over a depth of 15 m as defined previously. A depth of 15 m was selected from statistical analyses of the depth that contributes significantly to settlement. The same SB value can be applied to the D_r -based and the ψ_o -based models without introducing significant biases.

Most of the bias in the residuals are eliminated with application of C and SB; however, a bias remained as a function of earthquake moment magnitude. Duration is captured in the calculation of FS_L through the magnitude scaling factor (MSF), so initially another magnitude scaling factor was not thought to be required. However, the residuals indicated a dependence on M_w as shown in Figures 4.12a and 4.12b for hydraulic fills and natural soil deposits, respectively. The observed trend in these residuals are eliminated by applying a Magnitude Factor (MF) as

$$MF = \exp(0.214 \cdot M_w - 1.498) \tag{4.10}$$

The variation of MF with M_w is shown in Figure 4.12c. In retrospect, laboratory testing on sand specimens by Lee and Albaisa (1974) found that additional loading cycles applied beyond initial liquefaction induced larger volumetric strains, which indicates that larger M_w earthquakes with a larger number of equivalent cycles of loading should induce larger settlement, because liquefaction is typically triggered before the end of ground shaking in the case histories used to develop liquefaction triggering procedures. The same MF value is applied to natural soil deposits and hydraulic fills using either the D_r-based or the ψ_o-based volumetric strain models.

4.5 Final Model and Illustrative Application of the Procedure

4.5.1 Final Model

The final proposed model to estimate free-field post-liquefaction ground settlement is

$$S_v = C \cdot MF \cdot SB \cdot \sum_i [\varepsilon_{vi} \cdot \Delta z_i] \cdot e^{\varepsilon} \tag{4.11}$$

where the error term ε is normally distributed with zero mean and σ = 0.54 in natural log

units for hydraulic fill and σ = 0.61 in natural log units for natural soil for the D_r-based volumetric strain model, and σ = 0.53 and σ = 0.61 for the hydraulic fill and natural soil, respectively, for the ψ_o-based volumetric strain model. As expected, the uncertainty is lower estimating post-liquefaction ground settlement in constructed hydraulic fills than in natural soil deposits. Also, C = 1.05 for hydraulic fills and C = 1.50 for natural soil deposits for the reasons mentioned previously. Eq. 4.9 is used to calculate SB as a function of I_{c15}, and Eq. 4.10 is used to calculate MF as a function of M_w. As described previously, ε_{v_i} is the post-liquefaction volumetric strain calculated using the Olaya and Bray (2022b) model, which is calculated using either its D_r-based or ψ_o-based FS_L-γ_{max} and γ_{max} - ε_v relationships in which FS_L and D_r or ψ_o are estimated using CPT data at each depth i, and ΔZ_i is the thickness of the unit at depth i. The model is based on the mean estimate of FS_L with P_L = 50% using the two simplified liquefaction triggering produces mentioned previously and on the mean estimate of D_r or ψ_o using the two procedures mentioned previously.

The residuals for the final model for hydraulic fills and natural soil deposits are shown in Figures 4.13a and 4.13b, respectively. The final model provides reasonable estimates of liquefaction-induced ground settlement. The error term describes the uncertainty in the estimate of S_v given the values of the input parameters. In a deterministic assessment, the post-liquefaction ground settlement should be provided as a likely range of settlement using the 16% and 84% values. In a probabilistic assessment, the uncertainty in the input parameters can be considered by including the uncertainty in the estimate of the ground motion parameter PGA in a seismic hazard assessment and by capturing the uncertainty in the key input parameters through a logic tree approach.

4.5.2 Illustrative Application of Procedure

The application of the proposed liquefaction-induced volumetric-induced ground settlement procedure is illustrated using two case histories described in Olaya and Bray (2022a).

Case history CP-K16-S4 is a hydraulic fill site located in Wellington, New Zealand. The ground settlement is estimated for the 2016 Kaikoura M_w 7.8 earthquake that generated a nonliquefied site ground surface PGA = 0.25 g. The site has 10 to 20 m thick silty/sandy gravel fill atop marine sediments and alluvium that do not liquefy. The site is characterized by the 6 CPTs shown in Figure 4.8 with the groundwater table located between 3.0 m to 3.5 m below the ground surface. I_{c15} varies between 1.91 to 2.25 for the 6 CPTs. The average of the D_r estimated using Eq. 4.5 and Robertson and Cabal (2015) varies between 30% and 95% in the profile and the average of the P_L = 50% FS_L estimated using the Boulanger and Idriss (2016) and Robertson and Wride (1998)/Robertson (2009b)/Ku et al. (2012) procedures varies between 0.30 and 2.0. Use of Eqs. 4.1 and 4.3 with the average D_r and FS_L values at each depth in the profile provides estimates of ε_v between 0 and 4.0%. SB is estimated to be between 0.74 and 0.93 using Eq. 4.9. MF is estimated as 1.19 using Eq. 4.10. C = 1.05 because it is a hydraulic fill. The median estimate of settlement for each of the 6 CPTs using Eq. 4.11 is between 225 mm and 425 mm with the site's geomean value of S_v = 325 mm and the 16% to 84% range of 190 mm to 550 mm (σ = 0.54). The estimated range of ground settlement is consistent with the surveyed ground settlement range of 200 mm – 350 mm (Dhakal et al. 2020).

Case history Ch-S167 is a natural soil deposit site located in Christchurch, New Zealand. Ground settlement is estimated for the 2011 M_w 6.2 June earthquake with a nonliquefied site ground surface PGA = 0.29 g. The site profile is composed primarily of silty sand layers with occasional lenses of clayey soil. The groundwater depth is estimated to be 2.0 m, and 3 CPTs are available at this site (Olaya and Bray 2022a). I_{c15} varies between 1.63 to 1.79. Following the same procedure as in the previous example, the average D_r varies between 20% and 90% in the profile and the average of the P_L = 50% FS_L varies between 0.60 to 2.0. Use of Eqs. 4.1 and 4.3 with the average D_r and FS_L values at each depth provides estimates of ε_v between 0 to 3.6%. SB is estimated to be 1.0 (I_{c15} < 1.8), MF = 0.84, and C = 1.50 (natural soil deposit). The median estimate of settlement for each of the 3 CPTs using Eq. 4.11 is between 50 mm and 80 mm with the site's geomean value of S_v = 60 mm and the 16% to 84% range of 30 mm to 110 mm (σ = 0.61). The estimated range of ground settlement is consistent with the LiDAR-based measured settlement range of 30 mm – 90 mm (Olaya and Bray 2022a).

4.6 Liquefaction-Induced Building Settlement

Liquefaction-induced building settlement (S_t) is the combination of shear-induced settlement (S_s), volumetric-induced settlement (S_v), and ejecta-induced settlement (S_e) as

$$S_t = S_s + S_v + S_e \tag{4.12}$$

Due to the related mechanisms of these liquefaction-induced building settlement components, the correlation among them should be considered. Currently, ejecta-induced settlement can be estimated using the approximate correlation of settlement with the general ejecta severity criteria of the CPT-based method proposed by Hutabarat and Bray (2022). There is insufficient statistical rigor to examine a correlation of S_e to S_v and S_s. Though uncertain, S_e is often negligible (e.g., at highly stratified soil sites). It is not often severe-to-extreme. In cases when it is minor or moderate, S_e is likely less than 50 mm or 100 mm, respectively. Mean best estimates of S_e are subtracted from S_t to analyze the joint occurrence of S_v and S_s for building settlement case histories.

Bray and Macedo (2017) developed a set of 19 well documented liquefaction-induced building settlement case histories with estimates of observed S_s, S_v, and S_e. These case histories are used to evaluate the relation between S_s and S_v after subtracting S_e as explained before. The Bray and Macedo (2017) shear-based settlement model and the proposed volumetric-based model (Eq. 4.11) are employed for the statistical evaluation of the correlation between S_s and S_v. These models are probabilistic and produce normally distributed estimates of ln(S_s) and ln(S_v) with error terms that are zero-mean and normally distributed as

$$\ln(S_s) = f_s(\theta_s) + \delta_{S_s}\sigma_{S_s} \tag{4.13a}$$

$$\ln(S_v) = f_v(\theta_v) + \delta_{S_v}\sigma_{S_v} \tag{4.13b}$$

where $f_s(\theta_s)$ and $f_v(\theta_v)$ represent the parameters of each functional model, σ_{S_s} and σ_{S_v}

are the models' standard deviations, and δ_{S_s} and δ_{S_v} represent the randomness in each model.

The correlation coefficient (ρ) between the residuals of the ln(S_s) and ln(S_v) models quantify the dependency between S_s and S_v (Baker and Cornell 2006). The relation between the residuals of the models for ln(S_s) and ln(S_v) using the available 19 case histories results in ρ = 0.72. The correlation coefficient ρ is then employed to obtain correlated values of δ according to Eq. 4.14 (Baker and Cornell 2006).

$$\delta_{S_v|S_s} = \rho \cdot \delta_{S_s} + N\sqrt{1-\rho^2} \tag{4.14}$$

where N is a normally distributed random variable with zero mean and unit standard deviation. Correlated samples for ln(S_s) and ln(S_v) can be generated by combining Eq. 4.14 with Eq. 4.13. A Monte Carlo approach with a sufficient number of realizations for ln(S_s) and ln(S_v) is then used to approximate the mean (μ_s) and standard deviation (σ_s) of $S_s + S_v$.

The application of the proposed liquefaction-induced building settlement procedure is illustrated for the CTUC building site shown in Figure 4.14 for the 2011 M_w 6.2 Christchurch earthquake. Observed settlements for the NE and SE corners of the building are provided in Luque and Bray (2017). No ejecta was observed in the NE corner, whereas S_e was estimated to be between 70 mm to 150 mm in the SE corner. Hence, the range of settlement after subtracting S_e is 160 mm to 260 mm for the NE corner and 250 mm to 450 mm for the SE corner of the building. For the NE corner, the Bray and Macedo (2017) median estimate of S_s is 70 mm with σ_{S_s} = 0.50 and the proposed model (Eq. 4.11) median estimate of S_v is 100 mm with σ_{S_v} = 0.61. A set of 1000 realizations of $S_s + S_v$ are produced using Eqs. 4.13 and 4.14 from which the estimated mean total settlement is 170 mm with a range of 100 mm to 290 mm (σ_s = 0.53 ln units). This settlement range is consistent with the observed settlements of 160 mm to 260 mm at the building's NE corner. For the SE corner, the median estimate of S_s is 180 mm with σ_{S_s} = 0.50 and the median estimate of S_v is 140 mm with σ_{S_v} = 0.61. Again, a set of 1000 realizations of $S_s + S_v$ are generated using Eqs. 4.13 and 4.14 from which the total median settlement is 325 mm with a range of 190 mm to 545 mm (σ_s = 0.52 ln units). This settlement range is also consistent with the observed settlements of 250 mm to 450 mm at the building's SE corner.

4.7 Conclusion

Great challenges remain in geotechnical earthquake engineering. Professor H. Bolton Seed forged a path to advance knowledge in geotechnical earthquake engineering which can be followed. Throughout his career he integrated field case histories, laboratory experiments, and analyses in his studies. Analyses were not conducted to find the answer, but instead to gain insight. The authors employed Professor H. Bolton Seed's approach to evaluate liquefaction effects. Through examining field case histories, experiments, and analyses, insights are shared on the effects of liquefaction in the built environment.

Liquefaction-induced building settlement mechanisms are shear, volumetric, and ejecta. The problem is best viewed by examining soil response at the element level and soil deposit

performance through its system response. The state of a unit of uniform clean sand, sandy gravel, nonplastic silty sand, and nonplastic silt can be examined in a unified manner using relative density and the state parameter. The cyclic responses of uniform fine sand, uniform nonplastic silty sand, and uniform coarse nonplastic silt are generally similar if at the same state and effective stress and loaded similarly. Post-liquefaction volumetric strain models are presented that capture this important soil response in a unified manner. In many cases, sandy gravels that are controlled by their sand matrix and clayey silts that respond similarly to nonplastic silts can be captured using models developed for sand, silty sand, and nonplastic silt.

The system response of a soil deposit often governs the consequences of liquefaction triggering. System response features affect greatly the formation of ejecta and its effects on infrastructure. Ejecta-induced building settlement is challenging to estimate. However, through dynamic nonlinear effective stress analysis the importance of capturing the post-shaking hydraulic mechanisms that govern the upward flow of water was identified. The ejecta potential index indicates when ejecta are likely to occur and how extensive it would likely be when it occurs. A CPT-based method can be used to evaluate ejecta severity when there are insufficient resources to support effective stress analyses. Its liquefaction ejecta demand parameter L_D tends to increase systematically as ejecta severity increases at thick clean sand sites. Low L_D values are estimated at stratified soil sites that did not produce ejecta, which resolves the apparent overestimation by other liquefaction indices at stratified soil sites. The $L_D - C_R$ liquefaction ejecta severity chart separates cases with severe or extreme ejecta, which have high L_D and low C_R values, from cases with no ejecta, which have low L_D and high C_R values. The CPT-based liquefaction ejecta severity chart provides a preliminary estimate of the free-field, level ground ejecta-induced ground settlement.

The CPT should be the primary site investigation tool in most liquefaction evaluations. The CPT should be complemented with cyclic tests performed on high-quality samples when they are informative. The insights derived from cyclic tests support effective stress analyses which provides additional insights. However, there is no substitute for characterizing the depositional environment. Geologic details matter. Soil fabric is only indirectly assessed through most field and laboratory testing methods. Detailed logging of high-quality continuous samples to examine soil fabric and other important details should be performed when it is suspected that key factors will be missed using conventional sampling and in situ testing.

A probabilistic CPT-based post-liquefaction ground settlement procedure is proposed. It takes advantage of a recently compiled comprehensive laboratory database of post-liquefaction testing and a recently compiled comprehensive field case histories database of post-liquefaction settlement measurements. The volumetric strain of nonplastic soil with uniform gradation (SP, SM, and ML) can be estimated using D_r-based or ψ_o-based volumetric strain models. New correlations are developed to estimate D_r or ψ_o to enable use of the volumetric strain models. A calibration factor is required to adjust the estimates of natural soil deposits as these deposits have characteristics not well represented in the laboratory tests used to develop the volumetric strain models. The calibration factor is not required for hydraulic fills. A soil behavior factor dependent on I_{c15} and a magnitude factor dependent on M_w are incorporated in the model to capture their effects on post-liquefaction ground settlement. The calibrated model captures the trends in the field measurements of post-liquefaction ground settlement well.

Additional studies to develop alternative models and perspectives are warranted. As stated previously, great challenges remain in geotechnical earthquake engineering, especially in the evaluation of liquefaction effects. Liquefaction research can advance the state-of-the-art by focusing on understanding and evaluating the effects of liquefaction and developing innovative mitigation methodologies.

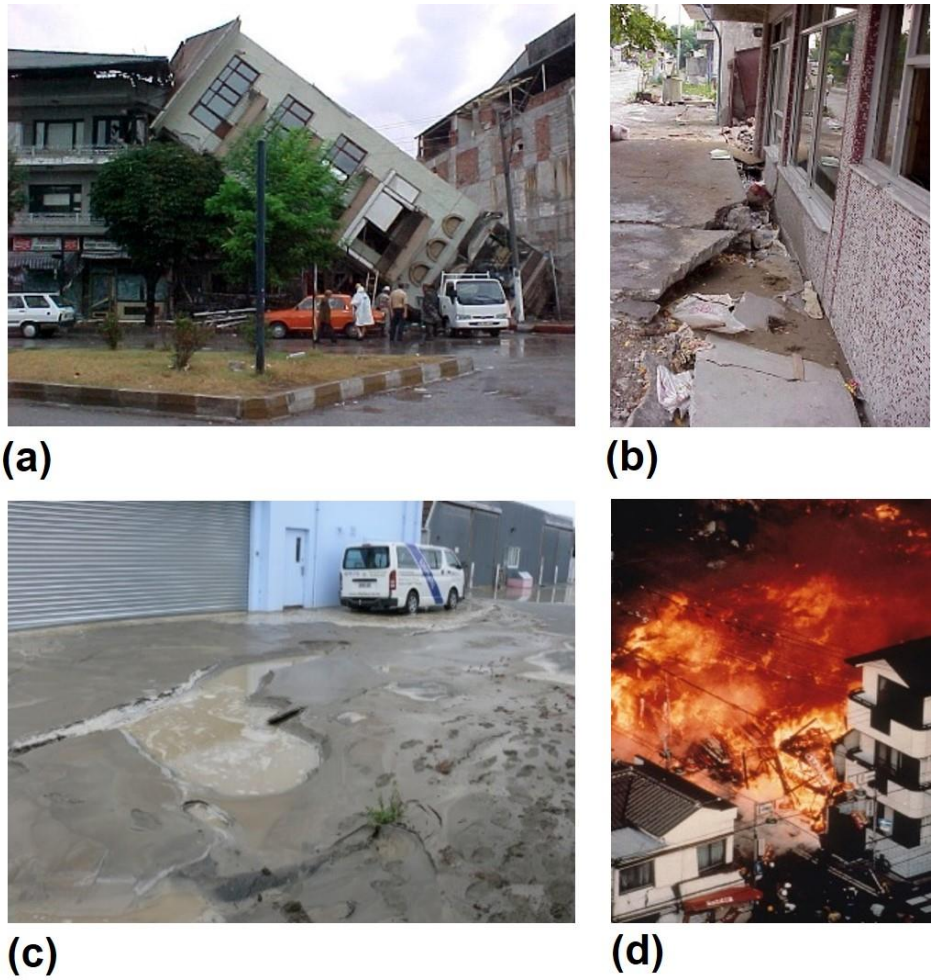

Figure 4.1. Buildings damaged by liquefaction: (a) overturned 5-story building in Adapazari, (b) laterally displaced and settled building in Adapazari, (c) ejecta affecting building in Christchurch, and (d) fire in Kobe (images from Bray et al. 2004, 2014a, Akai et al. 1995).

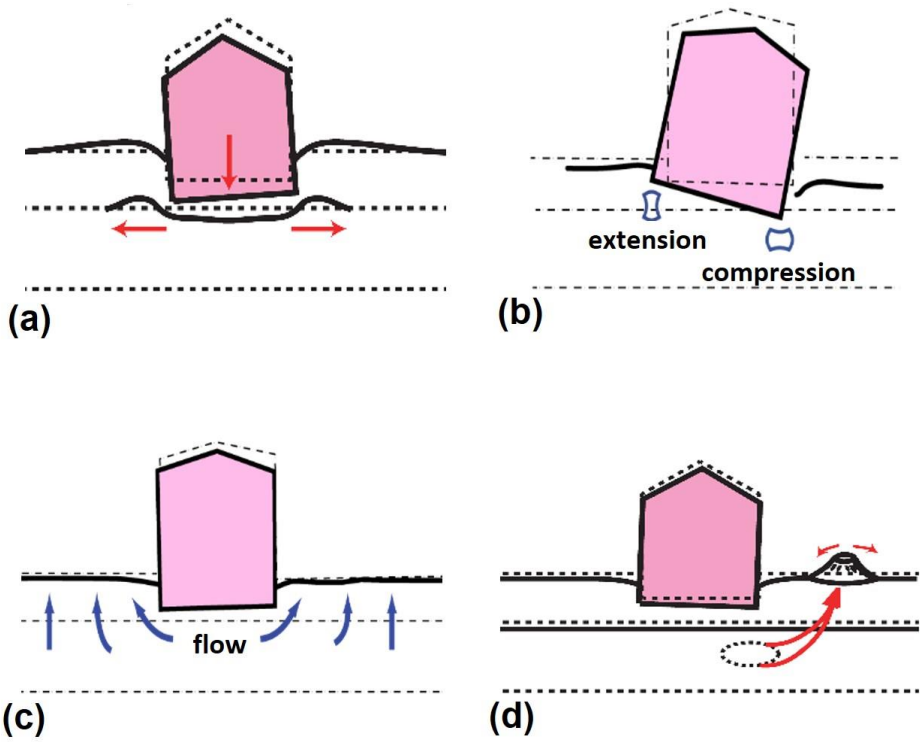

Figure 4.2. Liquefaction-induced building displacement mechanisms: (a) shear-induced punching failure, (b) shear-induced SSI ratcheting, (c) volumetric-induced reconsolidation settlement, and (d) ejecta-induced ground loss.

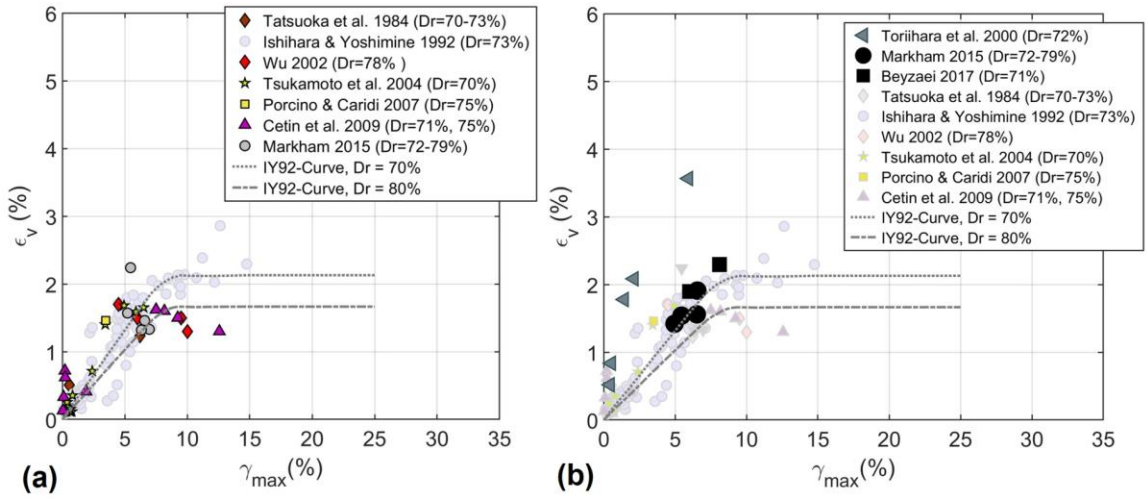

Figure 4.3. Volumetric strain vs. maximum shear stress test data for D_r = 70% - 80: (a) Clean uniform sand (Ishihara and Yoshimine 1992 clean sand data are shown in light blue), and (b) nonplastic to low-plasticity silty sand (clean uniform sand data shown in light blue) (Olaya and Bray 2022b).

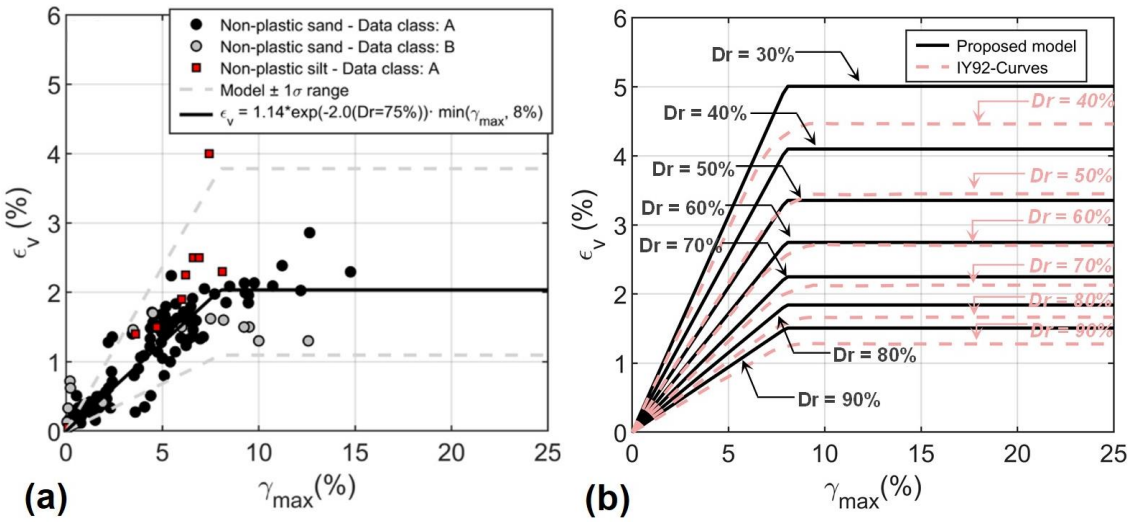

Figure 4.4. Nonplastic uniform soil $\varepsilon_v - \gamma_{max}$ proposed model in terms relative density: (a) D_r = 70% - 80%, and (b) model contours (Olaya and Bray 2022b).

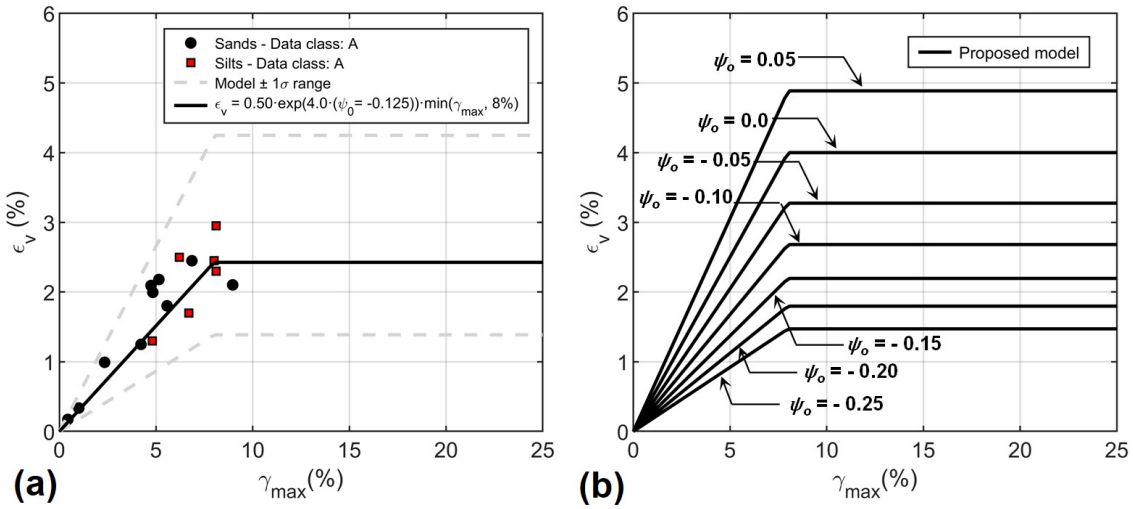

Figure 4.5. Nonplastic uniform soil $\varepsilon_v - \gamma_{max}$ proposed model in terms of state parameter: (a) ψ_o = -0.15 to -0.10, and (b) model contours (Olaya and Bray 2022b).

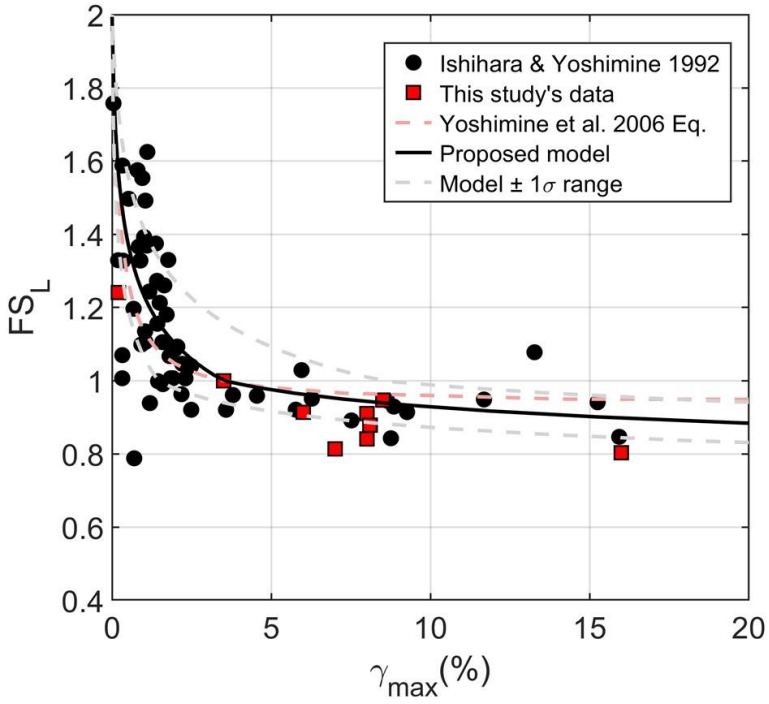

Figure 4.6. γ_{max} – FS_L data and proposed model in terms relative density for D_r = 40% - 50% (Olaya and Bray 2022b).

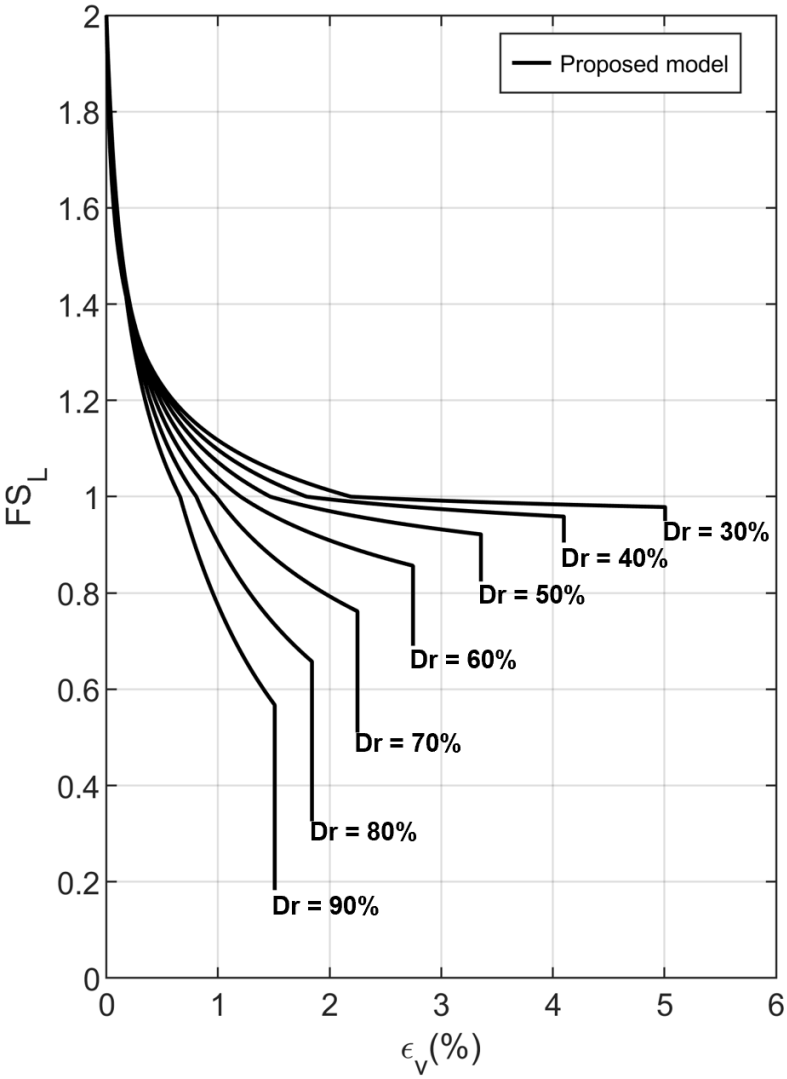

Figure 4.7. Relationship between ε_v and FS_L in terms of D_r (Olaya and Bray 2022b).

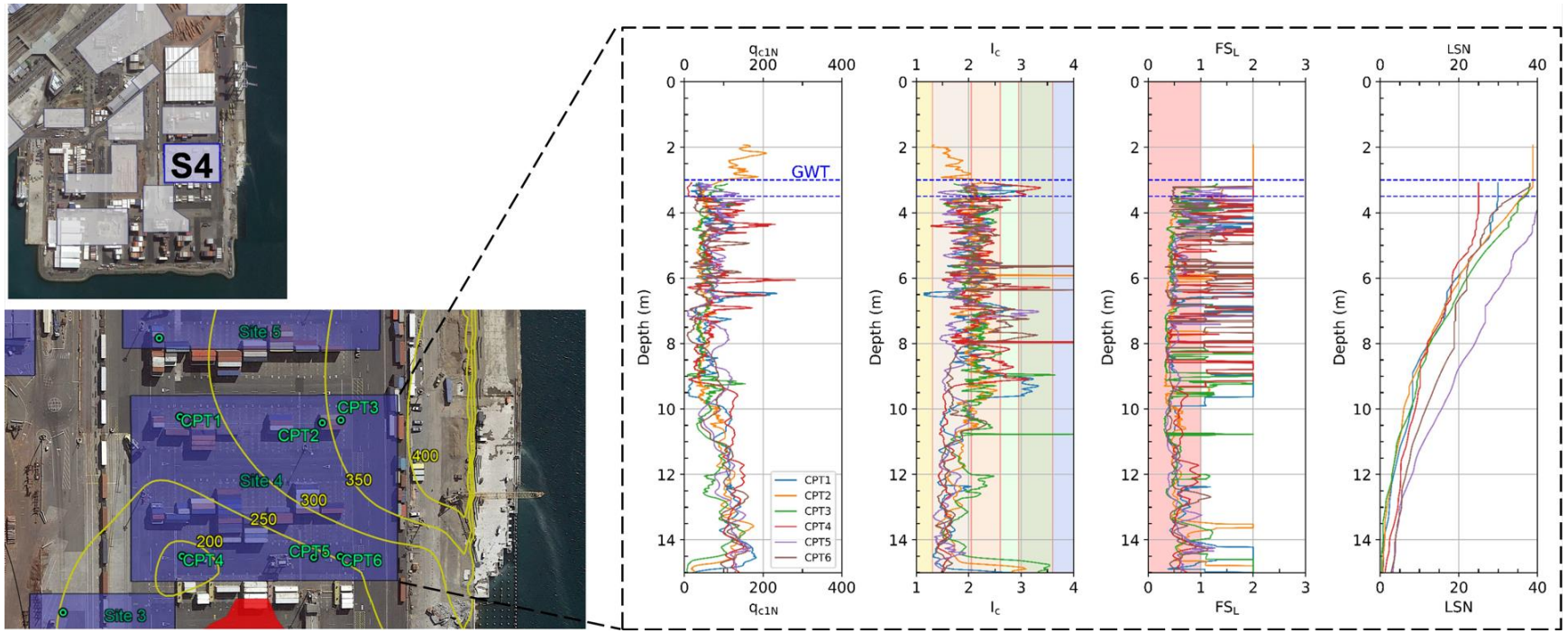

Figure 4.8. CentrePort with enlarged image of Site 4 showing CPT locations and mean ground settlement (mm) contours with q_{c1n}, I_c, FS_L, and *LSN* profiles (data from Dhakal et al. 2022, Olaya and Bray 2022a, and images from Google Earth®).

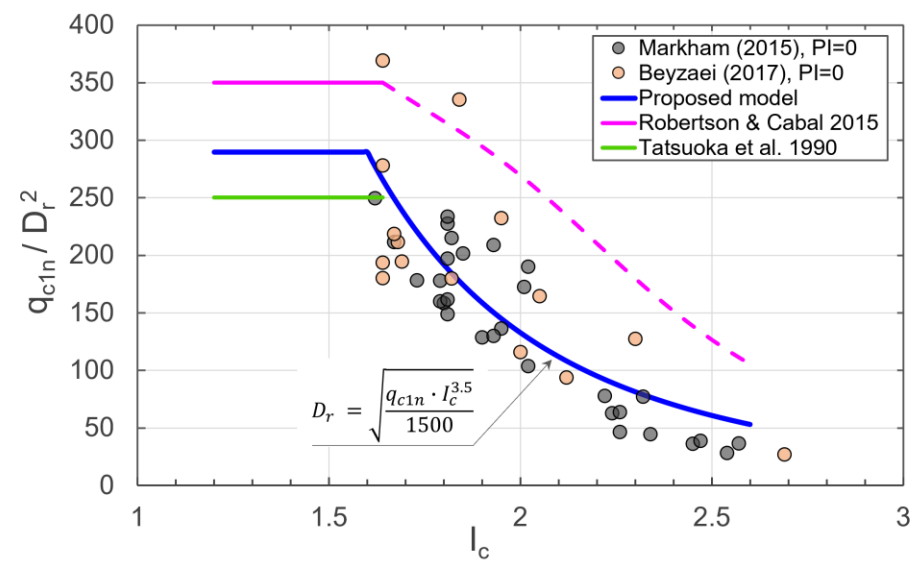

Figure 4.9. Influence of soil compressibility (through I_c) on the ratio of CPT tip resistance to D_r^2.

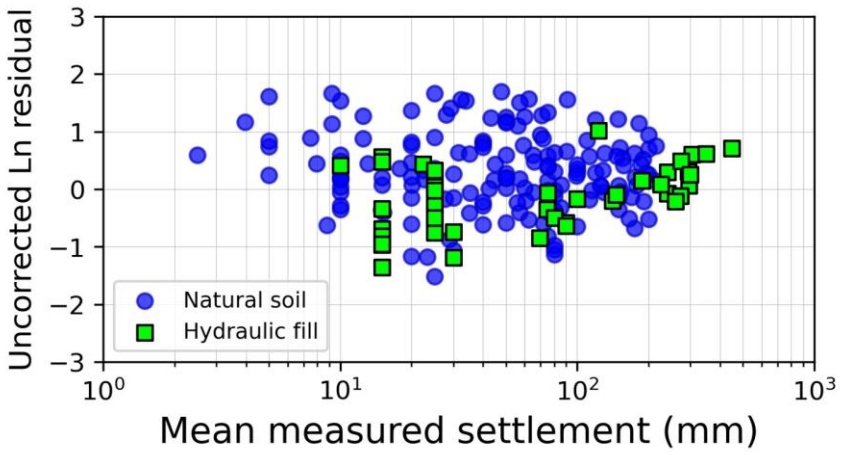

Figure 4.10. Initial residuals ($\ln(S_{v\_meas}) - \ln(S_{v\_est})$) using the Olaya and Bray (2022b) post-liquefaction volumetric strain model without adjustments.

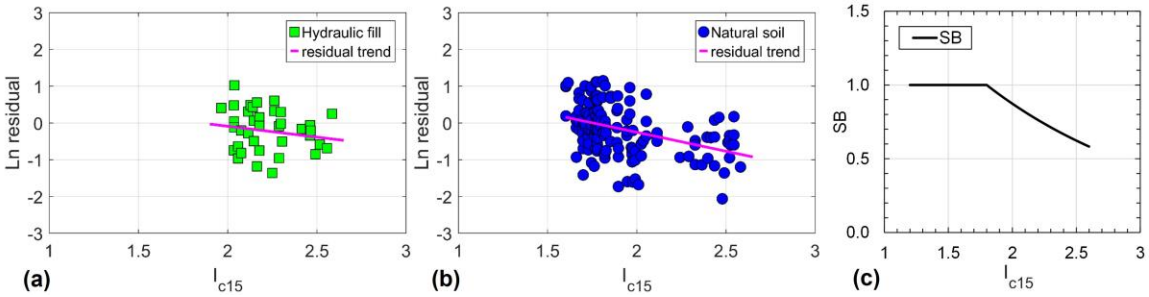

Figure 4.11. Residuals ($\ln(S_{v\_meas}) - \ln(S_{v\_est})$) vs. I_{c15} for: (a) hydraulic fill and (b) natural soil deposit, and (c) Soil Behavior factor relationship.

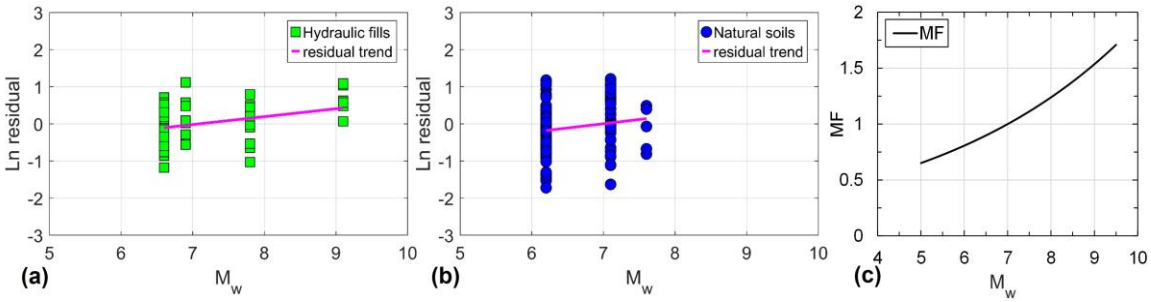

Figure 4.12. Residuals (ln(S_{v_meas}) – ln(S_{v_est})) vs. M_w for: (a) hydraulic fill and (b) natural soil deposit, and (c) Magnitude Factor relationship.

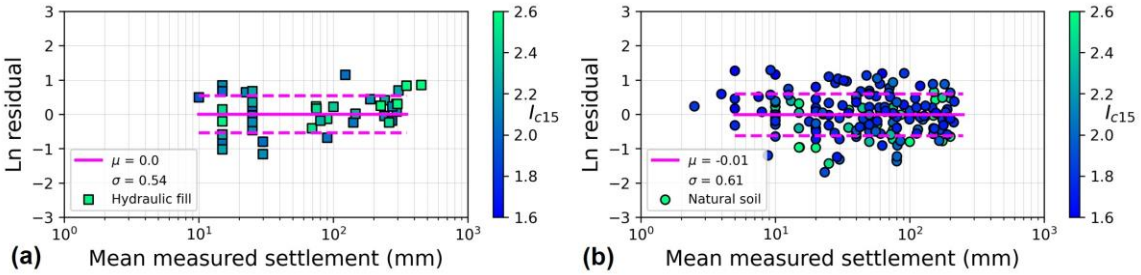

Figure 4.13. Final model residuals ($\ln(S_{v\_meas}) - \ln(S_{v\_est})$) for: (a) hydraulic fill and (b) natural soil deposit.

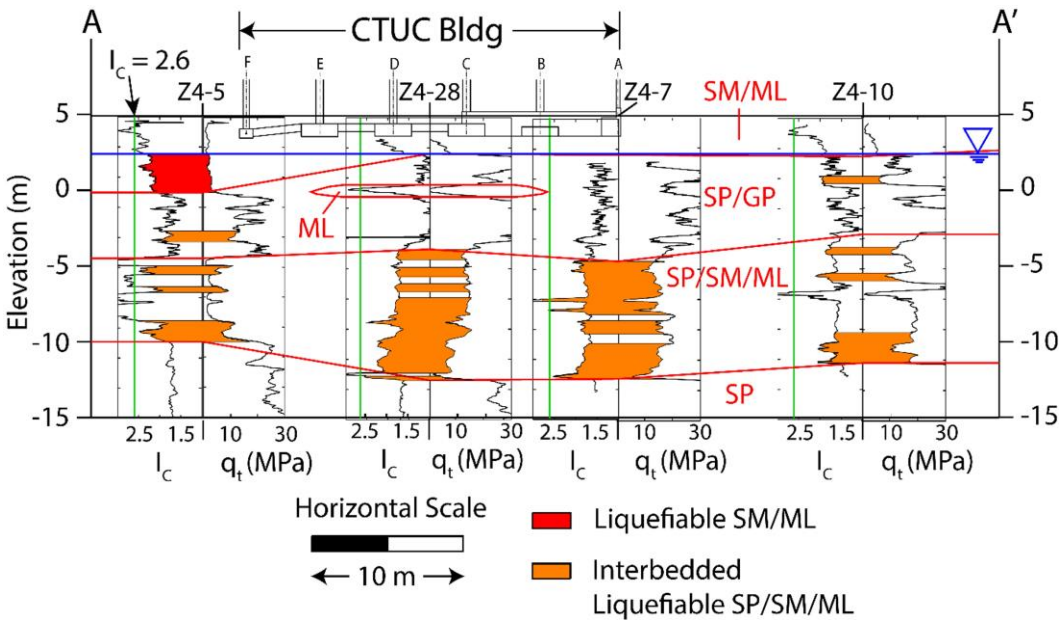

Figure 4.14. CTUC building case history, Christchurch (from Luque and Bray 2017).

5 Performance-Based Probabilistic Liquefaction-Induced Ground Settlement Procedure

The contents of this chapter are primarily from a journal article being submitted to the Earthquake Spectra Journal of the Earthquake Engineering Research Institute (EERI) by Olaya, F.R., Bray, J.D., and Abrahamson, N. entitled: "Performance-Based Probabilistic Liquefaction-Induced Ground Settlement Procedure."

5.1 Introduction

Soil liquefaction at free-field level ground sites can produce ground settlement because of the accumulation of volumetric strains resulting from post-liquefaction sedimentation and reconsolidation processes (e.g., Ishihara and Yoshimine 1992, Zhang et al. 2002, and Bray and Olaya 2023). The estimation of the likely amount of ground settlement due to liquefaction is of engineering importance because differential ground settlement can lead to failure of structures, buried utilities, and roadways. Additionally, liquefaction-induced ground settlement can lead to flooding of coastal infrastructure. As examples, Figure 5.1a shows the post-liquefaction free-field level ground settlement at Port Island after the January 17, 1995 M_w = 6.5 Hyogoken-Nanbu (Kobe, Japan) earthquake, and Figure 5.1b shows flooding of areas of the city of Iskenderun due to the February 6, 2023 M_w = 7.8 Pazarcik (Southeast Türkiye) earthquake. The 1995 Kobe earthquake produced widespread liquefaction in the loose sandy hydraulic fill at Port Island. Away from the edges of the island, liquefaction produced an average of 0.5 m of relatively uniform ground settlement. The monorail system to the right in Figure 5.1a and the low- and high-rise buildings in the area performed well during the earthquake because they were supported by deep foundation systems that reached competent material below the hydraulic fill. The monorail system did not show signs of vertical displacement, which indicated the ground settlement at this part of Port Island was largely due to one-dimensional liquefaction-induced volumetric sedimentation/reconsolidation. The 2023 Türkiye earthquake triggered liquefaction in some of the coastal areas of Iskenderun. Lateral spreading and post-liquefaction reconsolidation settlement mechanisms lowered the ground surface, which allowed high water events to flood areas of the city as shown in Figure 5.1b. Rebuilding of the infrastructure in these areas of Iskenderun will require addressing the increased flood hazard due to ground settlement.

The amount of liquefaction-induced free-field ground settlement (S_v) is used directly to assess the seismic performance of infrastructure at sites with liquefaction-induced ground settlement. The estimate of S_v is also used as an index of ground damage due to liquefaction. The estimation of liquefaction-induced ground settlement is largely based on empirical procedures (e.g., Ishihara and Yoshimine 1992, Zhang et al. 2002, and Idriss and Boulanger 2008), because dynamic nonlinear effective stress analyses using continuum-based methods do not currently capture sedimentation and reconsolidation processes

effectively. Thus, the number of field case histories used to calibrate and to validate procedures developed using conceptual models of soil response observed in laboratory tests (e.g., Ishihara and Yoshimine 1992) is important.

Currently employed liquefaction-induced ground settlement procedures, however, are based on a limited number of case histories. For example, the widely used Zhang et al. (2002) procedure is calibrated using a few sites in the Marina district and Treasure Island in the San Francisco Bay Area after the 1989 Loma Prieta earthquake. The uncertainty of the estimate of liquefaction-induced ground settlement in the field is difficult to assess with only a few case histories from one earthquake event. Reconnaissance efforts after the 2010-2011 Canterbury earthquake sequence and the 2013-2016 northern South Island, New Zealand earthquakes as well as documentation of liquefaction ground settlement of sites affected by the 1999 Chi-Chi and 2011 Tohuko earthquakes enabled Olaya and Bray (2023) to develop a database of 205 well-documented field case histories of liquefaction-induced ground settlement characterized by the cone penetration test (CPT). This database differentiates natural soil deposit sites from hydraulic fill sites to account for their different formation processes and their different seismic performance. The enlarged field case history database documents a wide range of liquefaction-induced ground settlement observations at a large range of soil conditions, ground motion intensity measures, and liquefaction severity indexes. Hence, the database provides a robust basis to evaluate the mechanisms of post-liquefaction ground settlement and to assess the uncertainty in its estimation.

In current engineering practice, the procedures to assess S_v generally follow deterministic or pseudo-probabilistic approaches as defined by Rathje and Saygili (2008). In these approaches, the assessment of the ground motion intensity measure (*IM*) is not incorporated into the computation of S_v. In the deterministic approach, the *IM* is obtained from a selected earthquake scenario consisting of M_w, source-to-site distance (R), and the number of standard deviations above the median ground motion (ε). Subsequently, S_v is estimated from empirical models that are usually a function of the soil's relative density (D_r) and the factor of safety against liquefaction (FS_L) computed using the M_w and *IM* defined by the selected earthquake scenario. In a pseudo-probabilistic approach, a hazard curve for the *IM* (λ_{IM}) is developed through a probabilistic seismic hazard assessment (PSHA) that accounts for all relevant earthquake scenarios (M_w, R, and ε). The λ_{IM} determines the mean annual rate of exceedance of a wide range of different *IM* levels. A design hazard level (or return period) is prescribed, and the corresponding *IM* value is selected. S_v is then estimated using the FS_L computed using the M_w and *IM* compatible with the selected λ_{IM} considering the D_r of the soil deposit. In the pseudo-probabilistic approach, it is implicitly assumed the selected design hazard level of the *IM* (λ_{IM}) is consistent with the hazard level for the engineering demand parameter, S_v. However, this assumption is not always valid as will be shown later in this paper.

In a performance-based approach, the hazard evaluation for *IM* is incorporated explicitly in the assessment of S_v by combining λ_{IM} with the probability of exceeding different S_v levels. Hence, the sources of variability contributing to λ_{IM} are included directly in the evaluation of S_v. In addition, the uncertainty of the inputs to the model for S_v are also included in a performance-based evaluation. The objective of this approach is to develop the mean hazard curve for S_v (i.e., $\lambda(S_v)$). The variability in $\lambda(S_v)$ can be explored if required by including information on sources of epistemic uncertainty relevant to the calculation of

S_v. The hazard curve for S_v enables different hazard levels (or return periods) for S_v to be evaluated directly in contrast to the pseudo-probabilistic approach where it is assumed the hazard level of the *IM* is the same as that of S_v. In this paper, a performance-based procedure for the assessment of S_v is developed and its application illustrated. The procedure is straightforward to implement, and it has the flexibility to incorporate different sources of uncertainty related to the *IM* and S_v components in the probabilistic procedure used to estimate S_v.

5.2 Previous Studies

State of practice approaches for evaluating liquefaction-induced free-field level-ground settlement are largely empirical. Lee and Albaisa (1974) provided initial recommendations for estimating post-cyclic reconsolidation of sands deposits. They related the amount of volume change due to reconsolidation observed in cyclic triaxial test specimens with the peak excess pore water pressure ratio ($r_{u,\ peak}$) reached during the test. To enable the estimation of $r_{u,\ peak}$ under field conditions, a relationship between the number of equivalent uniform cycles caused by the design earthquake and $r_{u,\ peak}$ was presented. Ishihara and Yoshimine (1992) developed a framework for computing post-liquefaction ground settlement that is based on a laboratory-based volumetric strain (ε_v) model and the standard penetration test (SPT) to capture soil density. In the Ishihara and Yoshimine procedure, S_v is the result of the cumulative effect of volumetric strains that develop within a soil profile as a consequence of liquefaction. Post-liquefaction volumetric strains are obtained as a function of the estimated D_r and FS_L values of each soil layer in the deposit at the site.

The data and framework proposed by Ishihara and Yoshimine (1992) are the basis for several other empirical methods. For instance, Zhang et al. (2002) adapted the Ishihara and Yoshimine (1992) relationship between FS_L and ε_v to develop a widely used method based on the CPT for estimating liquefaction-induced ground settlement. Similarly, Idriss and Boulanger (2008) used the Ishihara and Yoshimine (1992) relationship to estimate ε_v as a function of FS_L to develop a liquefaction-induced ground settlement model based on SPT and CPT correlations. Juang et al. (2013) expanded on the Zhang et al. (2002) work by including the probability of liquefaction into the CPT model formulation and by including 32 case histories (with a site often defined by a single CPT) to evaluate their model. Wu and Seed (2004) proposed a SPT ground settlement procedure based on cyclic simple shear tests performed on Monterey 0/30 sand. In contrast to Ishihara and Yoshimine (1992), their model uses a normalized cyclic stress ratio as a proxy for the earthquake demand (instead of FS_L). Cetin et al. (2009a) expanded the Wu and Seed (2004) work by using the Cetin et al. (2009b) model for ε_v, that is based on a larger number of cyclic test data representative of different sands, in conjunction with 49 case histories to develop a probabilistic post-liquefaction ground settlement model based on SPT data. Duku et al. (2008) utilized cyclic simple shear test data on partially saturated specimens from 16 different sands to formulate a probabilistic model for seismic-compression-induced volumetric strain of clean sand. The model is not intended to capture post-liquefaction settlement; it uses 15 equivalent uniform cycles of earthquake loading as the reference condition to estimate ground settlement of compacted fills.

Kramer et al. (2014) formulated a performance-based method for ε_v that uses the hazard curve for FS_L and the Wu and Seed (2004) data and model for ε_v to limit the amount of ε_v

possible at large return periods associated with high *IMs*. Franke et al. (2021) used the performance-based method of Kramer et al. (2014) with the Ishihara and Yoshimine (1992) and Cetin et al. (2009b) models for ε_v to formulate an SPT-based performance-based approach to evaluate S_v. An important aspect in this method is that the uncertainty in ε_v for a soil layer is considered to be the same as the uncertainty in S_v. A key requirement to implement a performance-based approach is to have a model for S_v that quantifies the uncertainty in the estimate of settlement, so the probability of exceedance can be computed.

In summary, several SPT-based probabilistic procedures to estimate liquefaction-induced ground settlement exist which could be implemented in a performance-based approach (e.g., Franke et al. 2021). However, the CPT is superior to the SPT as a soil characterization tool because it provides nearly continuous sampling of the soil with depth and is more repeatable and consistent in its measurements. Widely used empirical CPT-based liquefaction-induced ground settlement procedures (e.g., Zhang et al. 2002, and Idriss and Boulanger 2008) are deterministic and cannot be implemented as currently presented in a performance-based approach. Thus, a recently developed probabilistic CPT-based procedure to estimate S_v (Bray and Olaya 2023) is implemented in a performance-based approach in this study. The database of S_v field case histories developed by Olaya and Bray (2023) can be used to estimate the amount of free-field ground settlement at sites affected by liquefaction.

The total amount of liquefaction-induced ground settlement also provides an estimate of the seismic performance of the ground affected by liquefaction and light-weight structures supported on it (i.e., 1-2 story buildings not affected significantly by shear-induced settlement). Total liquefaction-induced free-field level ground settlement less than 100 mm is typically considered acceptable, whereas liquefaction-induced ground settlement more than 100 mm is often considered significant. Thus, the threshold of damage to light-weight residential buildings due to total liquefaction-induced free-field level ground settlement is often taken at S_v = 100 mm with the assumption that the differential settlement due to different ground conditions under the building will be less than half this value (i.e., New Zealand Ministry of Business, Innovation and Employment (MBIE) Guidance 2012). Negligible liquefaction-induced ground settlement (< 10 mm) can be considered as None, and ground settlement greater than 300 mm can be considered severe. Considering this information and the accuracy in estimating liquefaction-induced ground movements, four categories of total liquefaction-induced free-field level ground settlement are proposed as shown in Table 5.1.

5.3 Probabilistic Liquefaction-Induced Ground Settlement Model

The Ishihara and Yoshimine (1992) framework is a sound basis for the development of a probabilistic procedure to estimate liquefaction-induced ground settlement. However, it is important to note that the data and relationships used by Ishihara and Yoshimine (1992) to develop their procedure are derived from one series of cyclic tests performed on one uniform clean sand (Fuji River sand). It is not clear if these relationships can be applied universally to all clean sands, to silty sands, and to silts. Olaya and Bray (2022) developed a comprehensive laboratory database of post-liquefaction volumetric strain measurements containing information on 10 clean sands, 2 gravelly soils, 3 silty sands, 5 silts, and 3 clayey soils to investigate the relationship between FS_L, the earthquake-induced maximum shear

strain (γ_{max}), and the ε_v for uniform nonplastic clean sand, silty sand, and silts. This new database enabled the formulation of new models relating FS_L, γ_{max}, and ε_v as function of D_r (and the state parameter ψ) for nonplastic soils as shown in Eqs. 1 and 2 (Olaya and Bray 2022).

$$\gamma_{\max} = 3.5 \cdot \left[\frac{2^A - {FS_L}^A}{2^A - 1}\right] \cdot e^{\delta_\gamma} \qquad (5.1)$$

$$\gamma_{\max} = 0 \; ; \quad \text{for } FS_L \geq 2.0$$

$$A = \begin{cases} -2.8 \cdot {D_r}^2 + 10.2 \cdot D_r - 9.8 \; ; & FS_L \geq 1.0 \\ -275 \cdot \exp(-6.6 \cdot D_r) \; ; & FS_L < 1.0 \end{cases}$$

$$\varepsilon_v = 1.14 \cdot \exp\left(-2.0 \cdot D_r\right) \cdot \min(\gamma_{\max}, 8\%) \cdot e^{\delta_v} \qquad (5.2)$$

where ε_v (as a percentage) is obtained as function of γ_{max} (as a percentage) for a specified value of D_r (as a decimal), and the standard deviation of the error terms of ε_v and γ_{max} are $\delta_v = 0.62$ and $\delta_\gamma = 0.88$ in natural log units. These standard deviations can be reduced to $\delta_v = 0.52$ and $\delta_\gamma = 0.72$ if the data for ε_v and γ_{max} are limited to values greater than 0.5% as the uncertainty reduces significantly when small values of strain are excluded. The relationship between ε_v and FS_L as a function of D_r obtained from combining the median values of Eqs. 1 and 2 is shown in Figure 5.2.

As mentioned previously, Olaya and Bray (2023) developed a well-documented database of 205 field case histories of liquefaction-induced ground settlement to interrogate the data, to develop a new procedure, and to assess the uncertainty of the estimate of S_v. In this database, a case history is defined as the combination of (1) a site with laterally uniform soil stratigraphy with at least one CPT, (2) an earthquake event represented by its M_w, ground surface *PGA* or other *IM*, and (3) consistent post-liquefaction volumetric-induced free-field, level ground settlement measurements. A site is not defined by a CPT. Instead, a site is defined by its consistent subsurface soil characteristics and seismic performance. Reclaimed land is typically the result of sequential hydraulic filling of borrowed granular material that produces relatively uniform and loose fills. Case histories of the performance of hydraulic fills, such as those during the 1995 Kobe earthquake (e.g., Yasuda et al. 1996), indicate that uniformly deposited hydraulic fills tend to exhibit relatively uniform settlement (Figure 5.1a). In contrast, natural soil deposits are heterogenous because of the complex depositional processes involved, as a result, natural soils can show varying degrees of lateral variability in addition to aging effects. Due to their differing formation processes and seismic performance, the Olaya and Bray (2023) case histories are categorized into 42 cases of hydraulic fills and 163 cases of natural soil deposits.

In this study, the probabilistic liquefaction-induced free-field ground settlement model of Bray and Olaya (2023) is employed to evaluate the hazard of S_v. This model was developed following the Ishihara and Yoshimine (1992) framework with volumetric strains, ε_v, computed using the median values of Eqs. 1 and 2. The model captures the influence of the ground motion characteristics (e.g., intensity and duration) at the site in the development of earthquake-induced cyclic shear strain and the resulting volumetric strain of soil as a function of its state. The model uses the unbiased FS_L at a probability of liquefaction triggering (P_L) of 50% calculated using the average of two simplified liquefaction triggering procedures: (1) the Robertson and Wride (1998) procedure as

updated by Robertson (2009) and converted to a probabilistic method by Ku et al. (2012), and (2) the Boulanger and Idriss (2016) procedure. To estimate the soil state, the average of the CPT-based correlations for D_r of Bray and Olaya (2023) and Robertson and Cabal (2015) are used. Alternatively, ψ can be used instead of D_r. The in-situ state parameter, ψ, is obtained as the average of the CPT-based correlations of Olaya and Bray (2022) and Robertson (2010). Use of alternative liquefaction triggering procedures or correlations for D_r or ψ can alter the estimate of S_v in a manner dependent on the procedure or correlation employed.

A calibration factor (*C*), a soil behavior factor (*SB*), and a magnitude factor (*MF*) are incorporated in the Bray and Olaya (2023) model. The factor *C* arises from the inherent differences between the characteristics of natural soil deposits and the reconstituted soil test specimens used in the laboratory tests that form the basis of Eqs. 1 and 2 (e.g., soil fabric, and time under sustained loading). The calibration factor is $C = 1.50$ for natural soil, and it is nearly one for constructed hydraulic fill that more closely reflects the conditions of newly prepared soil test specimens (i.e., $C = 1.05$ for hydraulic fill). The soil behavior factor *SB* results from the trends of residuals observed when plotted against the average I_c over the upper 15 m of the soil profile (I_{c15}) where *SB* reduces as I_{c15} increases. The magnitude factor *MF* captures the increase in ground settlement due to additional cycles of loading after liquefaction is triggered which is correlated to increasing values of M_w as a proxy for the duration of strong shaking. The Bray and Olaya (2023) model is summarized in Eqs. 3 through 5.

$$S_v = C \cdot MF \cdot SB \cdot \sum_i [\varepsilon_{vi} \cdot \Delta z_i] \cdot e^{\delta_{Sv}} \tag{5.3}$$

$$SB = \exp\left(-0.675 \cdot \max\left(I_{c_{15}}, 1.8\right) + 1.215\right) \tag{5.4}$$

$$MF = \exp(0.214 \cdot M_w - 1.498) \tag{5.5}$$

where $C = 1.50$ for natural soil and $C = 1.05$ for hydraulic fill, ε_{vi} (as a decimal) is the volumetric strain of each soil layer i with thickness Δz_i obtained from the median values of Eqs. 1 and 2, and δ_{Sv} is the error term of the model which has zero mean and a standard deviation of 0.54 in natural log units for hydraulic fill and 0.61 in natural log units for natural soil for the D_r-based volumetric strain model, and 0.53 and 0.61 for the hydraulic fill and natural soil, respectively, for the ψ-based volumetric strain model. As expected, the uncertainty in the estimate of liquefaction-induced ground settlement is lower for constructed hydraulic fills than for natural soil deposits. The model residuals using the D_r-based volumetric strain model are shown in Figure 5.3 for *PGA* and D_r. The observed spread in the residuals illustrates the uncertainty in the model's estimate of S_v given these key input parameters.

5.4 Performance-Based Assessment of Liquefaction-Induced Ground Settlement

Performance-based earthquake engineering (PBEE) integrates the estimate of the ground motion *IM* into the evaluation of the system response with the objective to quantify the annual rate of exceedance of the system response. The annual rate of exceedance provides useful information to make engineering decisions within a risk-based framework.

In this study, the system response is represented by the engineering demand parameter S_v. The annual rate at which a specified amount of liquefaction-induced free-field ground settlement (Z) is exceeded ($S_v > Z$) for a given level of *IM* at a site can be evaluated through the Pacific Earthquake Engineering Research Center (PEER) PBEE framework (Deirlein et al. 2003). In the PEER framework, the information from the seismic hazard evaluation is convolved with an empirical model for S_v to produce the hazard curve $\lambda(S_v)$ for liquefaction-induced ground settlement using Eq. 6.

$$\lambda(S_v) = \int_{IM} G(S_v|IM) \cdot |d\lambda_{IM}| \cdot \mathrm{d}(im) \tag{5.6}$$

where $G(S_v|IM)$ is the probability of S_v exceeding a specified threshold conditioned on *IM*, $|d\lambda_{IM}|$ denotes the derivative of the seismic hazard for the *IM* of interest, and d(*im*) is the integration step. The PEER integral in Eq. 6 can be expanded by incorporating the dependencies of the Bray and Olaya (2023) S_v model (Eqs. 3 through 5) as shown in Eq. 7.

$$\lambda(S_v) = \int_{M_w} \int_{PGA} P(S_v > Z|PGA, M_w, I_{c15}, \Sigma_i[\varepsilon_{v,i} \cdot \Delta z_i]) \cdot f(M_w|PGA) \left|\frac{d\lambda_{PGA}}{d(pga)}\right| \cdot d(pga) \cdot dm \tag{5.7}$$

where $P(S_v > Z|PGA, M_w, I_{c15}, \Sigma_i[\varepsilon_{v,i} \cdot \Delta z_i])$ is the probability that a ground settlement amount Z is exceeded conditioned on *PGA*, M_w, I_{c15}, and $\Sigma_i[\varepsilon_{v,i} \cdot \Delta z_i]$, $f(M_w|PGA)$ is the probability of occurrence of M_w given *PGA* and captures the contribution of different M_w scenarios to the seismic hazard for *PGA* which can be obtained from the seismic hazard deaggregation for *PGA*, and $|d\lambda_{PGA}/d(pga)|$ is the derivative of the hazard curve for *PGA*.

In the context of the Bray and Olaya (2023) model, the conditional probability that $S_v > Z$ in Eq. 7 can be evaluated as

$$P(S_v > Z|PGA, M_w, I_{c15}, \Sigma_i[\varepsilon_{v,i} \cdot \Delta z_i]) = 1 - \Phi\left(\frac{Ln(Z) - Ln\left(\widehat{S_v}\right)}{\sigma_{Ln(S_v)}}\right) \tag{5.8}$$

where Φ is the standard normal cumulative distribution function, $\widehat{S_v}$ is the median estimate according to Bray and Olaya (2023), and $\sigma_{Ln(S_v)}$ is the standard deviation of the error term in Eq. 3.

The evaluation of the derivative of λ_{PGA} is performed using the rate of occurrence approach for λ_{PGA} as

$$\left|\frac{d\lambda_{PGA}}{d(pga)}\right|_k = \frac{\lambda_{PGA_{k+1}} - \lambda_{PGA_{k-1}}}{\Delta PGA_{(k+1)-(k-1)}} \tag{5.9}$$

where $\lambda_{PGA_{k+1}} - \lambda_{PGA_{k-1}}$ is the rate of occurrence of λ_{PGA_k} and k represents the k^{th} *PGA* bin. Hence, the seismic hazard curve for *PGA* is discretized into an appropriate

number of *PGA* bins to capture the shape of the hazard curve. In this study 12 bins or more adequately captured the hazard curve for *PGA*. The term $\Sigma_i[\varepsilon_{v,i} \cdot \Delta z_i]$ in Eq. 7 represents the cumulative contribution of volumetric strain with depth in the soil profile, which has been divided into layers. As discussed in the previous section, $\varepsilon_{v,i}$ is estimated from the median values of Eqs. 1 and 2, hence the term $\Sigma_i[\varepsilon_{v,i} \cdot \Delta z_i]$ is representative of a median quantity.

5.5 Primary Sources of Uncertainty in Liquefaction-Induced Free-Field Ground Settlement

In the context of the PEER PBEE framework, the uncertainty in the performance-based assessment of S_v is categorized as either aleatory or epistemic. The aleatory component of uncertainty is characterized by the standard deviation of the ground motion models (GMMs) considered in the PSHA and by the standard deviation of the empirical model employed to estimate S_v. The uncertainty related to the soil characterization (i.e., CPT measurements within a site) is evaluated as epistemic and is treated using a logic-tree approach because it produces alternative hazard curves for each branch in the logic tree. The primary CPT measurements are the corrected cone tip resistance (q_t) and the sleeve friction (f_s) which are used as inputs to the correlations to estimate D_r or ψ and the liquefaction triggering procedures to calculate FS_L. Subsequently, D_r or ψ and FS_L are used as inputs to Eqs. 1 and 2 to estimate ε_v. These calculations are performed for each layer in the soil profile as illustrated in Figure 5.4.

In the application of the Bray and Olaya (2023) S_v model, the volumetric strain contribution from all layers, $\Sigma_i[\varepsilon_{v,i} \cdot \Delta z_i]$, and the average, I_{c15}, are used as inputs. Hence, in the Bray and Olaya (2023) S_v model, alternative values of q_t and f_s are reflected as alternative values of I_{c15} and $\Sigma_i[\varepsilon_{v,i} \cdot \Delta z_i]$. Therefore, logic tress for I_{c15} and $\Sigma_i[\varepsilon_{v,i} \cdot \Delta z_i]$ can be used to capture the variability in the soil characterization parameters q_t and f_s. Interrogation of the well-documented filed case histories in the Olaya and Bray (2023) database enables characterization of the variability of I_{c15} and $\Sigma_i[\varepsilon_{v,i} \cdot \Delta z_i]$ in the form of the coefficient of variation (COV) values shown in Tables 5.2 and 5.3. The input parameter's variability characterized in Table 5.2 is the I_{c15} at the site, and the input parameter's variability characterized in Table 5.3 is the average I_c for the liquefiable materials at the site with $FS_L \leq 1.0$ (I_{c_liq}). Both input parameters were characterized to explore the dependency of the volumetric strain estimate on each parameter because I_{c15}, while straightforward, includes the characteristics of liquefiable and non-liquefiable soil layers, whereas I_{c_liq} depends only on the characteristics of the liquefiable soil layer, though it requires the calculation of FS_L. The resulting COVs of $\Sigma[\varepsilon_{v,i} \cdot \Delta z_i]$ do not differ in a meaningful way, so I_{c15} can be used in this application.

The sources of epistemic uncertainty related to the source characterization and ground motion modeling are typically evaluated during the PSHA (Wang and Rathje 2015, Macedo et al. 2018), thus they are not examined in the evaluation of $\lambda(S_v)$. However, in cases where it is necessary, the epistemic uncertainty in λ_{IM} may be evaluated along with the epistemic uncertainty in S_v. To show the effect of the epistemic uncertainty in λ_{IM} and S_v, a simplified PSHA is performed for two seismic sources in a crustal seismic setting

where three alternative characteristic magnitudes, two annual activity rates, and one distance metric for each fault are considered as shown in Figure 5.5. For the hazard analysis, densities following a delta function are considered for magnitude and distance, and two GMMs were utilized to characterize the *PGA* at the site. GMM1 has a standard deviation of 0.65 natural log units and a weight of 0.6 and GMM2 has a standard deviation of 0.62 natural log units with a weight of 0.4. Given the alternative M_w, rates, and GMMs, a total of 72 alternative hazard curves for *PGA* can be constructed for the two seismic sources in the example shown in Figure 5.5.

The epistemic uncertainty in the soil characterization was estimated from Table 5.2 for a natural soil deposit. For the parameter I_{c15} a COV of 0.04 is considered and a COV of 0.20 for $\Sigma_i[\varepsilon_{v,i} \cdot \Delta z_i]$ is used. To better capture the distribution of the alternative values of the soil parameters, a five-branch logic tree was used for I_{c15} and $\Sigma_i[\varepsilon_{v,i} \cdot \Delta z_i]$ with weights of 0.065, 0.24, 0.39, 0.24, and 0.065 for each branch as illustrated in Figure 5.6. The mean I_{c15} for this example is 1.82 whereas the $\Sigma_i[\varepsilon_{v,i} \cdot \Delta z_i]$ term varies depending on the M_w and *PGA* scenario being analyzed, thus Figure 5.6 shows the alternative values corresponding to a M_w = 6.3 and *PGA* = 0.30 g. The previously summarized S_v model of Bray and Olaya (2023) is used. The convolution of the 72 alternative hazard curves for *PGA* with the alternative realizations of the S_v model yields a total of 1800 hazard curves for S_v as shown in Figure 5.7. The 10th to 90th fractile range is shown with the median and mean hazard S_v curves. In engineering practice, the mean hazard curve for the engineering demand parameter [i.e., $\lambda(S_v)$] is usually selected in a performance-based seismic displacement assessment (e.g., Wang and Rathje 2015, and Macedo et al. 2018).

5.6 Summary of Proposed Performance-Based Liquefaction-Induced Ground Settlement Procedure

The proposed performance-based procedure consists of four steps:

1. Perform a PSHA at the site of interest and obtain the mean hazard curve for *PGA* and the deaggregation information for different magnitude bins at several PGA values (typically, within the range of 0.01 g to 10 g).
2. Evaluate the epistemic uncertainty of the soil characterization parameters at the site in terms of I_{c15} and $\Sigma_i[\varepsilon_{v,i} \cdot \Delta z_i]$ as defined in Bray and Olaya (2023). The values of epistemic uncertainty may be estimated from the variability observed in the CPTs performed at the site. A sufficient number of CPTs should be available so variability can be sampled confidently (i.e., use 5 or more representative CPTs). The COV ranges provided in Tables 5.2 and 5.3 can be used to inform the amount of variability to consider in cases with fewer CPTs available or as a guide in performing a site-specific estimate of the variability of the CPT profiles at a site.
3. Eq. 7 is used to compute the seismic hazard of liquefaction-induced ground settlement. It is recommended to evaluate $\lambda(S_v)$ at settlement values up to 1000 mm to ensure that low hazard levels (e.g., 10^{-5}) are captured. The range of the possible seismic ground displacement hazard curves can be evaluated by including alternative values for I_{c15} and $\Sigma_i[\varepsilon_{v,i} \cdot \Delta z_i]$.
4. Select the return periods of interest (i.e., hazard levels) for the seismic evaluation.

In engineering practice, return periods of 475 and 2475 years are often used to assess the seismic performance of the ground affecting new structures. Lower return periods are typically used to assess the seismic performance of existing structures (e.g., 225-year return period). Estimate the mean and 16^{th} and 84^{th} percentile fractal values of the liquefaction-induced ground settlement at the selected return periods.

5.7 Illustrative Example

The performance-based evaluation of liquefaction-induced free-field ground settlement is illustrated for a test site located in the Sierra Nevada area in California. Six CPTs are used to show the soil profile characteristics at the site as illustrated in Figure 5.8. Overall, the soil at the site is composed of a 2-3 m crust of high I_c (>2) material followed by uniform thick layers of clean sands and silty sands with the I_c fluctuating around the I_c = 1.8 sand-like limit (Beyazei et al. 2018) with a representative I_{c15} of 1.86. At a depth of about 12 m there is a thin layer of clayey material, and a layer of siltier soil is located at depth of 18 - 19 m. The groundwater table is located at a depth of 2 m. The normalized cone tip resistance increases with depth at the site (Figure 5.8), and the soil units located from a depth of 2 m to a depth of 13 m contribute the most to the potential for liquefaction-induced settlement as illustrated by the distribution of FS_L in Figure 5.8, which corresponds to an earthquake event consistent with the 475-year return period *PGA* at the site.

The test site is in the active seismic area of the northern Sierra Nevada fault zone where earthquakes of magnitudes on the order of M_w = 6.0 have been recorded. The PSHA was performed with the open-source software *Haz45.V3* (Abrahamson 2020). *Haz45.V3* allows the user to evaluate the contribution of a large number of seismic source scenarios, use or implement alternative GMMs, and it contains post-processing routines that produce different outputs such as the uniform hazard spectrum, the conditional mean spectrum, and the seismic source deaggregation by different metrics. For the performance-based assessment of S_v, the mean total hazard curve for *PGA* and the deaggregation by magnitude and *PGA* are required. Figure 5.9a shows the mean total hazard curve at the test site for the *PGA*. The contribution to the total hazard from individual sources is also shown in Figure 5.9a as color lines.

Initially, the hazard evaluation for S_v was performed using Eq. 7, the mean hazard curve for *PGA* and the deaggregation for PGA (Figure 5.9a, 5.9b), and CPT_24630 that is representative of the average soil characteristics at the site (Figure 5.7) which leads to an estimate of the mean $\lambda(S_v)$. Figure 5.10 shows the comparison between the mean hazard curve for *PGA* (Figure 5.10a) and the mean hazard curve for S_v (Figure 5.10b). The 475-year and 2475-year return periods are superimposed for reference. It is apparent that the curvatures of the two hazard curves differ, particularly at low hazard levels (or large return periods). The increase in curvature of the hazard curve for S_v is a direct consequence of the additional aleatory variability contributed from the empirical model for S_v.

Another useful comparison is of the liquefaction-induced ground settlement values estimated using the pseudo-probabilistic approach and the performance-based approach for two return periods. Ground settlement can be read directly from the hazard curve for S_v in the case of the performance-based approach (Figure 5.10b). In the pseudo-probabilistic

approach, the input *PGA* and M_w values at the return periods of interest are first obtained. For the test site, the *PGAs* are 0.32g and 0.61g for the 475-year and 2475-year return periods, and the governing M_w is 6.4 using the results of the PSHA in terms of *PGA*. The resulting values of the estimated liquefaction-induced ground settlement are presented in Table 5.4.

The pseudo-probabilistic approach overestimates the liquefaction-induced ground settlement relative to the more robust performance-based approach. The overestimation is small at the 2475-year return period where the slopes of the hazard curves do not differ significantly. However, the pseudo-probabilistic approach produces a mean liquefaction-induced ground settlement that is nearly double the mean estimate of ground settlement using the performance-approach at the 475-year return period because the slopes of the hazard curves differ markedly at this return period. Examination of the annual activity rate in the Sierra Nevada zone is useful to interpret the results in Table 5.4. The annual activity rate at the test site is on the order of 1/1000 earthquakes per year; hence, a median ground motion will be exceeded with a rate of about ~ 1/2000. Therefore, a rate of *PGA* of 1/475 is expected to produce a greater contribution to S_v compared to the median ground motion in this example. Conversely, it is expected that the rate 1/2475 of *PGA* will be similar to the 1/2000 rate associated to the median ground motion at the site. These observations are consistent with the liquefaction-induced ground settlement values presented in Table 5.4. The performance-based approach is a sound framework for evaluating S_v because it incorporates explicitly the information from the seismic hazard assessment into the evaluation of S_v. Differences between the pseudo-probabilistic and performance-based seismic displacement estimate approaches have been reported by other researchers (e.g., Kramer and Mayfield 2007, Rathje and Saygili 2011, Franke et al. 2016, Macedo et al. 2018, and Franke et al. 2021).

The test site evaluated in this example is also used to illustrate the effects of considering uncertainty in the soil characterization (i.e., I_{c15} and $\Sigma_i[\varepsilon_{v,i} \cdot \Delta z_i]$). The six CPTs used to characterize the soil at the site yield a COV(I_{c15}) = 0.02 and a COV($\Sigma_i[\varepsilon_{v,i} \cdot \Delta z_i]$) = 0.15, hence those values are used to assess uncertainty. However, to further illustrate the effect of including uncertainty in the soil characterization, the upper limits of COV(I_{c15}) = 0.05 and COV($\Sigma_i[\varepsilon_{v,i} \cdot \Delta z_i]$) = 0.30 in Table 5.2 based on the site's I_{c15} = 1.86 are also evaluated. The resulting variability in $\lambda(S_v)$ is shown as a range in Figure 5.11. Uncertainty in I_{c15} does not significantly affect the liquefaction-induced ground settlement hazard curve shown in Figure 5.11a. The range of hazard curves for COV(I_{c15}) = 0.02 and 0.05 are not too different with the upper bounds being coincident. This occurs because I_{c15} takes minimum values of 1.79 and 1.67 for COVs of 0.02 and 0.05 respectively, for which *SB* in Eq. 4 takes a value of 1.0 (I_{c15} < 1.80), thus yielding the same $\lambda(S_v)$. Conversely, the uncertainty in $\Sigma_i[\varepsilon_{v,i} \cdot \Delta z_i]$ can have a significant effect on the S_v hazard curve at low hazard levels (i.e., or large return periods) as illustrated in Figure 5.11b. Increasing the COV($\Sigma_i[\varepsilon_{v,i} \cdot \Delta z_i]$) from 0.15 to 0.30 doubles approximately the range of the estimated liquefaction-induced ground settlement at return periods between 2475 years and 10,000 years.

5.8 Conclusions

The recently developed Bray and Olaya (2023) probabilistic procedure to estimate liquefaction-induced ground settlement is incorporated in a performance-based procedure to estimate ground settlement while accounting for key sources of uncertainty. Performance-based procedures are preferred to state-of-practice procedures that treat the assessment of seismic demand and engineering response parameters independently. The PEER PBEE framework is utilized to capture explicitly the features of the ground motion intensity measure at the site by including this seismic hazard information as well as the uncertainty of the estimate of liquefaction-induced ground settlement as a function of the ground motion characteristics. The ground motion intensity and ground settlement estimations are integrated to produce alternative hazard curves for liquefaction-induced ground settlement in the proposed approach. The mean hazard curve for ground settlement links different hazard levels (or return periods) with their corresponding values of ground settlement by evaluating a wide range of ground motion intensities and ground characterization parameters with their uncertainties. In contrast to the pseudo-probabilistic approach frequently used in practice, the performance-based procedure produces an estimate of liquefaction-induced ground settlement compatible with the specified design hazard level.

The recently developed Bray and Olaya (2023) probabilistic procedure to estimate liquefaction-induced ground settlement is incorporated in a performance-based procedure to estimate ground settlement while accounting for key sources of uncertainty. Performance-based procedures are preferred to state-of-practice procedures that treat the assessment of seismic demand and engineering response parameters independently. The PEER PBEE framework is utilized to capture explicitly the features of the ground motion intensity measure at the site by including this seismic hazard information as well as the uncertainty of the estimate of liquefaction-induced ground settlement as a function of the ground motion characteristics. The ground motion intensity and ground settlement estimations are integrated to produce alternative hazard curves for liquefaction-induced ground settlement in the proposed approach. The mean hazard curve for ground settlement links different hazard levels (or return periods) with their corresponding values of ground settlement by evaluating a wide range of ground motion intensities and ground characterization parameters with their uncertainties. In contrast to the pseudo-probabilistic approach frequently used in practice, the performance-based procedure produces an estimate of liquefaction-induced ground settlement compatible with the specified design hazard level.

Importantly, key sources of uncertainty are included in the evaluation of $\lambda(S_v)$. Although the epistemic uncertainty in the ground motion is typically evaluated during the seismic hazard assessment of the ground motion, the uncertainty in the soil deposit as characterized through the CPT can be included during the performance-based evaluation of liquefaction-induced ground settlement. Ranges of the COV of I_{c15} and $\Sigma_i[\varepsilon_{v,i} \cdot \Delta z_i]$ are provided based on the interrogation of the comprehensive Olaya and Bray (2023) database of field case histories. A logic tree approach is employed to assess the effect of the uncertainty of the geotechnical parameters on the ground settlement hazard curve. A five-

branch logic tree with weights of 0.065, 0.24, 0.39, 0.24, and 0.065 captured well the uncertainties in the key parameters and terms of I_{c15} and $\Sigma_i[\varepsilon_{v,i} \cdot \Delta z_i]$ (e.g., Figure 5.6).

The use of the proposed procedure was illustrated at a site located in eastern California. Post-liquefaction ground settlement (S_v) estimates at this level ground site were obtained at two hazard levels (i.e., return periods of 475-year and 2475-year) using the performance-based approach as well as the conventional pseudo-probabilistic approach typically used in engineering practice. It was shown that the performance-based procedure yielded estimates of liquefaction-induced ground settlement consistent with the target hazard levels; whereas the pseudo-probabilistic approach overestimated significantly the liquefaction-induced ground settlement at the 475-year return period due to the vastly different slopes of the *PGA* and S_v hazard curves at this return period. Hence, the performance-based procedure developed in this study is recommended for use in engineering practice over currently used approaches. Additionally, the performance-based procedure permits the evaluation of different sources of uncertainty and their effect on liquefaction-induced ground settlement.

Table 5.1. Liquefaction-induced free-field level ground settlement severity categories

Category	Total liquefaction-induced ground settlement (mm)
None	< 10
Moderate	10 – 100
Significant	100 – 300
Severe	> 300

Table 5.2. Range of variability in I_{c15} and $\Sigma[\varepsilon_{v,i} \cdot \Delta z_i]$ in terms of I_{c15}

Site	COV (I_{c15})			COV ($\Sigma[\varepsilon_{v,i} \cdot \Delta z_i]$)		
	I_{c15} < 1.8	1.8 ≤ I_{c15} < 2.2	I_{c15} ≥ 2.2	I_{c15} < 1.8	1.8 ≤ I_{c15} < 2.2	I_{c15} ≥ 2.2
Natural soil	0.01 - 0.04	0.03 - 0.05	0.03 - 0.05	0.10 - 0.40	0.10 - 0.30	0.20 - 0.40
Hydraulic fill	-	0.02 - 0.04	0.03 - 0.04	-	0.10 - 0.20	0.20 - 0.30

Table 5.3. Range of variability in I_{c15} and $\Sigma[\varepsilon_{v,i} \cdot \Delta z_i]$ in terms of the I_c of the liquefiable soils

Site	COV (I_{c15})			COV ($\Sigma[\varepsilon_{v,i} \cdot \Delta z_i]$)		
	$I_{c\_liq} < 1.8$	$1.8 \leq I_{c\_liq} < 2.2$	$I_{c15} \geq 2.2$	$I_{c\_liq} < 1.8$	$1.8 \leq I_{c\_liq} < 2.2$	$I_{c\_liq} \geq 2.2$
Natural soil	0.01 - 0.03	0.03 - 0.05	Natural soil	0.01 - 0.03	0.03 - 0.05	Natural soil
Hydraulic fill	-	0.03 - 0.04	Hydraulic fill	-	0.03 - 0.04	Hydraulic fill

Table 5.4. Comparison of the amount of liquefaction-induced ground settlement estimated using the pseudo-probabilistic and performance-based approaches at the 475-year and 2475-year return periods

Return Period (yr)	Liquefaction-induced free-field Ground settlement, S_v (mm)	
	Pseudo-Probabilistic	Performance-Based
475	110	65
2500	310	300

(a) (b)

Figure 5.1. (a) Post-liquefaction free-field settlement at Port Island after the 1995 Kobe earthquake (Akai et al. 1995), and (b) Flooding of the inland street and buildings in Iskenderun after the 2023 Türkiye earthquake (Photograph from the GEER 2023 reconnaissance).

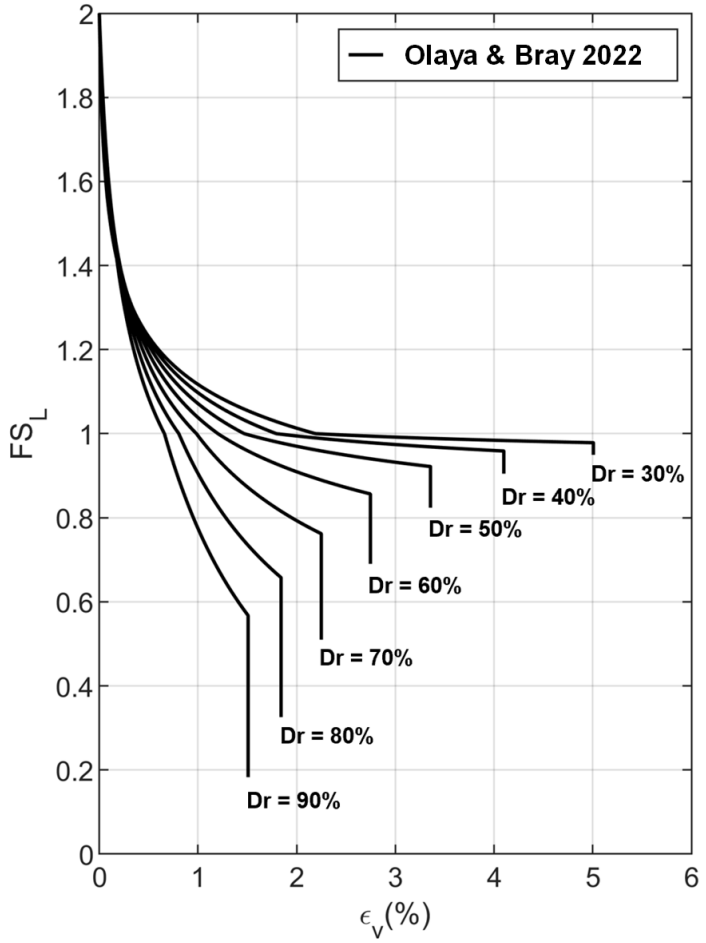

Figure 5.2. Olaya & Bray 2022 volumetric strain potential median model as a function of D_r

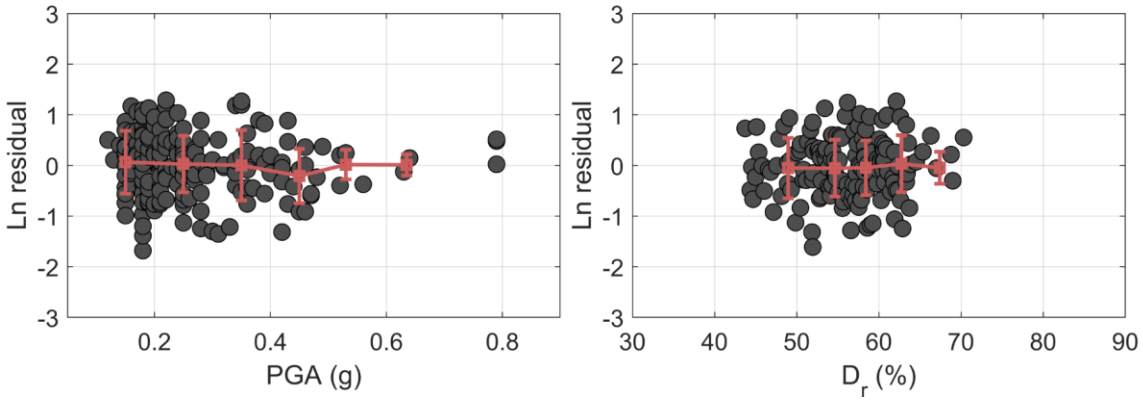

(a) (b)

Figure 5.3. Bray & Olaya (2023) model residuals for: (a) *PGA* and (b) relative density.

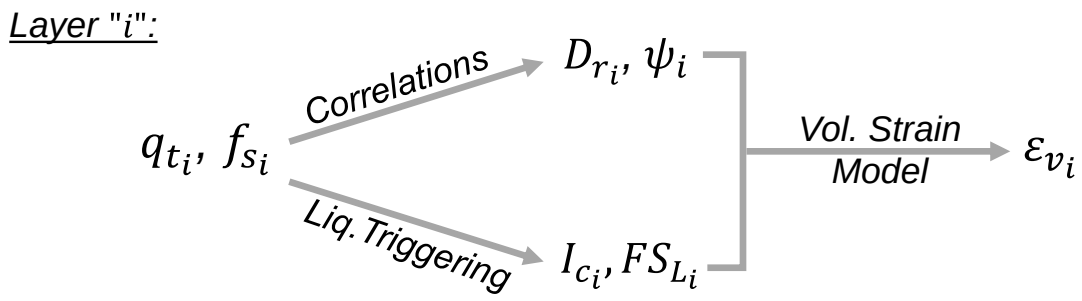

Figure 5.4. Diagram showing the CPT data processing.

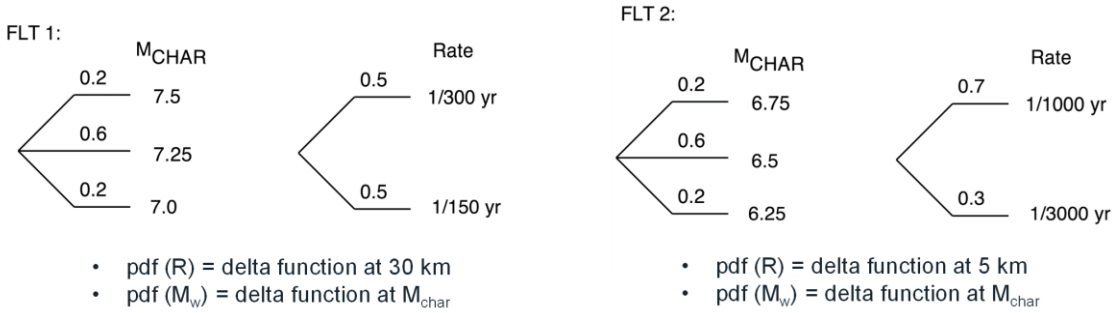

Figure 5.5. Example of epistemic uncertainty treatment in ground motion hazard analysis.

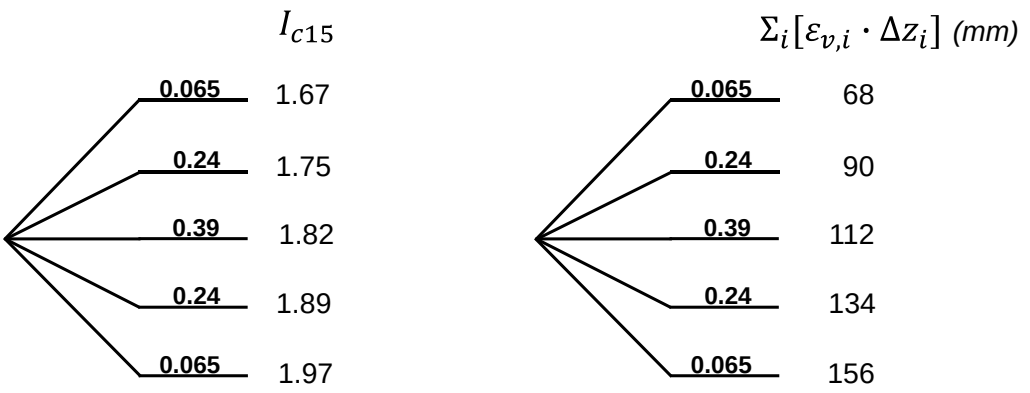

**Scenario: M_w=6.3, PGA=0.30 g*

Figure 5.6. Example of epistemic uncertainty in the soil characterization.

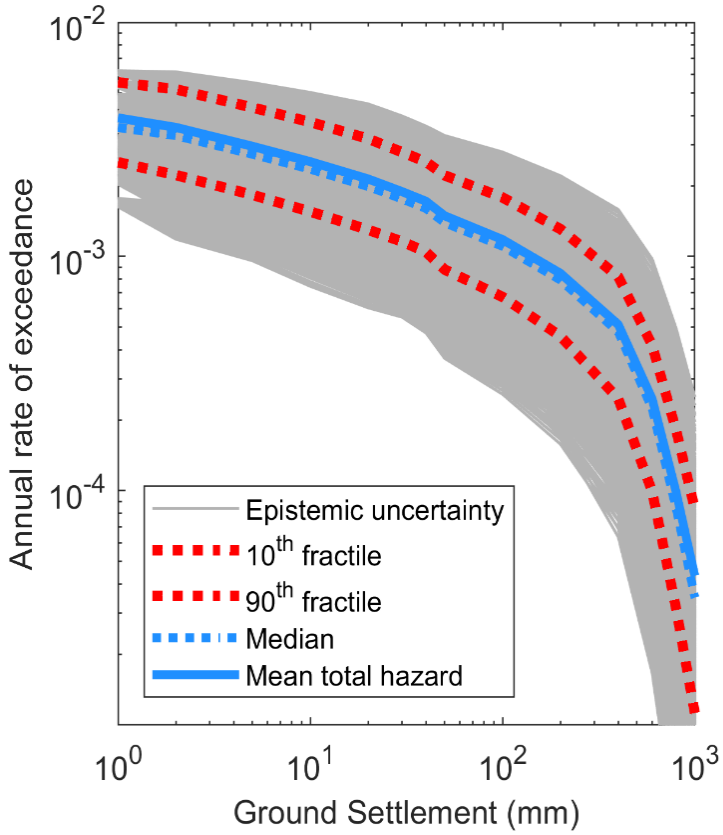

Figure 5.7. Alternative liquefaction-induced free-field ground settlement hazard curves.

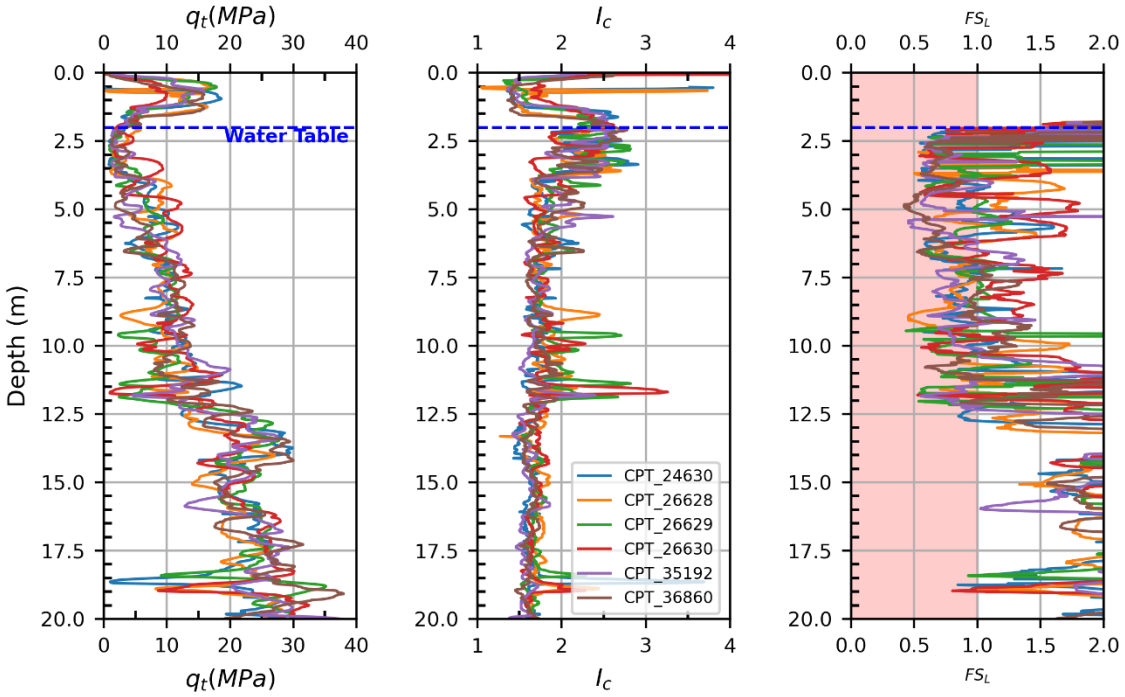

Figure 5.8. CPT data at test site with the calculation of the FS_L at the 475-year hazard level.

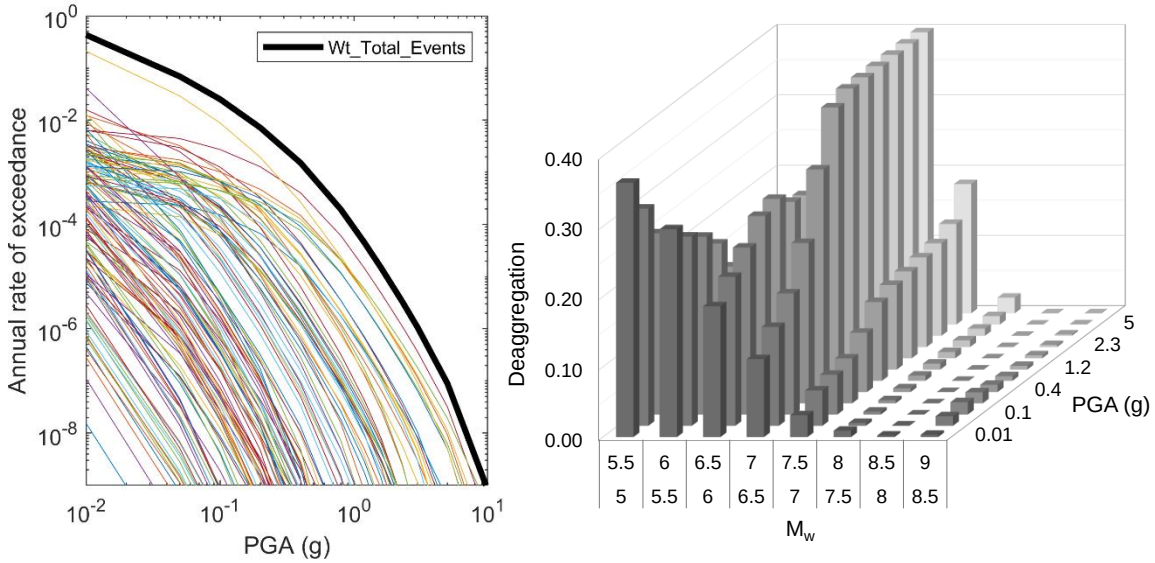

(a) (b)

Figure 5.9. (a) Mean total hazard curve at the test site for *PGA*. Contribution to hazard from individual sources are shown in color lines. (b) Seismic hazard deaggregation by magnitude at *PGA* values.

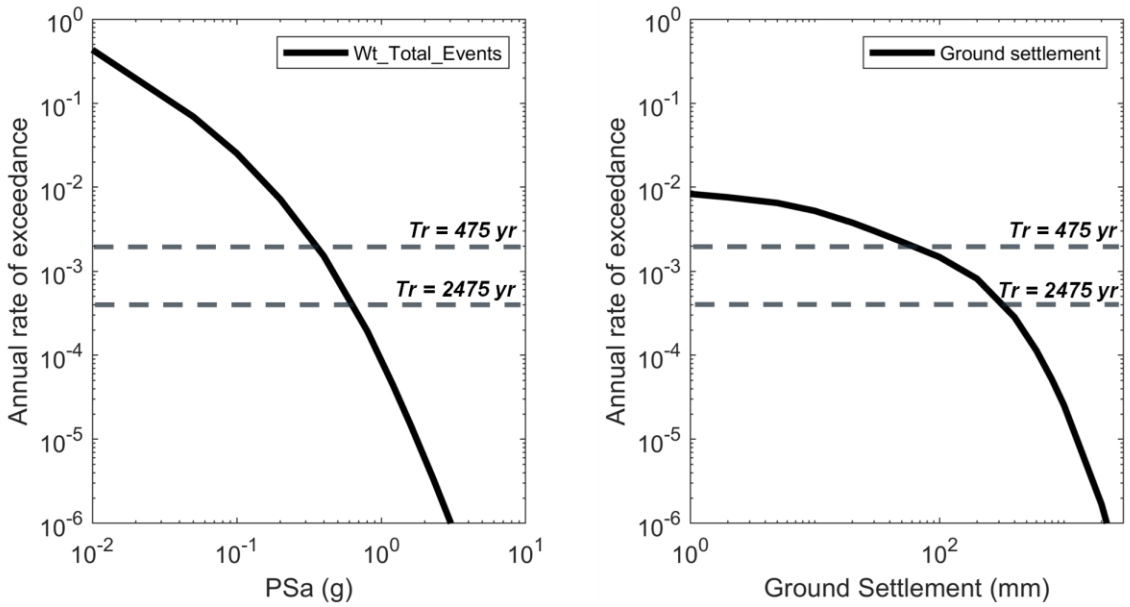

(a) (b)

Figure 5.10. (a) Mean total hazard curve at the test site for *PGA*, and (b) Mean hazard curve for S_v.

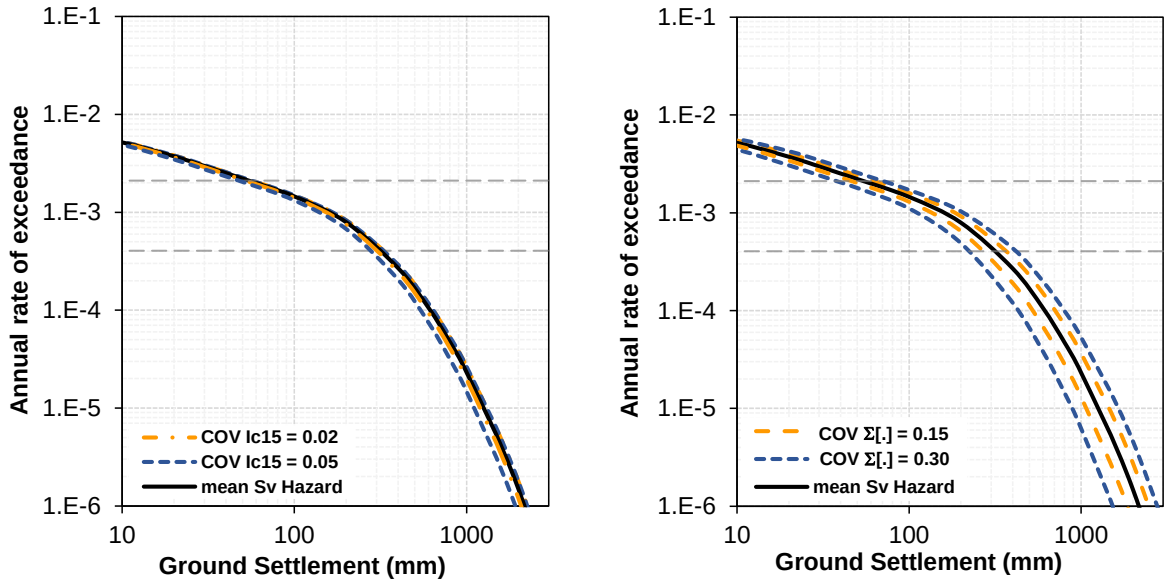

(a) (b)

Figure 5.11. Effect of uncertainty of soil characterization on the $\lambda(S_v)$: (a) uncertainty in I_{c15}, and (b) uncertainty in $\Sigma_i[\varepsilon_{v,i} \cdot \Delta z_i]$.

6 Static Instability of Tailings in Constant Shear Drained Stress Path

6.1 Introduction

Static flow liquefaction of loose saturated tailings has been identified during the failures of large tailings facilities (TSFs) such as the 1966 coal waste flow slide of Aberfan (Figure 6.1a) and the 2019 Brumadinho tailings storage facility failure (Figure 6.1b). These failures were catastrophic. The Aberfan flow slide caused 144 deaths while the Brumadinho disaster caused 300 deaths with associated costs on the order of US $5 billion (Reuters, 2019). Other recent relevant case histories of TSFs liquefaction flow failures are 1994 Merruespruit in South Africa (Fourie et al. 2001), 2015 Fundao in Brazil (Morgenstern et al. 2016), and 2018 Cadia in Australia (Morgenstern et al. 2019). This sequence of failures shows the need to improve our understanding of the mechanisms leading to liquefaction flow failure. A common feature of static-liquefaction-induced failures is the sudden transition from a drained and stable response of the tailings material to a rapid flow type of mechanism triggered by an external or internal perturbation within the dam (Jefferies, 2021). TSFs are large structures, typically constructed using hydraulic deposition with the tailings being separated into a sand fraction that is used to construct the retention dam of the TSF while the finer fraction is deposited into the TSF impoundment. Due to their formation process, tailings can be angular cohesionless materials composed primarily of sand-sized and silt-sized particles with no to low plasticity. Due to the construction methods, a significant amount of the tailings materials in the TSF impoundment are typically loose saturated sand and silts.

Soil response is a function of the current void ratio (e) and the in-situ stress ratio (η) defined as the ratio of the deviatoric stress (q) to the mean effective stress (p), $\eta = q/p$. For a soil element at an initial e, external loading increases q which in turns increases η. Thus, a common stress path from a sustained incremental loading mobilizes the state of a soil towards its critical state, $\eta \rightarrow M = q_c/p_c$ (where subscript c indicates critical state). Figure 6.2 shows different stress paths leading to flow liquefaction for a soil specimen in the laboratory. Stress path A corresponds to an isotropically consolidated undrained triaxial test where η steadily increases until it reaches the instability condition at the peak of the stress path (η_{IL}) after which η decreases rapidly towards the critical state. Stress path B represents an undrained cyclic test with an anisotropic initial state that gradually approaches η_{IL} as the mean confinement stress decreases with the instability condition being followed by a flow type of response. Stress path C is interesting, because it involves an anisotropic initial state from which the soil specimen moves towards the critical state in drained unloading by reducing p while keeping q constant which causes η to increase. As shown in Figure 6.2, an instability condition is also reached during unloading and eventually failure.

Stress paths A and B are familiar and have been widely studied in geotechnical practice (e.g., Castro 1969, Seed 1979, Ishihara 1993, Idriss and Boulanger 2008, Jefferies and Been 2016). However, loading conditions following stress path C (as shown in Figure 6.2) have been less investigated. The loading stress path C where failure is reached under drained

conditions by reducing p while keeping q constant is referred to as the Constant Shear Drained (CSD) stress path.

Investigations of the 1966 Aberfan and the 2015 Fundao failures, as reported in Jefferies and Been (2016) and Morgenstern et al. (2016), respectively, suggest the CSD stress path was the trigger mechanism for the slides. Olson et al. (2000) evaluated the static liquefaction failure of the North Dike of Wachuset dam. They found that a drained instability mechanism likely led to static liquefaction during the first reservoir filling. This type of mechanism involving a rising phreatic surface under drained shear conditions resembles that of the CSD stress path. The CSD stress path is also attributed to the failure of natural colluvial soil slopes induced by rainfall, snowmelt, or other sources of transient rise of the phreatic surface (e.g., Anderson and Riemer 1995, Anderson and Sitar 1995, Zhu and Anderson 1998). A key characteristic of the CSD stress path is that collapse occurs suddenly because the instability condition is reached at relatively low strain, and as a consequence, failure occurs with no warning in the field (e.g., incipient deformation patterns or cracks). Hence, the investigation of static instability triggered by this particular stress path is warranted.

In this study, different conditions leading to instability under the CSD stress path are investigated for a sample of tailings silty sand using a series of advanced laboratory tests and numerical modeling. The physical and mechanical properties of the tailings silty sand subject of this study are characterized as part of the testing program using index, one dimensional compression, and isotropically consolidated triaxial tests. The critical state parameters for the tailings are provided. A series of CSD tests were carried out at a range of densities covering loose of- and dense of critical states with initial stress ratios (η_o) ranging from 0.45 to 0.80. The NorSand critical-state constitutive model is used to numerically explore the behaviors observed during the isotropically consolidated triaxial tests and the CSD tests. An update of the stress-dilatancy rule for the yielding condition during unloading proposed by Jefferies (1997) is provided as part of this study. NorSand is calibrated using conventional triaxial test data and then applied to the CSD tests measurements. Modifications of some of the aspects of the NorSand constitutive model capture adequately the observed behaviors in the CSD tests.

6.2 Constant Shear Drained Stress Path

The CSD stress path was initially investigated to understand the failure of natural slopes induced by a transient rise in the water table induced by rain infiltration (e.g., Brand et al. 1981, and Harp et al. 1990). Laboratory test programs aimed to capture soil response under the CSD stress path have been performed primarily on standard laboratory sands using the triaxial (TX) test device (e.g., Sasitharan et al. 1993, di Prisco and Imposimato 1997, Gajo et al. 2000, Chu et al. 2012, and Chu et al. 2015). The CSD TX tests performed by Sasitharan et al. (1993) found that failure occurred at an axial strain of about 0.4% in a rapid and uncontrolled way that made it difficult to collect detailed data. Anderson and Riemer (1995) used an oil piston that restricted the rate of deformation during unloading. This modification to the test setup allowed to obtain soil response measurements throughout the test. Junaideen et al. (2010) performed a series of CSD tests using a servo-controlled TX test system that maintained the drained condition and enabled data acquisition during the test. In this study an approach similar to the one used by Anderson

and Riemer (1995) was used to perform the CSD tests as will be described later in this chapter.

Anderson and Sitar (1995) and Anderson and Riemer (1995) performed CSD TX tests on undisturbed samples of natural clayey colluvial soil to investigate the potential for rainfall-induced instability. Their results show negative volumetric strains (expansion) during the unloading phase of the test and limited collapse was observed because the colluvial soil approached the critical state with moderate axial strains. Junaideen et al. (2010) tested two well graded granitic residual soils using their servo-controlled CSD TX test equipment. The tests on loose and dense specimens showed elastic swelling during unloading up to the point of collapse followed by rapid flow failure; however, the stress ratios at which collapse occurred differed. The dense specimens collapsed at a stress ratio higher than M while the loose specimens at a stress ratio lower than M.

The extent of damage to infrastructure and the environment, and the deaths have results fro some of the recent tailings dam failures (e.g., 2015 Fundao and 2019 Brumadinho TSFs) have motivated a series of research efforts on the triggering mechanisms leading to static flow liquefaction. However, studies of the failure of tailings triggered by the CSD stress path are limited compared to liquefaction triggered under monotonic undrained loading. An example of an informative study is Fotovvat et al. (2022) who performed an experimental investigation on the instability of gold tailings under the CSD stress path where the instability conditions observed during CSD TX loading were compared with the instability conditions under undrained TX loading. In this chapter, the key findings of the implemented test program on mine tailings are presented. The main objectives of the study are (1) to provide experimental data on the response of a sample of tailings silty sand subjected to a series of CSD tests for different densities and consolidation states, and (2) to share insights on the mechanical behavior of tailings during unloading under drained conditions leading to static flow liquefaction. The NorSand constitutive model is employed and expanded to capture the observed response of the tailings material in the laboratory.

6.3 Laboratory Testing

6.3.1 Test Material

The soil tested is a sample of tailings silty sand collected from the dam of a TSF in South America. The sample was retrieved from a depth of 1 to 2 m. All laboratory tests were performed at the UC Berkeley geotechnical laboratory. The tailings used in this study and its grain size distribution according to the ASTM C136-16 procedure are shown in Figure 6.3. According to the USCS classification system, the tailings classify as a silty sand with a fines content of FC = 20% and no plasticity (SM, PI = 0). To complement the sieve analysis, Scanning Electron Microscope (SEM) imaging was used to inspect the size, shape, and angularity of the tailings particles as shown in Figure 6.4. These tailings are composed of angular particles with medium to low sphericity. Soils with angular particles exist at a wider range of initial void ratios compared to rounded particles that upon shearing tend to form assemblies with stable and interlocked contacts associated with high shear strengths and stiffness (Mitchell and Soga 2005). The SEM images also show binding between smaller and larger particles of tailings which is the result of the physiochemical formation processes (Figures 6.4b, 6.4c). The minimum (e_{min}) and maximum (e_{max}) void ratios were

obtained using the Japanese standard JIS A 1224:2000 (2002) based on the procedures presented in Mijic et al. (2021a). The tailings' specific gravity of solids (G_s) was measured following the ASTM D 854-14 standard. Table 6.1 summarizes the index properties of the sample of tailings.

The state of the specimens at different stages during a test is primarily described with the state parameter (Been and Jefferies 1985) as shown in Eq. 6.1.

$$\psi = (e - e_c)|_p \tag{6.1}$$

where e represents the current void ratio (as defined previously) at the current mean effective confining pressure p, and e_c is the critical state void ratio at the same p. Alternatively, relative density (D_r) and e are also used.

6.3.2 One-dimensional Compression Tests

One-dimensional compression tests with constant strain rate (ASTM D4186-06) were conducted on four tailings specimens prepared at different initial void ratios. Similar to the findings of Jefferies and Been (2000), a series of normal compression lines of similar curvature were obtained. For each compression test, three unloading-reloading cycles were considered as shown in Figure 6.5.

6.3.3 Triaxial Tests

The UC Berkeley TX apparatus and software were used for the monotonic drained and undrained triaxial testing. The TX test device includes a loading frame, two pressure actuators that control the cell and back pressures, LVDT sensors to record axial deformation, and pressure and volume transducer that record data throughout the test.

The specimens were prepared using the moist-tamping method proposed by Ladd (1978) using a 6-layer tamping schedule and a moisture content of 6% to reach a nominal specimen height of 150 mm and diameter of 62 mm. The moist-tamping method was selected because a wide range of specimen densities can be achieved with accurate control of the target density while producing relatively uniform test specimens. The test specimens were built encased in a flexible membrane within a split-mold directly mounted on the bottom cap of the triaxial cell. A vacuum of about 30 kPa was gradually applied to the top cap on the specimen before dismantling the split-mold. Then a differential vacuum of about 50 kPa was maintained within the specimen as de-aired water was flushed from the bottom-up to facilitate initial saturation. Once the initial saturation was completed, the vacuum was replaced by backpressure saturation in the triaxial test device. Backpressure saturation was completed in incremental steps until the desired stress state was reached and a B-value of at least 0.95 was obtained. Following backpressure saturation, each specimen was consolidated under isotropic conditions (K_c=1.0) to the prescribed stress state prior to shearing.

Isotropically consolidated undrained and drained TX tests were carried out. The shear strain rate for the drained tests was chosen based on the time to reach 50% consolidation (t_{50}) during the consolidation stage of the test so pore water pressure did not build up within the test specimen. An axial shear rate of 0.5 mm/min was found to be adequate to maintain

drained shear for this tailings silty sand in the employed TX test device. To perform the undrained TX tests, the specimen drainage line was closed and the same shear rate as in the drained tests was applied to ensure a uniform distribution of the excess pore water pressure during undrained loading. The drained and undrained tests were not sheared beyond axial strains on the order of 22% with the objective to avoid excessive distortion of the specimen when estimating the critical state condition.

Prior to backpressure saturation, the void ratio of each as-prepared moist tamped specimen was obtained by measuring the height and diameter of the specimen. Then the change in void ratio due to vacuum saturation was tracked from the changes in specimen dimensions. During backpressure saturation, consolidation, and shear the change in void ratio was tracked by the testing software. The vertical load applied to the specimen is affected by the cell pressure acting on the load piston, hence a net vertical load was obtained by subtracting the load on the piston due to cell pressure from the applied vertical load (Lade 2016). Similarly, the stresses acting on the soil specimen due to the rubber membrane deformation were corrected using the large-strain correction factors of Duncan and Seed (1967).

Nine (9) TX tests were performed to characterize the stress-strain mechanical response and the critical state of the tailings silty sand in this study as illustrated in Figure 6.6. Figures 6.6a and 6.6b show the measured stress-strain and stress path responses measured during the undrained TX tests. Responses ranging from highly contractive with strain softening to highly dilative with strain hardening were observed with the peak strengths occurring at axial strains less than 1% in all cases. Tests CU94_098_40 and CU232_091_55 showed a contractive response with the critical state identified at a deformation between 18 to 20%. Test CU157_089_58 developed a dilatant response up to an axial strain close to 16%, beyond which the response changes and tends to stabilize with limited dilatancy (Figure 6.6a). However, the critical state could not be identified for this test within the range of axial strains during the test (i.e., ~20%). Tests CU80_087_62, CU91_070_98, and CU328_076_86 dilated throughout the test and did not reach the critical state at the end of the test. Figs 6c and 6d show the behavior during the drained shearing of loose samples. Tests CD_120_097_42 and CD_256_091_54 contracted during most of the test generating mostly positive volumetric strains (Figure 6.6d) with the critical state identified near the end of the test (i.e., between 20% – 22% axial strain). Test CD_365_085_66 stopped short at 16% axial strain; hence, the specimen was still contracting towards critical state at the end of shearing. Extrapolation of the data of the other two drained tests indicate that a final volumetric strain of about 6.4% corresponds to the critical state for test CD_365_085_66, which is the value used to estimate the position of the CSL. Table 6.2 summarizes the TX testing program performed on the tailings silty sand.

6.3.4 Constant Shear Drained Triaxial Tests

The CSD TX tests were conducted using the UC Berkeley stress-controlled loading software based on the original CKC TX testing program (Li et al. 1988). The specimens were prepared with the moist tamping method in a similar manner as it was done for the triaxial tests discussed previously. The specimens were then vacuum and backpressure saturated at the desired void ratios. In contrast to the previously described triaxial testing,

the CSD TX specimens were consolidated anisotropically in a series of small stress increments to different initial stress ratios (η_o = 0.45 to 0.80) and to void ratios that are denser of and looser of the CSL.

The shearing stage of the CSD TX tests were carried out in two stages through the stress-controlled loading software by gradually reducing the total confining stress while maintaining a constant back-pressure. First, the total confinement stress was reduced at a rate of about 2 kPa/min until the specimen was close to the failure condition (M). Then, the total confinement stress was reduced at a rate of about 0.5 - 1 kPa/min to ensure that data are collected with sufficient resolution as the test specimen approaches collapse. As mentioned in the previous section, an oil piston system acting on the principal stress direction was used to apply the axial load during the test. The oil piston system contains a valve that restricts the flow of oil during load application that limits the rate of deformation of the specimen (Anderson and Riemer 1995). The flow rate of oil can be controlled throughout the duration of the test which enables control of the specimen deformation, particularly during the rapid part of the test. The CKC system employed for the CSD TX tests enabled to maintain a constant deviatoric stress during the mean effective stress reduction stage of the test and it facilitated the collection of test data in the form of the changes in axial strain and volumetric strain by recording the changes in height, diameter, and volume of pore water during testing.

Two CSD TX tests showed dilatant responses (CSD4_426_077 and CSD_5_424_077) as illustrated in Figures 6.7a and 6.7b. The initial state of test CSD4_426_077 was denser than the CSL and therefore displays a dilatant response throughout the test. The state plot (Figure 6.7b) shows that much of this test corresponds to elastic unloading until the specimen becomes unstable and fails. The stress path of test CSD4_426_077 (Figure 6.7a) is insightful as it shows that this dense specimen can mobilize a η = 1.57 which is greater than the critical state stress ratio, M. At this point, the specimen cannot sustain further reduction in the mean effective stress p (or increase in η) and sudden failure occurs with η collapsing towards M (Figure 6.7a). Test CSD_5_424_077 is interesting because the initial state is above the CSL. During the elastic unloading portion of the test, the specimen crossed the CSL at a mean effective stress $p \approx 175$ kPa which corresponds to η = 1.38, at that point, the deviator stress oscillated around the prescribed q = 241 kPa (+/- 3 kPa). Additional unloading produced continued dilation of the specimen up to η = 1.61 followed by collapse of the specimen towards the critical state. A similar response was observed by Anderson and Riemer (1995) on their specimen S5 of Monterey #0 Sand subjected to CSD loading. The remaining 6 CSD tests of this study were prepared to initial conditions well above the CSL, hence they produced a rapid contractive collapse once the stress ratio could no longer be sustained. Tests CSD1_374_097, CSD2_380_096, and CSD3_260_095 did not reach the CSL within the limits of the test setup (i.e., LVDT length and cell pressure capacity). Even though these tests did not end at the critical state, they provide valuable insights on the response of tailings under CSD loading. For example, the initiation of instability is clearly captured in each test (Figure 6.7b). Tests CSD6_242_095, CSD7_387_089, and CSD8_224_094 underwent elastic unloading following a similar slope in the $p - e$ compared to the other CSD tests and after collapse, the final state for each test was very close to the CSL. The stress paths followed by all the loose-of-critical CSD tests show that instability and collapse are triggered at η below the critical stress ratio M (Figure 6.7a).

The change in void ratio during the CSD TX testing reported in Figure 6.7b illustrates the amount of strain the specimens mobilized at the moment of collapse. For all specimens, collapse initiates at volumetric strains on the order of 0.5% which is similar to amount of axial strain mobilized at moment of collapse (i.e., ~ 0.5% – 1%). This amount of strain mobilized right before the triggering of an uncontrolled run-away type of failure, which was typically less than 1%, is consistent with field observations of the sudden failures in the Aberfan (1966) and Fundao (2015) case histories. Table 6.3 summarizes key test conditions of the series of CSD tests performed as part of this study.

6.4 Tailings Properties

6.4.1 Critical State

Critical state soil mechanics is a theory for particulate media that relates the mechanical response to external or internal loading to void ratio (or density). Its origin dates back to the experiments on hydraulic fill sands by Casagrande (1936) and recently has been effectively used in the back-analysis of four case histories involving tailings failure (Shuttle et al. 2021): Tar Island Dyke in 1974, Fundao Tailings Dam in 2015, Cadia Dyke in 2018, and Brumadinho in 2019.

The critical state locus (CSL) for the tailings silty sand was defined from a combination of isotropic drained and undrained triaxial test results. An additional drained triaxial test with unloading-reloading cycles was also included to confirm the position of the CSL. All tests but one were not sheared beyond 22% axial strain with the objective to identify the critical state without localization or excessive distortion of the soil specimen. Following the approach taken by Been et al. (1991), the final critical state that appears to continue unchanged with shearing was taken as the critical state. The final critical state was estimated as described previously when the test ended before the critical state condition was reached. Table 6.2 summarizes the critical state conditions identified for each triaxial test. Figure 6.8a shows the CSL for the tailings silty sand in the p – e state plot. The CSL projection on the p – q stress path space was determined from stress-state at the phase transformation and at the critical state determined from the drained and undrained triaxial tests as shown in Figure 6.8b. The curvature of the CSL is apparent for this material (Figure 6.8a). Hence, an exponential idealization for the CSL is fitted to the measured data. The critical state locus is defined by the two relations in Eq. 6.2.

$$e_c = 1.057 - 0.145 \cdot \left(\frac{p}{p_{\text{ref}}}\right)^{0.43} \tag{6.2a}$$

$$q = 1.5 \cdot p \tag{6.2b}$$

where e_c is the critical state void ratio at the mean effective confining stress p, p_{ref} is a pressure of reference usually taken as 100 kPa, and q is the deviatoric stress as defined previously. In Eq. 6.2b, the critical state stress ratio (q/p) is M = 1.50.

6.4.2 Elastic Properties

The dependency of the elastic shear modulus (G_o) on the mean effective confinement

stress p as a function of void ratio was explored using a series of bender element tests. Jefferies and Been (2000) provides a functional form that is adequate for capturing these factors on the G_o. The series of bender element tests were fitted to the elastic model of Jefferies and Been (2000) to provide a first estimate of the elastic parameters to use in the calibration of the constitutive model to the test data. The model in Eq. 6.3 is used to fit bender element data.

$$G_o = \frac{14.7}{e - 0.69} \cdot \left(\frac{p}{p_{\text{ref}}}\right)^{0.61} \tag{6.3}$$

where e, p, and p_{ref} are defined in Eq. 6.2. It is noted that the constants in Eq. 6.3 can be updated using forward modeling of the triaxial test data. Figure 6.9 shows elastic shear modulus data and model used. A constant Poisson's ratio v = 0.20 was assumed for this tailings material as it is a reasonable value for a sand-sized granular material (Jefferies and Been 2016).

6.5 NorSand Constitutive Model

NorSand is a critical state constitutive model that is intended to model a wide range of uncemented soil types. It is based on associated plasticity for soil following the ideas of Drucker et al. (1957) and includes an internal cap that limits the amount of hardening possible that emanates from self-consistency conditions and that is calibrated with empirical data. The core concepts underlying NorSand are presented in Jefferies (1993). This original version of the model was developed for triaxial conditions with subsequent updates formally defining the nature of the internal cap that limits hardening and the generalization to 3D stress and strain conditions (i.e., Jefferies 1997 and Jefferies and Shuttle 2002). The derivation and documentation of the NorSand model are provided in Jefferies and Been (2016).

The state parameter (Eq. 6.1) is used in NorSand to represent the state of the soil during shearing and is intrinsically related to the maximum hardening available for a given state. A key aspect of NorSand is the introduction of the image state which corresponds to the state of zero change of volumetric strain ($\dot{\varepsilon}_v = 0$); this is an image of the critical state because the rate of change of ε_v is not zero ($d\dot{\varepsilon}_v \neq 0$). In NorSand, the state parameter at the image state (ψ_i) is used to formulate the hardening rule that controls the change in size of the yield surface. It is the use of the image state that differentiates NorSand from other critical-state-based models (Cambridge-type models) such as Cam clay (Roscoe et al. 1963) that do not produce realistic dilation upon shearing.

The stress-dilatancy rule for NorSand arises from an energy balance between the work done on a soil element and the distribution and dissipation of energy as shown in Eq. 6.4

$$D^p = M_i - \eta \tag{6.4}$$

where $D^p = d\varepsilon_v^p / d\varepsilon_q^p$ is the dilatancy, ε_q is the deviatoric strain, superscript p denotes the plastic component of strain, and M_i is the stress ratio at the image state. By including normality and by considering the rate of change of deviatoric stresses, the yield surface is obtained as

$$\frac{\eta}{M_i} = 1 - \ln\left(\frac{p}{p_i}\right) \tag{6.5}$$

In Eq. 6.5, the mean effective stress at the image, p_i, state is used to define the yield surface in contrast to typical Cambridge-type models that use the mean effective stress at the critical state, p_c. Data on a number of soils ranging from silts to sands suggest that the maximum amount of dilatancy ($D^p_{\min}$, the subscript "min" arises from the sign convention in geotechnical engineering of dilation being associated to negative volumetric strains) follows a linear relationship with the ψ_i as

$$D^p_{\min} = \chi_i \cdot \psi_i \tag{6.6}$$

where χ_i is a linear scaling parameter for the state-dilatancy relationship measured at the image state. The relationship between χ_i and the χ_{tc} measured under triaxial conditions is obtained as per Eq. 6.7

$$\chi_i = \frac{\chi_{tc}}{1 - \chi_{tc}\lambda/M_{tc}} \tag{6.7}$$

where subscript *tc* indicate measured in triaxial compression conditions and λ is the slope of the CSL (i.e., *de/dp*). Parameter χ_i takes typical values from 2 to 4 for cohesionless soils. An expression for M_i can be obtained by combining the effect of the maximum dilatancy and a term that quantifies the amount of volumetric work dissipation proposed by Nova (*N*). Eq. 6.8 shows the formulation for M_i as a function of the critical state stress ratio under triaxial conditions as

$$M_i = M\left(1 - \frac{N\chi_i|\psi_i|}{M_{i,tc}}\right) \tag{6.8}$$

The hardening rule determines the change in size of the yield surface and is presented as a measure of the distance from the current stress-state to the maximum allowable hardness which is related to the amount of maximum dilatancy. Hence, the hardening rule is formulated as a rate equation that approaches the maximum dilatancy condition with incremental deviatoric strains as shown in Eq. 6.9.

$$dp_i = H\left(p_{i,mx} - p_i\right)d\varepsilon_q^p \tag{6.9}$$

In Eq. 6.9, *H* is a hardening modulus which is calibrated against laboratory data, $p_{i,mx}$ is the maximum mean pressure associated to the current image state, $d\varepsilon_q$ is increment in deviatoric strain, and superscript *p* denotes the plastic component of strain. Figure 6.10 shows the yield surface of the NorSand constitutive model and its associated key components.

6.5.1 Model Calibration

The parameters defining the CSL, the stress ratio at the critical state, the volumetric coupling term, and the state-dilatancy scaling factor are the primary inputs to NorSand. This set of parameters are primarily obtained from TX test data. For the tailings silty sand in this study, the TX test results summarized in the previous sections are used to produce initial estimates of the parameters for NorSand. These initial estimates are then optimized using a forward iterative modeling approach (Jefferies and Shuttle 2020) in which the computed response obtained with the set of parameters is compared with the measured response. The parameters are then adjusted by minimizing the mismatch between the computed and observed responses. The objective of the iterative modeling approach is to produce a set of parameters that overall produces computed responses that capture the responses observed in a group of tests with a range of initial densities and mean confinement pressures. A key feature of a constitutive model based on critical state theory concepts is that a single set of parameters should produce the range of observed responses for different void ratios and confinement pressures because the properties that are intrinsic of the soil are independent of the density or confinement. This approach also enables the estimation of model parameters that are not easily obtained from laboratory data such as the hardening modulus.

The elastic properties (G_o and ν) are key to reproduce the response to undrained loading; hence, the elastic properties of this tailings were also initially estimated from the laboratory test measurements and then they were optimized as part of the model calibration process because it has been found that the measured elastic modulus with geophysical techniques tends to produce stiffer responses than those observed during triaxial loading.

Table 6.4 lists the set of NorSand calibrated parameters for the tailings silty sand in this study. An example of the comparison between the computed and measured responses obtained with the calibrated parameters is presented in Figure 6.11. During the calibration process, adjustment of the initial void ratio is allowed. This is done to account for the small uncertainty in the void ratio estimation during the vacuum saturation stage of the tests. An accuracy on the order of ±0.01 to ±0.03 for moist tamped specimens with initial void ratio estimation from external measurements is considered (Been et al. 1991, Jefferies and Been 2016). Figures 6.11a and 6.11b illustrate the fit to the stress-train and stress-path curves for undrained test CU94_098_40. Key features such as the peak and critical-state undrained strengths, initial stiffness, and softening behavior are well captured. This test shows post-peak instability with rapid deformation during softening. This rapid deformation is captured in NorSand by numerically allowing an additional softening term in the hardening modulus. The same set of parameters (Table 6.4) were used to model the drained triaxial test CD_120_097_42. For this test, NorSand produces a good fit to the stress-train and stress-path curves (Figures 6.11c and 6.11d). In this case, the initial stiffness and its reduction with strain are well captured, the peak drained strength is slightly underestimated with a small deviation in deviatoric stresses starting at about 5% axial strain. NorSand is an isotropic model with the yield surface expanding or shrinking centered along the mean effective stress axis (p-axis); hence, NorSand does not account for the effects of fabric on the soil response (Jefferies 1993). Therefore, part of the mismatch between the computed and measured responses is because of the unquantified fabric in both the laboratory and in the numerical model.

6.6 Yield in Unloading

6.6.1 Unloading in Critical State Plasticity

Jefferies (1997) developed the idea of an internal cap to the yield surface of critical-state-based constitutive models to reproduce realistic amounts of soil dilatancy. The existence of a cap to the yield surface has implications for stress paths involving unloading (e.g., CSD stress path). For example, take the unloading stress path indicated by the arrow in Figure 6.12. Initially, the soil experiences elastic unloading (inside the yield surface) until the stress path meets the internal vertical cap where dilatancy is maximum. Because dilatancy cannot exceed D_{min}, the yield surface must shrink so the stress state remains on the cap with associated plastic deformation and yielding (Jefferies 1997).

In NorSand, the yield surface changes size as a function of the image state (Eq. 6.9). The limiting pressure that defines the model internal cap (p_{cap} in Figure 6.12) and the mean image-state effective stress (p_{im} in Figure 6.12) are therefore related through the following expression:

$$p_{cap} = exp\left(\chi_i \cdot \psi_i / M_{i,tc}\right) p_{im} \tag{6.10}$$

For stress paths involving unloading, Eq. 6.10 is used to evaluate the stress-state of a soil element under unloading with respect to the yielding condition on the model cap as shown in Eq. 6.11.

$$\begin{aligned} p &> p_{cap} \rightarrow \text{Elastic unloading} \\ p &= p_{cap} \rightarrow \text{Yielding on cap} \end{aligned} \tag{6.11}$$

There are differences between the CSD stress path in which the deviatoric stress is held constant (or decreases only slightly) and other unloading stress paths where the deviatoric stress is reduced at a higher rate than the reduction in mean effective stress. Mathematically, the CSD stress path can be described with the following expression:

$$d\eta \geq 0 \text{ and } d\varepsilon_q > 0 \tag{12}$$

In Eq. 6.12, the change in stress ratio is zero or positive because the change in mean effective stress is greater than the change in deviatoric stress (i.e., $dp > dq$) or there is no change in the deviatoric stress (i.e., $dq = 0$). Also, it is recognized that the progressive reduction in mean effective stress induces incremental deviatoric strains; hence, the soil moves towards the critical state. For unloading stress paths like that presented in Jefferies (1997) there is a reversal of deviatoric stress which produces the condition in Eq. 6.13:

$$d\eta < 0 \text{ and } d\varepsilon_q < 0 \tag{6.13}$$

6.6.2 NorSand in CSD Unloading

The developments of Drucker et al. (1957) and Drucker (1959) that form the basis of

the plasticity idealization in NorSand are derived from a balance of work transfer mechanisms under loading conditions. Hence, the hardening law and stress-dilatancy expressions described in the previous section are applied to the curved portion of the yield surface (See Figure 6.10). For stress-states on the vertical cap, however, some changes need to be introduced to reflect the physics of work balance during unloading. As mentioned before, initially, the CSD stress path involves elastic strains and those are controlled by the elastic properties of the material. The consistency condition for yielding on the cap is $dp = dp_{cap}$ which enforces the current state of stress to move with the shrinking yield surface.

Jefferies (1997) explored the implications of the Nova's flow rule on the condition for yielding in unloading following the conditions in Eq. 6.13 as

$$D^p = \frac{-M - \eta}{1 + N} \tag{6.14}$$

where the negative sign of the critical state stress ratio, M, emanates from the reversed direction in deviatoric strains (Eq. 6.13) and N accounts for the recovered energy associated to volumetric dilation. The stress dilatancy in Eq. 6.14 is derived from the sawtooth model of soil strength in which a reverse of deviatoric strains ($d\varepsilon_q < 0$) from a given dilatancy state would involve a tendency of particles to return to their original position (Jefferies 1997). The case of CSD loading is different as the deviatoric demand does not change significantly with increasing deviatoric strains (Eq. 6.12). Initial attempts to capture yielding under CSD loading investigated the projection of stress states on the yield surface cap on to an original Cam clay yield surface to avoid inadmissible dilatancies. However, the projection of the stress states does not align with the original developments of the critical state theory that underlines the NorSand formulation (Jefferies, personal comm. 2022).

Rowe (1962) suggested M to be a function of amount of mobilized strain. In accordance with these ideas, Manzari and Dafalias (1997) proposed the critical state stress ratio to evolve with the soil state i.e., $M = M(\psi)$. In the case of the CSD stress path, it is desirable that the stress-dilatancy rule reflect the likely less amount of work associated to a system being unloaded compared to an active loading condition (Jefferies, personal comm. 2022). Eq. 6.15 is used to model the dilatancy during CSD unloading.

$$D^p = \mu M - \eta \tag{6.15}$$

where μ is a coefficient that is less than 1.0 by definition. For the tailings silty sand in this study, a first estimate of the material parameter μ can be obtained from the volumetric coupling term N as $\mu \approx 1/(1+N)$ and used in a forward iterative modeling approach. In this study, Eqs. 6.12 and 6.15 and the consistency condition $dp = dp_{cap}$ are included in the NorSand formulation to model the CSD responses observed in the laboratory test program. This version of the NorSand model is referred to as NorSandU and it is used in the following sections.

6.6.3 Simulation of CSD Tests with NorSand

The evolution of the NorSandU yield surface for test CSD4_426_077 is shown in Figure 6.13. Point *U* denotes the onset of unloading and the yield surface for this initial condition is shown as the solid curve. Sustained unloading produces an elastic response that takes place inside the yield surface up to point *Y* which denotes the initiation of yielding. Inspection of the test data indicates that yielding occurred at a mean effective stress on the order of p = 255 kPa which is close to the NorSandU prediction of p = 262 kPa. In addition, the stress path followed by CSD4_426_077 indicates that the vertical cap indicates the end of elastic unloading which is close to the lab data (i.e., point *Y*). The portion of the test between points *Y* and *C* corresponds to condition of yielding on the cap for which Eqs. 6.12 and 6.15 and the material parameter μ are relevant. Once point *C* is reached the collapse of the specimen occurs.

The ability of NorSandU to capture various aspects of sand behavior under the CSD stress path is illustrated by the modeling of tests CSD2_380_096 and CSD4_426_077 as illustrated in Figure 6.14. Test CSD2_380_096 is representative of a specimen prepared at a loose state above the CSL (ψ = 0.157) which displayed a contractive response upon failure. Conversely, CSD4_426_077 is a specimen with an initial state denser than the CSL (ψ = -0.012) that dilated throughout the test with the rate of dilation upon failure being much faster than that of the elastic unloading phase.

An initial value of μ = 1/ (1+0.15) = 0.87 was used for the modeling of the CSD TX tests. However, after a series of iterations, μ = 0.89 yielded better fits to the measured data overall. Hence this value was used to run the simulations shown in Figure 6.14. The comparison of the computed responses with the measured CSD data is provided in the form of (1) stress paths, (2) histories of volumetric strain, and (3) the change of void ratio in the state plot. Overall, a good agreement is observed between NorSandU and the measured data. Two circles are plotted on Figures 6.14a and 6.14d and they indicate the predicted yielding and collapse points (like Figure 6.13). NorSandU captures fairly well the initiation of plastic unloading and the onset of collapse at an η less than *M* for the loose specimen and at an η greater than *M* for the dense specimen. The volumetric strains produced upon collapse of test CSD2_380_096 are captured well up to axial strain of about 8%. In a similar way, the void ratio change is well reproduced. In the case of test CSD4_426_077, the volume change estimated with NorSandU is higher than that of the laboratory data. This overestimation of volumetric strain is also reflected in the state plot where higher void ratios than measured are estimated by NorSandU.

6.7 Conclusions

The CSD stress unloading path is of engineering interest because uncontrolled failure is triggered at small deformations (See Figure 6.7) and largely elastic as shown in the laboratory data presented in this study. This type of soil response could be dangerous in the field, where small strains are difficult to detect and measure. The CSD data presented in this study also shows that dense specimens can also fail rapidly (e.g., CSD4_426_077) if unloaded in a drained condition. Soil specimens prepared at initial positive state parameters (looser of critical) develop initially limited elastic rebound followed by plastic

deformation until the point of failure is reached at which all test specimens collapsed in an uncontrolled way. The experimental data also suggest that looser of critical specimens that reach the CSL at small to moderate strains can subsequently fail in dilation (e.g., CSD5_424_077).

The soil response observed during the CSD TX unloading can be captured mechanistically with the NorSandU constitutive model which is derived from critical state soil mechanics concepts. A comprehensive laboratory testing program including isotropically consolidated drained and undrained triaxial tests, one-dimensional compression tests, and bender element tests were used to characterize the mechanical response of the tailings silty sand in this study and to calibrate the NorSand model in its original form. The primary inputs to the NorSand model were obtained from conventional drained and undrained triaxial compression tests.

In this study, an extended kernel for the NorSand model (NorSandU) is used so it adequately captures yielding in unloading happening on the internal cap of the model. The modifications introduce a material parameter μ that represents the work transfer mechanism during unloading. It was found that $\mu \approx 1/(1+N)$ gives a good first approximation which can then be refined using forward iterative modeling of test data as shown in this study. It is found that NorSandU captures key changes in the soil response (i.e., yielding and collapse points). Also, the computed responses adequately reproduce the measured laboratory data.

The experimental data (i.e., index tests, 1D compression, triaxial compression, and CSD TX unloading tests) presented in this study provide a comprehensive characterization of the response of the nonplastic sitly sand tested in this research program. The tests cover a wide range of initial state parameters and initial stress ratios. The results of these tests form the basis of the findings of this study. The widely used NorSand constitutive model is extended in its formulation, so it adequately captures the responses measured in CSD unloading. The conventional triaxial and CSD TX laboratory data produced as part of this study are provided in two separate spreadsheets in Appendix C.

Table 6.1. Tailings Index Properties

D_{50}	C_u	FC (%)	G_s	PI	e_{max}	e_{min}	USCS	Particle shape
0.17	~4.5	20	2.72	0	1.17	0.69	SM	Angular

Table 6.2. Summary of drained and undrained triaxial tests to identify critical state

Test Conditions		Initial condition before shear				End of test after shear			Critical State
ID	Mode	e_o	D_{ro} (%)	ψ_o	p' (kPa)	e_f	q (kPa)	p' (kPa)	
CD120-097-42	Drained	0.968	42	0.071	120	0.848	365	239	Yes
CU94-098-40	Undrained	0.982	40	0.066	94	0.982	30	19	Yes
CU157-089-58	Undrained	0.889	58	0.007	157	0.889	271	177	Close, dilation
CU91-070-98	Undrained	0.701	98	-0.217	91	0.701	314	197	No, dilation
CU232-091-55	Undrained	0.910	55	0.059	232	0.910	144	101	Yes
CU328-076-86	Undrained	0.763	76	-0.055	328	0.763	334	224	No, dilation
CU80-087-62	Undrained	0.870	62	-0.055	80	0.870	104	75	No, dilation
CD256-091-54	Drained	0.909	54	0.068	256	0.772	686	479	Yes
CD365-085-66	Drained	0.849	66	0.043	365	0.735	958	680	Close

Table 6.3. Summary of drained and undrained CSD triaxial tests

Test ID	Initial condition				Instability condition			
	e_o	p' (kPa)	q (kPa)	η_o	e_f	p' (kPa)	q (kPa)	η_f
CSD1_374_097	0.972	374	289	0.77	0.943	196	288	1.47
CSD2_380_096	0.962	380	303	0.80	0.942	225	304	1.35
CSD3_260_095	0.953	260	198	0.77	0.953	167	199	1.19
CSD4_426_077	0.779	426	328	0.77	0.797	205	323	1.57
CSD5_424_087	0.866	424	241	0.57	0.884	144	232	1.61
CSD6_242_095	0.947	242	140	0.58	0.915	93	138	1.48
CSD7_387_089	0.897	387	173	0.45	0.901	113	172	1.52
CSD8_224_094	0.938	224	114	0.51	0.933	75	111	1.48

Table 6.4. NorSand Parameters for the tailings materials tested in this program

Parameter	Value
M_{tc}	1.50
N	0.15
χ_{tc}	2.2
H_o	40
H_u	10
G_{exp}	0.50
v	0.2

a) b)

Figure 6.1. (a) 1966 Aberfan, UK slope failure that killed 144 people, which was attributed to constant shear drained stress path loading (Stava Foundation 2021), and (b) Fundao tailings dam failure (Morgenstern 2016).

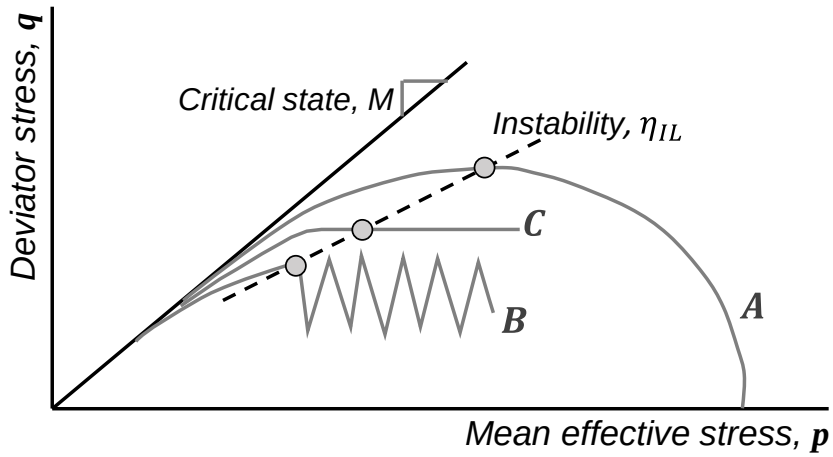

Figure 6.2. Loading paths leading to flow liquefaction under controlled conditions in the laboratory (Adapted from Lade 1992).

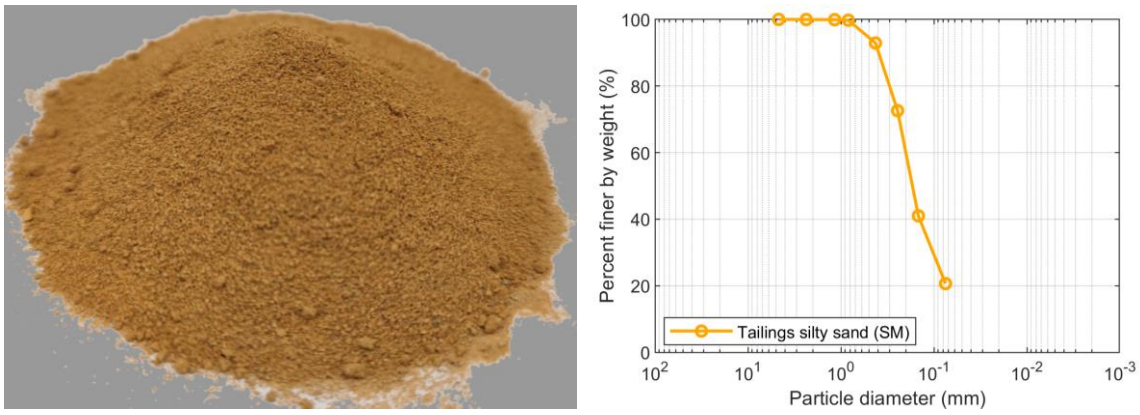

a) b)

Figure 6.3. Tailings silty sand used in this study: (a) Collected sample, and (b) Grain size distribution.

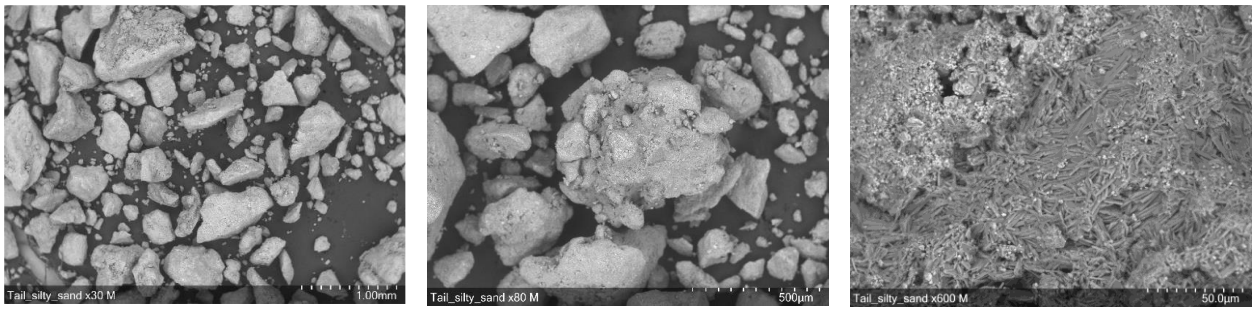

a) b) c)

Figure 6.4. SEM images of the Tailings sample used in this study.

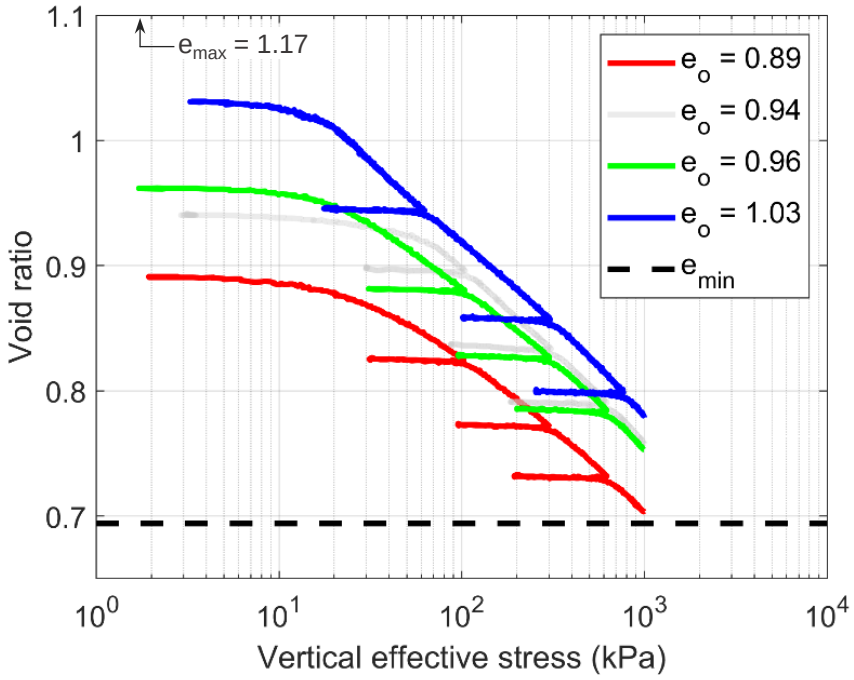

Figure 6.5. One-dimensional loading-unloading responses at different initial densities.

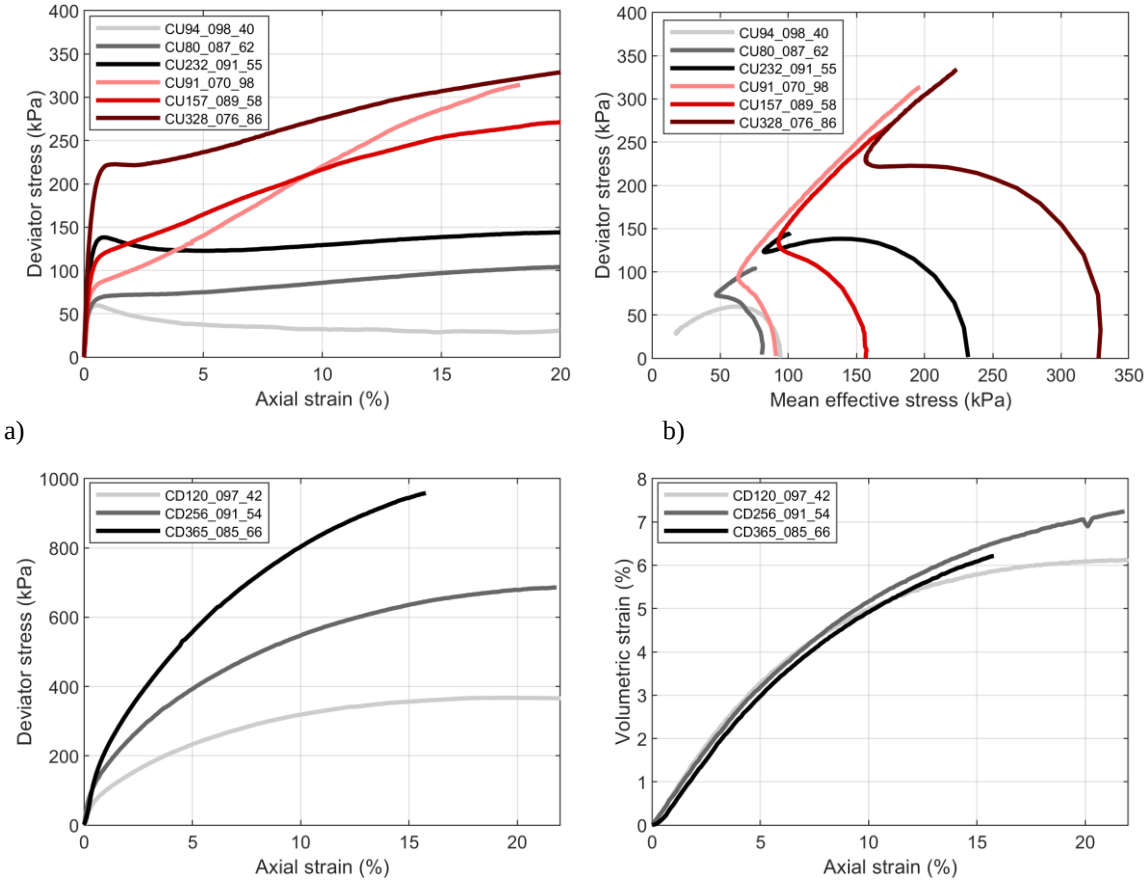

a) b)

c) d)

Figure 6.6. Triaxial test responses: 1. Undrained (a) stress-strain and (b) stress paths; and 2. Drained (c) stress-strain and (d) volumetric strains histories.

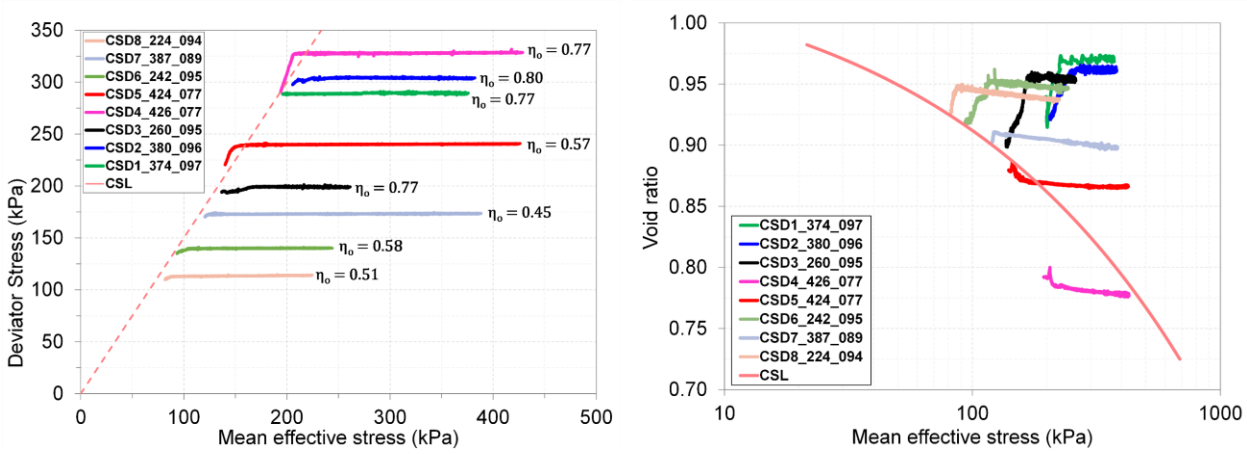

a) b)

Figure 6.7. Constant Shear Drained test results: (a) stress path and (b) state plot.

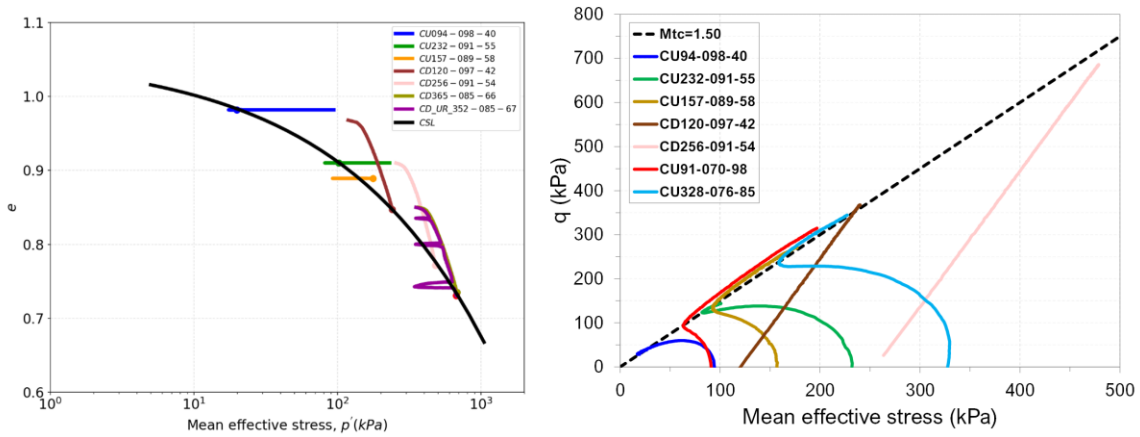

a) b)

Figure 6.8. Critical state line of the tailings silty sand: (a) state plot and (b) stress path.

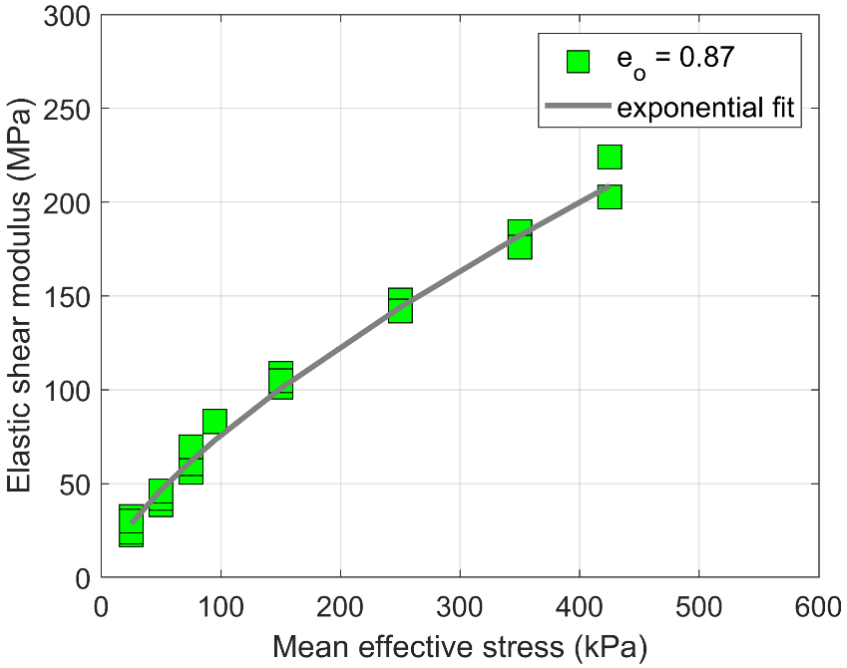

Figure 6.9. Elastic shear modulus as a function of the mean effective confining stress.

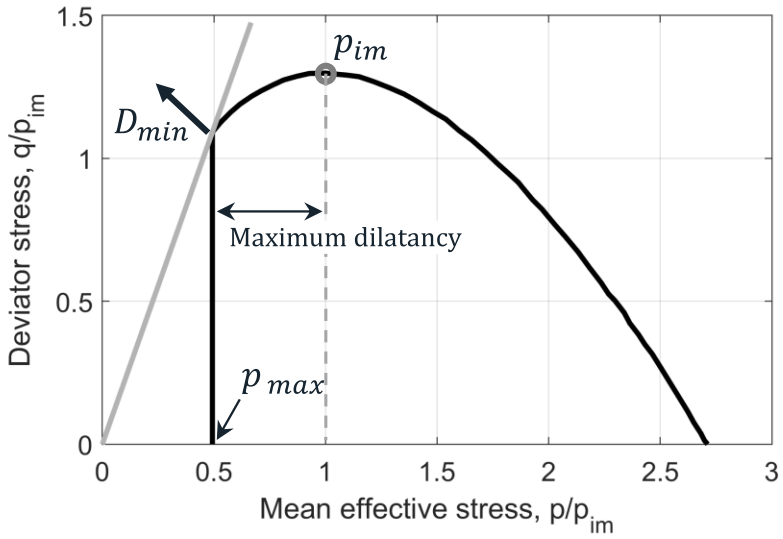

Figure 6.10. NorSand yield surface and its associated key components.

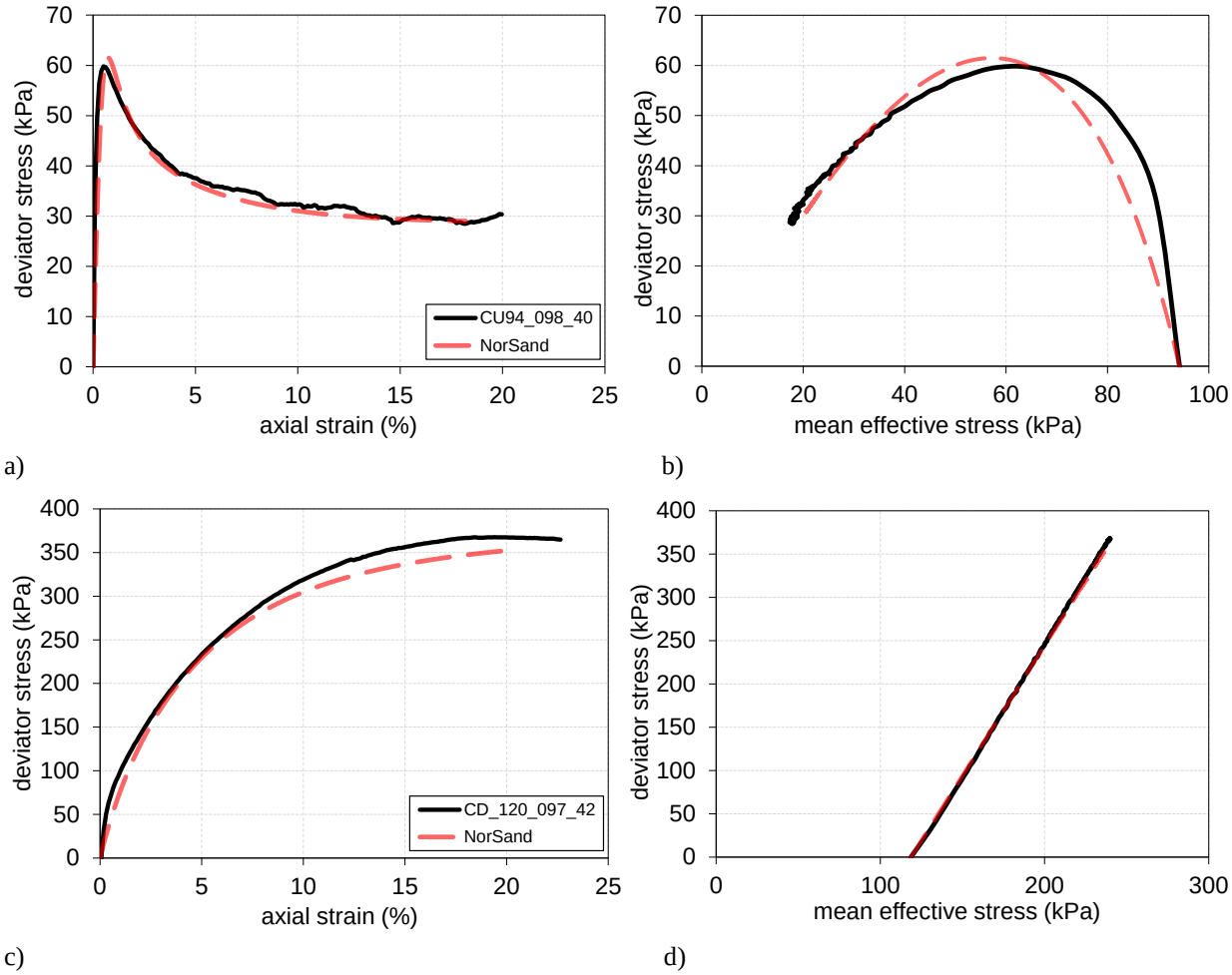

Figure 6.11. Comparison of NorSand to triaxial test results.

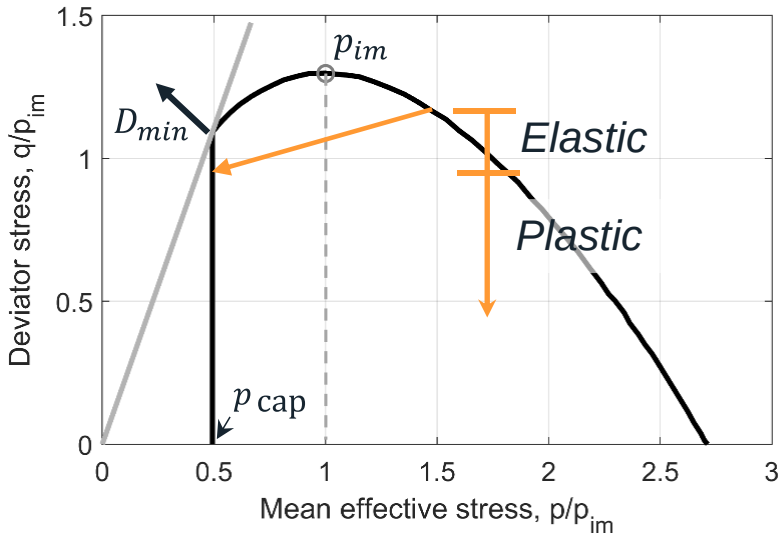

Figure 6.12. Typical stress-path followed during a CSD test.

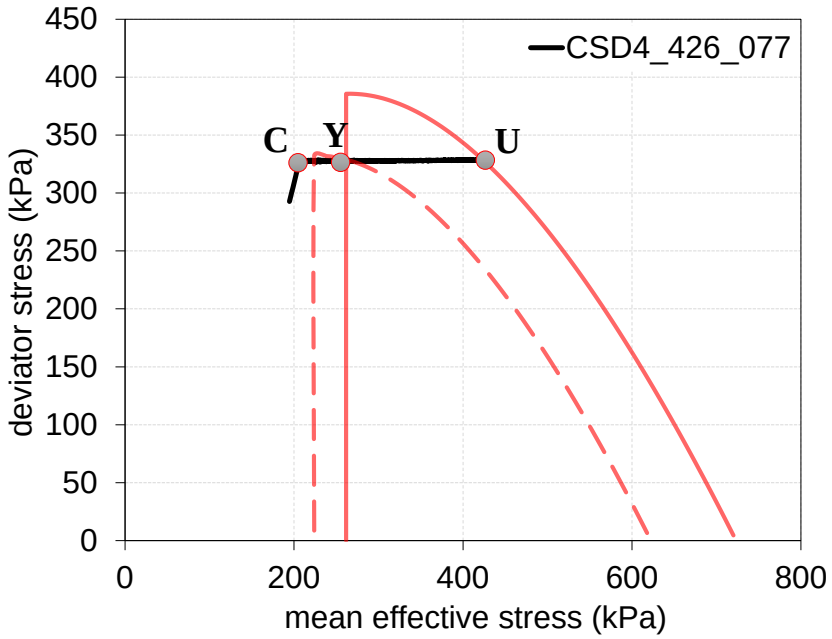

Figure 6.13. NorSandU modeling of CSD4_426_077 test.

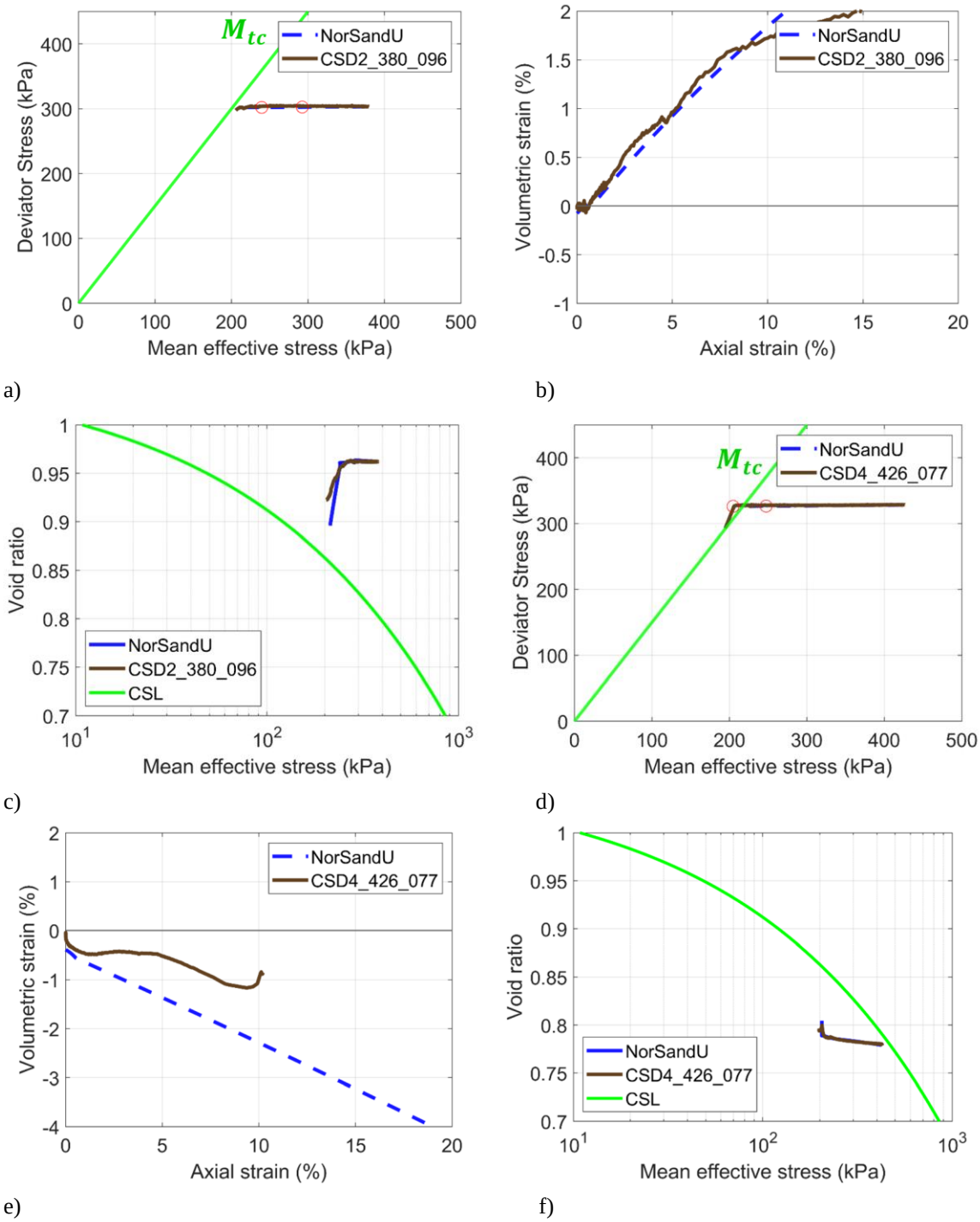

Figure 6.14. Comparison of NorSandU to CSD test results.

7 Conclusion

7.1 Summary

Through this research a CPT-based probabilistic procedure for estimating the amount of liquefaction-induced free-field ground settlement was developed. This probabilistic procedure is informed by a set of new functional models for estimating the strain potential of liquefied soils and is constrained by a comprehensive database of liquefaction-induced free-field ground settlement case histories developed as part of this research. Furthermore, this study investigated the instability conditions leading to static liquefaction of a sample of mine tailings subjected to the constant shear drained stress path through a comprehensive experimental program and subsequent numerical modeling using an extended version of the NorSand constitutive model.

CPT-based methods for estimating liquefaction-induced free-field ground settlement currently used in practice are generally: (1) rooted on strain models derived from data on only one clean sand, (2) largely deterministic, and (3) validated against a limited number of field case histories. It is not clear if these current methods can be broadly applied to all clean sands, silty sands, and to silts. Furthermore, they do not quantify the uncertainty in the estimate of liquefaction-induced ground settlement. A large laboratory database of post-liquefaction volumetric strain measurements containing information on 10 clean sands, 2 gravelly soils, 3 silty sands, 5 silts, and 3 clayey soils was compiled and then interrogated to develop a new set of strain potential models that are adequate for nonplastic uniform soil. The soil state is characterized through relative density (D_r), void ratio (e), and state parameter (ψ) in the models.

A database of 205 well-documented field case histories of liquefaction-induced ground settlement characterized by the CPT was also developed. This database differentiates natural soil deposit sites from hydraulic fill sites to account for their different formation processes and their different seismic performance. The enlarged field case history database documents a wide range of liquefaction-induced ground settlement observations at a large range of soil conditions, ground motion intensity measures, and liquefaction severity indexes. Hence, the database provides a robust basis to evaluate the mechanisms of post-liquefaction ground settlement and to assess the uncertainty in its estimation.

The integration of the newly developed strain potential models and the well-documented field case histories led to the development of a probabilistic procedure for liquefaction-induced free-field ground settlement. The procedure captures the influence of the ground motion characteristics (e.g., intensity and duration) at the site in the development of earthquake-induced cyclic shear strain and the resulting volumetric strain of soil as a function of its state. The procedure uses the unbiased FS_L at a probability of liquefaction triggering of 50% calculated using the average of two simplified liquefaction triggering procedures (i.e., the Robertson and Wride (1998) procedure as updated by Robertson (2009) and converted to a probabilistic method by Ku et al. (2012), and the

Boulanger and Idriss (2016) procedure). The average of the CPT-based correlations for D_r of Bray and Olaya (2023) and of Robertson and Cabal (2015) are used to estimate the soil state. Alternatively, ψ can be used instead of D_r. The in-situ state parameter, ψ, is obtained as the average of the CPT-based correlations of Olaya and Bray (2022) and Robertson (2010).

The probabilistic procedure to estimate liquefaction-induced ground settlement is incorporated in a performance-based procedure to estimate ground settlement while accounting for key sources of uncertainty in the soil characterization and the ground motion intensity estimations. Performance-based procedures are preferred over state-of-practice procedures that treat the assessment of seismic demand and engineering response parameters independently because a performance-based approach captures explicitly the features of the ground motion intensity at the site by including the seismic hazard information as well as the uncertainty of the estimate of liquefaction-induced ground settlement as a function of the ground motion characteristics. The ground motion intensity and the ground settlement estimations are integrated in this approach to produce alternative hazard curves for liquefaction-induced ground settlement. The mean hazard curve for liquefaction-induced ground settlement links different hazard levels (or return periods) with their corresponding values of ground settlement by evaluating a wide range of ground motion intensities and ground characterization parameters with their uncertainties. In contrast to the pseudo-probabilistic approach frequently used in practice, the performance-based procedure produces an estimate of liquefaction-induced ground settlement consistent with the specified design hazard level.

Static flow liquefaction of loose saturated tailings was identified as a key contributor to the failures of several large tailings storage facilities, such as the 1966 coal waste flow slide of Aberfan and the 2019 Brumadinho TSFs. A common feature of these static-liquefaction-induced failures is the sudden transition from a drained and stable response of the tailings material to a rapid flow type of mechanism triggered by an external or internal perturbation within the dam (Jefferies, 2021). This stress path is especially of engineering interest because uncontrolled failure is triggered at small deformations that are difficult to detect and measure in the field. However, the data available from tests performed with this stress path are largely limited to clean sands. Few tests have been performed on materials. A thorough experimental investigation, including index tests, isotropically consolidated drained and undrained triaxial tests, one-dimensional compression tests, and a series of dense-of-critical and loose-of-critical constant shear drained stress path tests, were performed on a tailings material to gain insight. An extended formulation of the NorSand generalized critical state constitutive model (NorSandU) was then used to reproduce key response features observed during the laboratory tests.

7.2 Findings

The following are the key findings resulting from the present research:

- A comprehensive database of post-liquefaction volumetric strain measurements containing 579 ε_v and 299 γ_{max} data points representative of 10 clean sands, 2 gravelly soils, 3 silty sands, 5 silts, and 3 clays was developed. The collected data are from soils with primarily uniform particle distributions, but with different origin, particle shapes, and effective confining stress.
- The post-liquefaction volumetric response of nonplastic uniform soil can be characterize using three measures of state: D_r, ψ, or e. This study shows that the variability in estimating ε_v is smaller when ψ is used compared to D_r or e.
- A set of new functional models for estimating ε_v was developed using the database of post-liquefaction volumetric strain measurements. These models are representative of nonplastic uniform sand, silty sand, and silt soils and are recommended for the evaluation of liquefaction-induced ground settlement of uniform cohesionless soil.
- A well-documented database of 205 liquefaction-induced free-field ground settlement field case histories was developed. This new database differentiates natural soil deposit sites from hydraulic fill sites to account for their different formation processes and their different seismic performance. This database provides a robust basis to evaluate the mechanisms of post-liquefaction ground settlement and to assess the uncertainty in its estimation.
- In the database of liquefaction-induced free-field ground settlement case histories, a case history is defined as the combination of (1) a site with laterally uniform soil stratigraphy with at least one CPT, (2) an earthquake event represented by its M_w, ground surface *PGA* or other *IM*, and (3) consistent post-liquefaction volumetric-induced free-field, level ground settlement measurements. A site is not defined by a CPT. Instead, a site is defined by its consistent subsurface soil characteristics and seismic performance.
- The new strain potential models and the database of liquefaction-induced free-field ground settlement case histories enabled the development of a procedure to estimate liquefaction-induced free-field ground settlement. The model captures the influence of the ground motion characteristics (e.g., intensity and duration) at the site in the development of earthquake-induced ground settlement as a function of its state.
- Engineers typically employ deterministic or pseudo-probabilistic evaluations of liquefaction-induced ground settlement. However, a performance-based approach should be used because it properly accounts for the uncertainty in the ground motion intensity measure and the soil characterization. In addition, a performance-based approach provides ground settlement estimates that are consistent with the selected design return periods. The proposed performance-based approach represents an improvement over current state-of-practice procedures that treat the assessment of seismic demand and engineering response parameters independently.
- The primary inputs to the proposed performance-based procedure are the mean seismic hazard curve for *PGA*, the deaggregation information by magnitude at different *PGA* values, and the empirical model of Bray and Olaya (2023) for

estimating free-field liquefaction-induced ground settlement. The hazard curve for *PGA* is processed using the rate of occurrence approach to capture properly its derivative, and the deaggregation information for different magnitude bins is used to incorporate the contribution to hazard for *PGA* from different earthquake events with differing magnitudes.

- Key sources of uncertainty are included in the evaluation of the liquefaction-induced ground settlement hazard. The uncertainty in the soil deposit (as characterized through the CPT) can be included in the performance-based evaluation of liquefaction-induced ground settlement. Representative ranges of the COV of the soil characterization parameters (i.e., I_{c15} and $\Sigma_i[\varepsilon_{v,i} \cdot \Delta z_i]$) are provided. A logic tree approach is employed to assess the effects of the uncertainty of the geotechnical parameters on the ground settlement hazard curve. A five-branch logic tree (with weights of 0.065, 0.24, 0.39, 0.24, and 0.065) captured well the uncertainties in the key parameters and terms of I_{c15} and $\Sigma_i[\varepsilon_{v,i} \cdot \Delta z_i]$.
- The constant shear drained stress unloading path is of engineering interest because uncontrolled failure is triggered at low strains (typically less than 1%). This type of soil response could be dangerous in the field, where small deformations are difficult to detect. The CSD stress path is a key triggering mechanism that has been attributed to several mine tailings dam failures (e.g., 2015 Fundao mine tailings failure).
- The data available from tests performed with the CSD stress path are largely limited to clean sands, with only a few tests performed on tailings materials that often have significant fines. A series of dense-of-critical and loose-of-critical state constant shear drained stress path triaxial tests performed on a mine tailings materials with fines provides an important test dataset to gain insights and to calibrate constitutive models.
- The CSD TX test data presented in this study shows that dense specimens can fail suddenly if unloaded initially in a drained condition. Tailings test specimens prepared at initial positive state parameters (looser of critical) developed initially limited elastic rebound followed by plastic deformation until the point of failure was reached at which all test specimens collapsed in an uncontrolled way. The experimental data also suggests that looser of critical specimens that reach the CSL at small to moderate strains can subsequently fail while dilating slightly.
- The primary inputs to the NorSand model were obtained from conventional drained and undrained triaxial compression tests. The soil response observed during CSD unloading can be captured mechanistically with the NorSandU model which is an extension of the NorSand model. An additional parameter μ is introduced for NorSandU.
- A modified kernel for the NorSand model is used to capture yielding in unloading during CSD unloading. The modifications introduce a material parameter μ that represents the work transfer mechanism during unloading. It was found that $\mu \approx 1/(1+N)$ gives a good first approximation which can then be refined using forward iterative modeling of test data. The formulation of NorSandU captures key changes

in the soil response (i.e., yielding and collapse points). Importantly, the computed responses reproduce the measured laboratory test results.

7.3 Future Research Recommendations

Future research recommendations emerge from the results of the current research on free-field ground settlement and static instability of liquefiable soil. Future research recommendations are:

- The developed database of post-liquefaction volumetric strain measurements is representative of cohesionless nonplastic soils with uniform particle distributions. Future research should investigate the strain potential of well-graded cohesionless soils and low plasticity silty soils. Laboratory testing programs aimed to evaluate the post-liquefaction volume change of these materials are recommended.
- The state parameter is a superior state variable compared to relative density. However, currently the post-liquefaction volumetric strain data in terms of the state parameter is about one fifth of the data in terms of relative density. New research in this topic should develop the critical state line of the tested soils so the state parameter can be used to characterize the soil.
- The current research has focused on the post-liquefaction response of natural uniform soils. But there are other engineering materials susceptible to liquefaction. For example, tailings materials are typically prone to liquefaction and subsequent deformation. Hence, research on the post-liquefaction response of these manufactured materials, which typically have angular-shaped particles, is warranted.
- A critical feature in the development of liquefaction-induced free-field ground settlement is to have pre- and post-earthquake ground elevation measurements. Future reconnaissance efforts should include high resolution Unmanned Aerial Vehicles (UAVs) and technologies such as LiDAR and InSAR to obtain detailed information about land deformation after the earthquake. Additionally, areas prone to ground deformation due to earthquake shaking should be surveyed to collect the critically important pre-earthquake data.
- The probabilistic procedure to estimate liquefaction-induced ground settlement employs the average of the triggering procedures of Boulanger and Idriss (2016) and Robertson (2009) for a probability of liquefaction of 50%. To estimate the soil state, the average of the CPT-based correlations for D_r of Bray and Olaya (2023) and Robertson and Cabal (2015) are used. The use of alternative liquefaction triggering procedures or correlations for D_r can alter the estimate of ground settlement in a manner dependent on the procedure or correlation employed. The impact of using alternative procedures should be investigated and quantified to inform engineers.
- It is difficult to capture post-liquefaction reconsolidation and sedimentation with current continuum-based constitutive models. There is merit in examining the

capabilities of large-strain numerical approaches for capturing the processes involved in post-liquefaction volumetric strains. The empirical information assembled as part of this study provides a basis of comparison for such techniques. These numerical evaluations should consider first the response at the element level to gain insights before attempting to capture the system response in a column of soil.

- Insights on the triggering of static instability of tailings materials subjected to the CSD unloading stress path were derived from a comprehensive laboratory testing of just one tailings material. Future research efforts should focus on different tailings (e.g., different gradations). In addition, in this study, the CSD tests were performed under triaxial conditions. It is encouraged to investigate drained instability of tailings materials under simple shear conditions and other modes of shearing.
- The extended NorSandU constitutive model was employed in this study. Additional numerical modeling investigations should be performed using different constitutive models. Comparison of the similarities and differences among different constitutive models will provide useful insights.

References

Abrahamson, N. A. (2020). Haz45 computer program. Accessed 2020. https://github.com/abrahamson/HAZ.

Abrahamson C., Shi M.H., Yang B. (2016). Ground-Motion Prediction Equations for Arias Intensity Consistent with the NGA-West2 Ground-Motion Models. *PEER Report 2016/05*, University of California, Berkeley, California.

Akai et al. (1995). Geotechnical Reconnaissance of the Effects of the January 17, 1995, Hyogoken-Nanbu Earthquake, Japan," Sitar, N., ed., Earthquake Engineering Research Center, Report No. UCB/EERC-95/01, Univ. of California, Berkeley, July.

Anderson, S. A., and Riemer, M. F. (1995). Collapse of saturated soil due to reduction in confinement. *J. Geotech. Eng.*, 121(2), 216–219.

Anderson, S. A., and Sitar, N. (1995). Analysis of rainfall-induced debris flows. *J. Geotech. Eng.*, 121(7), 544–552.

ASTM (2012). ASTM D4186-06 Standard Test Method for One-Dimensional Consolidation Properties of Saturated Cohesive Soils Using Controlled-Strain Loading. West Conshohocken, PA, USA: ASTM International.

ASTM (2015). ASTM C136 Standard Test Method for Sieve Analysis of Fine and Coarse Aggregates. West Conshohocken, PA, USA: ASTM International.

ASTM (2016). ASTM D854-14 Standard Test Methods for Specific Gravity of Soil Solids by Water Pycnometer. West Conshohocken, PA, USA: ASTM International.

Baker J.W., Cornell, C.A. (2006). Correlation of response spectral values for multi-component ground motions. *Bull. Seismol. Soc. Am*. 96, 215–227

Been, K. and Jefferies, M.G. (1985). A State Parameter for Sands. *Geotechnique*, 35(2), 99-112.

Been, K., Jefferies, M.G. and Hachey, J.E. (1991) The critical state of sands. *Geotechnique*, 41(3), 365–381.

Bennett M.J. (1990). Ground Deformation and Liquefaction of Soil in the Marina District. Effects of the Loma Prieta Earthquake on the Marina District San Francisco, California. *USGS Open-file Report 90-253.*

Bennett M.J. (1998). Sand Boils and Settlement on Treasure Island After the Earthquake. The Loma Prieta, California, Earthquake of October 17, 1989 – Liquefaction. *USGS Profesional Paper 1551-B.*

Beyzaei, C. Z. (2017). Fine-Grained Soil Liquefaction Effects in Christchurch, New Zealand. *Ph.D. Dissertation*. Berkeley, Univ. of California, Berkeley, CA.

Beyzaei C.Z., Bray J.D., van Ballegooy S., Cubrinovski M., Bastin S. (2018a). Depositional Environment Effects on Observed Liquefaction Performance in Silt Swamps During the Canterbury Earthquake Sequence, *Soil Dyn. Earthq. Eng.*, 107,303–321.

Beyzaei, C.Z., Bray JD, Cubrinovski M, Riemer M, Stringer M. (2018b). Laboratory-based characterization of shallow silty soils in southwest Christchurch. *Soil Dyn. Earthquake Eng*, 110, 93–109.

Bilge, H.T. (2010). Cyclic Volumetric and Shear Strain Response of Fine-Grained Soils. *Ph.D. Dissertation*. Turkey, Middle East Technical University.

Bolton, M.D (1986). The strength and dilatancy of sands. *Geotechnique*, 36(1), 65-78.

Boulanger R.W., Idriss I.M. (2016). CPT-based liquefaction triggering procedures. *J Geotech Geoenviron Eng*., ASCE, 142(2), 04015065.

Boulanger, R.W. and Ziotopoulou, K. (2015). PM4Sand (Ver 3) - A Sand Plasticity Model for Earthquake Engineering Applications. *Report No. UCD/CGM-15/01, Cen. Geotech. Modeling*, Dept. of Civil & Env. Eng., Univ. of Calif., Davis, CA; 108 pp.

Bradley B.A. (2014) Site-specific and Spatially-distributed Ground Motion Intensity Estimation in the 2010-2011 Christchurch Earthquakes. *Soil Dyn. Earthq. Eng.* 48, 35–47

Brand, E.W. (1981). Some thoughts on rain-induced slope failure. *Proc. 10th International Conference on Soil Mechanics and Foundation Engineering, 3*. Netherlands. Rotterdam, pp. 373–376.

Bray, J.D. and Macedo, J. (2017). 6th Ishihara Lecture: Simplified Procedure for Estimating Liquefaction-induced Building Settlement. *Soil Dyn. Earthq. Eng*.102, 215-231.

Bray J.D. and Olaya F.R. (2023). 2022 H. Bolton Seed Medal Lecture - Evaluating the Effects of Liquefaction. *J Geotech Geoenviron Eng.*, ASCE, in press.

Bray, J. D. and Sancio, R. B. (2006). Assessment of the liquefaction susceptibility of fine-grained soils. *J. Geotech. Geoenviron. Eng*., ASCE, 132(9), 1165–1177.

Bray, J.D., Stewart, J. P. (2000). Damage Patterns and Foundation Performance in Adapazari. *Earthquake Spectra* J., Suppl. A to V. 16, EERI, 163-189.

Bray, J. D., R. B. Sancio, H.T. Durgunoglu, A. Onalp, T. L. Youd, J. P. Stewart, R. B. Seed, O.K. Cetin, E. Bol, M. B. Baturay, C. Christensen, and T. Karadayilar. (2004). Subsurface characterization at ground failure Sites in Adapazari, Turkey. *J. Geotech. Geoenviron. Eng.* , ASCE, V.130(7), 673-685.

Bray, J.D., Cubrinovski, M., Zupan, J., and Taylor, M. (2014). Liquefaction effects on buildings in the Central Business District of Christchurch. *Earthquake Spectra J.*, EERI, V. 30(1), 85-109, DOI: 10.1193/022113EQS043M.

Bray J.D., Cubrinovski M., Dhakal R., and de la Torre C. (2019). Seismic Performance of CentrePort Wellington. *ASCE GeoCongress 2019 GSP 308*. 76 – 89.

Bray, J.D., Boulanger, R.W., Cubrinovski, M, Tokimatsu, K., Kramer, S.L., O'Rourke, T., Rathje, E., Green, R.A., Robertson, P., and Beyzaei, C.S. (2017). U.S.–New Zealand–Japan International Workshop, Liquefaction-Induced Ground Movements Effects, *2–4 November 2016 PEER Report 2017/02*, University of California, Berkeley, California.

Bullock Z., Karimi Z., Dashti S., Porter K., Liel A.B., and Franke K. W. (2019). A physics-informed Semi-empirical Probabilistic Model for the Settlement of Shallow-founded Structures on Liquefiable Ground. *Geotechnique* 69(5), 406 – 419.

California Department of Conservation. (2021). CGS Map Sheet 48: Shear-wave Velocity in Upper 30m of Surficial Geology (Vs30). https://gis.data.ca.gov/datasets/cadoc::cgs-map-sheet-48-shear-wave-velocity-in-upper-30m-of-surficial-geology-vs30/about, accessed September 2021.

Campbell K.W., Bozorgnia Y. (2012). A Comparison of Ground Motion Prediction Equations for Arias Intensity and Cumulative Absolute Velocity Developed Using a Consistent Database and Functional Form, *Earthq. Spectra*, 28, 931–941.

Casagrande, A. (1936) Characteristics of cohesionless soils affecting the stability of earth fills. *J. of Boston Society of Civil Engineers*, 23, 257–276.

Castro, G. (1969). Liquefaction of sands. *Ph.D. Dissertation*, Harvard University, Cambridge, MA (Harvard Soil Mechanics Series 81).

Cetin KO, Bilge HT, Wu J, Kammerer AM, Seed RB. (2009a). Probabilistic models for cyclic straining of saturated clean sands. *J Geotech Geoenviron Eng*, 135(3), 71–86.

Cetin K.O., Bilge H.T., Wu J., Kammerer A.M., Seed R.B. (2009b). Probabilistic models for cyclic straining of saturated clean sands. *J Geotech Geoenviron Eng*, 135(3), 71–86.

Chin, R. (1987). Volumetric strain characteristics of saturated sand under cyclic loadings. *Proc. 9th Southeast Asian Geotechnical Conference*, Bangkok, Thailand, 7.81-7.90

Chu B.L., Hsu S.C., Chang Y.M. (2003). Ground Behavior and Liquefaction Analyses in Central Taiwan-Wufeng. *Engineering Geology*, 71, 119 -139.

Chu D. B., Stewart J.P., Lee S., Tsai J.S., Lin P.S., Chu B.L., Seed R.B., Hsu S.C., Yu M.S., Wang M. CH. (2004). Documentation of Soil Conditions at Liquefaction and Non-liquefaction Sites from 1999 Chi-Chi (Taiwan) Earthquake. *Soil Dyn. Earthq. Eng*. 24, 647 - 657, data available at: https://rb.gy/s5mx7y, accessed September 2021.

Chu, J. , Leong, W.K. , Loke, W.L. , Wanatowski, D. (2012). Instability of loose sand under drained conditions. *J. Geotech. Geoenviron. Eng.* 138 (2), 207–216.

Chu, J., Wanatowski, D., Leong, W.K., Loke, W.L. , He, J. (2015). Instability of dilative sand. *Geotech. Res.* 2 (1), 35–48.

Cox B.R., Boulanger R.W., Tokimatsu K., Wood C.M., Abe A., Ashford S., Donahue J., et al. (2013). Liquefaction at Strong Motion Stations and in Urayasu City During the 2011 Tohoku-Oki Earthquake. *Earthq. Spectra*, 29, S55 – S80.

Cubrinovski M. (2019). Some important considerations in the engineering assessment of soil liquefaction. *New Zealand Geomechanics News*. 97.

Cubrinovski M, Ishihara K. (2000). Flow potential of sandy soils with different grain compositions. *Soils Found*., 40(4), 103–113.

Cubrinovski M, Ishihara K. (2002). Maximum and minimum void ratio characteristics of sands. *Soils Found*., 42(6), 65–78.

Cubrinovski M., Bray J.D., de la Torre C., Olsen M., Bradley B., Chiaro G., Stocks E., Wotherspoon L., Krall T. (2018). Liquefaction-Induced Damage and CPT Characterization of the Reclamations at CentrePort, Wellington. *Bull. Seismol. Soc. Am.* 108: 1695 – 1708.

Cubrinovski M, Rhodes A, Ntritsos N, van Ballegooy S. (2019). System response of liquefiable deposits. *Soil Dyn. Earthq. Eng*; 124(1), 212–29.

Deierlein, G., Krawinkler, H., and Cornell, C., (2003). A Framework for Performance-based Earthquake Engineering, *Pacific Conference on Earthquake Engineering*, 13–15 February 2003, Christchurch, New Zealand.

Dhakal R., Cubrinovski M., Bray J. D. (2020). Geotechnical Characterization and Liquefaction Evaluation of Gravelly Reclamations and Hydraulic Fills (port of Wellington, New Zealand). *Soils Found.*60(6),1507–31.

Dhakal R., Cubrinovski M., Bray J.D. (2022). Evaluating the Applicability of Conventional CPT-based Liquefaction Assessment Procedures to Reclaimed Gravelly Soils. *Soil*

Dyn. Earthq. Eng. 155 107176.
Di Prisco, C. and Imposimato, S. (1997). Experimental analysis and theoretical interpretation of triaxial load controlled loose sand specimen collapses. *Mechanics of Cohesive frictional Materials*, 2, 93–120.
Dobry, R. and Ladd, R. (1980). Discussion on "Soil liquefaction and cyclic mobility evaluation for level ground during earthquakes and Liquefaction Potential: Science versus Practice". *ASCE J Geotech Eng Div*, 106, 720–724.
Donahue, J. L. (2007). The Liquefaction Susceptibility, Resistance, and Response of Silty and Clayey Soils. *Ph.D. Dissertation*. Berkeley, Univ. of California.
Drucker, D.C. (1959). A definition of stable inelastic material. *J. of Applied Mechanics*, 26, 101–106.
Drucker, D.C., Gibson, R.E. and Henkel, D.J. (1957). Soil mechanics and work hardening theories of plasticity. *Trans. American Society of Civil Engineers*, 122, 338–346.
Duku, P.M., Stewart, P.M., Whang, D.H., and Yee, E. (2008). Volumetric Strains of Clean Sands Subject to Cyclic Loads. *ASCE J Geotech Eng Div*, 134(8), 1073–1078.
Duncan, J. M., Wright, S. G., Brandon, T. L. (2014). Soil Strength and Slope Stability. *Germany: Wiley*.
Duncan, J.M. and Seed, H.B. (1967). Corrections for strength test data. *J. Geotech. Eng. Division.* 93(SM5) 121–137.
ENGEO (2015). Geotechnical Data Report (GDR), Sub-Phase 1A, Treasure Island, San Francisco, California, *Project No 7091.000.000*.
ENGEO (2019a). Geotechnical Exploration, Wastewater Treatment Plant, Treasure Island, San Francisco, *Project No. 7091.000.005*.
ENGEO (2019b). Geotechnical Characterization Report, Treasure Island Stages 2 and 3 Major Phase 1, Subphases 1A, 1D, 1F, 1G, 1H, 1I Infrastructure Improvements, San Francisco, California, *Project No. 7091.000.003*.
ENGEO (2019c). Geotechnical Design Report, Treasure Island Stages 2 and 3 Major Phase 1, Subphases 1A, 1D, 1F, 1G, 1H, 1I Infrastructure Improvements, San Francisco, California, *Project No. 091.000.003*, DRAFT.
Fotovvat, A., Sadrekarimi, A., and Etezad M. (2022). Instability of gold mine tailings subjected to undrained and drained unloading stress path. *Geotechnique*, 0, 1-19.
Foulser-Piggott, R., and K. Goda (2015). Ground-motion Prediction Models for Arias Intensity and Cumulative Absolute Velocity for Japanese Earthquakes Considering Single-station Sigma and Within Event Spatial Correlation, *Bull. Seismol. Soc. Am*. 105, no. 4, 1903–1908.
Fourie, A.B., Blight, G.E. and Papageorgiou, G. (2001). Soil liquefaction as a possible explanation for Merriespruit tailings dam failure. *Can Geotech J*., 38(4), 707–719.
Franke, K. W., Ulmer, K. J., Ekstrom, L. T., and Meneses, J. F., (2016). Clarifying the difference between traditional liquefaction hazard maps and probabilistic liquefaction reference parameter maps, *Soil Dynamics and Earthquake Engineering* 90(2016), 240–249.
Franke, K. W., Peterson, B. D., Error, B. M., He, J., and Harper, J. N., (2021). Probabilistic seismic loading considerations for the assessment of liquefaction-induced volumetric settlements in the free field. *J Geotech Geoenviron Eng*., ASCE, 147(3), 04020175.

Gajo, A., Piffer, L. and De Polo, F. (2000). Analysis of certain factors affecting the unstable behavior of saturated loose sand. *Mechanics of Cohesive-Frictional Materials*, 5(3), 215–237.

Geyin M., Maurer B. (2020). Fragility Functions for Liquefaction-Induced Ground Failure. *J Geotech Geoenviron Eng*, 146(12) 04020142.

Gregor, N., Abrahamson, N.A., Atkinson, G.M., Boore, D.M., Bozorgnia, Y., Campbell, K.W., Chiou, B.S.J., Idriss, I.M., Kamai, R., Seyhan, E. and Silva, W. (2014). Comparison of NGA-West2 GMPEs. *Earthquake Spectra*, 30(3),1179-1197.

Harp, E.L., Wells, W.G., Sarmiento, J.G. (1990). Pore pressure response during failure in soils. *Geol. Soc. Am. Bull*. 102 (4), 428–438.

Holzer, T. L., Noce, T.E., and Bennett., M.J. (2010). Maps and documentation of seismic CPT soundings in the central, eastern, and western United States: U.S. Geological Survey Open-File Report 2010-1136.

Hryciw R. D. (1991). Post Loma Prieta Earthquake CPT, DMT and Shear Wave Velocity Investigations of Liquefaction Sites in Santa Cruz and on Treasure Island. *Final Report to the USGS Award No. 14-08-0001-G1865*.

Hubler, J. F. (2017). Laboratory and In-situ Assessment of Liquefaction of Gravelly Soils. *Ph.D. Dissertation*. University of Michigan, MI.

Hutabarat D., Bray J.D. (2021). Seismic Response Characteristics of Liquefiable Sites with and without Sediment Ejecta Manifestation," *J Geotech Geoenviron Eng.*, 147(6), 10.1061/(ASCE)GT.1943-5606.0002506.

Hutabarat D., Bray J.D. (2022). Estimating the Severity of Liquefaction Ejecta Using the Cone Penetration Test. *J Geotech Geoenviron Eng.* 148(3), 10.1061/(ASCE)GT.1943-5606.0002744.

Idriss I, Boulanger R. (2008). Soil liquefaction during earthquakes. *Earthquake Engineering Research Institute (EERI)*, MNO-12.

Ishihara, K. (1993). Thirty third Rankine lecture: Liquefaction and flow failure during earthquakes. *Geotechnique*, 43(3), 349–415.

Ishihara K, Yoshimine M. (1992). Evaluation of settlements in sand deposits following liquefaction during earthquakes. *Soils Found*., 32(1),173–188.

Japanese Geotechnical Society. (2000). JIS A 1224:2000 - Test Methods for Minimum and Maximum Densities of Sands, *Soil Testing Standards*; 136-138 (In Japanese).

Jefferies, M.G. (1993). NorSand: A simple critical state model for sand. *Geotechnique*, 43, 91–103.

Jefferies, M.G. (1997). Plastic work and isotropic softening in unloading. *Geotechnique*, 47, 1037–1042.

Jefferies, M.G. (2021). Improving governance will not be sufficient to avoid dam failures. *Geotech. Eng.*, 175(2), 166–180.

Jefferies, M.G. and Been, K. (2000) Implications for critical state theory from isotropic compression of sand. *Geotechnique*, 50(4), 419–429.

Jefferies M, Been K. (2016). Soil liquefaction: A critical state approach, 2nd edition. *Florida: Taylor & Francis Group*.

Jefferies, M.G. and Shuttle, D.A. (2002). Dilatancy in general Cambridge-type models. *Geotechnique*, 52(9), 625–637

Jefferies, M. and Shuttle, D. (2020) Critical State Soil Mechanics: Notes. *Vancouver*

Geotechnical society, 1 – 57.
Juang C.H. (2002). Investigation of Soil Liquefaction in the 1999 Chi-Chi, Taiwan, Earthquake, National Science Foundation, CMMI-0085143, data available at: http://hsein.people.clemson.edu/, accessed September 2021.
Juang C.H., Yuan H., Lee DH, Ku CS. (2002). Assessing CPT-based Methods for Liquefaction Evaluation with Emphasis on the Cases from the Chi-Chi, Taiwan, Earthquake. *Soil Dyn. Earthq. Eng.* 22, 241–258.
Juang C, Ching J, Wang L, Khoshnevisan S, Ku C-S. (2013). Simplified Procedure for Estimation of Liquefaction-induced Settlement and Site-specific Probabilistic Settlement Exceedance Curve Using Cone Penetration Test (CPT). *Can Geotech J* 2013;50(10).
Junaideen, S.M., Tham, L.G., Law, K.T., Dai, F.C. and Lee, C.F. (2010). Behaviour of recompacted residual soils in a constant shear stress path. *Can Geotech J.*, 47(4), 648–661.
Katsumata K., Tokimatsu K. (2012). Relationship Between Seismic Characteristics and Liquefaction Damages of Urayasu City Induced by the 2011 Great East Japan Earthquake. *9th International Conference on Urban Earthquake Engineering/ 4th Asia Conference on Earthquake Engineering.*
Kayen R.E., Mitchell J.K. (1997). Arias Intensity Assessment of Liquefaction Test Sites on the East Side of San Francisco Bay Affected by the Loma Prieta, California, Earthquake of 17 October 1989. *Natural Hazards* 16: 243–265, 1997.
Kazama, M. (2011), Residual deformation property of liquefied soil and related phenomena, *The 14th Asian Regional Conference on* Soil *Mechanics and Geotechnical Engineering*, Hong Kong.
Kokusho T., Nagao Y., Ito F., Fukuyama T. (2014). Sand Liquefaction Observed During Recent Earthquake and Basic Laboratory Studies on Aging Effect. *Earthquake Geotechnical Engineering Design 28*.
Kramer, S. L., Y. M. Huang, and M. W. Greenfield. (2014). Performance-based assessment of liquefaction hazards. *In Geotechnics for catastrophic flooding events*, 17–26. London: Taylor and Francis Group.
Kramer, S. L., and R. T. Mayfield. (2007). Return period of soil liquefaction. *J. Geotech. Geoenviron. Eng*. 133 (7): 802–813.
Ku C.S., Juang, C. H., Chang, C. W., and Ching J. (2012). Probabilistic Version of the Robertson and Wride Method for Liquefaction Evaluation: Development and Application. *Can. Geotechnical J.*, 49(1), 27-44
Ladd, R.S. (1978). Preparing test specimens using undercompaction. *Geotechnical Testing Journal*, GTJOAD, ASTM, 1(1), 1–8.
Lade, P. V. (1992). Static instability and liquefaction of loose fine sandy slopes. *J. Geotech. Eng. Division*. 118, 51-71.
Lade P.V. (2016). Triaxial Testing of Soils. *John Wiley & Sons, Ltd*.
Lee, K. L., and Albaisa, A. (1974). Earthquake induced settlements in saturated sands. *J. Geotech. Eng. Division*. GT4, 387-406.

Lee W.F., Ishihara K., Chen S.H., Chu B.L. (2011). Liquefaction Induced Ground Failures Caused by Strong Ground Motion. *5th international Conference on Earthquake Geotechnical Engineering*. Paper No. ASOLE.

Li X.S., Chan C.K., Shen C.K. (1988). An automated triaxial testing system. West Conshohocken, PA: ASTM International. 95–106.

Liu, K.S., Tsai, Y.B. (2015). A Refined Vs30 Map for Taiwan Based on Ground Motion Attenuation Relationships. *Terrestrial, Atmospheric and Oceanic Sciences Journal.* 26 (6)

Luque, R, and Bray, J.D. (2017). Dynamic analyses of two buildings founded on liquefiable soils during the Canterbury earthquake sequence. *J Geotech Geoenviron Eng*. 143(9), 04017067, 1-14

Macedo J, Bray J, Abrahamson N, Travasarou T. (2018). Performance-based probabilistic seismic slope displacement procedure. *Earthq Spectra*; 34(2):673–95.

Macedo J., Abrahamson N., Bray J.D. (2019). Arias Intensity Conditional Scaling Ground-Motion Models for Subduction Zones. *Bull. Seismol. Soc. Am*. 109, no. 4, 1343 – 1357.

Macedo J., Abrahamson N., Liu C. (2021). New Scenario-Based Cumulative Absolute Velocity Models for Shallow Crustal Tectonic Settings. *Bull. Seismol. Soc. Am*. 111, no. 4, 157 – 172.

Marcuson, W.F., Hynes, M.E., and Franklin, A.G. (1990). Evaluation and use of Residual Strength in Seismic Safety Analysis of Embankment. *Earthq Spectra*, 6(3), 529-572

Markham, C. S. (2015). Response of Liquefiable Sites in the Central Business District of Christchurch, New Zealand, *Ph.D. Dissertation*. Berkeley, Univ. of California.

Markham C.S., Bray J.D., Macedo J., Luque R. (2016). Evaluating Nonlinear Effective Stress Site Response Analyses Using Records from the Canterbury Earthquake Sequence. *Soil Dyn. Earthq. Eng.* 82, 84–98.

Markham, C.S., Bray, J.D., Cubrinovski, M. and Riemer, M. (2018). Liquefaction resistance and steady-state characterization of shallow soils within the Christchurch central business district. *ASCE J Geotech Geoenviron Eng*, 144(6), 04018032.

Mayne, P.W. and Styler, M. (2018). Soil Liquefaction Screening Using CPT Yield Stress Profiles. *Proc. Geotech Earthq Eng Soil Dyn V*, Austin, Texas, 605-616.

Maurer B.W., Green R.A., van Ballegoy S., Wotherspoon. L. (2019a). Development of Region-specific Soil Behavior Type Index Correlations for Evaluating Liquefaction Hazard in Christchurch, New Zealand. *Soil Dyn. Earthq. Eng.* 117, 96–105.

Maurer B.W., Green R.A., Cubrinovski M., Bradley B.A. (2019b). Evaluation of the Liquefaction Potential Index for Assessing Liquefaction Hazard in Christchurch, New Zealand. *J Geotech Geoenviron Eng*, 140 04014032-1.

Mesri G., Shahien M., Kane T. (2018). Seismically Induced Settlement of Ground Experiencing Undrained Shaking and Laterally Constrained Compression. *Can Geotech J*, 1-18.

Mijic, Z., Bray, J.D., Riemer, M.F., Cubrinovski, M., and Rees, S.D. (2021a). Test method for minimum and maximum densities of small quantities of soil. *Soils Found*, 61(2), 533–540.

Mijic, Z., Bray, J.D., Riemer, M.F., Rees, S.D., and Cubrinovski M. (2021b). Cyclic and monotonic simple shear testing of native Christchurch silty soil, *Soil Dyn. Earthquake*

Eng, 148.
Mijic Z., Bray J.D., van Ballegoy S. (2021c). Detailed Evaluation of Insightful Liquefaction Ejecta Case Histories for the Canterbury Earthquake Sequence, New Zealand. *USGS G20AP00079 Technical Report.*
Mijic, Z, Bray, J.D., and van Ballegooy, S. (2022). Liquefaction Ejecta Case Histories for 2010-11 Canterbury Earthquakes. *International Journal of Geoengineering Case Histories*, ISSMGE, in press.
Ministry of Business, Innovation and Employment (MBIE) (2012) Guidance: Repairing and rebuilding houses affected by the Canterbury earthquakes. Version 3, December. ISBN: 978-0-478-39907-3.
Mitchell, J. and Soga, K. (2005). Fundamentals of soil behavior, 3rd edition. *John Wiley & Sons*, Hoboken.
McGann, C.R., Bradley B.A., Cubrinovski M. (2017). Development of a Regional Vs30 Model and Typical Vs Profiles for Christchurch, New Zealand from CPT Data and Region-specific CPT-Vs correlation. *Soil Dyn. Earthq. Eng*. 95.
Morgenstern N.R., Vick S.G., Viotti C.B. and Watts B.D. (2016). Fundao Tailings Dam Review Panel: Report on the Immediate Causes of the Failure of Fundao Dam. *Cleary Gottlieb Steen & Hamilton*, LLP, New York, NY, USA.
Morgenstern N.R., Jefferies M., Van Zyl D.V. and Wates J. (2019). Report on NTSF Embankment Failure, Cadia Valley Operations. Newcrest, Melbourne, Australia.
Nagase H, Ishihara K. (1988). Liquefaction-induced compaction and settlement of sand during earthquakes. *Soils Found*, 28, 65–76.
National Research Council (NRC) (2016). State of the Art and Practice in the Assessment of Earthquake Induced Soil Liquefaction and Its Consequences. *Committee on Earthquake Induced Soil Liquefaction Assessment*. Washington, DC: The National Academies Press.
New Zealand Geotechnical Database (NZGD) (2021). New Zealand Geotechnical Database. New Zealand Earthquake Commission. https://www.nzgd.org.nz/, accessed September 2021.
O'Rourke T.D., Roth B.L. (1990). Performance of Pipeline Systems in the Marina. Effects of the Loma Prieta Earthquake on the Marina District San Francisco, California. *USGS Open-file Report 90-253.*
Olaya F.R., and Bray J.D. (2022a). CPT case histories of post-liquefaction free-field ground settlement. *J Geotech Geoenviron Eng*., *11 July 2022 Geosystems Engineering Report UCB/GT 2022-02*, Univ. of California, Berkeley.
Olaya F.R., Bray J.D. (2022b). Strain Potential of Liquefied Soil. *J Geotech Geoenviron Eng*., ASCE, in press.
Olaya F.R., and Bray J.D. (2023). Post-liquefaction free-field ground settlement case histories. *Int. J of Geoeng. Case histories*., ISSMGE, in press.
Olson, S. M., Stark, T. D., Walton, W. H., and Castro, G. (2000). 1907 static liquefaction flow failure of the north dike of Wachusett dam. *J. Geotech. Geoenviron. Eng*., 126(12), 1184–1193.
Parra, A.M. (2016). Otawa F-65 Sand Characterization, *Ph.D. Dissertation*. Davis: Univ. of California.
Porcino, D. and Caridi, G. (2007). Pre- and Post-Liquefaction Response of Sand in Cyclic

Simple Shear. *Proc ASCE Geo-Denver 2007*, Denver, Colorado.
Power M.S., Egan J.A., Shewbridge S.E., deBecker J., Faris R. (1998). Analysis of Liquefaction-induced Damage on Treasure Island. The Loma Prieta, California, Earthquake of October 17, 1989 – Liquefaction. *USGS Profesional Paper 1551-B.*
Rathje, E. M., and Saygili, G., (2008). Probabilistic seismic hazard analysis for the sliding displacement of slopes: scalar and vector approaches, *J. Geotech. Geoenviron. Eng*, ASCE 134(6), 804–814.
Rathje, E. M., and Saygili, G., (2011). Pseudo-probabilistic versus fully probabilistic estimates of sliding displacements of slopes, *J. Geotech. Geoenviron. Eng*, ASCE 137(3), 208–217.
Reuters (2019). Brazil's Vale Swings to Loss as Dam Burst Charges Near $5 bln. See https://www.reuters.com/article/us-vale-sa-resultsidUSKCN1SF2O6 (accessed April 2023).
Robertson, P.K. (2009a). Interpretation of Cone Penetration Tests – A Unified Approach. *Can Geotech J*, 46(11): 1337–1355.
Robertson P.K. (2009b). Performance-based Earthquake Design Using the CPT. *International Conference on Performance-Based Design in Earthquake Geotechnical Engineering* (Is-Tokyo 2009).
Robertson, P.K. (2010). Estimating In-situ State Parameter and Friction Angle in Sandy Soils from CPT. *2nd International Symposium on cone Penetration Testing*.
Robertson, P.K. (2016). Cone Penetration Test (CPT)-based Soil Behaviour Type (SBT) Classification System – an Update. *Can Geotech J*, 00, 1–18.
Robertson P.K., Cabal K.L. (2015). Guide to CPT for Geotechnical Engineering, 6th ed., *Gregg Drilling Testing, Inc*. Signal Hill, CA.
Robertson P.K., Wride C.E. (1998). Evaluating Cyclic Liquefaction Potential Using the Cone Penetration Test, *Can. Geotech. J*., 35(3):442–459.
Roscoe, K.H., Schofield, A.N. and Thurairajah, A. (1963). Yielding of clays in states wetter than critical. *Geotechnique*, 13, 211–240.
Roscoe, K.H., Schofield, A. N., and Wroth C.P. (1958). On The Yielding of Soils. *Geotechnique*; 8, 22-53
Russell, J., and van Ballegooy, S. (2015). Canterbury Earthquake Sequence: Increased Liquefaction Vulnerability Assessment Methodology. *T+T Report 0028-1-R-JICR-2015 prepared for the Earthquake Commission.*
Sadeghi H., Pak A., Pakzad A., Ayoubi P. (2021). Numerical-probabilistic Modeling of the Liquefaction-induced Free Fields Settlement. *Soil Dyn. Earthq. Eng.* 149, 106868.
Sancio, R. B. (2003). Ground Failure and Building Performance in Adapazari, Turkey. *Ph.D. Dissertation*. Berkeley: Univ. of California.
Sasitharan, S., Robertson, P.K., Sego, D.C. and Morgenstern, N.R. (1993). Collapse behaviour of sand. *Can Geotech J.*, 30(4), 569–577.
Seed, H.B. (1979). Soil liquefaction and cyclic mobility evaluation for level ground during earthquakes. *J. Geotech. Eng. Division*. GT2, 201-255.
Seed, H.B., Idriss, I. M., Makdisi, F., and Barnerjee, N. (1975). Representation of irregular stress time histories by equivalent uniform stress series in liquefaction analyses. *Earthquake Engineering Research Center, Report No. EERC 75-29.*

Sento N., Kazama M., Uzuoka R., Matsuya A., Ishimaru M. (2004). Liquefaction-induced volumetric change during re-consolidation of sandy soil subjected to undrained cyclic loading histories. *Proc. Cyc Behaviour of Soil and Liq Phenomena*, 199-207, Taylor and Francis.

Shamoto Y, Sato M, Zhang J. (1996). Simplified estimation of earthquake-induced settlements in saturated sand deposits. *Soils Found*, 36, 39–50.

Shuttle, D.A and Cunning J. (2007). Liquefaction Potential of Silts from CPTu. *Can Geotech J*, 45, 140–141.

Shuttle, D.A and Cunning J. (2008). Reply to the Discussion by Robertson on "Liquefaction Potential of Silts from CPTu". *Can Geotech J*, 45,142–145.

Shuttle D., Marinelli F., Brasile S., and Jefferies, M. (2021). Validation of computational liquefaction for tailings: Tar Island slump. *Geotech. Res.*, 9(1), 32-55.

Silver M.L., Seed H.B. (1971) Volume changes in sands during cyclic loading. *J. Soil Mechanics and Foundations Division ASCE*; 97(9),1171–82.

Stava Foundation (2021). The Aberfan mineral waste facility failure, 1966. See https://www.stava1985.it/the-aberfan-disaster-uk-1966/?lang=en (accessed December 2021).

Tatsuoka, F., Sasaki, T. and Yamada, S. (1984). Settlement in saturated sand induced by cyclic undrained simple shear. *Proc 8th World Conference on Earthquake Engineering*, California, 3, 398-405.

Tatsuoka, F., Zhou, S., Sato, T., and Shibuya, S. (1990). Method of evaluating liquefaction potential and its application. In Report on seismic hazards on the ground in urban areas, Ministry of Education of Japan, Tokyo. (in Japanese.)

Thevanayagam, S., and Shenthan, J. (2010). Cyclic Pore Pressure Generation, Dissipation and Densification in Granular Mixes. *Int. J Geotech Earthq Eng*, 42–60.

Thevanayagam S, Shenthan T, Mohan S, Liang J. (2002). Undrained fragility of clean sands, silty sands, and sandy silts. *ASCE J Geotech Geoenviron Eng*, 128(10), 849–859.

Toriihara, M., Yamada,Y., Morimoto, I. and Ishihara, K. (2000). The characteristics of settlement after liquefaction for sand containing fines, *Proc 35th Japan Conference on Geotechnical Engineering*, 3, 1655-1656. (In Japanese).

Tokimatsu K., and Seed, H.B. (1977). Evaluation of settlement in sands due to earthquake shaking. *J.Geotech. Eng. Division*. 113(8), 861-878.

Tokimatsu K., Katsumata K. (2012). Liquefaction-induced Damage to Buildings in Urayasu City During the 2011 Tohoku Pacific Earthquake. *International Symposium on Engineering Lessons Learned from the 2011 Great East Japan Earthquake.*

Tsukamoto Y, Ishihara K, Sawada S. (2004). Settlement of silty sand deposits following liquefaction during earthquakes. *Soils Found*, 44, 135–148.

USGS (2021a). United States Geological Survey - Map of CPT Data. https://earthquake.usgs.gov/research/cpt/data/, accessed September 2021.

USGS (2021b). United States Geological Service Vs30 Models Marina District and Treasure Island sites. https://earthquake.usgs.gov/data/vs30/, accessed September 2021.

Vantassel, J., Cox, B., Wotherspoon, L., and Stolte, A., 2018. Mapping Depth to Bedrock, Shear Stiffness, and Fundamental Site Period at CentrePort, Wellington, Using

Surface-Wave Methods: Implications for Local Seismic Site Amplification. *Bull. Seismol. Soc. Am.* 108(38).

Whang, D. H. (2001). Seismic Compression of Compacted Soils, *Ph.D. Dissertation*. Los Angeles: Univ. of California.

Wang, S. and Luna, R. (2014). Compressibility Characteristics of Low-Plasticity Silt before and after Liquefaction. *J. Materials in Civil Eng*. 26(6), 04014014 1-6.

Wang, Y., and Rathje, E., (2015). Probabilistic seismic landslide hazard maps including epistemic uncertainty, *Engineering Geology.* 196, 313–324.

Wu, J. (2002). Liquefaction Triggering and Post-Liquefaction Deformation of Monterrey 0/30 Sand under Uni-directional Cyclic Simple Shear Loading, *Ph.D. Dissertation*. Berkeley: Univ. of California.

Wu, J., and Seed, R. B. (2004). Estimating of Liquefaction-induced Ground Settlement Case Studies. *Proc., 5th Int. Conf. on Case Histories in Geotechnical Engineering*, Paper 3.09.

Wu J., Kammerer, A.M., Riemer, M.F., Seed, R.B., and Pestana J.M. (2004). Laboratory study of liquefaction triggering criteria. *Proc. 13th World Conf. on earthquake engineering*. Paper No. 2580.

Yasuda S., Ishihara K., Harada K., Shinkawa, N. (1996). Effect of Soil Improvement on Ground Subsidence due to Liquefaction. *Soils Found*, Special Issue, 99-107.

Yoshimine, M., Nishizaki, H., Amano, K., and Hosono, Y. (2006). Flow deformation of liquefied sand under constant shear load and its applications to analysis of Flow slide in infinite slope. *Soil Dyn. Earthquake Eng*, 26, 253–264.

Youd, T. L. (1972). Compaction of sands by repeated shear straining. *J. Geotech. Eng. Div.* SM7, 709-725.

Zhang G, Robertson PK, Brachman RWI. (2002). Estimating liquefaction-induced ground settlements from CPT for level ground. *Can Geotech J*, 39, 1168–1180.

Zhang G., Robertson P.K., and Brachman R.W.I. (2004). Estimating liquefaction induced lateral deformations from SPT and CPT, *ASCE. J Geotech Geoenviron Eng*. 130(8). 861–871.

Zhu, J. H., and Anderson, S. A. (1998). Determination of shear strength of Hawaiian residual soil subjected to rainfall-induced landslides. *Geotechnique*, 48(1), 73–82.

Zimmaro P., Brandenberg S.J., Stewart J.P., Kwak D.Y., Franke K.W., Moss R.E.S., Cetin K.O., Can G., Ilgac M., Stamatakos J., Juckett M., Mukherjee J., Murphy Z., Ybarra S., Weaver T., Bozorgnia Y., Kramer S.L. (2019). Next-Generation Liquefaction Database. Next-Generation Liquefaction Consortium. DOI: 10.21222/C2J040. https://www.nextgenerationliquefaction.org/, accessed September 2021.

Appendix A: Maximum shear strain and post-liquefaction volumetric strain data and trends (electronic).

This appendix contains the following electronic files:

- Characteristics of the materials and test results in Chapter 2
- Additional trends of maximum shear strain and post-liquefaction volumetric strain data

Appendix B: Data supporting the development of the 205 case histories of liquefaction-induced free-field ground settlement (electronic).

This appendix contains the following electronic files:

- Flatfile summarizing the characteristics of the 205 case histories
- Publicly available CPT data that support the case histories development
- Details of each field case history

Appendix C: Laboratory data (electronic).

This appendix contains the following electronic files:

- Isotropically consolidated triaxial test data
- Constant shear drained triaxial test data